



Annese, Valerio Francesco (2021) *A portable metabolomics-on-CMOS platform for point-of-care testing*. PhD thesis.

<http://theses.gla.ac.uk/82001/>

Copyright and moral rights for this work are retained by the author

A copy can be downloaded for personal non-commercial research or study, without prior permission or charge

This work cannot be reproduced or quoted extensively from without first obtaining permission in writing from the author

The content must not be changed in any way or sold commercially in any format or medium without the formal permission of the author

When referring to this work, full bibliographic details including the author, title, awarding institution and date of the thesis must be given

Enlighten: Theses
<https://theses.gla.ac.uk/>
research-enlighten@glasgow.ac.uk



University
of Glasgow

**A Portable Metabolomics-on-CMOS
Platform for Point-of-Care Testing**

Valerio Francesco Annese

A Thesis submitted to

James Watt School of Engineering

University of Glasgow

in fulfilment of the requirements for the degree of

Doctor of Philosophy

February 2021

Abstract

Metabolomics is the study of the metabolites, small molecules produced during the metabolism. Metabolite levels mirror the health status of an individual and therefore have enormous potential in medical point-of-care (POC) applications. POC platforms are miniaturised and portable systems integrating all steps from sample collection to result of a medical test. POC devices offer the possibility to reduce the diagnostic costs, shorten the testing time, and, ultimately, save lives for several applications. The glucose meter, arguably the most successful example of metabolomics POC platform, has already demonstrated the dramatic impact that such platforms can have on the society. Nevertheless, other relevant metabolomic tests are still relegated to centralised laboratories and bulky equipment.

In this work, a metabolomics POC platform for multi-metabolite quantification was developed. The platform aims to untap metabolomics for the general population. As case studies, the platform was designed and evaluated for prostate cancer and ischemic stroke. For prostate cancer, new affordable diagnostic tools to be used in conjunction with the current clinical standard have are needed to reduce the medical costs due to overdiagnosis and increase the survival rate. Thus, a novel potential metabolic test based on L-type amino acids (LAA) profile, glutamate, choline, and sarcosine blood concentrations was developed. For ischemic stroke, where the portable and rapid test can make a difference between life and death, lactate and creatinine blood levels were chosen as potential biomarkers. All the target metabolites were quantified using an optical method (colorimetry).

The platform is composed of three units: the cartridge, the reader, and the graphical user interface (GUI). The cartridge is the core of the platform. It integrates a CMOS 16x16 array of photodiodes, capillary microfluidics, and biological receptors onto the same ceramic package. To measure multiple metabolites, a novel method involving a combination of replica moulding and injection moulding was developed for the monolithic integration of microfluidics onto integrated chips.

The reader is composed of a custom PCB and a microcontroller board. It is used for addressing, data digitisation and data transfer to the GUI. The GUI - a software running on a portable electronic device - is used for interfacing the system, visualise, acquire, process, and store the data.

The analysis of the microfluidic structures showed successful integration. The selection of the specific chemistry for detecting the analytes of interest was demonstrated to be suitable

for the performance of the sensors. Quick and reliably capillary flow of human plasma, serum and blood was demonstrated.

On-chip quantification of the target metabolites was demonstrated in diluted human serum and human plasma. Calibration curves, kinetics parameter and other relevant metrics were determined. For all the metabolites, the limits of detection were lower than the physiological range, demonstrating the capability of the platform to be used in the target applications.

Multi-metabolite testing capability was also demonstrated using commercially and clinically sourced human plasma. For multiplexed assays, reagents were preloaded in the microfluidic channel and lyophilised. Lyophilisation also improved the shelf-life of the reagents. Alternative configurations, involving the use of paper microfluidics, integration of passive blood filter and use of whole blood, were investigated.

The characterisation of the platform culminated with a clinical evaluation for both the target applications. The same platform with minimal modification of the cartridge was able to provide clinically relevant information for both the distinct applications, highlighting the versatility of the platform for POC determination of metabolic biomarkers.

For prostate cancer, the platform was used for the quantification of the potential metabolic biomarker in 10 healthy samples and 16 patients affected by prostate cancer. LAA, glutamate and choline average concentrations were elevated in the cancer group with respect to the control group and were therefore regarded as metabolic biomarkers in this population. Metabolomic profiles were used to train a classifier algorithm, which improved the performance of the current clinical blood test, for this population.

For ischemic stroke, lactate determination was performed in clinically sourced samples. Clinical evaluation for ischemic stroke was performed using 10 samples from people diagnosed with ischemic stroke. Results showed that the developed platform provided comparable results with an NHS-based gold standard method in this population. This comparison demonstrated the potential of the platform for its on-the-spot use.

The developed platform has the potential to lead the way to a new generation of low-cost and rapid POC devices for the early and improved diagnosis of deadly diseases.

Author's declaration

Unless otherwise acknowledged, the content of this thesis is the result of my own work. None of this material has been submitted for any other degree at the University of Glasgow or any other institution.

Valerio Francesco Annese

Acknowledgements

This doctoral degree has been a life-changing experience, a long journey which would not have been possible without the support of many people. My gratitude cannot be expressed in these few lines, but I will give it a try.

First, I would like to recognize the invaluable guidance that my supervisor, Professor David Cumming, provided me during my study. His expertise and support were vital in inspiring me to think outside the box, from multiple perspectives to form a unique creative process. I would also like to pay my special regards to my second supervisors, Michael Barrett and Samadhan Patil, for their insight and assistance regarding metabolomics.

I'd also like to extend my wholehearted gratitude to all members, current and previous, of the Microsystem Technology Group. In particular, thanks to my dear friends Gianluca Melino and Claudio Accarino for making me feel at home. Thanks to James Grant for his encouragement, invaluable contribution, and practical suggestions for aspects of the work regarding fabrication and wire-bonding. Thanks to Srinivas Velugotla, Boon Cheah and Yash Shah which helped me navigate the topic at the beginning of my degree. Thanks to Christos Giagkoulovits, Mohammed Al-Rawhani and James Beeley for their support regarding the technical details of the chip. Thanks to Samadhan Patil, Chunxiao Hu, Ana-Maria Nastase and Andreea Stroia for their advice, guidance and laboratory space when performing biological experiments. Thanks to Ivonne Escorcia Carranza, Mitch Kenney, Vincenzo Pusino, Yasaman Alimi for your chats which helped me get through the journey. I am also indebted to who actively contributed to this thesis. Thanks to all of you for having welcomed me in this academic family. Without you, this journey would not have been the same.

The interdisciplinary nature of the project allowed me also to work in different environments, where I always found amicable and helpful people. I wish to express my deepest gratitude to staff and users of the James Watt Nanofabrication Centre, the Glasgow Laboratory for Advanced Detector Development, the laboratory in the Glasgow Biomedical Research Centre, the Beatson Institute for Cancer Research and the West Glasgow Ambulatory Care Hospital.

I wish to show my gratitude to the Engineering and Physical Sciences Research Council (EPSRC) for the financial support to this work.

I also wish to express my gratitude to all the people whose assistance was a milestone in the completion of this project.

Besides my academic life, I am incredibly grateful to my half, Martina, which is probably the only one which knows all the shades of this journey. We both started this journey, having only each other and a 20 kg piece of luggage. I know it has not been easy for her too, and I will always be grateful for being everything I could ever ask for. Thanks for being in my life.

I would also like to express my deepest gratitude to my parents and my brothers, for their endless love and support throughout my whole life. I would have never achieved my goals without your help.

I'd like to extend my thanks to my whole family, including grandparents, uncles and cousins, for being just the way they are.

I would also like to thank all my friends who have wished me well and believe in me.

Thanks to the University of Glasgow, Scotland, the Highlands, the castles, the sceneries, and landscapes, which I will always bring with me.

Thanks immensely to all of you,

Valerio

Outcomes of the Research Activity

My activity during my PhD research project led to the following outcomes:

Spin-out company (1)

The findings of this PhD research project have contributed to the creation of a spin-out company ‘Multicorder DX Limited’, of which I am co-founder and shareholder.

Multicorder DX has exclusive rights from the University of Glasgow to a portfolio of intellectual property that underpin this project. This portfolio comprises three pending patent applications and soft intellectual property on the design of several multimodal CMOS chips.

Filed patent (1)

A patent was filed on 08 April 2020 (application number: GB2005170.2) entitled ‘Apparatus and method for biomarker detection’. The patent is mainly based on my research activity.

Publications in international journals (7)

1. **V.F. Annese**, S.B. Patil, C. Hu, C. Giagkoulovits, M. A. Al-Rawhani, J. Grant, M. Macleod, D.J. Clayton, L.M. Heaney, R. Daly, C. Accarino, Y.D. Shah, B.C. Cheah, J. Beeley, T.R.J Evans, R. Jones, M.P. Barrett, D.R.S. Cumming. ‘A monolithic single-chip point-of-care platform for metabolomic prostate cancer detection’. *Microsystems and Nanoengineering*. In print.
2. C. Accarino*, **V.F. Annese***, B.C. Cheah, M.A. Al-Rawhani, Y.D. Shah, J. Beeley, C. Giagkoulovitis, S. Mitra, and D.R.S Cumming. "Noise characteristics with CMOS sensor array scaling." *Measurement* 152 (2020): 107325. ***both authors contributed equally to this work.**
3. C. Hu, **V.F. Annese**, S. Velugotla, M. A. Al-Rawhani, B.C. Cheah, J. Grant, M. Barrett, and D.R.S. Cumming. "Disposable Paper-on-CMOS Platform for Real-time Simultaneous Detection of Metabolites." *IEEE Transactions on Biomedical Engineering* (2020).
4. C. Accarino, G. Melino, **V.F. Annese**, M.A. Al-Rawhani, Y.D. Shah, D. Maneuski, C. Giagkoulovits, J.P. Grant, S. Mitra, C. Buttar, D.R.S. Cumming. “A 64x64 SPAD Array

- for Portable Colorimetric Sensing, Fluorescence and X-Ray Imaging". *IEEE Sensors Journal* (2019).
5. M.A. Al-Rawhani, C. Hu, C. Giagkoulovits, **V.F. Annese**, B.C. Cheah, J. Beeley, S. Velugotla, C. Accarino, J.P. Grant, S. Mitra, M.P. Barrett, S. Cochran, D.R.S. Cumming. "Multimodal integrated sensor platform for rapid biomarker detection." *IEEE Transactions on Biomedical Engineering* (2019).
 6. G. Melino, C. Accarino, M. Riehle, M. Potter, P. Fineron, **V.F. Annese**, J. P. Grant, M. Al-Rawhani, J. Beeley, I.E. Carranza, and D.R.S Cumming, "Capsule endoscopy compatible fluorescence imager demonstrated using bowel cancer tumours." *IEEE Sensors Journal* (2020).
 7. Y.D. Shah, J.P. Grant, P.W.R. Connolly, D. Hao, C. Accarino, X. Ren, M. Kenney, **V.F. Annese**, M.A. Al-Rahwani, K.G. Rew, Z.M. Greener, Y. Altmann, D. Faccio, G.S. Buller and D.R.S. Cumming. 'Ultralow light level color image reconstruction using high- efficiency plasmonic metasurface mosaic filters'. *Optica*.

Papers to be submitted in international journals (1)

1. S.B. Patil, **V.F. Annese**, C. Delles, P. Welsh, J. Dawson, M.P. Barrett and D.R.S. Cumming, "Testing utility of Multicorder: a CMOS based handheld platform to screen the stroke samples for the inflammation and kidney injury" to be submitted to PNAS, PLOS or Point of Care.

Book chapters (1)

1. S.B. Patil, **V.F. Annese**, D.R.S. Cumming. Commercial Aspects of Biosensors for Diagnostics and Environmental Monitoring. 2019. In *Advances in Nanosensors for Biological and Environmental Analysis* (pp. 133-142). Elsevier.

Publication in conference proceedings (1)

1. **V.F. Annese**, C. Hu, C. Accarino, C. Giagkoulovits, S.B. Patil, M.A. Al-Rawhani, J. Beeley, B.C. Cheah, S. Velugotla, J.P. Grant, and D.R.S. Cumming. The Multicorder: A Handheld Multimodal Metabolomics-on-CMOS Sensing Platform. 2019, June. In *2019 IEEE 8th International Workshop on Advances in Sensors and Interfaces (IWASI)* (pp. 130-135).

Oral presentations (2)

1. **V.F. Annese** and D.R.S. Cumming. ‘Development and clinical testing of a metabolomics-on-CMOS platform for prostate cancer’. Presented at ‘Electronic and Nanoscale Engineering (ENE) away day’. 31 May 2019. The Lighthouse, Glasgow, UK. Best PhD student presentation award.
2. **V.F. Annese**, C. Hu, C. Accarino, C. Giagkoulovits, S.B. Patil, M.A. Al-Rawhani, J. Beeley, B.C. Cheah, S. Velugotla, J.P. Grant, and D.R.S. Cumming. The Multicorder: A Handheld Multimodal Metabolomics-on-CMOS Sensing Platform. 2019, June. In 2019 IEEE 8th International Workshop on Advances in Sensors and Interfaces (IWASI) (pp. 130-135).

Poster presentations (4)

1. **V.F. Annese** and D.R.S. Cumming. ‘Integration of microfluidics with CMOS technology for multi-metabolite sensing’. Poster presented at ‘Electronic and Nanoscale Engineering (ENE) away day’. 18 June 2018. The Lighthouse, Glasgow, UK.
2. **V.F. Annese**, S.B. Patil and D.R.S. Cumming. ‘CMOS/microfluidics hybrid microsystem for multiple metabolites sensing’. Poster presented at ‘MegaMeet, the EPSRC Healthcare Technologies Conference’. 18 April 2018. The Playfair library hall, Old College, Edinburgh, UK.
3. **V.F. Annese**, S.B. Patil and D.R.S. Cumming. ‘CMOS/microfluidics hybrid microsystem for multiple metabolites sensing’. Poster presented at ‘Multicorder IAB Meeting’, 2018. University of Glasgow, Glasgow, UK.
4. **V.F. Annese**, S.B. Patil and D.R.S. Cumming. ‘Drop-on-demand inkjet printing for enzyme printing’. Poster presented at ‘Multicorder IAB Meeting’, 2017. University of Glasgow, Glasgow, UK.

Workshops (1)

1. ‘Sensorthon’ in partnership with Sensor City. 28 November 2019. The Royal Liverpool Hospital, Liverpool.

Table of Contents

Abstract	ii
Author's declaration.....	iv
Acknowledgements	v
Outcomes of the Research Activity.....	vii
Table of Contents	x
List of Acronyms	xiv
1 Chapter 1: Introduction to the Research Project	1
1.1. Motivations.....	1
1.2. Aims and Objectives	5
1.3. Platform Requirements	7
1.4. Thesis Outline.....	9
2 Chapter 2: Application Background.....	11
2.1. Introduction	11
2.2. Biosensors	12
2.2.1. Enzyme-based biosensors	13
2.2.2. Discussion on the detection methods	16
2.2.3. Colorimetric biosensors	19
2.2.4. Integration of the bioreceptors	21
2.2.5. Biosensors metrics	23
2.3. Integrated Optical Sensors.....	24
2.3.1. CMOS technology.....	24
2.3.2. Photodetectors	24
2.3.3. Photodetectors metrics	31
2.3.4. Other photodetectors	33
2.4. Metabolomics	35
2.4.1. Metabolomics for cancer.....	38
2.4.2. Metabolomics for prostate cancer	43
2.4.3. Metabolomics for cardiovascular diseases.....	46
2.4.4. Other metabolomics applications.....	48
2.5. Microfluidics	49
2.6. Point-of-care Systems.....	52
2.6.1. Review of POC platforms	52
2.6.2. Market Review	56
2.6.3. Discussion on platform affordability	58
2.7. Summary of the Chapter.....	60

3	Chapter 3: Embedded Platform Development	61
3.1.	Introduction	61
3.2.	The Cartridge.....	63
3.2.1.	Target applications	63
3.2.2.	Detection strategy for the target metabolites	65
3.2.3.	Simulations of colorimetric reactions	66
3.2.4.	The Multicorder chip.....	70
3.2.5.	The photodiodes array	72
3.3.	The Reader	74
3.4.	The Graphical User Interface (GUI).....	77
3.4.1.	Data acquisition.....	78
3.4.2.	Data analysis	81
3.5.	Connectivity	84
3.6.	Graphical User Interface Benchmark	86
3.6.1.	Data acquisition mode.....	86
3.6.2.	Data processing mode	87
3.7.	Summary of the Chapter.....	89
4	Chapter 4: Microfluidic System.....	90
4.1.	Introduction	90
4.2.	Microfluidic Fabrication Techniques	91
4.3.	Microfluidic integration with CMOS technology	94
4.4.	Microfluidics Design	98
4.4.1.	Design considerations	98
4.4.2.	Preliminary active microfluidics	99
4.4.3.	Passive Microfluidics	103
4.5.	Microfluidics Fabrication	108
4.6.	Microchannel Functionalisation	112
4.7.	Fabrication Results	113
4.8.	Spectral Analysis	118
4.9.	Sensor Array Characterisation.....	120
4.9.1.	Photodiode spectral analysis	120
4.9.2.	Photodiode output characteristic	121
4.9.3.	Sensor array characterisation	123
4.10.	Capillary Flow Characterisation	125
4.11.	Summary of the Chapter	128
5	Chapter 5: Metabolomics-on-CMOS	129

5.1.	Introduction	129
5.2.	Experimental Setup	129
5.3.	Metabolomics-on-CMOS in Diluted Serum.....	131
5.3.1.	Materials and Methods	131
5.3.2.	PCa Metabolites	134
5.3.3.	Ischemic Stroke Metabolites	137
5.3.4.	Discussion	139
5.3.5.	Test Duration.....	141
5.4.	Microchannel Functionalisation	143
5.4.1.	Deposition and Regents Printing.....	143
5.4.2.	Freeze-drying	147
5.4.3.	Reagents stability	149
5.5.	Multiplexed Assays	152
5.5.1.	Multiplexed Assays in Human Plasma	152
5.5.2.	Paper Microfluidics: An Alternative Approach	155
5.6.	Whole Blood Experiments	159
5.7.	Summary of the Chapter.....	162
6	Chapter 6: Clinical Evaluation	164
6.1.	Introduction	164
6.2.	Platform Optimisation for Clinical Evaluation	164
6.3.	Research Ethics and Data Protection.....	165
6.4.	Prostate Cancer Clinical Evaluation.....	166
6.4.1.	Materials and Methods	166
6.4.2.	Calibration.....	169
6.4.3.	Blind validation.....	172
6.4.4.	Clinical evaluation	174
6.4.5.	Validation against standard methods	180
6.4.6.	Classification.....	182
6.4.7.	Discussion	186
6.5.	Ischemic Stroke Clinical Evaluation	188
6.5.1.	Materials and Methods	189
6.5.2.	Calibration.....	190
6.5.3.	Clinical evaluation	192
6.5.4.	Validation against standard method	193
6.5.5.	Discussion	194
6.6.	Multiplexed Assay with Clinical Samples	195

6.7. Summary of the Chapter.....	198
7 Chapter 7: Conclusion.....	200
7.1. Introduction	200
7.2. Limitations and Future Works.....	201
7.2.1. Technology limitations and future works	201
7.2.2. Limitations and future work of the clinical studies.....	204
7.2.3. Additional potential applications	206
7.2.4. Towards a commercial device.....	207
Appendix.....	209
A. Matlab Modelling of Colorimetric Reactions.....	209
B. Microcontroller firmware (C++).....	210
C. Extract of the data acquisition code (Matlab).....	210
D. Extract of the data processing Code (Matlab)	213
E. Contact angle measurements	217
F. Matlab Modelling of a Passive Microfluidic Channel with Rectangular Section 220	
G. Wire Bonding and Packaging Protocol.....	223
H. Biochemical Protocol for reagents preparation used for diluted serum experiments	225
I. Biochemical Protocol for reagents preparation used for microchannel functionalisation.....	226
J. Enzyme printing protocol.....	227
K. Ethical approval letters	228
L. Procedure for clinical sample collection.....	232
M. PCA scores for classification.....	234
Bibliography.....	235

List of Acronyms

4AAP	4-aminoantipyrine
ADC	Analog-to-digital converter
APD	Avalanche photodiode
ATP	Adenosine triphosphate
AUC	Area under the curve
CCD	Charge-coupled device
ChOx	Choline oxidase
CMOS	Complementary-MOS
CNN	Creatininase
CPGA	Ceramic Pin Grid Array
CTN	Creatinase
CVD	Cardiovascular disease
DI	Deionised
DNA	Deoxyribonucleic acid
ELISA	Enzyme-linked immunosorbent assay
FDA	Food and drug administration
FN	False negatives
FoM	Figure of merit
FP	False positives
FPN	Fixed pattern noise
Fps	Frames per second
FWHM	Full width half maximum
GC-MS	Gas chromatography MS
GDh	Glucose dehydrogenase
GlOx	Glutamate oxidase
Gox	Glucose oxidase
GP	General practice
GPIO	General-purpose input-output
GUI	Graphical user interface
HCl	Hydrochloric acid
HDL	High-density lipoprotein
HIV	Human immunodeficiency virus
HRP	Horseradish peroxidase
I/O	Input/output
IC	Integrated circuit
ICU	Intensive care unit
ID	Identification
IPA	Isopropyl alcohol
ISFET	Ion-sensitive field-effect transistor
IUPAC	International Union of Pure and Applied Chemistry
JWNC	James Watt Nanofabrication Centre
K2EDTA	Dipotassium ethylenediaminetetraacetic acid
KNN	K-nearest neighbours
LAA	L-amino acid
LAAOx	LAA oxidase
LaOx	Lactate oxidase
LC	Liquid chromatography
LDL	Low-density lipoprotein
LED	Light emitting diode
LFA	Lateral flow assay
LOD	Limit of detection

LOQ	Limit of quantification
LSB	Least significant bit
MEMS	Microelectromechanical system
MIS	Metal-insulator-semiconductor
MOSFET	Metal-oxide-semiconductor field effect transistor
MS	Mass spectroscopy
MSB	Most significant bit
MST	Microsystem technology
NAD	Nicotinamide adenine dinucleotide
NEMS	Nanoelectromechanical system
NEP	Noise equivalent power
NHS	National Health Service
NMOS	N-type MOS
NMR	Nuclear magnetic resonance
OXPHOS	Oxidative phosphorylation
PBS	Phosphate-buffered saline
PC	Personal computer
PCa	Prostate cancer
PCA	Principal Component Analysis
PCB	Printed circuit board
PDMS	Polydimethylsiloxane
PMMA	Poly(methyl methacrylate)
PMOS	P-type MOS
POC	Point-of-care
PPP	Pentose phosphate pathway
PSA	Prostate-specific antigen
PVA	Polyvinyl alcohol
RMSE	Root mean square error
RNA	Ribonucleic acid
ROC	Receiver operating characteristic curve
SaOx	Sarcosine oxidase
Sn	Sensitivity
SNR	Signal to noise ratio
Sp	Specificity
SPAD	Single-photon avalanche diode
SSE	Sum of squares error
SVM	Support Vector Machine
TCA	Krebs cycle
TCP/IP	Internet protocol suite
TN	True negative
TNR	True negative rate
TP	True positives
TPR	True positive rate
UART	Universal Asynchronous Receiver/Transmitter
UPLC-MS/MS	Ultra-performance liquid chromatography-tandem mass spectrometry
USB	Universal serial bus
UV	Ultraviolet
ZIF	Zero insertion force

Chapter 1: Introduction to the Research Project

1.1. Motivations

Point-of-care (POC) technology refers to all the miniaturised, portable, automatised devices capable of providing healthcare close to or near the patient [1]. In practice, POC platforms are portable diagnostic devices that can be operated by the general population in any location, including home, ambulance, hospitals, critical care facilities and remote locations. POC testing is a new emerging healthcare model. Nowadays, the most commonly used approach for testing in healthcare throughout the world is the centralised laboratory [1]. Typically, samples are collected by trained personnel from various locations, including general practice surgeries and hospitals. Samples are then transferred to a laboratory where they are analysed by trained personnel. Results are then communicated to the patient.

The use of POC devices simplifies the process of sample testing by providing an on-the-spot sample-to-answer test in a few minutes. POC provides results rapidly thereby saving time that would be spent with samples being transferred to the laboratory. There is no need to wait for a trained personal to run the tests and thus the results do not need to be transmitted and collected. POC platforms can therefore reduce the response of a test from hours/days to minutes [2]. Table 1.1 illustrates the two different processes in healthcare testing.

The rapidity and portability of POC testing might be more advantageous than laboratory testing in specific applications. The rapidity of POC testing can make a difference between life-or-death for applications requiring immediate availability of diagnostic data, such as sudden and acute medical conditions [2]. For instance, sepsis survival rate improves by 7.6% per hour of earlier diagnosis [3]. For acute cardiovascular events, such as ischemic stroke, early intervention within the so-called golden period (1-2 hours after the event) improves the survival rate by 80% [4].

Table 1.1 Comparison of of traditional testing vs POC testing.

	Traditional testing	Poin-of-care testing
Sample collection	Sample is collected by trained personnel in specilised facilities, including general practice, hospital, clinic, critical care.	Sample is collected by the user/carer anywhere, including home, ambulance, remote locations.
Analysis	Sample is analysed in a laboratory by trained personnel. Sample processing might be required.	Sample can be analysed anywhere by the user/carer. Minimal sample processing might be required.
Duration	From sample to answer in hours/days.	From sample to answer in minutes.

27 The portability of POC platforms has the potential to improve healthcare quality in rural and
28 remote areas [1]. Testing infectious diseases in resource-poor locations, for instance, has the
29 potential to save many lives by providing clinical information for conditions otherwise
30 undiagnosed [1].

31 The need for rapid, adaptable and low-cost POC testing platform providing reliable and
32 quick results have been outlined in pandemic scenarios [5]. The recent Covid-19 pandemic
33 required population-wide strategies, including mass-testing and contact tracing, both
34 potentially deliverable using POC technologies and challenging to implement when adopting
35 centralised testing [5].

36 POC technology has the potential to reduce medical costs in some applications. For instance,
37 in the case of prostate cancer (PCa), the widely used prostate-specific antigen (PSA) test, the
38 current standard blood test for diagnosis, has been found to be unreliable. Fewer than one in
39 three men with an elevated PSA will have PCa [6][7]. The high number of misdiagnosis due
40 to PSA unreability can lead to unnecessary medical procedures (e.g. digital rectal
41 examination, biopsy, etc). Besides being painful, invasive, and having the potential to cause
42 complications, PSA downstream tests can be expensive [8], accounting for more than 70%
43 of the medical costs associated with PCa screening. The adoption of a new blood test for
44 PCa, supplementary to the PSA test, has the potential to reduce misdiagnosis, hence costs,
45 and improve quality of health [9]. Candidate metabolic biomarkers have been identified for
46 PCa. POC technology has the potential to enable detection of those candidate metabolomics
47 biomarkers at a lower cost with respect to the equipment traditionally used for these analyses.
48 Besides PCa, candidate metabolic markers have been identified for a variety of diseases.
49 With its unique capability of describing the phenotype of the individual [10], [11],
50 metabolomics - the study of the molecules produced by cells during the metabolism - is
51 considered to have enormous potential in POC testing [12], [13]. While the study of
52 metabolites is widely exploited in pharmacology [14], metabolomics for diagnostics and
53 screening is very much research laboratory-based, mainly because the equipment
54 traditionally employed for metabolomics is bulky and expensive [12], [15].

55 Metabolomics POC platforms have already demonstrated a dramatic social impact with
56 handheld glucose meters forging 85% of the overall POC market [16]. To date, POC testing
57 devices share a noteworthy market of approximately \$21 billion [16]. It is projected that this
58 market will keep growing in the next years, reaching an estimated value of \$36 billion by
59 2025 [16]. North America market may witness the highest growth until 2024, although major

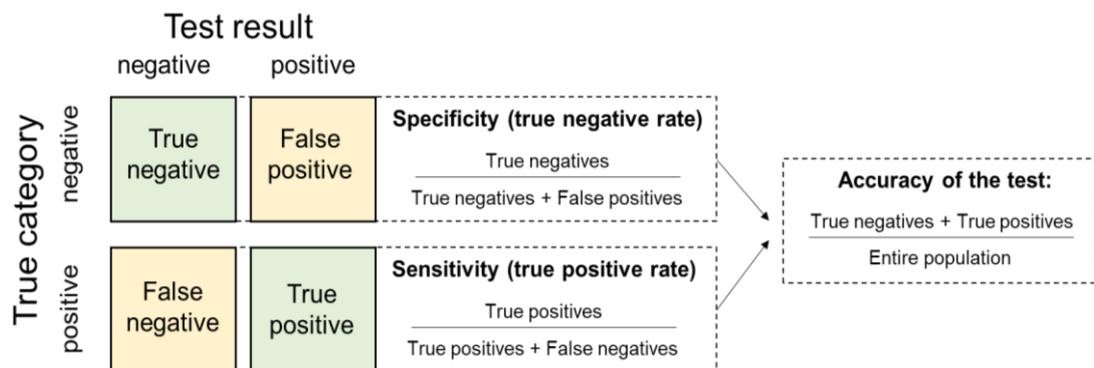
60 market growth is expected also in Europe, India, and Asia [16]. Currently, the market is
 61 dominated by a small number of well-established companies, including Roche, Abbott,
 62 Siemens, GE Healthcare and Medtronic [16].

63 Several limitations and challenges are slowing down the process of widespread of
 64 diagnostics POC devices in the market. The main challenges for the development of
 65 commercial POC platforms are discussed in the following.

66 **Accuracy vs. Application.** When a medical test is performed, the outcome typically yields
 67 to a positive (i.e. abnormal) or negative (i.e. normal) result with respect to a certain disease.
 68 Ideally, the test should be able to provide a certain and reliable result, with no false positive
 69 or negative. However, in practice this is not the case. Thus, the performance of the test is
 70 usually quantified by the diagnostic (or clinical) sensitivity, specificity, and accuracy (see
 71 Figure 1.1). The diagnostic sensitivity, also referred to as true positive rate (TPR), is the
 72 portion of positive samples correctly classified as positives [17] [18]. The diagnostic
 73 specificity, also known as true negative rate (TNR), is the portion of negative samples
 74 correctly classified as negatives [17] [18]. The diagnostic accuracy is the ratio between the
 75 sum of the true positive and negatives over the entire population [17].

76 The diagnostic capability mainly depends on two factors: the analytical performance of the
 77 sensor and the target analyte. Laboratory equipment has typically higher analytical
 78 performance than POC devices. This is because POC devices are more inclined to errors,
 79 interferences, outliers and device-to-device variability than laboratory equipment because
 80 they are operated in a variety of settings [2]. POC platform also uses unprocessed and readily
 81 available specimens (i.e. finger-prick blood, saliva, etc) and techniques aiming at reducing
 82 the cost of the test. Nevertheless, the POC platform must be capable of delivering
 83 satisfactory diagnostic performance with respect to the application.

84



85

86 *Figure 1.1 Schematic illustration of diagnostic specificity, sensitivity, and accuracy.*

87 **Multi-analyte platform.** The demand for multi-analyte POC platforms with accuracy
88 suitable for providing clinically relevant information is another relevant challenge in the
89 field of commercial POC testing [1], [2]. Running multiple simultaneous tests can be
90 required for many assays which are unreliable without control measurements. Multi-analyte
91 platforms can also test a panel of biomarkers, enabling the use of classification algorithm
92 and improving the accuracy of the test by performing additional supporting measurements
93 [2]. Lastly, multi-analyte POC platforms are desirable because they avoid the need for
94 manufacturing, use and disposal of several devices [1].

95 **System integration.** POC platforms are composed of different subsystems which need to be
96 integrated. Subsystems also include sensors and biological reagents. Although both
97 electronics and biology can rely on robust methods and procedures, their integration for a
98 commercial purpose is still quite challenging. The procedures used for surface
99 functionalisation is usually strongly dependent on the application. Recipes are usually tuned
100 by experimental studies and empirical observation [19]. These limitations are particularly
101 problematic for multi-analyte platforms, where multiple functionalisations of different
102 sensing areas are required [20]. In this case, the procedures involved in the fabrication of the
103 device must avoid crosstalk between different reaction zones [20].

104 Typically, reagents are biological molecules and it is fundamental to preserve their activity
105 against non-ideal conditions of temperature, pH, humidity and time [2]. This might require
106 strategies for the compensation of any sample-to-sample, test-to-test and device-to-device
107 variability, loss in activity of the reagents, environmental conditions, external noise,
108 transient effects and any other source of variability [2]. Furthermore, the POC should work
109 with no or minimal sample pre-processing [2].

110 **Cost of the platform.** The trade-off between the cost of the platform and its frequency of
111 use is another main challenge. The POC platform is required to be affordable by the final
112 user but the affordability is related to its frequency of use. For instance, moder commercial
113 glucose meters cost about £30, with a cost per test as low as £0.50. Glucose meters are used
114 very frequently by the user (more than once a day), hence the very low cost. However,
115 platforms used less frequently have an increased cost on the market. Typically, the reduction
116 of the selling price can be achieved by employing appropriate mass-production strategies.
117 However, the challenges illustrated above can require strategies which are not suitable for
118 mass-manufacturing [21]. This discussion is addressed in detail in Paragraph 2.6.3.

119

120 1.2. Aims and Objectives

121 This research project is part of the ‘Multicorder project’ [22], [23], aimed at developing a
 122 broad-spectrum sensor platform by integrating several biosensors on a single device to sense
 123 the personal metabolome. The Multicorder project aims at developing a personal
 124 metabolome machine for precision healthcare. It is supported by the UK Engineering and
 125 Physical Sciences Research Council, with Professor David Cumming as the head of the
 126 project. Within the Multicorder project, many integrated sensing chips have been developed
 127 using the complementary metal-oxide–semiconductor (CMOS) technology.

128 In this frame, my PhD project consisted of developing and testing a POC platform for the
 129 quantification of metabolic biomarkers. The target metabolic biomarkers were detected
 130 using a colorimetric approach and were selected for two case studies: PCa and ischemic
 131 stroke. The former application aims to demonstrate the potential of a metabolomics based
 132 POC platform in a context where new diagnostic tools can improve the current clinical
 133 practice in terms of medical costs and survival rate. The latter application aims to show the
 134 potential of the device as a rapid diagnostic tool that can make a difference between life or
 135 death. The two case studies are intended as a proof-of-concept. The platform has the
 136 versatility and capability of adapting to a wide range of biological assays with no or minimal
 137 modifications. For the development of the platform, a CMOS chip developed within the
 138 Multicorder project, was employed. The CMOS chip integrates a 16x16 array of multi-
 139 sensor elements. Each element integrates a photodiode, a single-photon avalanche diode
 140 (SPAD) and an ion-sensitive field-effect transistor (ISFET). Only the photodiodes were used
 141 in this work. The specific objectives of this PhD project and the contributions for each of the
 142 completed task within the project are shown in Table 1.2.

143

144

Table 1.2 Table of contributions for this PhD project.

Chapter	Task / Activity	Main investigators
2, 3	Identification of a potential metabolic biomarker panel for prostate cancer	- Valerio F. Annese (literature survey) - Prof. Rob Jones ² (discussion/validation)
2, 3	Identification of a potential metabolic biomarker panel for ischemic stroke	- Valerio F. Annese (literature survey) - Dr Samadhan Patil ¹ (discussion/validation)
3	Design of the CMOS chip	- Dr Mohammed Al-Rahawani ¹ - Dr Christos Giankulovitch ¹ - Dr James Beeley ¹
3	Fabrication of the CMOS chip	Outsourced (Austriamicrosystems)
3	Development of the reader (hardware)	- Dr Mohammed Al-Rahawani ¹ - Dr Christos Giankulovitch ¹ - Dr Claudio Accarino ¹

3	Development of the reader (software)	- Valerio F. Annese
3	Development of the graphic user interface	- Valerio F. Annese
3	Enzymatic reactions modelling and simulations	- Valerio F. Annese
3	Embedded Platform testing	- Valerio F. Annese
4	Microfluidics design and modelling	- Valerio F. Annese
4	Integration of capillary microfluidics on the CMOS chip	- Valerio F. Annese
4	Packaging for multiplexed wet assays	- Valerio F. Annese
4	Characterisation of the microfluidic structures	- Valerio F. Annese
4	Spectral characterisation of the photodiode array	- Valerio F. Annese - Dr Mohammed Al-Rahawani ¹ - Dr Christos Giankulovitch ¹
4	Characterisation of the cartridge	- Valerio F. Annese
4	Characterisation of sample flow in the microfluidic system	- Valerio F. Annese
5	Development of the experimental setup	- Valerio F. Annese
5	Assay formulations	- Well established in the literature
5	Assay optimisations for this platform	- Valerio F. Annese
5	Characterisation of the platform when measuring PCa-related metabolites in diluted serum	- Valerio F. Annese
5	Characterisation of the platform when measuring ischemic stroke-related metabolites in diluted serum	- Valerio F. Annese
5	Quantification of the test duration	- Valerio F. Annese
5	Reagents printing for microchannel functionalisation	- Valerio F. Annese
5	Reagents lyophilisation for microchannel functionalisation	- Valerio F. Annese
5	Quantification of the reagents shelf-life after lyophilisation	- Valerio F. Annese
5	Multiplexed assays in human plasma	- Valerio F. Annese
5	Multiplexed assays with paper microfluidics (2 metabolites)	- Dr Chunxiao Hu ¹ (designed the work and performed experiments) - Dr Srinivas Velugotla ¹ (developed the paper strips) - Valerio F. Annese (developed and applied functionalisation method of the paper strips)
5	Whole blood experiments	- Valerio F. Annese
6	Optimisation for clinical evaluation	- Valerio F. Annese
6	Clinical evaluation with PCa samples	- Valerio F. Annese
6	Clinical evaluation with ischemic stroke samples	- Valerio F. Annese
6	Multiplexed assays with PCa samples	- Valerio F. Annese
	Affiliation at the time of completion of the task: ¹ <i>Microsystem Technology Group, James Watt School of Engineering, University of Glasgow.</i> ² <i>Institute of Cancer Sciences, University of Glasgow, Beatson West of Scotland Cancer Centre, Glasgow.</i>	

146 **1.3. Platform Requirements**

147 This project aims to develop and characterise a portable metabolomics-on-chip platform for
148 ischemic stroke and PCa. This raises the question: which are the requirements of the
149 platform? This paragraph addresses this question with initial qualitative considerations.
150 Quantitative requirements are then set in the next chapter, alongside the identification of
151 strategies necessary to meet the criteria. Table 1.3 summarises the requirements of the
152 platform developed in this research project.

153 The general requirements of a POC platform have been illustrated by the World Health
154 Organisation [1], [13]. A POC test is required to be Affordable, Sensitive, Specific, User-
155 friendly, Rapid & Robust, Equipment-free, Delivered [1]. Those specifications are generally
156 referred to as ASSURED requirements [1]. In addition to the ASSURED requirements, there
157 are two requirements specific to this research project: versatility and multi-analyte
158 capabilities.

159 **Affordability** means that the platform must have a cost suitable for the general population.
160 As already mentioned, the affordability of the platform depends on its frequency of use. We
161 can assume that a platform designed for daily use should have a lower cost than a platform
162 used, for instance, once a month. Evidence of this assumption is also provided by the cost of
163 the POC platforms on the market.

164 **Sensitivity and specificity** are considered top-priority requirements [1]. The level of clinical
165 sensitivity and specificity depend on the application. However, sensitivity and specificity
166 levels similar (or better) than the current clinical standard are expected.

167 **User-friendliness.** The POC platform is required to be user-friendly, meaning that a member
168 of the general population should be able to use it with a minimal set of instructions without
169 any previous training. The user-friendly requirement implies that the platform must be easy
170 to use, intuitive and largely automatised.

171 **Rapidity & Robustness.** The POC platform is required to provide a rapid result. By
172 comparison with the POC devices currently on the market, we can assume that the test must
173 have a duration in the order of minutes.

174 The POC platform is required to be robust. The platform must have strategies in place to
175 standardise the measurement and provide reliable and replicable results against device-to-
176 device and sample-to-sample variability. The platform should also recognise when a test is

177 invalid and have strategies in place to ‘fail safely’, for example by notifying the user that the
178 result is not trustworthy.

179 **Equipment-free.** The POC platform is required to be equipment-free, meaning that the
180 platform must be capable of running the test without any external equipment required.

181 The World Health Organisation also illustrates that the platform must be delivered, meaning
182 that it must be possible to safely transport and ship the platform to the final user.

183 **Versatility.** This work is part of a larger vision and employs a sensor platform which
184 integrates additional sensors. Although the metabolomic biomarkers targeted in this work
185 needs to be specific to address the case studies, the developed methods and procedure must
186 apply to a larger variety of detection methods and biomarkers.

187 **Multi-analyte testing.** The platform also requires to be capable of multi-analyte testing.
188 Multi-analyte testing means that the platform must have the potential to perform multiple
189 measurements (involving different biomarkers or/and control measurements) within a single
190 test routine.

191

192

Table 1.3 Requirements of the platform.

Requirement	Definition
Affordability ¹	The platform and the single test must have a cost suitable for the general population (depending on its frequency of use).
Sensitivity ¹	The platform must have the capability of providing clinically relevant measurement (high true positive rate).
Specificity ¹	The platform must be specific for a determined application (high true negative rate).
User-friendly ¹	The general population must be capable of operating the platform with a minimal set of instructions.
Rapid ¹	The platform must provide the result in minutes.
Robust ¹	The platform must have solutions in place to standardise the measurement against device-to-device and sample-to-sample variability. The platform should also be capable of failing safely.
Equipment-free ¹	No external equipment must be necessary to run the test. The platform should be portable, ideally handheld.
Delivered ¹	The platform must be suitable for transport and shipping.
Multi-analyte capability ²	The platform must be capable of measuring multiple metabolic biomarkers at the same time.
Versatility ²	The platform should be capable of accommodating several applications with minimal modifications.
¹ Requirement outlined by the World Health Organization.	
² Requirement for this specific project.	

193 **1.4. Thesis Outline**

194 The present thesis work is divided into seven chapters. A flow chart of the research project
195 in Figure 1.2 guides the reader through the thesis. A brief description of the following
196 chapters is also provided below.

197 **Chapter 2** sets the quantitative requirements of the platform. This is achieved by discussing
198 relevant scientific literature and devices on the market. The literature review mainly focuses
199 on five topics, namely enzyme-based biosensors, integrated optical sensors, microfluidics,
200 metabolomics and POC systems.

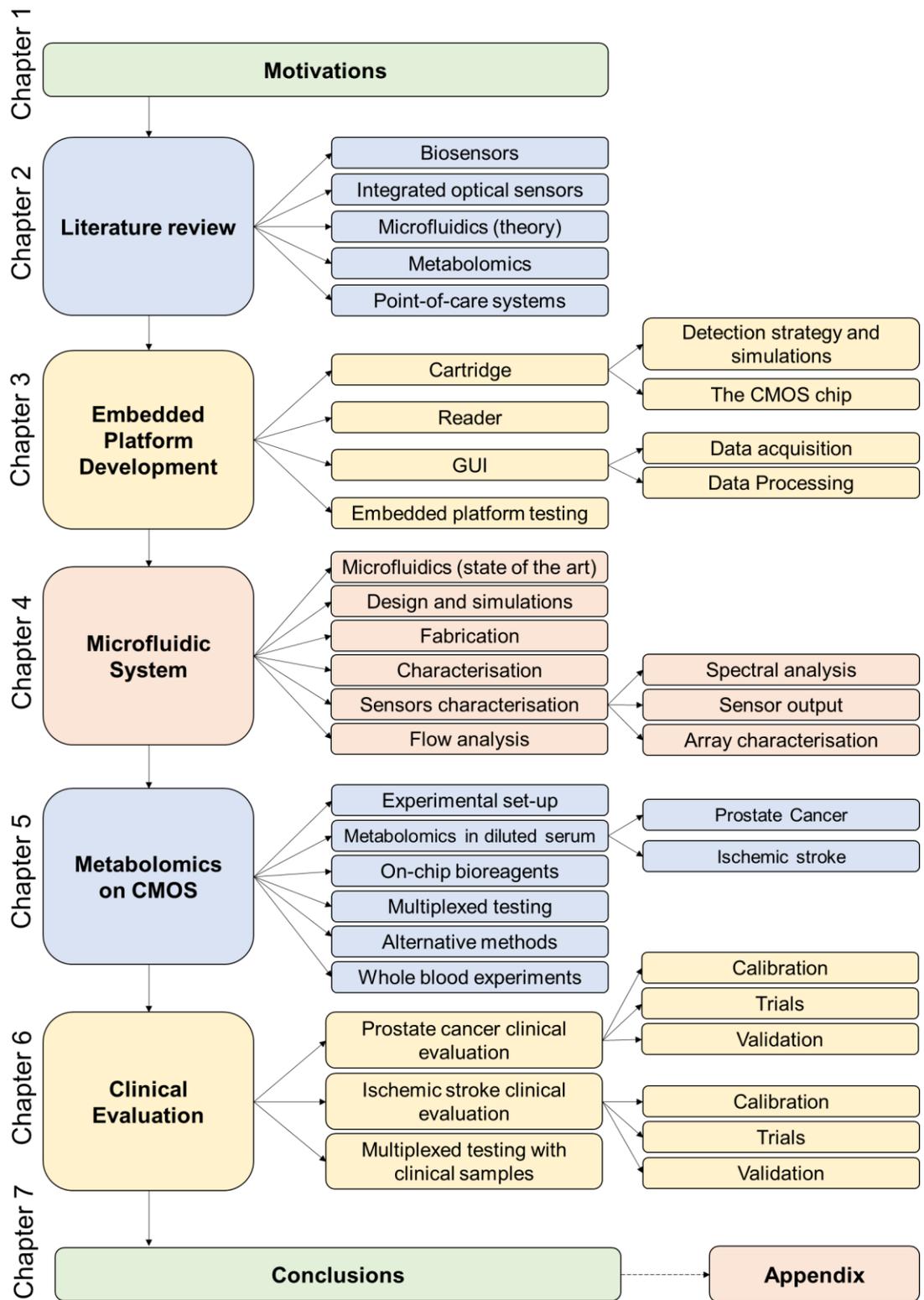
201 **Chapter 3** describes the development of the embedded platform. All the units composing
202 the platform are singularly analysed, reporting the design and the development stages.

203 **Chapter 4** presents the development and characterisation of microfluidics. It illustrates the
204 properties of the developed microfluidics, the spectral properties of the colorimetric reagents
205 and the characterisation of the sensor array.

206 **Chapter 5** illustrate results related to the quantification of the proposed metabolic
207 biomarkers for both PCa and ischemic stroke in diluted serum using the developed platform.
208 This chapter also demonstrates the capabilities of the platform for simultaneous multi-
209 metabolite quantification.

210 **Chapter 6** presents the clinical evaluation of the platform. Results related to the
211 quantification of the proposed metabolic biomarkers for both PCa and ischemic stroke in
212 clinically sourced samples of human plasma are presented.

213 **Chapter 7** concludes this research work by summarising the main findings and discussing
214 potential future work.



215

216

Figure 1.2 Flow chart of the research project.

217 Chapter 2: Application Background

218 2.1. Introduction

219 This chapter aims to set quantitative requirements for the platform. Strategies necessary to
 220 address the requirements are also discussed. This is done by providing theoretical knowledge
 221 and discussing the relevant state of the art. Table 2.1 recapitulates the objectives and the
 222 requirements of this work for ease of reading.

223 Five main topics are analysed in this chapter. The first theme herein discussed is biosensors.
 224 The section is mainly oriented to integrated enzyme-based optical biosensors. The second
 225 topic discussed, integrated optical sensors, illustrates the complementary metal-oxide-
 226 semiconductor (CMOS) technology, and provides theoretical knowledge on optical sensors.
 227 The third theme examined in this chapter is microfluidics. Theoretical knowledge is provided
 228 in this chapter. The state of the art and the discussion about its integration with the integrated
 229 circuit is discussed in Chapter 4. The fourth aspect herein covered is metabolomics, with a
 230 special focus on the case studies of this platform, i.e. PCa and ischemic stroke. The final
 231 aspect herein discussed is POC platforms for healthcare. Both experimental and commercial
 232 POC apparatuses are discussed, presenting challenges, limitations, and successful examples
 233 of the technology.

234

235 *Table 2.1 Summary of objectives, applications, and requirements of the platform.*

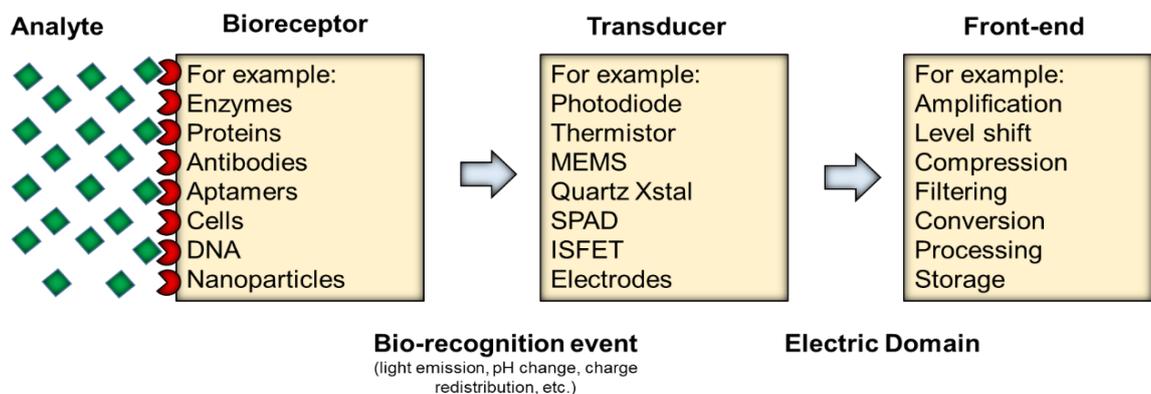
Requirement	Definition
Objective	Development and characterisation of a metabolomics-on-CMOS platform
Applications	<ul style="list-style-type: none"> - Ischemic stroke - Prostate cancer
Requirements	<ul style="list-style-type: none"> - Affordability - Sensitivity - Specificity - User friendly - Rapid - Robust - Equipment-free - Delivered - Multi-analyte capability - Versatility

236 2.2. Biosensors

237 A biosensor is a device that couples one or more molecular recognition elements (biological
 238 receptors or reagents) with a transducer to convert a biological response into an electric
 239 signal [24]–[26]. A biosensor usually aims to detect or quantify a target substance, namely
 240 the analyte, typically restrained into a sample. The reasons for their rapid evolution since the
 241 development of the first biosensor by Clark and Lyon in 1962 [27], include the wide range
 242 of applications, including defence, healthcare, security, pharmaceuticals, food safety and
 243 quality, environmental monitoring [28], and their higher performance if compared to
 244 traditional bulky instrumentation regarding specificity, sensitivity, cost, rapidity,
 245 multiplicity and portability [28]. As shown in Figure 2.1, a biosensor can be usually divided
 246 into the following essential elements [28]:

- 247 • *the bioreceptors*, the biological elements that specifically recognise the target analyte;
- 248 • *the transducer*, the system capable of converting the physical changes accompanying the
 249 interaction between analyte and bioreceptor into a measurable electric signal;
- 250 • *the front-end*, an electrical circuit responsible for signal conditioning (amplification,
 251 filtering, digitisation) and reading.

252 The elements mentioned above are mutually connected. The target analyte depends on the
 253 application. Nucleic acids, proteins, metabolites, ions, antigens, pollutants are just a few
 254 examples of the potential target analyte. Accordingly, the bioreceptor is selected for
 255 interacting with the analyte with a high degree of selectivity and specificity. Examples of
 256 bioreceptors are enzymes, antibodies, nucleic acids, proteins, aptamers [29]. The transducer
 257 is selected for detecting the modification in chemical, biological or physical properties of
 258 the sample or the environment induced by its interaction with the organic reagents. Finally,
 259 the front-end depends on the specific application and the selected transducer.



260

261 *Figure 2.1 Schematisation of a generic biosensor. Reproduced and modified from [30].*

262 2.2.1. Enzyme-based biosensors

263 The use of biomolecules rather than synthesised molecules as bioreceptor is becoming a
 264 priority in modern biotechnology [31]. There are several advantages when using
 265 biomolecules. They are usually easier to obtain than synthetic molecules [32], exhibit high
 266 specificity and selectivity of binding [28] and can be labelled by fluorescent probes [32].
 267 Knowledge and procedures for biomolecules manipulation are also well-established [32].
 268 Among all types of bio-molecules, enzymes have found widespread use in biosensors
 269 because of their inherent specificity, selectivity and catalytic properties [33].

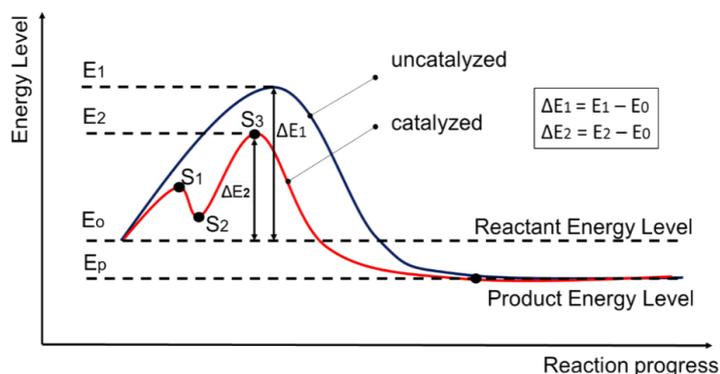
270 Enzymes are folded chains of amino acids which catalyse specific reactions transforming a
 271 substrate into a product by lowering the activation energy of the reaction. This is achieved
 272 by inducing transition states with lower free energy, as shown in Figure 2.2 [24], [34].

273 The model of ‘the lock and the key’ provides an intuitive explanation of the high selectivity
 274 of enzymes [35]. Enzyme and substrate might be conceptualised with complementary
 275 geometric shapes that fit precisely into one another. Today, this model has been overcome
 276 due to some limitations but intuitively describes the specificity of the binding [36].

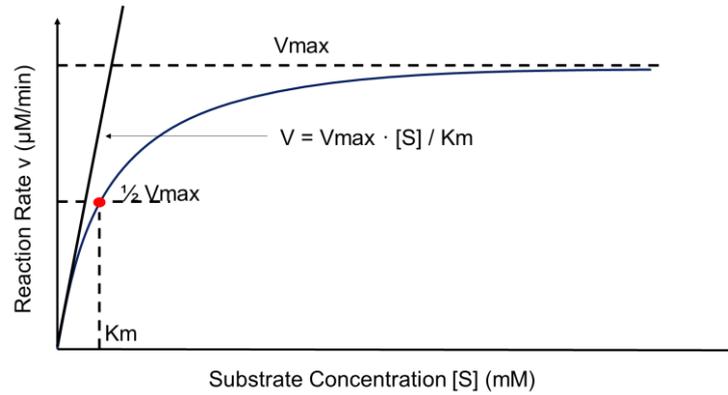
277 According to the Michaelis-Menten theory [24], [34], which illustrates the kinetics of
 278 enzyme action, the reaction sequence can be described as:



279 Where E is the enzyme, S is the substrate, ES is the bound complex, P is the product, k_{+1} , k_{-1}
 280 and k_{+2} are the rate constants (typically $k_{+1} > k_{-1}$, k_{+2}) [24]. By calculating the rate equations
 281 of the reaction, applying the boundary conditions and after mathematical manipulations
 282 reported in [24], it is possible to derive the Michaelis-Menten equation (Figure 2.3):



283
 284 *Figure 2.2 Due to the introduction of transition states (S_1 , S_2 , S_3), the catalysed reaction has*
 285 *lower activation energy than the one of the uncatalysed reaction ($\Delta E_2 < \Delta E_1$). Reproduced*
 286 *and modified from [24].*



287

288

Figure 2.3 Reaction rate vs substrate concentration (Michaelis-Menten model) [24].

289

$$\frac{d[P]}{dt} = v = k_{+2} [ES] = \frac{k_{+2} [S][E]_0}{[S] + K_m} = \frac{V_{\max} [S]}{[S] + K_m} = \frac{V_{\max}}{1 + \frac{K_m}{[S]}} \quad (2.2)$$

$$K_m = \frac{k_{-1} + k_{+2}}{k_{+1}} \approx \frac{k_{-1}}{k_{+1}} \quad (\text{when } k_{+2} \gg k_{-1}) \quad (2.3)$$

290 Where v is the rate of the reaction, $[X]$ denotes the concentration of X , $[E]_0$ is the initial
 291 concentration of the enzyme, V_{\max} is the maximum rate of reaction (occurring when the
 292 substrate completely saturates the enzyme), and K_m is the Michaelis constant (typical values
 293 10^{-1} : 10^{-5} M) defined in Equation (2.3).

294 There are two general approaches to enzymatic substrate estimation: end-point analysis or
 295 rate measurement analysis [37]. The end-point method compares the condition of the sample
 296 or the environment before and after the chemical reaction is completed.

297 Differently, the rate measurement analysis employs the Michaelis-Menten equation. By
 298 monitoring the initial rate of the reaction v_0 by an appropriate transduction method with
 299 known V_{\max} , K_m and $[E]_0$, it is possible to calculate the initial concentration of the substrate
 300 $[S]_0$ as:

$$[S]_0 = \frac{v_0 K_m}{V_{\max} - v_0} \quad (2.4)$$

301 This estimation method is usually quicker than the alternative approach based on the reaction
 302 endpoint because it is required only to monitor the first part of the reaction.

303 There are mainly two types of biosensors: electrochemical and physical [38].
 304 Electrochemical biosensors detect alterations of the charge distribution of the sample or
 305 environment [38]. Amperometric, potentiometric, impedimetric and voltametric are the
 306 most common electrochemical biosensors. pH biosensing usually performed thoroughly
 307 integrated pH sensors such as the ion-sensitive field-effect transistors (ISFET), are also a

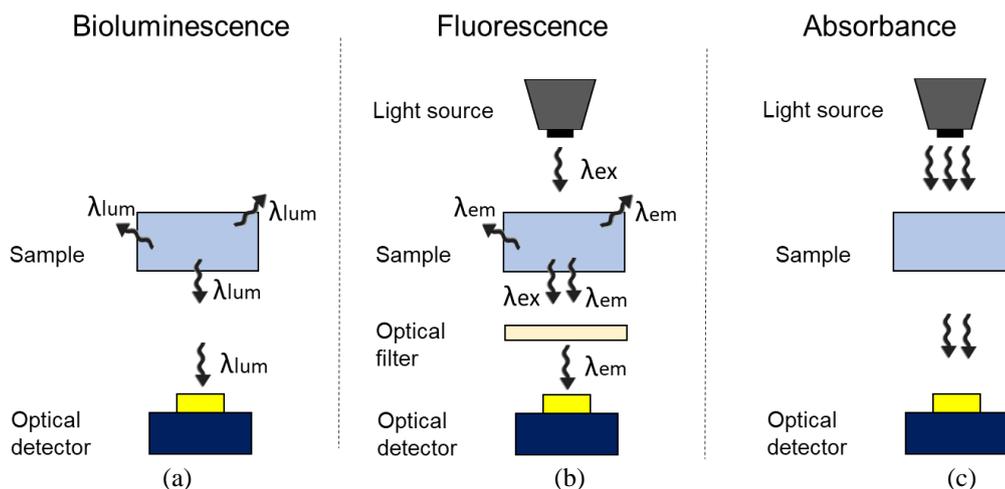
308 widespread electrochemical sensing technique [2]. Among electrochemical detection
309 methods, amperometric is probably the most commonly used approach [39].

310 Amperometric sensors generate a current flow proportional to the concentration of the
311 analyte [39]. This class of biosensors use a catalytic electrode, classically platinum, for the
312 oxidation of specific chemical species (e.g. hydrogen peroxide or NADH) generated
313 alongside an enzymatic reaction [40]. The electrode where the oxidation takes place is
314 called the working electrode (anode). The potential of the working electrode is kept constant
315 with respect to a reference electrode for the oxidation of the desired species, hydrogen
316 peroxide in this example. Generated electrons from the oxidation of the target species create
317 a detectable current and are usually recombined on the counter electrode (cathode),
318 classically made of silver/silver chloride (Ag/AgCl).

319 Physical biosensors detect modifications of the physical properties or condition of the
320 sample or environment [38]. Calorimetric, mechanical, and optical biosensors are the most
321 common physical biosensors. Calorimetric biosensors detect heat exchange accompanying
322 the reaction of the analyte with the bioreceptors. Mechanical biosensors usually detect mass
323 modifications of the biological component after the interaction with the bioreceptors. Optical
324 biosensors usually employ a light sensor which detects a variation of the optical properties
325 of the sample or the environment. They can mainly be divided into three categories according
326 to the principle of operation: bioluminescence, fluorescence, and absorbance [38].

327 Bioluminescent biosensors use specific bioreceptors (e.g. luciferase) selected to produce
328 photons when interacting with the substrate. The light production mechanism involves
329 biochemical reactions relying on the oxidation of the substrate [41]. When the light-
330 producing reactions are chemical (inorganic reagents, e.g. luminol), this phenomenon is
331 usually referred to as chemiluminescence [41]. The setup of a generic bioluminescence-
332 based biosensor is described in Figure 2.4(a). The interaction of the bioreceptors and the
333 analyte within the sample produces the generation of photons, usually with a wavelength
334 λ_{lum} in the visible or near-infrared range [41]. Light production is omnidirectional. Produced
335 photons can be sensed by an optical sensor typically operated in a dark environment.

336 Fluorescent biosensors use specific bioreceptors (e.g. fluorophore) selected to produce a
337 change in the fluorescence properties when interacting with the target analyte. Fluorescence
338 is the emission of light that occurs after the absorption of light that is typically of shorter
339 wavelength [42]. The setup of a generic fluorescence-based biosensor is described in Figure
340 2.4(b). Unlike bioluminescence, fluorescence requires incident excitation radiation.



341 *Figure 2.4 Working principle of (a) bioluminescence-based biosensors, (b) fluorescence-*
 342 *based biosensors and (c) absorbance-based biosensors.*

343

344 A light source emitting excitation light with a wavelength λ_{ex} is used to illuminate the sample.

345 Due to the reaction between analyte and bioreceptors within the sample, photons with a
 346 wavelength λ_{em} are omnidirectionally emitted. The emitted photons can be sensed using an
 347 optical sensor, typically preceded by an optical filter cancelling out the excitation light.

348 Absorbance-based biosensors use bioreceptors to produce a change in the light absorbance
 349 of the sample when interacting with the target analyte [39]. Since the change in the
 350 absorbance property of the sample is usually measured only for a selected range of
 351 wavelengths, absorbance-based biosensors are also referred to as colorimetric.

352 The setup of a generic colorimetric biosensor is described in Figure 2.4(c). A fixed
 353 wavelength is shone on the sample under test. The wavelength is typically selected to be a
 354 compromise between the responsivity of the detector and the peak absorption of the light-
 355 absorbing species in the visible range. Light transmitted through the sample is then
 356 monitored with an optical sensor during the chemical reaction. The intensity of the incident
 357 light is kept constant and usually in a linear region of the optical sensor dynamic range.

358

359 **2.2.2. Discussion on the detection methods**

360 Electrochemical and optical biosensors have shown comparable performance [43].
 361 However, when considering integrated solutions for multi-analyte sensing, there are some
 362 aspects to be considered. To date, mass-produced optical sensors have good performance at
 363 affordable costs, mainly driven by the consumer electronics industry. Arrays of optical
 364 sensors with variegated dimensions (e.g. camera and imagers) can be easily manufactured.

365 Related bio-chemistry accompanying the optical transduction is also robust and well-
366 established [43]. Platforms utilising optical modalities also have a great deal of potential for
367 customisation due to the large numbers of probe molecules available [43]. The main issue
368 related to optical biosensors is the necessity of samples pre-processing such as blood pre-
369 filtration since red cells and other large molecules can create noise and artefacts [43].

370 Electrochemical platforms, such as amperometric devices, are less convenient to miniaturise.
371 First, the selection of the metals used for the electrodes is crucial [44]. Some of the metals
372 to be used in amperometric sensing are incompatible with standard manufacturing processes
373 and need to be deposited after fabrication in cleanroom facilities [45]. The consequent need
374 for additional fabrication steps, which can also be purchased as service, can lead to an
375 increased cost of the platform. Additionally, the working principle of amperometric sensors
376 creates challenges when designing an array of amperometric sensors for multiple assays due
377 to potential interferences related to other chemical species nearby of the potential window
378 used for the oxidation of the target compound [45].

379 With reference to the requirements of this platform outlined in Table 1.3, the electrochemical
380 methods have a lower multi-analyte capability than the optical methods. For this reason, an
381 optical detection mechanism was selected for the developed platform. Among the optical
382 detection methods, a colorimetric approach has been adopted in this work. The reasons
383 leading to this selection are illustrated in the following discussion (summary in Table 2.2).

384 For its ease-of-use bioluminescence is an excellent candidate to achieve non-invasive live-
385 cell imaging. The absence of a light source simplifies the required setup and also eliminates
386 the risk of photobleaching, which is the permanent photochemical modification of a probe
387 molecule due to light exposure [46]. Photobleaching is an intrinsic property of the receptors
388 and it is usually preponderant when exposing the dye probe to wavelength in the range 360–
389 440nm [42], [47]. It also depends on the intensity of the light source, on the duration of the
390 exposure and the concentration of the receptors [47].

391 However, bioluminescence suffers from its low-brightness nature largely caused by the slow
392 turnover of bioreagents and the omnidirectionality of light production [42]. Bioluminescence
393 intensity is strictly limited by the number of substrate molecules being catalysed by the
394 bioluminescent protein [46]. To increase the chance to sense the produced light,
395 bioluminescence is usually used over samples with macroscopic volume and detected with
396 high-performance optical transducers. Furthermore, optical transducers are typically
397 operated with long exposure times, which limit the spatiotemporal resolution of the

398 measurement [41]. Bioluminescence is therefore not adequate for this PhD project as the
399 platform requires small sample volumes (in the μL scale). The adequate temporal resolution
400 of the measurement is also needed for a correct estimation of the reaction rate.

401 One major advantage of fluorescent probes with respect to bioluminescence is that they can
402 be brighter than bioluminescent proteins [46]. The intensity of the emitted light can also be
403 increased by increasing the excitation light intensity. The difference between the exciting
404 and emitted wavelengths makes these biosensors highly specific and suitable for the
405 quantification of very low concentration of analytes [42].

406 Nonetheless, photobleaching is a limiting factor for fluorescence measurements [42]. On one
407 hand, this is because the wavelength of the light excitation source is typically in the range of
408 wavelength where photobleaching is more preponderant [42]. On the other hand, this is due
409 to the use of high-intensity excitation light [47]. The use of a high-intensity excitation light
410 also requires the use of an optical filter with a high rejection coefficient. The necessity of a
411 high-performance optical filter makes fluorescent biosensor expensive, especially in the case
412 of miniaturised platforms. Fluorescence is not adequate for this project as the cartridge needs
413 to be affordable, ideally disposable. The integration of an optical filter for fluorescence
414 biosensing would increase the cost of the cartridge. Also, the necessity of a filter between
415 the sample and sensor would implicitly undermine the usage of other sensors on the cartridge
416 (ISFET). A fluorescence approach is therefore incompatible with the versatility requirement.

417 Colorimetry is easy to operate, affordable and suitable for multi-metabolite sensing.
418 Colorimetric sensors have lower selectivity when compared to bioluminescent and
419 fluorescent biosensors. This is because any impurity within the sample can affect the light
420 absorbance and interfere with the sensing. Colorimetric sensors are also not suitable for
421 sensing analytes with a low concentration (in the range of pM, nM). Photobleaching is also
422 an issue for colorimetric sensors [48]. However, this might be minimised by using
423 wavelength where the effect is less evident (e.g. $> 450\text{ nm}$), a light source with irradiance
424 intensities in the range of tens of $\mu\text{W}/\text{cm}^2$ and limiting the duration of the light exposure to
425 a few minutes [47]. Colorimetry is the most promising approach for the target applications
426 as it is a trade-off among all the requirements. The target analytes of this platform have a
427 blood concentration in the μM to mM range (this is discussed in the metabolomics section
428 of this chapter), which is suitable for colorimetric detection. The platform is also required to
429 be affordable and easy to operate. For these reasons, the colorimetric method is the most
430 suitable for this project and it was adopted for the development of this platform.

431 *Table 2.2. Comparison of different optical detection methods. The suitability of the detection*
 432 *methods against the requirements of this project was scored (low, medium, high) and*
 433 *justified. Scores were assumed by literature investigation and only apply for this project.*

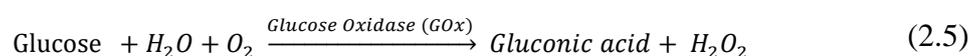
Requirement	Bioluminescence	Fluorescence	Colorimetry
Affordability	High (Easiest setup)	Low (Light source and expensive filter required)	Medium (Light source required but no filter)
Sensitivity	Low (Light glow has low intensity)	High (Suitable for nM to mM concentrations)	Medium (Suitable for μM to mM concentrations)
Specificity	High (Detection method is very specific)		Medium (Impurities might affect the measurement)
User-friendly	High (The user only requires inserting the sample, regardless of the detection method)		
Rapid	High (The initial reaction rate can be used to estimate substrate concentration)		
Robust	High (Controls tests can be run to increase the reliability of test)		
Equipment-free	High (The setup of the test can be integrated into a single equipment-free platform)		
Delivered	Medium (All the detection methods employ biological reagents which might require particular care when transported)		
Multi-analyte capability	Medium (Lateral crosstalk might be an issue. Large sample volume also required)	Medium (Lateral crosstalk might be an issue. The necessity of the filter complicates the monolithic integration)	High (Lateral crosstalk is lower - light is mostly unidirectional)
Versatility	High (Electrochemical sensors on the platform can be used)	Medium (Electrochemical sensors on the platform cannot be used)	High (Electrochemical sensors on the platform can be used)

434

435 2.2.3. Colorimetric biosensors

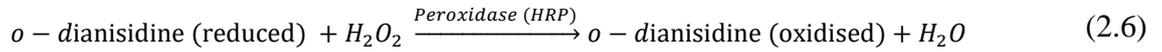
436 Since colorimetry was adopted in this work, a more detailed description of colorimetric
 437 biosensors is proposed in this paragraph.

438 The working principle of colorimetric sensors can be divided in two simultaneous phenomena:
 439 enzymatic reaction and reaction transduction [40]. The enzymatic reaction stage groups all
 440 the chemical reactions taking place. The most commonly employed enzymes belong to the
 441 oxidation and dehydrogenase classes [40]. For example, let us consider integrated enzyme-
 442 based biosensors for the determination of glucose. Today, glucose meters are the most
 443 popular portable quantitative platform employed in healthcare [2]. Glucose meters are
 444 mainly based on Glucose Oxidase (GOx), commonly employed in both amperometric and
 445 colorimetric biosensors [40]. GOx has a very high glucose selectivity, is easy to obtain, low-
 446 cost and very stable to pH, temperature and storing-time [40]. In the presence of water and
 447 oxygen, glucose reacts with GOx, producing gluconic acid and hydrogen peroxide [49]:



448 Cofactors (e.g. flavin adenine dinucleotide), can be used in combination with GOx. At this
 449 stage, there might be different strategies for the reaction transduction [40].

450 Absorbance biosensors employ an additional reaction step introduced to interact with
 451 hydrogen peroxide and produce light-absorbing species. O-dianisidine and the system
 452 phenol/4-aminoantipyrine (4AAP) are two well-established probes [49]. They are both
 453 oxidised by hydrogen peroxide in the presence of a catalysing enzyme, namely peroxidase
 454 (HRP), as reported in the following [49]:



455 Both oxidised o-dianisidine and quinone-imine have higher extinction coefficient than the
 456 initial solution, resulting in a higher absorbance around 450 - 500 nm. At this stage, an
 457 optical sensor can be used as a transducer to monitor the variation of the absorbance. Beyond
 458 the example of glucose, similar chemistries based on oxidation enzymes can be used to
 459 measure different analytes.

460 Colorimetric bioassays employ the Beer-Lambert law which states that the optical
 461 absorbance A of a solution depends on the concentration of the light-absorbing species $[P]$,
 462 its extinction coefficient ϵ and the optical length h [50] :

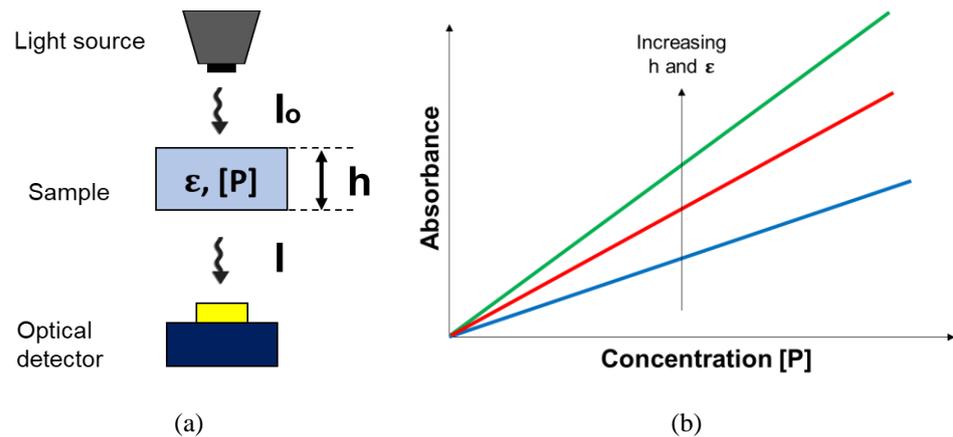
$$\epsilon \cdot h \cdot [P] = A = -\log T = -\log \frac{I}{I_0} \quad (2.8)$$

463 Where T is light transmittance, I is the transmitted light and I_0 is the incident light. Figure
 464 2.5 illustrates the Beer-Lambert law. The absorbance is directly proportional to the
 465 concentration of the light-absorbing species. Hence, a high concentration of analyte (in the
 466 order of μM) is required in order to create a detectable signal. Usually, ϵ , h and $[P]$ are
 467 measured in $\text{Lcm}^{-1}\text{mol}^{-1}$, cm and molL^{-1} , respectively. During the reaction, the absorbance
 468 changes and its profile can be referred to as $a(t)$. The quantities ϵ and h are usually constant;
 469 thus, $a(t)$ is proportional to the concentration profile of the light-absorbing species, referred
 470 to as $[p(t)]$. By differentiating the time-domain Beer-Lambert equation and plugging-in
 471 Michaelis-Menten equation (2.2), the following relation can be demonstrated:

$$a(t) = \epsilon \cdot h \cdot [p(t)] \rightarrow \frac{da(t)}{dt} = \epsilon \cdot h \cdot \frac{d[p(t)]}{dt} = \epsilon \cdot h \cdot \frac{V_{\max}}{1 + \frac{K_m}{[S]}} \quad (2.9)$$

472 where the notation mentioned above has been preserved. Beer-Lambert law is limited by the
 473 phenomenon of photobleaching for high concentrations of the light-absorbing species and
 474 high light intensities.

475



476 Figure 2.5 (a) Setup for colorimetric measurement. (b) Illustration of Beer-Lambert law.

477

478 2.2.4. Integration of the bioreceptors

479 Many approaches for the integration of the bioreceptor with the sensor have been developed.
 480 Currently, immobilisation and lyophilisation are the most commonly used approaches [51].
 481 Reagent immobilisation defines a set of procedures aiming to link the reagent to a substrate
 482 [51]. Reagent immobilisation has shown several advantages with respect to the reagent in a
 483 liquid state, including higher stability, easier shipment, easier process control, multi-enzyme
 484 processes, convenient handling, reusability [51].

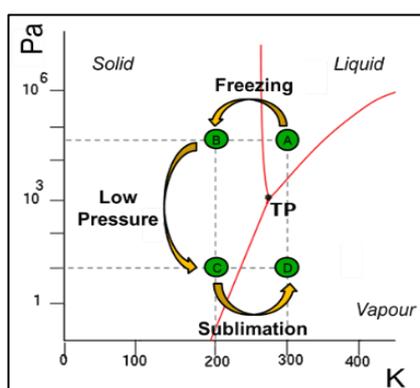
485 Immobilisation methods can be divided into physical methods and chemical methods. Physical
 486 methods include reagent entrapment, absorption and microencapsulation [51]. Reagent
 487 entrapment involves the cross-link of the reagent with a polymer (e.g. alginate) [51].
 488 Differently, reagent absorption methods allow the non-covalent link of the reagent with a
 489 substrate. This can be achieved by hydrophobic interactions, hydrogen bonding and Van der
 490 Waals forces [51]. Microencapsulation refers to the encasement of the reagent in semi-
 491 permeable polymer membranes with variable micrometric porosity. On the other hand,
 492 chemical methods include covalent attachment, cross-link, ionic binding and conjugation by
 493 affinity ligands [51]. A detailed description of protocol and techniques for enzyme
 494 immobilisation is reported in [51].

495 Reagent lyophilisation is also a widespread technique, especially in commercial devices [2].
 496 Lyophilisation, also known as freeze-drying, is a process in which water is removed from a
 497 product by direct sublimation. Freeze-drying is today a well-established technique, vastly
 498 employed by pharmaceutical industries to preserve drugs. Freeze-drying improves the
 499 stability of the biological sample over temperature, pH and time [52], [53]. The sublimation
 500 of the water content is obtained by controlling the temperature and pressure of the sample

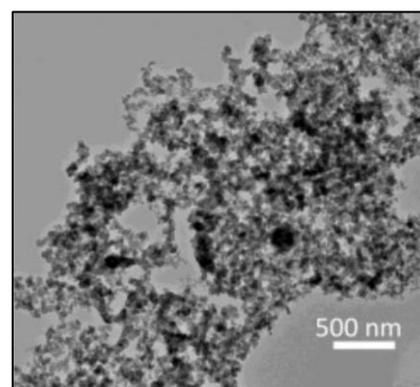
501 [54]. Usually, this is performed following a cycle, such as the one shown in Figure 2.6(a).
 502 Typically, the compounds to be freeze-dried are initially in a liquid state (state A in Figure
 503 2.6(a)). The process of lyophilisation starts with freezing the solution (state B). The freezing
 504 temperature depends on the specific composition of the solution (typical value: -50°C
 505 to -80°C). A low freezing temperature ensures that almost all the water content is in the solid
 506 state. Subsequently, the pressure of the chamber is reduced to 1-2 mPa through vacuum
 507 pumping (state C). The sublimation typically takes place partially during the permanence in
 508 state C and during the slow transition from state C to D, during which the temperature is
 509 gradually brought to room temperature. Figure 2.6 (b) shows an example of the product of
 510 the freeze-drying process of a glucose oxidase based solution [55].

511 Timings, temperatures and pressure are usually selected according to the application [54].
 512 Cryoprotective compounds, such as glycerol or sugars, can be used to optimise the process
 513 [54]. Freeze-dried enzymes have similar properties to immobilised ones [51]. However,
 514 there is no physical attachment of the molecules to the surface, so, once solubilised in the
 515 appropriate media, the reagent resembles its liquid form and does not allow reusability [51].
 516 Thus, this technique has been used in conjunction with microstructures [53], [56]. Once
 517 lyophilised into the microstructure, the bioreceptor is confined and trapped in the physical
 518 structure [53], [56]. The reagents are then rehydrated by the sample itself once introduced
 519 [52], [53], [56].

520



(a)



(b)

521 *Figure 2.6 (a) Working principle of the freeze-drying process. (b) Freeze-dried solution*
 522 *containing glucose oxidase. Reproduced from [55].*

523

524

525 **2.2.5. Biosensors metrics**

526 The performance of a biosensor is usually assessed by a set of parameters. The main metrics
 527 are illustrated in Table 2.3. Other metrics have also been standardised but are omitted in this
 528 review since unnecessary for the comprehension of this work. Additional readings in [49],
 529 [57]–[60] are suggested for a comprehensive description.

530

531

Table 2.3 Main biosensor metrics.

Metric	Definition	Relation	Eq.
Linear Range	It defines the range where the output of the sensor (y) shows a linear behaviour i.e. it is proportional to the substrate (x) by a constant (S) and has an offset (c) [57].	$y = S \cdot x + c$	(2.10)
Analytical Sensitivity (S) ¹	It quantifies the enhancement of the output signal (Δy) when increasing the quantity to be measured by a certain level (Δx) [37].	$S = \frac{\Delta y}{\Delta x}$	(2.11)
Analytical Selectivity ¹	It is defined as the ratio of the desired product formed to the undesired product formed expressed in moles [37].	$\frac{\text{Desired product (moles)}}{\text{undesired product (moles)}}$	(2.12)
Baseline (c)	It defines the offset c of the calibration curve [37]. It is also referred to as blank measurement or control.	$c = (y - S \cdot x)_{x=0}$	(2.13)
Absolute error (e)	It is the absolute difference between the test result (x_i) and the true value to be measured (X) [60].	$e = X - x_i $	(2.14)
Relative error (e _%)	It is the relative difference between the test result (x_i) and the true value to be measured (X) [60].	$e_{\%} = \frac{ X - x_i }{X} \cdot 100$	(2.15)
Root mean square error (RMSE)	It is the square root of the mean of the square of all of the errors [61].	$\sigma = \sqrt{\frac{\sum_i e_i^2}{N}}$	(2.16)
Sum of squares error (SSE)	It is the sum of the squared differences between each observation and its mean (μ) [62].	$SSE = \sum_i (x_i - \mu)^2$	(2.17)
Precision (σ)	It defines the closeness of agreement between independent results obtained by applying the experimental procedure under stipulated conditions. A measure of precision is the standard deviation (σ) over N repeated measurements (x_i) [60].	$\sigma = \sqrt{\frac{\sum_i (x_i - \mu)^2}{N}}$	(2.18)
Resolution (R)	It is defined as the smallest change in the concentration of an analyte required to bring a change in the biosensor response and therefore it is expressed in molarity [57].	$R = \frac{\sigma_{ctrl}}{S}$	(2.19)
Analytical Accuracy (acc.) ¹	It is the closeness of agreement between a test result and the true value. It is calculated as the average error (absolute or relative) over N measurements.	$acc = \left(\frac{\sum_i X - x_i }{N} \right)$	(2.20)
Limit of detection (LOD)	It defines the minimum detectable concentration by the biosensors. It is calculated as the sum of the mean (μ_{ctrl}) and 3.3 times the standard deviation (σ_{ctrl}) of the control measurements [58].	$LOD = \mu_{ctrl} + 3.3\sigma_{ctrl}$	(2.21)
Limit of quantification (LOQ)	It defines the minimum quantifiable concentration by the biosensors. It is calculated as the sum of the mean and 10 times the standard deviation of the control measurements [58].	$LOD = \mu_{ctrl} + 10\sigma_{ctrl}$	(2.22)
Correlation coefficient (R)	It measures the linear correlation between two sets of variables x and y. It has a value between -1 and 1 [63]	$R(x, y) = \frac{Cov(x, y)}{\sigma_x \sigma_y}$	(2.23)

¹ Analytical sensitivity, specificity and accuracy express different concepts than the diagnostic (or clinical) sensitivity, specificity and accuracy of the test, already defined in Chapter 1.

532 **2.3. Integrated Optical Sensors**

533 A colorimetric approach was selected for this platform. Thus, a light source and optical
534 sensors are required to measure the absorbance change of the sample accompanying the
535 enzymatic reaction. Typically, colorimetric probes show light absorbance change in the
536 visible spectrum. Regarding the portability requirement of this platform, a commercial light-
537 emitting-diode (LED) was used as the light source in this work. Therefore, the required
538 optical sensor must be capable of measuring light with intensity in the order of μW to mW
539 (typical light intensities for commercial LEDs [64]) and wavelengths in the visible range.

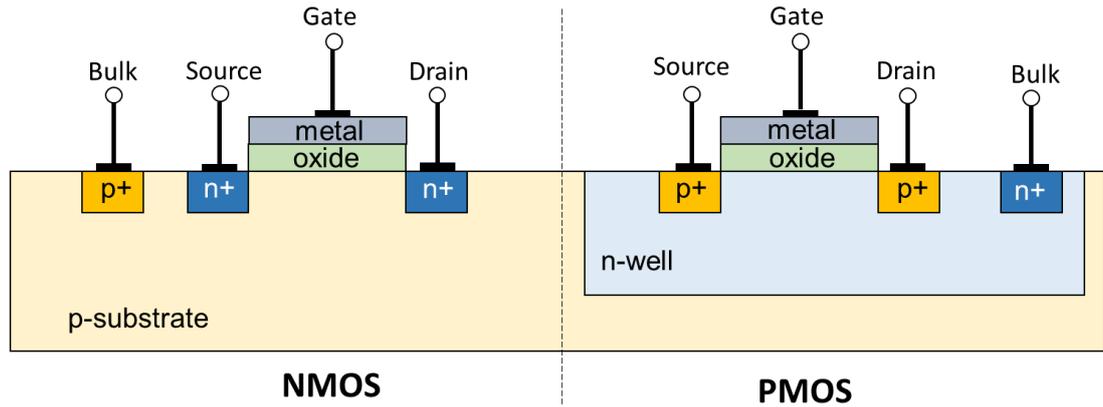
540

541 **2.3.1. CMOS technology**

542 In this work, the integration of optical sensors onto the same substrate was achieved using
543 the complementary metal-oxide-semiconductor (CMOS) technology. CMOS is today's
544 leading manufacturing process for the fabrication of integrated circuits. Developed for the
545 first time in the 60s by C. Sah. and F. Wanlass (Fairchild Semiconductor), in fifty years
546 CMOS technology was adopted for the fabrication of 99% of integrated circuits [65]–[67].
547 CMOS technology has the capability of integrating sensors, including optical sensors, with
548 read-out electronics on the same silicon chip.

549 Read-out circuitry developed in CMOS technology mostly use a combination of metal-
550 oxide-semiconductor field-effect transistors (MOSFET) in different configurations to
551 perform signal conditioning, including biasing, amplification and switching operations.
552 The most important property of semiconductors is that their conductivity can be varied over
553 a vast range by adding regulated quantities of impurity atoms into the semiconductor crystal
554 [65]. This process is generally referred to as doping. To increase the concentration of free
555 electrons, silicon can be doped with an element with a valence of 5, such as phosphorus [65].
556 The resulting material is an n-type semiconductor. Similarly, to increase the concentration
557 of holes, silicon can be doped with an element with a valence of 3, such as boron [65]. The
558 resulting material is a p-type semiconductor. A single silicon crystal can be doped differently
559 in different regions.

560 Figure 2.7 shows a schematic cross-section of an NMOS and a PMOS, fabricated with a
561 CMOS process. The process usually starts with a polished single crystal silicon wafer, doped
562 with p-type impurities (p-type substrate is assumed in this description). N-wells are then
563 fabricated on the substrate.



564

565 *Figure 2.7 Cross-section of two transistors in a CMOS gate. The figures assume the use of*
 566 *a p-type substrate and an n-well process. The schematic is a simplified version of the device*
 567 *and does not include all the material layers. Dimensions are not in scale. Well implants are*
 568 *expected to have rounded edges. Reproduced and modified from [65].*

569

570 For this aim, a SiO₂ layer is grown onto the substrate and selectively etched over desired
 571 areas. Donor atoms (n-type impurities) are subsequently implanted in the desired exposed
 572 areas. The silicon dioxide layer is then removed after the implant is completed. Similar
 573 lithographic steps are employed for the fabrication of a high resistance polycrystalline silicon
 574 (polysilicon) gate separated from the substrate by a thin silicon dioxide layer. Aluminium
 575 metal contacts are also used to interconnect bulk, source, drain and gate with other structures.
 576 At the end of the process, passivation layers (typically silicon nitride and polyimide) are
 577 used to protect the structure. Passivation layers are etched over the pads to enable wire-
 578 bonding connections to external instrumentation.

579 CMOS-based systems have been used for both digital and analogue applications. In the
 580 digital world, CMOS technology is in use for microprocessors and memories, for example.
 581 Antennas, sensors, signal processing circuitry (filtering, amplification, etc.) have been
 582 implemented with the same technology. Besides being scalable, reliable and low-cost, there
 583 are also technological advantages of CMOS-based chips, including its immunity against
 584 noise and low static power consumption [65].

585

586 2.3.2. Photodetectors

587 Optical detectors are devices capable of converting optical radiation into a detectable electric
 588 signal and have been successfully integrated with CMOS technology. There are many ways
 589 of interaction of electromagnetic radiation with material [68]. However, typically there are
 590 two main categories of photodetectors: thermal and photonic [68]. There are also further

591 classes of photodetectors which are widely described in the literature [68]. In thermal
 592 photodetectors, the absorption of light causes an increase in the device temperature with the
 593 consequent variation of a temperature-dependent physical parameter (e.g. the electrical
 594 conductivity) [68]. Whereas, in photonic detectors, photons interact directly with the
 595 electrons in a material [68].

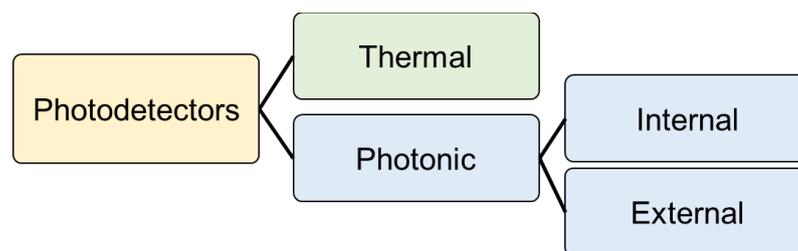
596 The photon detection process can be further divided into internal and external [68]. In
 597 detectors exploiting an internal photonic effect, photo-excited carrier (electron or hole)
 598 remains within the sample. On the other hand, in sensors utilising an external photonic effect,
 599 also known as the photoemissive effect, the incident photon causes the emission of an
 600 electron from the surface of the absorbing material [68]. The capability of internal photonic
 601 detectors of handling electrons within the device makes them usually the first choice for
 602 integrated systems. This was also the case for this project. The diagram in Figure 2.8
 603 summarises the main categories of photodetectors.

604 The photoelectric effect requires a minimum of photon energy to be triggered. If the energy
 605 of the incident photons is greater than the band-gap energy of the semiconductor, each
 606 absorbed photon can produce an electron-hole pair. The photon energy E is given by:

$$E = h \nu = h \frac{c}{\lambda} \quad (2.24)$$

607 Where h is the Planck constant, ν is the optical wave frequency, c is the light speed, and λ is
 608 the wavelength. Therefore, the photonic detectors have a maximum wavelength, beyond
 609 which they cannot operate.

610 Photodiodes are one of the most commonly used internal photonic detectors and have also
 611 been employed in this project. The principle of operation of a photodiode is based on a p-n
 612 junction. A p-n junction is formed on the same silicon crystal by creating two adjacent
 613 regions doped with p-type and n-type impurities. [65]. At the interface, due to the rapid
 614 recombination of diffused carriers from the n to the p region and vice versa, a depletion
 615 region is established [65].



616

617

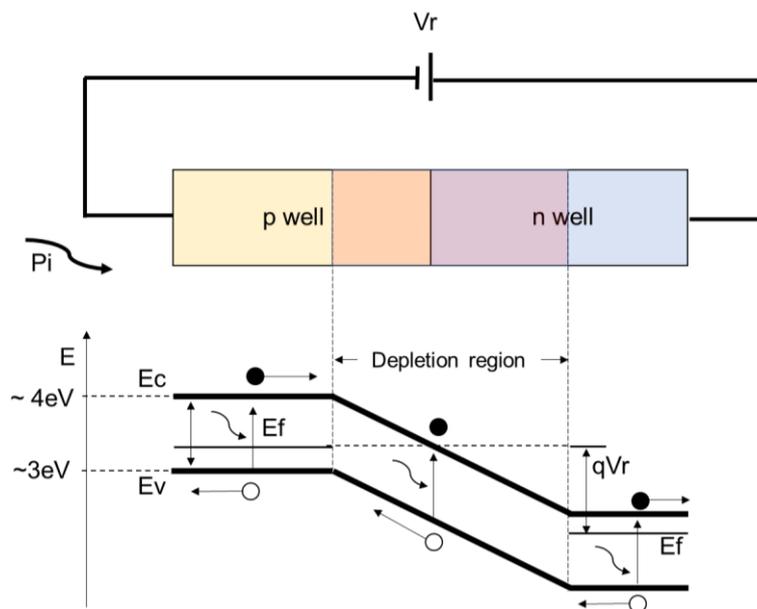
Figure 2.8 Main photodetectors categories.

618 In the depletion region, there is no free charge carrier, and an electric field is created, called
 619 built-in potential [65]. The built-in potential opposes the diffusion of holes into the n region
 620 and vice versa, acting as a potential barrier [65].

621 Photodiodes are p-n junctions and can be operated in both photoconductive and photovoltaic
 622 mode [68]. The photoconductive mode involves reverse biasing of the p-n junction, as shown
 623 in Figure 2.9. In this mode, when the junction is illuminated (for example, from the p-side),
 624 the photons absorbed in the depletion region can statistically produce electron-holes pairs.
 625 The generated carriers are separated, under the action of the electric field generated by the
 626 reverse bias: the electrons move towards the n zone and the holes toward the region p. Light
 627 can also be absorbed outside the depletion region and the carriers generated outside the
 628 depletion region are separated by diffusion. The diffusion current is a limiting factor in the
 629 response speed of the p-n photodiode, and it can be reduced by widening the depletion
 630 region. The extension of the depletion region can be controlled by tailoring structure
 631 conformation, doping concentrations, and the biasing.

632 Photodiodes operated in photovoltaic mode do not have any applied bias. The photocurrent
 633 generation is such as the one presented for the photoconductive mode, but the extension of
 634 the depletion region is exclusively due to the built-in-potential.

635



636

637 *Figure 2.9 Schematic representation of a photodiode in photoconductive mode. Dimensions*
 638 *are not in scale. V_r : bias voltage; E_c : conduction band; E_v : valence band; E_g : energy gap*
 639 *(for undoped silicon $E_g = 1.14\text{eV}$); E_f : Fermi level; q : elementary charge. Reproduced and*
 640 *modified from [68].*

641

642 The equivalent circuit of a silicon photodiode is shown in Figure 2.10 [69][70]. The model
 643 is composed of an ideal current source, an ideal diode (D_1), a capacitor (C_j), and two resistors
 644 (R_{sh} and R_s) connected as in the figure. The diode represents the p-n junction. C_j and R_{sh}
 645 represent the junction capacitance and resistance, respectively. Although an ideal photodiode
 646 should have an infinite R_{sh} , actual value ranges from 10 to 1000 M Ω [70]. R_s represents the
 647 resistance due to the connections. The ideal current source represents the contribution of the
 648 photogenerated current I_p . I_p is proportional to the incident optical P_i and the responsivity of
 649 the optical detector R_s :

$$I_p = R_s P_i \quad (2.25)$$

650 Using the above equivalent circuit, the output current (I_o) is given by the following equation
 651 [70]:

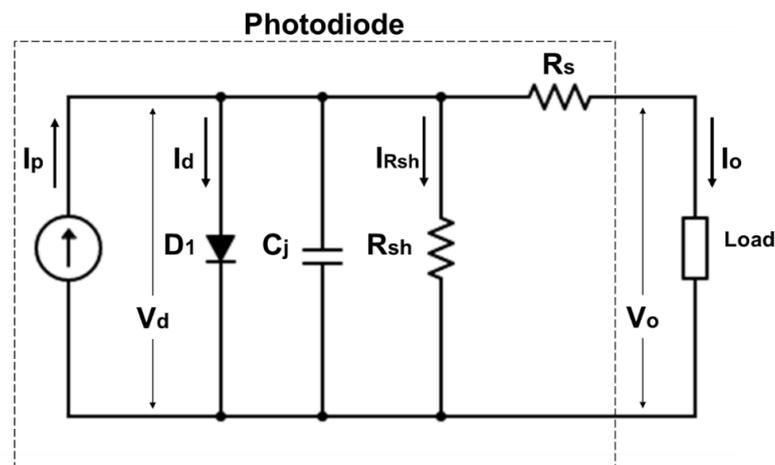
$$I_o = I_p - I_d - I_{Rsh} \quad (2.26)$$

652 If I_{Rsh} is negligible, the above equation can be rewritten as [69]:

$$I_o = R_s P_i - I_s (e^{\frac{qV_d}{kT}} - 1) \quad (2.27)$$

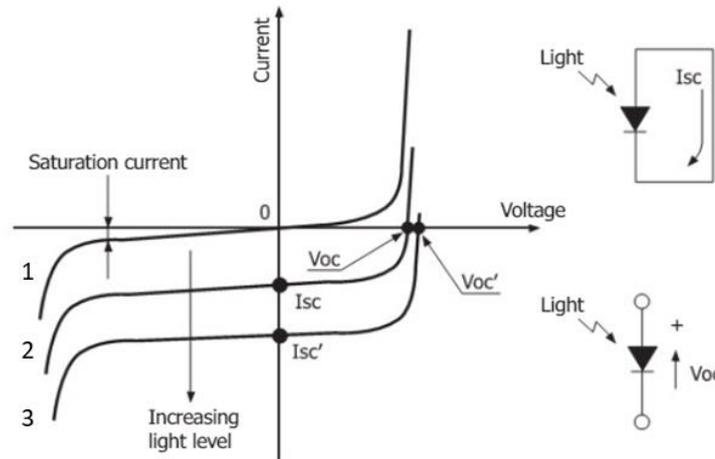
653 Where the first addend of the second member is given by equation (2.25) and the second
 654 addend is the diode equation. In the diode equation, I_s represents the saturation current of the
 655 diode, V_d is the voltage across the diode, q is the elementary charge ($\sim 1.6 \cdot 10^{-19}C$), k is the
 656 Boltzmann constant, T is the temperature in Kelvin.

657 Figure 2.11 illustrates the photodiode characteristic [69]. In dark conditions ($P_i = 0$), the
 658 photodiode characteristic is similar to the curve of a diode (see curve 1) [69]. However, when
 659 the photodiode is illuminated ($P_i > 0$), the characteristic function shifts downwards (see curve
 660 2). Increasing the light intensity produces a further shift of the characteristic (see curve 3)
 661 [69].



662

663 *Figure 2.10 Photodiode equivalent circuit. Reproduced and modified from [69].*



664
665 *Figure 2.11 Photodiode characteristic I-V curves. V_{oc} : open-circuit voltage. I_{sc} : short circuit*
666 *current. Reproduced and modified from [69].*

667

668 A photodiode is subject to various noise sources that degrade its performance. Noise sources
669 place a limit on the ability of subsequent detection electronics to detect small signals from
670 the photodiode [71], [72].

671 Specifically, the current flowing in a photodiode can be mainly divided into three
672 components: the photogenerated current I_p , the background current, and the dark current.
673 The three components can be considered additive. I_p is generated by the absorbed light and
674 is the desired output of the device. The background current is the undesired current due to
675 background radiation absorbed by the device. Therefore, this component depends on the
676 environment where the sensor operates. The dark current is undesired current observed even
677 in the absence of incident radiation.

678 There are many adding phenomena contributing to the dark current. Because of the
679 stochastic nature of the mechanism generating noise, noise sources are usually described
680 with statistical values such as power spectral density and root mean square value [73]. In the
681 absence of electrical bias, the absolute minimum internal noise is the thermal noise, also
682 known as Johnson noise or Nyquist noise [68]. Thermal noise is found in all resistive
683 materials, including semiconductors, and depends on temperature, resistance, and the
684 operating bandwidth of the device [65]. With the same notation illustrated above, the root
685 mean square of current fluctuation due to thermal noise ($i_{th,rms}$) is given by the following
686 equation:

$$i_{th,rms} = \sqrt{\frac{4kT\Delta f}{R_L}} \quad (2.28)$$

687 Where Δf is the operating bandwidth of the device and R_L is the load of the photodiode [74].

688 Any other form of internal noise, usually depending on the bias, is referred to as excess noise
 689 [68]. In general, a bias voltage across the photodetector increases excess noise. Shot noise
 690 and flicker noise are the two main causes of excess noise [68]. Shot noise is related to the
 691 discrete nature of the electric charge. The root mean square of the current fluctuation due to
 692 shot noise ($i_{sh, rms}$) is given by:

$$i_{sh, rms} = \sqrt{2qI_{avg}\Delta f} \quad (2.29)$$

693 Where the same notation as above are maintained and I_{avg} represent the average signal
 694 current flowing in the diode [71]. As shown in Figure 2.11, a saturation current (I_s) is
 695 expected under reverse bias and in dark condition. The saturation current is due to the
 696 diffusion of minority carriers. The saturation current of the device and depends on the
 697 conformation of the p-n junction, including doping levels and extension of the depletion
 698 region. Typical values of the saturation current are in the order of nA [75]. A mathematical
 699 model of the saturation current is illustrated in [75].

700 Flicker noise is associated with the presence of potential barriers at the contacts, interior, or
 701 surface of the semiconductor. Flicker noise is also known as 1/f noise due to its spectral
 702 density, being less evident at a higher frequency. The root mean square current due to flicker
 703 noise can be approximated by the following empirical equation:

$$i_{\frac{1}{f}, rms}(f) = \sqrt{\frac{K I_d^\beta \Delta f}{f^\gamma}} \quad (2.30)$$

704 Where I_d is the diode current, K , γ and β the empirical device coefficients depending on the
 705 fabrication process and doping profile, f is the operating frequency [76], [77].

706 All the above mechanism illustrated above are independent and contribute to the noise floor
 707 of the photodiode. The resulting root mean square current ($i_{n, rms}$) can be expressed as:

$$i_{n, rms} \approx \sqrt{i_{th, rms}^2 + i_{sh, rms}^2 + i_{\frac{1}{f}, rms}^2} \quad (2.31)$$

708 Therefore, while at low frequencies flicker noise dominates the power spectral density,
 709 broadband noise mechanisms prevail at a higher frequency. There are also additional sources
 710 of dark noise for photodiodes, including, generation-recombination (g-r) noise, leakage
 711 current and impact ionisation current [71]. A detailed discussion about dark current
 712 contributors can be found in [71], [78].

713 In the last decades, photodiodes experienced a profound revolution. Improved materials and
 714 architectures allowed the development of new types of photodiodes for specific

715 applications [79]. The photodiode material is usually selected in accordance with the
 716 operation wavelength. Silicon photodiodes are a common choice in application with an
 717 operating wavelength in the visible range [79]. Silicon photodiodes, widely fabricated with
 718 the CMOS technology, have been used for several applications, including imaging and
 719 biosensing.

720 In imaging applications, an array of photodiodes is typically used. A CMOS image sensor
 721 array is typically formed by the sensor array, row and column selectors, analogue signal
 722 processors timing and control [80]. The sensor array is a grid of sensors, each capable of
 723 producing a photogenerated current [81]. Each element of the array (usually referred to as a
 724 pixel) also integrates readout electronics. Pixel circuits are mainly divided into active pixels
 725 or passive pixels. A review on pixel circuits for imaging is reported in [80]. The readout
 726 method has an important influence on sensor performance [80]. Typically, the output of each
 727 pixel is usually addressed by row and column selectors [80]. To date, CMOS image sensors
 728 have been used for a varied range of applications, including vision systems, space,
 729 automotive, medical applications [80].

730 Photodiodes used for biosensing are typically coupled with biological receptors for the
 731 optical detection of the target analyte. Photodiodes have successfully been employed for the
 732 development of bioluminescent [82], fluorescent [83] and colorimetric sensing [84]. The
 733 review illustrated in Paragraph 2.6.1 includes several additional examples of the use of
 734 photodiodes for biosensing.

735

736 **2.3.3. Photodetectors metrics**

737 A set of metrics, here briefly discussed, are currently used for comparing different devices.

738 *Quantum efficiency* (η) is defined as the number of carriers generated per incident photon.

739 Formally, η can be expressed as [72]:

$$\eta = \frac{I_p}{\frac{q}{h\nu} P_i} \quad (2.32)$$

740 However, it is more practical to express the quantum efficiency as the ratio between the
 741 optical power P_a absorbed by the material and the incident optical power P_i [68]:

$$\eta = \frac{P_a}{P_i} \quad (2.33)$$

742 This expression can also be expressed as a function of the transmitted power P_t [68]:

$$P_a = P_i - P_t = P_i - P_i e^{-\alpha w} \rightarrow \eta = 1 - e^{-\alpha w} \quad (2.34)$$

743 Where α is the light absorption coefficient of the material and w is the depth of the substrate.
 744 The wavelength λ_c corresponding to $\alpha = 0$ and consequently $\eta = 0$ is called cut-off
 745 wavelength: the device is unresponsive for any $\lambda > \lambda_c$.

746 *Responsivity* (R_s), which has also been previously introduced, is defined as the ratio between
 747 the output current of the device and the incident light power determined in the linear region
 748 of response. Formally, R_s can be defined as [72]:

$$R_s = \frac{I_p}{P_i} \quad (2.35)$$

749 If the detector has a voltage output rather than a current, responsivity can be defined as the
 750 ratio of output voltage and optical power. This leads to units of V/W. If a photodiode is
 751 combined with some detector electronics generating a voltage output, the output voltage is
 752 the photocurrent times the trans-impedance of the electronics. Responsivity also depends on
 753 the wavelength of the incident light and is related to quantum efficiency as follows [72]:

$$\eta = \frac{h\nu}{q} R_s \quad (2.36)$$

754 *Dynamic range* quantifies the working range of the sensor considering the power of the
 755 incident light [85].

756 *Spectral range* quantifies the working range of the sensor considering the wavelength of the
 757 incident light [85].

758 *Gain* is the ratio between the output current of the device and the photogenerated current
 759 inside the device [72]. In some photodetectors, such as p-n junctions, the maximum possible
 760 gain is 1. In other devices, where a carrier multiplication effect is in place (such as avalanche
 761 photodiodes), the gain can be higher than one.

762 *Noise equivalent power (NEP)* is defined as the amount of light required to produce a signal
 763 to noise ratio (SNR) equal to 1 [72]. NEP depends on the light wavelength.

764 *Detectivity (D^*)* provides a representation of the noise level in a photodetector independently
 765 by its active area A and is formally defined as [72]:

$$D^* = \frac{\sqrt{A}}{NEP} \quad (2.37)$$

766 *Dark current*, as previously introduced, defined as the electrical noise detectable in the
 767 absence of light [72].

768 Other metrics have also been standardised but are omitted in this review, since unnecessary
769 for the comprehension of this work. Additional readings in [68], [71], [72] are suggested for
770 a full description.

771

772 **2.3.4. Other photodetectors**

773 Besides photoconductors and photodiodes, many other photodetectors have been
774 successfully developed [68]. It is beyond the scope of this work to thoroughly review all the
775 implemented photodetectors. However, the most commonly used photodetectors are briefly
776 described, and their advantages and disadvantages are discussed.

777 Photodiodes are an attractive choice for all those applications aiming to miniaturisation, low-
778 cost and easy usage. However, they have no amplification effect, and their gain is usually
779 lower than 1.

780 For use requiring high sensitivity, avalanche photodiodes (APD) are a common choice [68],
781 [71], [72]. APD are photodiodes (p-n or p-i-n junctions) with an internal mechanism of signal
782 amplification through an avalanche process. They are typically biased at a large reverse
783 voltage (see Figure 2.12(a)). The high electric field in the depletion region accelerates the
784 photo-generated carriers which generate secondary electron-hole pairs through impact
785 ionisation. Thus, the output of the device is the primary photocurrent multiplied by a factor
786 M . The photocurrent multiplication has a random nature, and this introduces additional
787 sources of noise. Every electron-hole pair is generated in a random location, so they do not
788 experience the same multiplication. Also, the multiplication effect amplifies both
789 background and dark current. More sophisticated APD structures have been proposed to
790 optimise the device metrics. However, APD manufacture requires very uniform doping
791 profiles, more complex designs, and a large reverse bias, usually resulting in higher
792 fabrication complexity and costs.

793 An APD operated in the ‘Geiger mode’ is known as a single-photon avalanche diode (SPAD)
794 [86]. SPADs are p-n junctions operated with a reverse bias voltage largely above the
795 breakdown voltage of the device (point 1 in Figure 2.12(b)). Due to the multiplication
796 mechanism, a single initial photogenerated carrier can trigger a self-sustaining avalanche
797 due to impact ionisation effects. Thus, a single photon can initiate a large internal current
798 flow. The avalanche can be quenched by reducing the bias voltage (see point 3 in Figure
799 2.12(b)). At this biasing point, the avalanche is no longer self-sustained and is quenched
800 [87]. Quenching circuits are typically used to decrease the voltage across the diode.

801 SPADs are usually employed in high-speed applications and are a common choice for
 802 detecting low light intensity (for instance lower than 1 nWcm^{-2} at 550 nm) [85]. They are
 803 also a popular choice in applications requiring high responsivity and high quantum
 804 efficiency [85], [86]. Although they share similar limitations with APDs, SPADs currently
 805 suffer from poor sensitivity due to noise and low fill-factors.

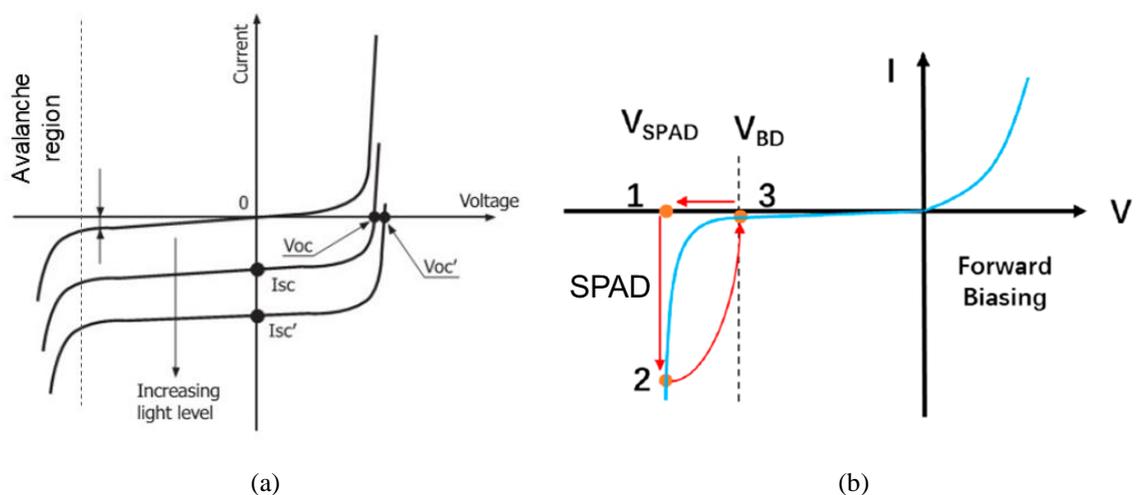
806 Although photodiodes, APDs and SPADs are all based on p-n junctions, they have structural
 807 differences designed to optimise their performance in their respective operation modality. A
 808 review illustrating the structural differences of these devices can be found in [87].

809 Photomultiplier tubes (PMTs) are also among the most-sensitive photodetectors for the
 810 visible light [72]. However, they are challenging to miniaturise; therefore, due to their high
 811 operating voltages, fragility, size and cost, there are many challenges to be addressed for
 812 their integration [72].

813 Charge-coupled devices (CCDs) are probably the biggest competitor of CMOS technology
 814 for image sensing applications [72]. A CCD is an array of metal-insulator-semiconductor or
 815 metal-oxide-semiconductor which can detect, store and transfer photogenerated charge.
 816 CCDs have high spatial resolution, low noise and high sensitivity [80].

817 However, CMOS outstands CCDs in terms of speed, integration capabilities, lower power
 818 consumption and capability of random access to single pixels [80], [88]. CMOS sensors and
 819 CCDs have comparable fabrication costs. However, CMOS usually requires a less complex
 820 read-out electronic, which can result in a less-expensive system [80], [88], [89].

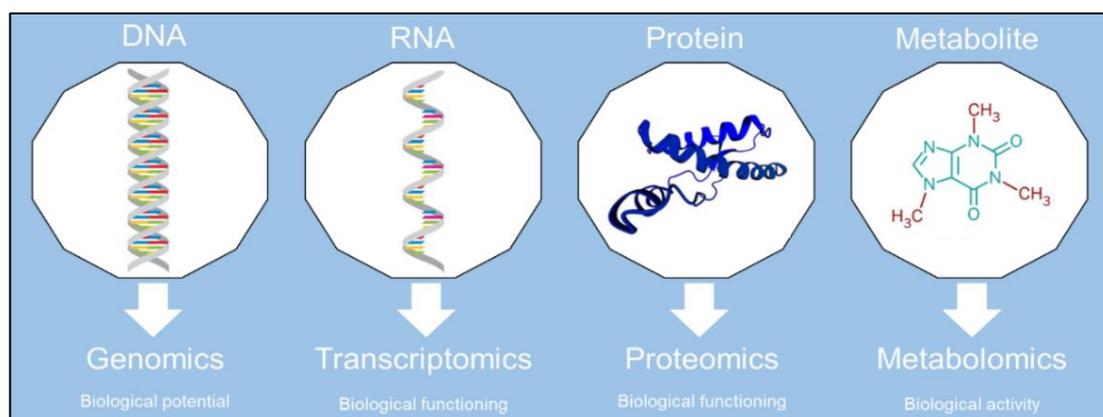
821



822 *Figure 2.12. (a) Avalanche region showed in the photodiode characteristic I-V curves.*
 823 *Reproduced and modified form [69]. (b) Operating principle of the Geiger mode.*
 824 *Reproduced and modified from [87].*

825 **2.4.Metabolomics**

826 One of the most promising fields of application of lab-on-chip platforms is metabolomics.
827 Metabolomics is the study of the relative variation of the collection of small molecules
828 (<1500 Da), known as metabolites, produced by cells during the metabolism [90]. The
829 increasing interest in metabolomics is related to its capability of describing the phenotype
830 and providing a ‘functional readout of the physiological health of an organism’ [11].
831 Metabolomics, together with the probably more well-known genomics, transcriptomics, and
832 proteomics, belongs to the omics sciences. Omics studies aim to identify, characterise, and
833 quantify all biological molecules that are involved in the structure, function, and dynamics
834 of a cell, tissue, or organism [91]. More precisely, genomics studies the structure, function,
835 evolution and mapping of nucleic acids and aims at the characterisation and quantification
836 of genes that guide the development of proteins with the aid of enzymes and messenger
837 molecules [91]. Transcriptomics is the study of the collection of all messenger RNA
838 molecules in a single cell, tissue, or organism [91]. Proteomics is the science that studies the
839 sum of all cell, tissue or organism proteins as related to their biochemical properties and
840 functional roles, as well as their modifications during the life of the organism [91].
841 Metabolomics is affected by both genetic and environmental factors and, therefore, can
842 bridge the gap between genotype and phenotype [11]. Metabolomics and other omics
843 sciences are complementary, and their integration is a promising research challenge [92].
844 The study of the metabolome is also considered to be more promising than other omics
845 science. This is because, unlike other omics studies, metabolic pathways are highly
846 conservative in mammalian species meaning that studies carried out on laboratory animals
847 can be easily related to humans [92]. An analysis of metabolomics can be carried out on a
848 variety of biological fluids and tissue types and can use a variety of different platforms of
849 technologies [91]. Currently, more than 114,000 metabolites have been detected and
850 quantified in human fluids, tissues or organs in different concentrations [90]. Among the
851 human fluids, blood metabolome is probably the most attractive one because of its intrinsic
852 physiological stability and collection convenience [90]. Blood is made up of two
853 components: a cellular component (red/white cells and platelets) suspended into a liquid
854 component, namely plasma [90]. Plasma can be obtained from blood by centrifugation or
855 filtration. The serum is also a body fluid obtainable by removing the clotting agents from
856 plasma.



857

858 *Figure 2.13 Metabolomics reflects the phenotype of an organism. Modified from [93].*

859

860 Blood, plasma and serum contain a variety of organic and inorganic substances such as
 861 proteins and peptides, nutrients, electrolytes, organic wastes and a variety of other small
 862 molecules suspended or dissolved [90]. The biological composition of plasma and serum is
 863 very similar and includes more than 4200 metabolites [90]. Unknown metabolites, expected
 864 to be discovered in support of metabolic pathways still not completely understood, are
 865 referred to as metabolic dark matter [94].

866 Four different conceptual approaches are widely adopted: target analysis, metabolite
 867 profiling, metabolomics, and metabolic fingerprinting [11]. Target analysis and metabolite
 868 profiling aim to quantify, respectively, a small set of known metabolites and a larger set of
 869 compounds (both identified and unknown) using a single analytical technique [11].
 870 Differently, metabolomics employs complementary methodologies to quantify as many
 871 metabolites as possible. Finally, metabolic fingerprinting looks for a specific metabolite in
 872 a large sample population by comparing specific features.

873 Due to the huge diversity of chemical structures, there is no single technology available to
 874 analyse the entire metabolome [90]. Although over the past two decades several techniques
 875 have been employed for metabolic profiling [90], nuclear magnetic resonance (NMR) and
 876 spectroscopy and mass spectrometry (MS) are the traditionally used approaches for
 877 metabolomics profiling [14], [94], [95]. NMR spectroscopy quantifies analyses based on
 878 their response to a radio-frequency excitation [90]. Differently, MS quantifies analyte based
 879 on their mass-to-charge ratio (m/z) by transforming the analyte molecules into a charged
 880 (ionised) state, with subsequent ion analysis and any fragment ions formed during the
 881 ionisation process [96]. There are several types of MS, depending on the technique for
 882 ionisation and ion analysis [96]. The most used MS techniques in metabolomics are gas

883 chromatography MS (GC-MS) and liquid chromatography MS (LC-MS). GC-MS provides
 884 molecules separation basing on their volatility at several temperatures. Differently, LC-MS
 885 provides separation depending on the solubility of the molecule in various solvents (e.g.
 886 water, methanol, acetonitrile, isopropyl alcohol, and hexane) [96]. Each technique has
 887 advantage and disadvantages when compared to the others, as summarised in Table 2.4. For
 888 additional details about the techniques mentioned above, [95]–[98] are suggested.

889 Nevertheless, they are often complementary since some analytes are solely quantifiable with
 890 a single technique. N. Psychogios et al. in [90] estimated that NMR is capable of quantifying
 891 only 1.2% of the human serum metabolome. Several MS techniques, all together, can instead
 892 obtain data on 84% of the serum metabolome [90]. Among the MS techniques, the authors
 893 in [90] suggest using LC-MS for human serum metabolomics. Metabolomics has been
 894 applied to a vast variety of applications: human and animal health, biomarker discovery,
 895 pharmacometabolomics, environmental monitoring are just some of them [14].

896 It is a shared vision that metabolomics has a large and still partially untapped potential in
 897 healthcare, where the large metabolome information can be combined by machine learning
 898 and classification algorithms [11], [14], [92], [93]. Currently, metabolomics is exploited
 899 mainly for pharmacology. The best-selling drugs on the market today act on the metabolic
 900 pathway by enzyme, inhibitors or any other suitable mean [14]. There is evidence that
 901 metabolomics can potentially be employed for the diagnosis and monitoring of the most
 902 deadly diseases, including cancer, cardiovascular diseases (CVD) and dementia [12]. In line
 903 with the aim of the present project, a focus is provided for metabolomics applied to PCa and
 904 ischemic stroke.

905

906 *Table 2.4 Comparison of most commonly used techniques for metabolomics [14].*

	NMR	GC-MS	LC-MS
Start-up cost	> \$1 million	> \$150k	> \$300k
Quantitative	✓	✓	✓
Destructive	x	✓	✓
Limit of detection (LOD)	5 μ M	0.5 μ M	0.5 nM
Test time (per sample)	5 min	20-40 min	20-40 min
Sample volume	0.1 – 0.5 mL	0.1 – 0.2 mL	10 – 100 μ L
Automated	Fully	Partially	Partially
Organic molecules	✓ (most of them)	✓ (most of them)	✓ (most of them)
Inorganic molecules	x	✓ (some of them)	✓ (some of them)
Novel compounds identification	✓	x	x

907 **2.4.1. Metabolomics for cancer**

908 One in two people will develop cancer at some point in their lifetime [13], [99]. The World
909 Health Organization estimates more than 18 million cases of cancer and more than 9.5
910 million cancer-related deaths worldwide, only in 2018 [13]. Although frequency and survival
911 rate are considerably variable with the cancer type, there is consistent evidence that patients
912 diagnosed at an early stage are more likely to survive [13], [99]. For some cancer types,
913 screening programs have already dramatically improved the survival rate. In the UK, the
914 NHS cervical and bowel cancer screening programs have reduced mortality by 70% and
915 15%, respectively [100], [101]. However, there are other types of cancer where the scientific
916 community is in desperate need of new criteria and tools [7].

917 Metabolomics has a largely untapped potential in the field of oncology [14], [102]. Cancer
918 cells have a different metabolism than healthy ones [103]. The altered metabolism of cancer
919 cells, together with their accelerated metabolism and the parallel angiogenesis, produce
920 substantial and detectable modifications in the entire human metabolism [104]. Cancer-
921 related metabolites accumulate in human body fluids [105], and their altered levels act as
922 indicators or biomarkers to diagnose or monitor the disease [14], [105]. It has been
923 demonstrated in the scientific literature that the use of a panel of metabolites rather than a
924 single biomarker has the potential to perform better than the current clinical standard [106].
925 Leichtle et al. [107], for instance, have developed a multi metabolomics marker model which
926 was superior to the conventional tumour marker CA 19-9 in differentiating between
927 pancreatic cancer, pancreatitis, and healthy controls. Similar results have also been achieved
928 for breast cancer [106]. Besides, Wang et al. [108] have demonstrated that it is possible not
929 only to diagnose but also to monitor oesophageal cancer stage by quantifying 12 metabolites
930 in tissue.

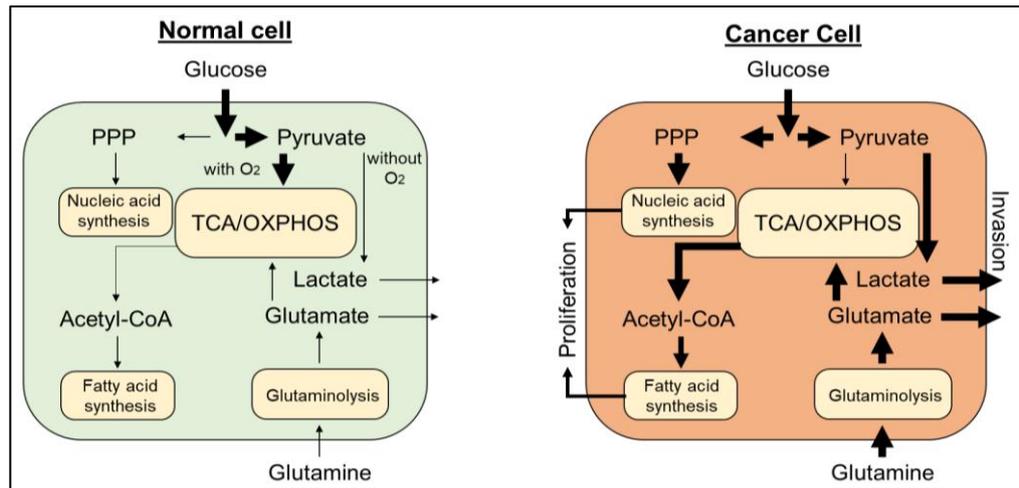
931 The main metabolic difference in cancer cells is how they use glucose to produce energy
932 [103]. Cancer cells usually proliferate from one aberrant cell to more than $2 \cdot 10^9$ cells per
933 cm^3 and modify their metabolic pathways to sustain their proliferative capacity [109]. In
934 cells, energy is usually stored using a series of 'building' (anabolic) processes and released
935 through a series of 'breaking-down' (catabolic) mechanisms. In the presence of O_2 (aerobic
936 conditions), healthy human cells transform glucose into energy under the form of adenosine
937 triphosphate (ATP). This process is carried out through a series of biological processes,
938 including the Krebs cycle (TCA) and the oxidative phosphorylation (OXPHOS), producing
939 residual CO_2 and water. Usually, this process provides 36 ATP molecules per glucose

940 molecule processed [103]. In the absence of oxygen (anaerobic or hypoxic conditions),
941 energy is obtained from different processes leading to the production of lactate, which is
942 later released outside the cell as a reaction residue. In parallel, glucose is also used for the
943 pentose phosphate pathway (PPP), which influences DNA replication [110].

944 Glutamine metabolism – the second most used nutrient after glucose – is also used to provide
945 energy after being converted in glutamate through the glutaminolysis cycle [110]. TCA and
946 OXPHOS are also related to the synthesis of fatty acids, primarily through the production of
947 citrate-related Acetyl-CoA.

948 In cancer cells, the standard mechanisms mentioned above are altered [103], [109], [110].
949 Even in the presence of oxygen, glucose is mainly converted to lactate for energy production
950 [110]. This mechanism is usually referred to as the Warburg effect [103]. The process is less
951 efficient when compared to the normal cycle since it only produces 4 ATP molecules per
952 glucose molecule [103]. The consequent increase in lactate secretion has been linked to the
953 capability of the cancer cell to accelerate the generation of new blood vessels (angiogenesis)
954 [110]. On the one hand, angiogenesis helps cancer cells to receive increased levels of
955 nutrients. On the other, it provides an easy way for aberrant cells to invade new tissues and
956 create metastasis [110]. Aiming to compensate for the glucose-related ATP production,
957 glutamine intake is also increased in cancer cells. Glutamine is converted into glutamate
958 which, when in excess, is also released by the cell [110]. The upregulated glutamine-
959 glutamate cycle also boosts fatty acid synthesis [110]. Increased synthesis of nucleic acids
960 and fatty acids has been linked to cell proliferation [110]. Metabolic differences related to
961 energy production and usage from glucose and glutamine are schematically represented in
962 Figure 2.14. Additional metabolic modifications have been discovered in cancer cells and
963 reviewed in the literature [103], [109], [110]. Among them, cancer cells take advantage of
964 ample supply of amino-acids, especially in the L-type form, vastly more abundant in humans
965 with respect to D-type amino acids [111]. The progression of cancer is associated with
966 increases in L-amino acids (LAA) uptake by cancer cells, also obtained by modifying the
967 specific transporters [112]. Choline metabolism is another well-established modified
968 pathway [113]. In many cancer types, the increase of choline and choline-related metabolites
969 have been related to a modification in choline-related enzymes and transporters [113].
970 Understanding cancer metabolism led to the development of specific drugs acting on critical
971 metabolic pathways proven essential for cancer cells [109], [114].

972



973

974 *Figure 2.14 Schematic representation of metabolic differences between a normal cell (left)*
 975 *and a cancer cell (right). Bold arrows indicate an upregulated pathway. Reproduced and*
 976 *modified from [110].*

977

978 Statins such as Simvastatin and Atorvastatin, for instance, act on the metabolic pathways for
 979 fatty acid synthesis [109]. Methotrexate, another anticancer approved agent, operates on the
 980 nucleic acid synthesis [114]. L-asparaginase is also an approved anticancer agent used in
 981 clinical practice to treat leukaemia by acting on asparagine metabolism [115]. Alongside the
 982 approved drugs, an increasing number of compounds are in clinical and pre-clinical trial
 983 stages [114]. A detailed review of cancer metabolism for therapeutic purposes has been
 984 published by U.E. Martinez-Outschoorn et al. [114].

985 Understanding cancer metabolism also provided essential knowledge for cancer diagnosis
 986 and monitoring. Several metabolites have been linked to cancer. Currently, a selection of
 987 marked metabolites is being used in clinical testing for imaging purposes [116]. Positron
 988 Emission Tomography scanning is used to image cancer after the intake of labelled
 989 metabolites such as, for example, Fludeoxyglucose, C-acetate, C-choline, F-choline, C-
 990 pyruvate [116]. Labelled metabolites are usually stable isotope and are selected because
 991 expected to accumulate more in cancer cells due to their upregulated intake [116].

992 Table 2.5 presents a review of metabolites linked to cancer. Interestingly, there is some
 993 crossover between the metabolic profiles. The set of the most recurrent metabolites,
 994 independently by the sample, have been summarised in Table 2.5. Confirming what
 995 previously described, the table highlights a set of metabolites crucial for cancer cells such as
 996 glucose/lactate, glutamine/glutamate, amino acids, and choline/choline-derived metabolites.

997

Table 2.5 Cancer-related metabolites documented in the scientific literature.

Cancer	Sample	Metabolites
Breast	Serum*	2-hydroxyglutarate [104], acetoacetate [117], beta-alanine [104], choline [118], fatty acid [119], glucose [120], glutamate [104], [117], glutamine [104], glycerol [117], glycerophosphocholine [118], histidine [117], [120], linoleic acid [119], lipids [120], mannose [117], n-acetyl glycoprotein [117], palmitic acid [119], phenylalanine [117], phosphocholine [118], pyruvate [117], steric acid [119], xanthine [104]
	Tissue**	acetoacetate [121], histidine [121], glycerol [121], mannose [121], phenylalanine [121], pyruvate [121], linoleic acid [122], glutamate [121], glutamine [122], myoinositol [106], phosphoethanolamine [106], taurine [106], asparagine [115], [123], isoleucine [122], threonine [122]
	Urine	4-hydroxyphenylacetate [124], 5-hydroxyindoleacetic acid [124], homovanillate [124], urea [124]
Colorectal	Serum*	2-Hydroxybutyrate [102], alanine [125], arginine [106], aspartic acid [102], [125], choline [126], cystamine [102], cysteine [106], fatty acid [106], glucose [106], glycine [126], glycine [125], histidine [125], inositol [126], isoleucine [125], kynurenine [102], lactate [126], leucine [126], lysine [125], methionine [125], oleamide [106], phenylalanine [126], phosphocholine [126], pyruvate [127], sarcosine [125], taurine [126], threonine [126], tryptophan [127], [128], tyrosine [125], [127], ultralong fatty acids [129], uridine [127], valine [125]
	Tissue**	2-aminobutyrate [130], 2-Hydroxybutyrate [130], 2-oxobutyrate [130], 5-Hydroxytryptamine [130], arginine [130], betaine [130], fatty acid [131], [132], glutamic acid [130], glutamine [131], [132], indoxyl [130], lactate [127], linoleic acid [130], N1-acetylspermidine [130], N-acetyl-5-hydroxytryptamine [130], nicotinic acid [130], proline [126], [130], symmetric dimethylarginine [130], threonine [130], uracil [130], urea [131]–[133], xanthine [130]
Pancreatic	Serum*	3,6-dihydroxy-5-cholan-24-oic acid [107], 3-hydroxybutyrate [106], 3-hydroxyisovalerate [106], 3-Hydroxybutyrate [134], [135], 3-hydroxyisovalerate [134], acetone [134], [136], alanine [137], arachidonic acid [138], arachidyl carnitine [139], butanoic acid [138], chenodeoxycholic acid [139], choline [137], citrate [136], creatine [134]–[136], cysteine [138], ethanol [134], formate [134], [136], glucose [134], [137], glutamate [134], glutamine [134], [138], glycerol [134], glycerol 2-phosphate [137], glycerol 3-phosphate [137], Glycholic acid [107], glycodeoxycholic acid [107], hydroxybutyrate [136], hypoxanthine [138], isoleucine [135], lactate [135], linoleic acid [137], lipids [136], lysine [138], malate [137], mannose [134], medium-chain acylcarnitines [140], myoinositol [137], N-acetyl glycoprotein [136], N-methylalanine [138], oleoyl carnitine [107], phenanthrenol [138], phenylalanine [134], [138], phosphatidylcholine [106], proline [134], quinaldic acid [139], sitosterol [139], tauro(ursodeoxy)cholic acid [138], tetradecanal oleamide [139], triglycerides [135], trimethylamine-N-Oxide [135], tyrosine [138]
	Tissue**	Alanine [108], arachidonic acid [141], asparagine [108], choline [108], citrate [142], fatty acid [142], glutamic acid [108], glutamine [141], glycerophosphocholine [143], ketones [142], lactate [108], leucine [108], lysine [141], lysophosphatidylcholine [144], N-methylalanine [141], phenylalanine [141], phosphatidylcholine [144], phosphocholine [143], sphingolipid [142], sphingomyelin [144], taurine [108], tauro(ursodeoxy)cholic acid [141], valine [108]
Ovarian, uterus, cervix	Serum*	2-Piperidinone [105], glycine [106], lysophosphatidylcholine [105], pyrimidine [106], tryptophan [105]
	Urine	1-methylguanidine [145], histidine [146], ketones [147], lactate [147], methylxanthine [145], mucin [146], N4-acetylcytidine [146], Nucleotide [146], proline [145], pseudouridine [146], pyridylacetic acid [145], succinic acid [146], theophylline [145], tryptophan [105], urate-3-ribonucleoside [146], uric acid [145], urocanic acid [145]

Prostate	Serum*	Alanine [148], [149], androsterone sulfate [150], arachidonoyl amine [150], arginine [148], [151], cholesterol [150], choline [152], citrate [148], [153], creatinine [154], [155], cysteine [150], dimethylheptanoyl carnitine [150], fatty acid [148], formate [150], glucose [151], glutamate [148], [150], glycine [150], isolithocholic acid [150], leucine [150], lysine [150], [151], phenylalanine [151], [156] phosphocholine [150], proline [148], testosterone sulfate [150]
	Tissue**	Alanine [156], arginine [157], asparagine [156], cholesterol [150], [157], [158], choline [150], [156], [159], citrate [150], cysteine [157], fatty acid [150], glutamate [150], glutamine [150], glycerol [150], [156], glycine [150], [159], lactate [150], [156], lactate [160], [161] leucine [71], myoinositol [156], phenylalanine [150], phosphocholine [150], [156], proline [150], [156], pyrimidine [150], [156]
	Urine	Alanine [156], choline, [156], citrate [156], creatinine [150], cysteine [150], fatty acid [150], glycerol [150], lactate [156], phosphocholine [156], pyrimidine [150]
Oesophageal	Serum*	adenosine monophosphate [162], NAD [162], acetoacetate [106], acetone [106], asparagine [157], aspartate [106], beta-hydroxybutyrate [163], citrate [163], creatine [106], cysteine [106], glucose [162], glutamate [106], glutamine [163], histidine [106], lactate [106], lactic acid [163], LDL [106], leucine [106], linoleic acid [163], lysine [163], methionine [163], myristic acid [163], phenylalanine [164], tryptophan [163], tyrosine [163], valine [163], VLDL [106],
	Tissue**	Acylcarnitines [165], carnitine [165], fatty acid [165], lysophosphatidylcholine [165]
Lung	Serum*	6-diaminopimelate [166], cholesteryl acetate [166], choline [167], fatty acid [167], [168], glutamine [169], lysophosphatidylcholine [166], [168], N-succinyl-2 [166], octanoylcarnitine [166], phosphatidylcholine [166], phosphatidylserine [166], sphingomyelin [168]
	Tissue**	Choline [170], fatty acids [170], glutamine [171]
Brain	Tissue**	arachidonic acid [141], glycerophosphocholine [141], lactate [141], lysophosphatidylcholine [141], phosphatidylcholine [141]
	CBF***	2-aminopimelic acid [172], citric acid [172], isocitric acid [172], methionine [172], serine [172], tyrosine [172], valine [172]
Leukaemia	Serum*	Acetone [173], alanine [173], arginine [173], cholesterol [173], [174], choline [173], creatine [173], cysteinyl-glycine [175], formate [173], glucose [173], glutamate [175], glycerol [174], histidine [173], lactate [173], [174], leucine [173], lysine [173], lysophosphatidylcholine [175], myoinositol [173], phenylalanine [173], phosphatidylcholine [175], phosphocholine [174], proline [173], pyruvate [174], trimethylamine-N-Oxide [173], tyrosine [173], uric acid [174], uridine [174], valine [173]
	Tissue**	Asparagine [123], [176], glutathione [177]
<p>* This group includes blood, serum, or plasma ** This group includes tissue, cells or locally collected biological fluid (e.g. secretions) *** Cerebrospinal fluid</p>		

1000

Table 2.6 Summary of metabolic cross-over between the metabolic profiles.

Analyte	Breast	Colorectal	Pancreas	Ovarian, Uterus, Cervix	Prostate	Oesophageal	Lung	Leukaemia	Brain
asparagine	✓		✓		✓	✓		✓	
choline	✓	✓	✓		✓		✓	✓	
cysteine		✓	✓		✓	✓		✓	
fatty acid		✓	✓		✓	✓	✓		
glucose	✓	✓	✓		✓	✓		✓	
glutamate	✓		✓		✓	✓		✓	
glutamine	✓	✓	✓		✓	✓	✓		
histidine	✓	✓		✓		✓		✓	
lactate		✓	✓	✓	✓	✓		✓	✓
leucine		✓	✓		✓	✓		✓	
lysophosphatidylcholine			✓	✓		✓	✓	✓	✓
phenylalanine	✓	✓	✓		✓	✓		✓	
phosphocholine	✓	✓	✓		✓			✓	
proline		✓	✓	✓	✓			✓	
tyrosine		✓	✓		✓	✓		✓	✓
valine		✓	✓		✓	✓		✓	✓

1001

1002 **2.4.2. Metabolomics for prostate cancer**

1003 PCa has the highest cancer incidence for male subjects in the UK (26 % in 2014), and it is
1004 expected to rise in the next 15 years, as the population ages [178]. In accordance with other
1005 cancer types, there is consistent evidence that patients diagnosed at an early stage are more
1006 likely to survive cancer. PCa patient 5-years survival rate is nearly 100% when the tumour
1007 is detected in a localised initial stage [178]. The same rate decreased to 34% when the tumour
1008 is diagnosed in a late metastatic stage [178]. This difference in the survival rate underlines
1009 the necessity of PCa screening program. Most PCa cases are diagnosed with a prostate-
1010 specific antigen (PSA) blood test, usually in combination with digital rectal examination,
1011 biopsy and imaging [150]. Once diagnosed, PSA is also used to monitor and assess the
1012 evolution of the disease [150]. This prediction has been related to the high false-positive rate
1013 of the PSA test: only less than one in three subjects with increased PSA will have PCa [7].
1014 PSA test also misses about 15% of cancers [7]. Currently, a PSA-based screening program
1015 remains controversial because of the number of false positives. This could unnecessarily
1016 deteriorate the quality of life of healthy subjects and increase clinical costs without
1017 significantly reducing mortality [179]. Besides being invasive, digital rectal examination and
1018 biopsy can even potentially miss cancer due to tumour heterogeneity [150]. As a

1019 consequence, several additional biomarkers are now being explored to improve the
1020 performance of the current clinical procedure [150].

1021 Metabolomics is being explored to address this necessity [150]. Lohkov et al. [150], for
1022 instance, have demonstrated that a set of metabolites from plasma can potentially
1023 discriminate PCa better than PSA. Specifically, in a group of 30 healthy controls and 40
1024 subjects affected by PCa, they demonstrated that increased levels of carnitine-related
1025 metabolites discriminated cancer and healthy groups with sensitivity and specificity of
1026 94.6% and 96.4%, respectively. They performed better than the PSA test, which scored a
1027 sensitivity of 35% and a specificity of 83.3% on the same samples. In a similar study, Zhang
1028 et al. [150] also provided a set of metabolites with diagnostic potential comparable to PSA.

1029 Table 2.7 demonstrates that metabolomics can be applied to PCa in all the stages of the
1030 disease, from early diagnosis to the stage assessment. Here, the link between PCa and
1031 metabolites have been broken down to four sub-categories. The first category groups all the
1032 metabolites which have been linked to PCa risk or recurrence. The second category groups
1033 all the metabolites which have shown diagnostic capability. This is usually assessed by
1034 comparing the metabolome of a healthy control group with one of the people recently
1035 diagnosed with PCa. The third category groups all the metabolites which have shown the
1036 capability of discriminating a malignant from a benign tumour. This is usually determined
1037 by comparing the metabolome of people diagnosed with a malignant PCa with subjects
1038 diagnosed with a benign PCa. The fourth category groups all the metabolites which have
1039 shown the capability of providing information about cancer stage, including the presence of
1040 eventual metastasis, usually evaluated by comparing the metabolome of people affected by
1041 PCa in several stages.

1042 Among the metabolites relevant to PCa, it is worth highlighting that the serum concentration
1043 of LAA is typically increased in PCa group, except for alanine and lysine showing a
1044 decreased level in late-stage cancer. Glutamate and choline, also demonstrate a very close
1045 link with PCa, being relevant in all the stages of the disease [148], [152]. A correlation
1046 between sarcosine and PCa is still a controversial topic. At this stage, there are studies both
1047 approving [150], [156], [157] and disapproving [180] serum sarcosine as a metabolic
1048 biomarker for PCa. Certainly, this topic requires further study.

1049

1050

1051 Table 2.7 Summary of metabolites which have been linked to PCa in literature, divided
 1052 according to sample type (serum*, tissue**, urine) and cancer stage.

Metabolite	Sample	Risk or recurrence	Diagnosis	Malignancy	Staging
Alanine ^{LAA}	Serum*		↔ [149]		↓ [148]
	Tissue**			↑ [156]	
	Urine			↑ [156]	
Androsterone sulfate	Serum*		↑ [150]		
	Tissue**				
	Urine				
Arachidonoyl amine	Serum*		↑ [150]		
	Tissue**				
	Urine				
Arginine ^{LAA}	Serum*			↑ [151]	↑ [148]
	Tissue**				↑ [157]
	Urine				
Asparagine ^{LAA}	Serum*			↑ [157]	↑ [156]
	Tissue**				
	Urine				
Carnitine	Serum*		↔ [150]		
	Tissue**				
	Urine				
Cholesterol	Serum*				↑ [150]
	Tissue**				↑ [150]
	Urine				
Choline	Serum*	↑ [152]	↑ [152]		
	Tissue**		↑ [150], [156]	↑ [150], [156]	↑ [150], [157], [159]
	Urine		↑ [156]	↑ [156]	
Citrate	Serum*	↔ [148]		↔ [148]	↓ [148], [181]
	Tissue**	↓ [150]	↓ [150]	↓ [150]	
	Urine		↓ [156]		↓ [156]
Creatinine	Serum*	↑ [154]			↑ [155]
	Tissue**				
	Urine			↓ [150]	
Cysteine ^{LAA}	Serum*	↔ [150]			
	Tissue**			↑ [157]	
	Urine	↔ [150]			
Fatty acid	Serum*	↔ [148]		↔ [148], [150]	↔ [148]
	Tissue**				↔ [150]
	Urine			↔ [150]	
Formate	Serum*			↔ [150]	↔ [150]
	Tissue**				
	Urine				
Glucose	Serum*			↑ [151]	
	Tissue**				
	Urine				
Glutamate ^{LAA}	Serum*	↔ [148]	↑ [150], [182]	↑ [148], [151], [182]	↑ [148], [150], [156], [182]
	Tissue**		↔ [150]	↑ [150]	↑ [156]
	Urine				
Glutamine ^{LAA}	Serum*		↑ [150]		
	Tissue**	↔ [150]	↔ [150]		
	Urine				
Glycerol	Serum*				
	Tissue**		↑ [150], [156]	↔ [150]	↑ [156]
	Urine		↑ [150], [156]		↑ [156]
Glycine ^{LAA}	Serum*		↑ [150]		
	Tissue**			↑ [150]	↑ [159]
	Urine				
Isolithocholic acid	Serum*		↓ [150]		
	Tissue**				
	Urine				
Lactate	Serum*		↑ [160], [161]		
	Tissue**		↑ [150], [156]	↑ [156]	
	Urine		↑ [156]	↑ [156]	
Leucine ^{LAA}	Serum*				↑ [150]
	Tissue**			↔ [150]	↑ [156]
	Urine				
Lysine ^{LAA}	Serum*		↔ [150]	↑ [151]	↓ [150]
	Tissue**				
	Urine				
	Serum*				

Myoinositol	Tissue**			↑ [157]	↑ [150], [156]
	Urine				
Phenylalanine ^{LAA}	Serum*			↑ [151]	↑ [156]
	Tissue**				↑ [150]
Phosphocholine	Urine				
	Serum*		↔ [150]		
	Tissue**		↑ [150], [156]	↔ [150]	↑ [156]
Proline ^{LAA}	Urine		↑ [156]		
	Serum*			↑ [148]	↑ [148]
	Tissue**		↑ [150]		↑ [156]
Pyrimidine	Urine				
	Tissue**		↓ [156]		
	Urine		↓ [150], [156]		
Sarcosine	Serum*		↑ [149]		
	Tissue**		↑ [150]	↑ [150], [156], [157]	↑ [150], [156], [159], [183]
Serine ^{LAA}	Urine				↑ [156], [157], [159], [183]
	Tissue**				↓ [157]
	Serum*				
Spermine	Serum*				↓ [119], [150], [157]
	Tissue**	↓ [150]	↓ [156]	↓ [156]	↓ [119], [150], [157]
	Urine		↓ [156]	↓ [156]	
Taurine ^{LAA}	Serum*				↑ [156]
	Tissue**			↔ [150]	↑ [150]
	Urine				
Tryptophan	Serum*	↔ [148]		↔ [148]	↑ [148]
	Tissue**				
	Urine				
Tyrosine ^{LAA}	Serum*				↔ [150]
	Tissue**				
	Urine				
Urea	Serum*	↔ [148]		↔ [148]	↑ [148], [153], [155]
	Tissue**				
	Urine				
Valine ^{LAA}	Serum*			↑ [151]	↑ [150]
	Tissue**		↓ [156]		
	Urine				
Xanthine	Serum*			↔ [148]	↑ [148], [157]
	Tissue**				
	Urine				
Testosterone sulfate	Serum*		↓ [150]		
	Tissue**				
	Urine				
↑: increased concentration level ↓: decreased concentration level ↔: altered concentration level but the trend is not easily reportable * This group includes blood, serum, or plasma ** This group includes tissue, cells or locally collected biological fluid (e.g. secretions) LAA Amino acid, mainly present in human blood in its l-type					

1053

1054 **2.4.3. Metabolomics for cardiovascular diseases**

1055 Globally, CVDs are the leading cause of death, claiming almost 18 million lives each year
 1056 [13]. CVDs group a variety of conditions related to the hearth and blood vessels. CVDs
 1057 might be divided into chronic and acute diseases. Chronic CVDs, including rheumatic heart
 1058 disease, congenital heart disease, coronary heart disease, are long term diseases. Differently,
 1059 acute CVDs include usually severe and immediate failure events. Acute events such as stroke
 1060 and heart attacks are mainly caused by a blockage that prevents blood from flowing correctly
 1061 [13]. Among acute CVDs, ischemic stroke is the second leading cause of death and the third

1062 leading cause of disability [184]. Ischemia is the sudden death of brain cells due to lack of
 1063 cell oxygenation [184]. This is usually related to a cardiovascular accident where blood
 1064 vessels are blocked or ruptured [184].

1065 Metabolomics is a powerful tool also for CVDs [185]. It is well-known that a high lipid
 1066 profile, excess of long-chain amino-acids and high glucose concentration in the blood
 1067 increase the risk of acute CVDs [13], [185]. Therefore, monitoring lipid profile, including
 1068 cholesterol, high-density lipoprotein (HDL) and low-density lipoprotein (LDL), is now
 1069 standard practice in the clinical environment to evaluate the risk of acute events [186].

1070 Lactate also has a clinical significance in acute cardiac patients and is clinically used for
 1071 patient stratification [187]. Authors in [187] suggest that patients with acute CVDs with an
 1072 admission lactate blood level lower than 2 mM usually have a better prognosis. Lactate has
 1073 been strongly related to acute inflammation and also gives account for any hypoxia condition
 1074 [188], [189]. The importance of lactate for critically ill patients is well-known, and today it
 1075 is the clinical practice to monitor lactate levels in intensive care units (ICU) [190].

1076 Besides lactate, serum creatinine is a diagnostically significant metabolic marker for acute
 1077 conditions [189]. Creatinine is also clinically used in ICUs for critically ill patients [154],
 1078 [191]. On top of these well-established metabolomic biomarkers for CVDs, several
 1079 additional metabolites have been linked to cardiovascular events and reported in Table 2.8.

1080

1081 *Table 2.8 A selection of metabolites and related cardiovascular disease.*

CVD	Sample	Metabolites
Risk	Serum	Betaine [192], branched-chain amino acids (BCAA) [185], cholesterol [193], choline [192], HDL [193], LDL [193], TMAO [185], [194], short-chain dicarboxylacetylcarnitine (SCDA) [185]
Heart failure	Serum	BCAA [185], acylcarnitines [185], fatty acids [185], glucose [185], ketones [185]
Myocardial infarction	Serum	Creatine [195], fatty acid [195], glucose [195], glutamate [195], glycerol [195], lactate [195], phenylalanine [195], phosphoethanolamine [195], pyrimidine [195], succinate [195], taurine [195], triglycerides [195], tyrosine [195]
Heart attack	Serum	Ceramide [192], cholesterol [192], choline metabolism [192], triacylglycerol [192]
Ischemic stroke	Serum	Acetic acid [196], alanine [189], aspartate [189], betaine [196], [197], carnitine [189], choline [192], [197], choline-related pathways [189], citric acid [189], [196], creatinine [189], cysteine [189], formate [189], free fatty acids [192], glutamate [189], glutamine [189], glycine [189], homocysteine [189], lactate [189], [196], phenylalanine [189], proline [189], pyruvate [189], pyruvic Acid [196], serine [189], threonine [189], tryptophan [189], [196], tyrosine [189], uric acid [189], valine [189], [196]

1082

1083

1084

1085 **2.4.4. Other metabolomics applications**

1086 There are many other healthcare applications where metabolomics could have a dramatic
1087 impact. It is beyond the scope of this work to review all the healthcare applications where
1088 metabolomics shows untapped potential. However, a few more uses are listed here to
1089 emphasise that metabolomics still has impressive unexploited potential.

1090 Metabolomics could be employed for Alzheimer's disease early diagnosis, currently
1091 affecting more than 5 million people in the US only [198]. A large number of serum
1092 metabolites, including choline [198], valine [198], carnitine [198], serine [198], have been
1093 linked to the disease. Serum metabolic profile could serve as an additional tool to increase
1094 the accuracy of diagnostic, to predict the disease progression [198].

1095 Metabolomics has also been linked to sepsis [199]. Globally, 31.5 million people develop
1096 sepsis each year, and this figure is expected to increase as the population ages [200]. Sepsis
1097 is both the most expensive condition to treat (US\$ 24 billion) and the leading cause of death
1098 in US hospitals, with a fatality rate ranging from 30% to 50%, depending on its severity
1099 [200]. Early diagnosis is crucial in sepsis, as where survival is reported to decrease by 7.6%
1100 with every hour of delay in the initiation of therapy [3]. There are many metabolites which
1101 have been linked to sepsis. Lactate, above all, is currently being used in clinical settings for
1102 sepsis diagnosis [199], [201]. Also, increased blood levels of 3-hydroxybutyrate [201],
1103 [202], acetate [201], acetoacetate [201], acylcarnitines [201], citrate [201], glucose [201],
1104 [202], isobutyrate [202], linoleic acid [201], lysophosphatidylcholine [201], malate [201],
1105 myoinositol [202], o-acetylcarnitine [202], phenylalanine [202], pyruvate [201], urea [202],
1106 and decreased blood levels of kynurenine [201], methanol [202], propylene glycol [201],
1107 ribitol [201], ribonic acid [201], valine [202] have been linked to sepsis.

1108 On top of all the mentioned applications, metabolomics has also been shown to be relevant
1109 for other widely spread diseases such as acute coronary syndrome, asthma, cardiovascular
1110 diseases, hepatitis, Parkinson's disease, rheumatoid arthritis, exotic diseases, acute renal
1111 injury [12]. In summary, at present metabolomics is very much research laboratory-based
1112 and needs to move out of academic laboratories and into the clinic [12], [15].

1113

1114

1115 **2.5. Microfluidics**

1116 A single miniaturised and automated diagnostic system made up of multiple integrated
 1117 biosensors, actuators, and electronic interfaces is called lab-on-chip [28], [203]. Lab-on-
 1118 chips incorporates numerous laboratory tasks onto a small device and has many advantages
 1119 than standard benchtop equipment. The main benefits of lab-on-chips are the speed of
 1120 analysis, ease of use, low reagent and sample consumption, high-throughput processing and
 1121 high reproducibility due to automation and standardisation [30]. Lab-on-chip devices
 1122 integrate all steps ‘from sample to answer’ and, for this reason, they are promising for
 1123 addressing environmental and medical challenges [31]. A lab-on-chip device is typically
 1124 more complex than a biosensor and it is composed of (i) multiple receptors, (ii) multiple
 1125 transducers, (iii) multiple readouts and a (iv) sample handling system [31]. The previous
 1126 sections have already discussed receptors, transducers, and readouts. Therefore, this section
 1127 is dedicated to the sample handling system.

1128 Microfluidics is the study of microstructures capable of handling small quantities of fluids.
 1129 Many microfluidic structures have been successfully used for a range of fluidic operation in
 1130 lab-on-chip platforms [204]. Microfluidic channels are microstructures which confine the
 1131 fluid and allow it to move in a controlled path. Microfluidic elements for controlling the flow
 1132 of the fluid in the microchannel have been developed, including pumps (active and passive)
 1133 and valves [205]. Microfluidic mixers are microstructures designed to favour the mixing of
 1134 two different fluids [205]. Microfluidic elements are usually combined to create microfluidic
 1135 networks. Currently, microfluidic networks can reach very high complexity level integrating
 1136 channels, valves, pump and mixers [206].

1137 In this work, capillary microchannels with rectangular cross-section were used. No
 1138 microfluidics pump or mixers were employed. Therefore, this paragraph will focus on
 1139 microfluidic theory for capillary and laminar flow regime. Additional resources for an
 1140 overview of microfluidic elements are here suggested [205], [207], [208].

1141 In microfluidic structures, the flow is primarily laminar, meaning that the behaviour of the
 1142 liquid can be decomposed into a series of infinitesimal layers flowing on top of each other
 1143 without mixing. The Reynolds number (Re) is typically used to define the flow regime in a
 1144 microfluidic structure. The Reynolds number is defined as the following:

$$\text{Re} = \frac{\text{Inertial Forces}}{\text{Viscous Forces}} = \frac{\rho ul}{\eta} = \frac{ul}{\nu} \quad (2.38)$$

1145 Where ρ is the fluid density (kgm^3), u is the velocity of the fluid in the structure (m/s), l is a
 1146 characteristic linear dimension of the structure (m/s), η is the dynamic viscosity of the fluid
 1147 ($\text{Pa}\cdot\text{s}$), and ν is the kinematic viscosity of the liquid (m^2/s) [209]. For a microstructure, $l \approx 10^{-6}$
 1148 so $\text{Re} < 1$. Turbulent flow is present when $\text{Re} > 4000$ while when $\text{Re} < 2000$ the flow is
 1149 laminar.

1150 The study of the fluid kinematics is usually carried out using the Navier-stokes equation. A
 1151 generic particle with mass m and velocity v is influenced by several independent forces (F_j):

$$m \frac{dv}{dt} = \sum_j F_j \rightarrow V^{-1} m \frac{dv}{dt} = V^{-1} \sum_j F_j \rightarrow \rho D_t v = \sum_j f_j \quad (2.39)$$

$$\sum_j f_j = \begin{cases} \rho \delta_t v_x & \text{1D Flow} \\ \rho \{ \delta_t v + (v \cdot \nabla) v \} & \text{3D Flow} \end{cases}$$

1152 Where V is the considered volume, f is the force density and D_t is the material time-
 1153 derivative defined as [208]:

$$D_t = \begin{cases} \delta_t, & \text{1D Flow} \\ \delta_t + (v \cdot \nabla), & \text{3D Flow} \end{cases} \quad (2.40)$$

1154 The final form of the Navier-Stokes equation can be calculated by inserting the complete
 1155 expression for the force densities:

$$\rho \delta_t v_x = -\delta_x p + \eta (\delta_y^2 + \delta_z^2) v_x + f_x \quad \text{1D Flow} \quad (2.41)$$

$$\rho \{ \delta_t v + (v \cdot \nabla) v \} = -\nabla p + \nabla^2 v + \{ \rho g + \rho_{el} E \} \quad \text{3D Flow} \quad (2.42)$$

1156 Where, in the second member, the first term is the pressure-gradient force density, the second
 1157 term is the viscous force density, and the third term is the body force density.

1158 One of the methods for resolving the Navier-Stokes equation is represented by the Hagen-
 1159 Poiseuille equation, valid in static conditions and in a rigid straight structure when a pressure
 1160 gradient Δp (Pa) is applied [208]:

$$\Delta p = R_h Q \quad (2.43)$$

1161 Where R_h is the hydraulic resistance ($\text{kg}/\text{m}^4\text{s}$), and Q is the flow rate (mole of fluid passing
 1162 through a section in a unit of time, m^3/s). There is a formal equivalence between the Hagen-
 1163 Poiseuille and the 2nd Ohm's law. The hydraulic resistance depends both on the geometry of
 1164 the structure both on the viscosity of the fluid. Specifically, for rectangular channels with
 1165 height h , length L and depth w the R_h is:

$$R_h = \frac{12\eta L}{\left\{ 1 - 0.63 \left(\frac{h}{w} \right) \right\} h^3 w} \quad (2.44)$$

1166 R_h is generally high for microfluidic structures due to height h and the width w having
1167 micrometric dimensions [208].

1168 In the absence of externally applied pressure and with channel height and width in the order
1169 of hundreds of micrometres, the liquid can spontaneously move due to cohesive forces
1170 within the liquid and adhesive forces between the liquid and its surroundings. This effect is
1171 commonly referred to as capillary action [210]. With reference to Figure 2.15, the capillary
1172 pressure gradient (Δp) is related to the property of the fluid and the geometry of the
1173 microchannel [208]:

$$\Delta p = \gamma \left(\frac{\cos\theta_b + \cos\theta_t}{h} + \frac{2\cos\theta_s}{w} \right) \quad (2.45)$$

1174 Where Θ denotes the contact angle of the different materials employed and γ the surface
1175 tension. According to equation (2.45), when $w \ll h$, the capillary pressure gradient depends
1176 only on w and the microchannel can even be left open [211], [212].

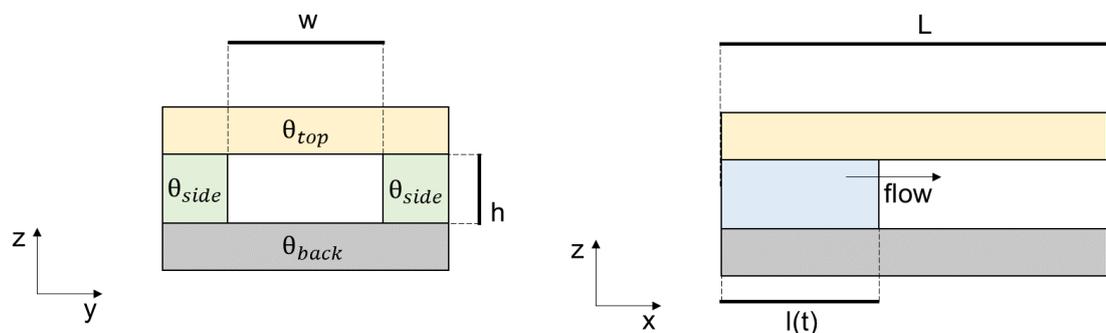
1177 Under the assumption of laminar, steady-state flow, and in the absence of gravitational
1178 effects, the position of the advancing liquid $l(t)$ can be obtained by manipulating Equation
1179 (2.44) and Equation (2.45) [208], [213]:

$$l(t) = h \sqrt{\frac{\Delta p}{6\eta L} \left(1 - 0.63 \frac{h}{w} \right) t} \quad (2.46)$$

1180 Where Δp is the capillary pressure gradient, R_h is the hydraulic resistance, Q is the flow rate,
1181 η is the dynamic viscosity, L is the microchannel length. Equation (2.46) can be used as a
1182 designing equation when developing capillaries.

1183 Many different methods have been used to fabricate microfluidic structures and integrate
1184 them with integrated circuits. A review of microfluidic fabrication and integration is reported
1185 in Chapter 4.

1186



1187
1188

Figure 2.15 Schematic representation of a passive rectangular microfluidic channel.

1189 **2.6. Point-of-care Systems**

1190 By potentially being useful for all the major causes of death [12], [13], metabolomics social
1191 impact would be impressive if it was untapped for masses through POC platforms [10]. The
1192 main advantages and challenges of POC systems have already been examined in Chapter 1.
1193 Particularly, the potential of such technologies for saving lives, time and money have been
1194 already discussed. The main technological and practical challenges slowing down the
1195 widespread of these technologies have also been analysed. In this section, a more in-depth
1196 literature review is proposed for both experimental and commercial POC devices.

1197

1198 **2.6.1. Review of POC platforms**

1199 Authors in [1] illustrate the key design components of a POC device which include user
1200 interface, sample delivery device, reagent storage strategy, reaction cell, sensors to detect
1201 the measurement reaction, control and communication system, data management storage.

1202 POC testing has been employed to a variety of samples, including tissue, urine and blood
1203 [39]. Among them, blood testing is particularly interesting because the concentration of
1204 specific biomarkers in the blood is directly related to the physiological state of the body.
1205 Therefore, testing blood is often used for preventions, identification and monitoring for a
1206 variety of diseases [39]. Blood, especially in a small volume, is also particularly easy to
1207 obtain for the majority of conditions [39].

1208 POC can be qualitative or quantitative [1]. Qualitative POC platforms usually do not provide
1209 a numerical result [199]. Typically, the output of this platform is only a binary result (i.e.
1210 positive or negative). Lateral flow assays (LFAs), introduced in 1988, are the most popular
1211 qualitative POC platforms [2]. LFAs are cellulose-based devices consisting of a strip, a
1212 sample pad, a reagent pad, and a test line. The sample is introduced at the sample pad. It
1213 migrates to the reagent pad via capillary forces, where bioreagents conjugated to the target
1214 analyte are immobilised. The formed antigen/antibody product continues to flow along the
1215 strip where is subsequently captured by a final biorecognition molecule. The result
1216 interpretation is usually a visual-coloured indicator.

1217 There are many advantages of LFAs. The inherent properties of the paper support capillary
1218 flowing; thus, no pumping or complicated fluidics is required [1]. Also, LFAs only requires
1219 a small sample volume, no sample pre-processing and the waste can be conveniently
1220 incinerated [1]. Besides, the device is usually low-cost and can accommodate easy

1221 functionalisation techniques. On the other hand, LFAs are challenging to use for multiple
1222 testing and have low sensitivity [1].

1223 Quantitative POC devices aim to provide a numerical measurement of the level of the target
1224 analyte. LFAs can be extended from qualitative to quantitative by the use of a coupled
1225 reading instrumentation [1]. However, quantitative POC platforms require sensors [1]. Then,
1226 it should not be surprising that CMOS technologies and lab-on-chip platforms are vastly
1227 used for the development of quantitative POC systems [1].

1228 POC platforms, very often supported by IC, have been used for a variety of healthcare
1229 applications including genomics, proteomics, and metabolomics. Other applications not
1230 discussed in this review also include biophysical analysis, cell separation and sorting,
1231 material and drug delivery, drug testing, and organs-on-chip [214]. Table 2.9 summarises
1232 the review on POC platforms proposed in this paragraph.

1233 **Genomics POC platforms.** POC testing in genomics and transcriptomic targets DNA and
1234 RNA [2]. Numerous methods have been proposed for detecting and amplifying the presence
1235 of nucleic acids [2]. The most commonly used process is the polymerase chain reaction
1236 which creates billions of copies of a DNA sequence by iterative replications [215]. POC
1237 testing in genomics and transcriptomic is particularly essential for detecting and identifying
1238 virus, bacteria, fungi, microbes, pathogens [2], necrotic and aberrant cells [1]. A significant
1239 challenge remains in integrating blood pre-treatment with DNA and RNA detection in a low-
1240 cost, robust and user-friendly platform [1].

1241 **Proteomics POC platforms.** POC testing in proteomics targets proteins, including
1242 enzymes, antibodies, and hormones [2]. Modern POC devices utilise immunoassay
1243 technology, which includes antigen-antibody binding [2]. These assays target protein
1244 biomarkers such as PSA for PCa, troponin I for CVDs, and bacterial and viral infection-
1245 related markers such as HIV, influenza, chlamydia, and hepatitis [2]. Most methods for
1246 protein analysis are based on the enzyme-linked immunosorbent assay (ELISA) method [1].
1247 In traditional ELISA tests, colorimetric, fluorescent readout signals are used to visualise the
1248 interaction of the target protein to the specific recognition molecule [1]. ELISA analysis
1249 usually requires several washing steps which creates additional complication when
1250 designing a POC device [1]. ELISA can be implemented on both LFA-based POC and
1251 quantitative platforms [1]. LFA-based ELISA test has been demonstrated to be convenient
1252 to develop [1]. However, work is now under development for creating multiplexed protein
1253 assays on qualitative platforms [1], [216]. Authors in [216], for instance, propose a CMOS-

1254 based device able to differentiate between serum samples containing either, neither, or both
1255 rabbit anti-mouse (RAM) antibodies and/or anti-HIV antibodies using a gold-nanoparticle
1256 promoted silver enhancement immunoassay. The authors claim that the proposed platform
1257 is the first step in creating a mass-manufacturable POC tool capable of multi-proteins
1258 quantification [216]. Several platforms have been developed for PSA detection [217].
1259 Electrochemical [218], optical [219], [220], cantilever-based [221] and other suitable
1260 sensors [221] have also been successfully employed for PSA quantification, recently leading
1261 to the first FDA approved POC PSA test [181]. Despite the need for new tools and standards
1262 for PCa, the development of POC remains confined to PSA detection because PSA-based
1263 functionalisation techniques are very stable and convenient.

1264 **Metabolomics POC platforms.** POC platforms for metabolic biomarkers have also been
1265 developed. The development of POC platforms for metabolomics is mainly driven to the
1266 cost and bulkiness of the equipment typically used for metabolites quantification. This also
1267 led to the development of commercial colorimetric and fluorescence assay kit to be used in
1268 combination with a spectrophotometer [222]. The current panel of metabolites most often
1269 targeted is wide and include glucose, amino acids, choline, sarcosine, lactate, creatinine,
1270 cholesterol and triglycerides, [2]. Besides glucose meters, today well-established, the interest
1271 of the research community is moving towards different metabolites.

1272 Biosensors for the quantification of amino acids profile, with particular reference to L-types,
1273 which are more relevant for humans, have been documented in the literature [223]. The
1274 bioreagents typically include L-amino acids oxidase (LAAOx), which can oxidase any type
1275 of LAA while producing hydrogen peroxide [49]. Both electrochemical and optical methods
1276 have been used for the quantification of LAA with a similar performance [223]. Among the
1277 targeted amino acids, glutamate is one of the most popular, especially for its link to
1278 neurodegenerative diseases [224]. Glutamate biosensors typically employ glutamate oxidase
1279 (GLOx) [49]. The interest in the quantification of choline is related to its involvement in
1280 several diseases [225]. Choline biosensors typically employed the specific enzyme choline
1281 oxidase (ChOx), which oxidases choline while producing hydrogen peroxide. The produced
1282 hydrogen peroxide has been used to develop both electrochemical and optical biosensors
1283 [225]. Similarly, sarcosine oxidase (SaOx) and lactate oxidase (LaOx) have been developed
1284 [2]. Authors in [226], for instance, employ SaOx for the colorimetric determination of
1285 sarcosine in the urine. Authors here demonstrate that the developed assay is capable of
1286 differentiating people with PCa from the healthy group [226]. However, the authors employ

1287 a benchtop spectrophotometer to run the experiment, thus no integrated platform has been
1288 achieved here [226]. Both electrochemical and optical methods have been used for lactate
1289 sensing [2][227]. Creatinine level is being currently tested for renal deficiencies [2]. The
1290 chemistry involved in creatinine biosensing is slightly more complicated since it involves
1291 creatininase (CNN) and creatinase (CTN) to convert creatinine in sarcosine. Sarcosine is
1292 then measured by employing SaOx [228]. POC platform monitoring lactate, cholesterol,
1293 triglycerides, and other lipids are getting progressively popular for the management of CVDs
1294 [2].

1295 Authors in [229] demonstrate the use of a CMOS sensor and an LED to provide comparable
1296 results to a commercial spectrophotometer for the colorimetric determination of bacterial
1297 concentrations. This work shares a similarity with the work presented in this thesis regarding
1298 the setup utilised and the colorimetric approach. However, the work in [229] uses a
1299 commercial CMOS sensor and no microfluidic integration was achieved. Similarly, authors
1300 in [230] employ a CMOS sensor to quantify H_2O_2 using a colorimetric approach. However,
1301 also in this case, there is not monolithically integration and the samples are retained into
1302 reaction cuvettes.

1303 **Multi-analyte metabolomics POC platforms.** Lab-on-chip devices are also being
1304 developed for quantifying multiple compounds [231]. Authors in [232], for instance, present
1305 a microfluidic lab-on-chip quantifying human body metabolites, using sub microliter
1306 droplets as reaction chambers. Authors demonstrate the suitability of the platform for
1307 glucose, glutamate, and pyruvate individually [232]. The lab-on-chip takes advantage of an
1308 electrowetting chip which transport and mix the sample and the reaction for the initiation of
1309 a colorimetric reaction [232]. The reaction takes place in microchannel fabricated by Teflon,
1310 perylene and glass. Chemistry and working principle developed in this work are very similar
1311 to the one adopted in this research project. However, the platform is not integrated and a
1312 single external photodiode is used to monitor the absorbance during the reaction [232]. The
1313 developed lab-on-chip also does not allow parallel assays [232]. PDMS microfluidic
1314 channels have been employed on the CMOS-based spectrophotometer system reported in
1315 [233]. The system was used for the determination of glucose, uric acid, and cholesterol.
1316 However, PDMS microfluidics is developed onto a glass substrate. The integration of
1317 microfluidics with the sensor array was not achieved in this work [233]. A more complex
1318 PMMA-based system has been developed by authors in [234] for the quantification of sorbic
1319 acid. Also in this case, microfluidic chip and sensors are two physically separated units.

1320

Table 2.9 State of the art of IC-based POC platforms.

Analytes (examples)	Common techniques	References
DNA and RNA (e.g. from virus, bacteria, fungi, aberrant cells)	Polymerase chain reaction. Detection methods: electrochemical.	[1], [2], [215]
Proteins (e.g. enzymes, antibodies, antigens, hormones, etc.)	Enzyme-linked immunosorbent assay (ELISA). Detection methods: optical and electrochemical.	[1], [181], [216]–[221]
Metabolites (e.g. LAA, glutamate, choline, sarcosine, lactate, creatinine, etc).	Enzyme-based assay. Detection methods: optical and electrochemical.	[49], [223], [232], [233], [224]–[231]
Other biomarkers (e.g. cells)	Various	[1], [2]

1321

1322 **2.6.2. Market Review**

1323 Sensing devices currently on the market for biomedical applications can be mainly divided
1324 into in-home or in-laboratory based diagnostics. While the market for in-home care
1325 monitoring has proliferated, the rate of acceptance of the new biosensors for the hospital or
1326 laboratory-based diagnostics has been comparatively lower [16].

1327 In-home POC devices are designed to be used by the generic public. This category of devices
1328 usually requires no or minimal sample pre-treatment, are cheaper, more robust and have a
1329 higher degree of portability. In-home POC can also take advantage of personal mobile
1330 devices such as smartphone or tablet for processing or data storage [235]. LFAs are the most
1331 commercially available tools for POC in-home testing [199]. Modern portable pregnancy
1332 tests are probably the widest spread example of LFA [2]. Semi-quantitative PSA lateral flow
1333 strips are also available on the market to help to diagnose PCa [221], [236]. However,
1334 glucose biosensors seem to have forged the most significant market share for in-home POC
1335 platforms [16]. Glucose biosensors account for approximately 85% of the entire biosensors
1336 market [2]. Most diabetics now regulate their condition at home by self-testing their blood
1337 with hand-held glucose meters [2]. Typically, two types of glucose sensors are commercially
1338 available in the market, namely electrochemical and optical. For effective management and
1339 to record patient history, most modern glucometers now have memory storage and computer
1340 interfaces so that the patients can keep track of their blood glucose levels over a period of
1341 time, and the data can then be shared with clinicians to prescribe a better course of medical
1342 treatment.

1343 Whatever the working principle, glucose market is so vast that standardisation agencies
1344 published a set of guidelines for their development. The most commonly cited guideline for

1345 glucose meter is from the International Organisation for Standards stating that the relative
1346 error of the measurement for glucose concentrations < 4.2 mM should be lower than 15%
1347 (95% confidence interval). The same quantity should be lower than 20% for glucose
1348 concentrations > 4.2 mM [1]. The Clinical and Laboratory Standard Institute indicates a
1349 requirement for meter results to be within 12.5% of laboratory results [1]. The Food and
1350 Drug Administration (FDA) has stipulated a maximum discrepancy of 10% between meter
1351 results and laboratory analysis [1]. Worryingly, independent studies indicated that not all the
1352 meters on the market are complainant with these recommendations [237].

1353 Cholesterol monitoring devices are also finding new demand world-wide, and this biosensor
1354 segment is expected to grow at a rate of around 8% over the next five years [16]. There is
1355 also an increasing instance of disorders due to obesity and hormonal imbalance, creating an
1356 escalation of cholesterol levels in the blood.

1357 In-laboratory based diagnostics are designed to be used by trained personnel. This category
1358 of devices can require sample pre-processing and can be more expensive and less portable
1359 than the previous class. In-laboratory based diagnostics usually aim to reduce the time
1360 patients spend in the emergency department and accelerate the clinical decision. They are
1361 also used for bedside testing or patients with reduced mobility. Acute conditions, such as
1362 stroke and sepsis, also gain advantages from the quick test provided by POC testing. A
1363 remarkable example of the category is the i-STAT by Abbott. The i-STAT is a 'handheld
1364 blood analyser for with-patient testing aimed at improving the quality, cost, and operational
1365 efficiency of health' [238]. The device is very versatile and allows to diagnose acute
1366 conditions in minutes. The i-STAT cartridges are available for a range of clinical tests,
1367 including cardiac markers, lactate, coagulation, blood gases, chemistries and electrolytes,
1368 and haematology [238].

1369 The most successful commercial POC device capable of DNA sequencing is probably the
1370 CMOS-based Ion Torrent platform by Thermo Fischer Scientific [239]. The platform uses
1371 an ISFET sensor array together with the polymerase chain reaction technique [239]. First,
1372 the genome sequence is divided into millions of fragments, which are attached to beads
1373 allocated in microwells. Microwells are iteratively washed with solutions containing one of
1374 the four bases (adenine, cytosine, guanine, and thymine). When a test base attaches to its
1375 complementary base, hydrogen ions are released and sensed by the pH sensor. By iterating
1376 the washing step and by repeating the test over millions of pH sensors, it is possible to
1377 reconstruct the sequence of the molecule under analysis.

1378 Figure 2.16 shows devices based on different technologies for biomedical applications,
 1379 including optical, pH, amperometric, electrochemical nano-mechanical and thermal
 1380 sensors [16]. Table 2.10 provides some examples of the currently available biosensors for
 1381 the detection, diagnosis and monitoring of biomedically relevant analytes [16].

1382

1383 2.6.3. Discussion on platform affordability

1384 Basing on the market review illustrated above, it is now possible to define the requirement
 1385 about the cost of the platform. With reference to Table 2.10, glucose meters have a very low
 1386 cost because they are used very frequently (more than once a day) by people affected by
 1387 diabetes. However, the platform developed in this work target applications where the
 1388 frequency of use is expected to be lower. Other platforms on the market have increased costs
 1389 for both the reader and the test. The cost of the reader for these platforms ranges from £ 250
 1390 to £ 5200, while the cost per test is in the range of £1.5 - £10. For both the target applications
 1391 of this work, we can assume a frequency of usage of once every three months (per patient).
 1392 This is similar to other multi-analyte platforms in the market, such as Accutrend Plus (Cobas-
 1393 Roche) and CardioChek PA (PTS diagnostics) – see Table 2.10.

1394

1395 *Table 2.10 Examples of commercial POC platforms. Devices information have been*
 1396 *retrieved from the respective websites of the platforms. Reproduced and modified from [16].*

Device	Analyte/test	Sensor type	Assay time	Cost per test /reader
i-stat (<i>Abbott</i>)	Multiple: (Troponin I, O ₂ , Glucose, lactate, pH, Hematocritmany)	Electrochemical	2-5 min	T: £ 10 R: £ 5200
MiniOn (<i>Nanopore technology</i>)	DNA sequencing	Nano-pore	-	T: n.d. R: £1000
CoagMax (<i>Microvisk</i>)	Blood viscosity	Micro-cantilever	-	n.d.
Contour (<i>Bayer</i>)	Glucose	Electrochemical (GDH)	< 30 s	T: < £ 0.5 R: £ 30
Optimum (<i>Abbott</i>)	Glucose	Electrochemical (GDH/NAD)	< 30 s	T: < £ 0.5 R: £ 30
Accu-check Performa (<i>Roche</i>)	Glucose	Electrochemical (GDH/PQQ)	< 30 s	T: < £ 0.5 R: £ 30
Accutrend Plus (<i>Cobas-Roche</i>)	Tot. Cholesterol Triglycerides Glucose, Lactate	Optical (absorbance)	30 s	T: < £ 1.5 R: £ 250
CardioChek PA (<i>PTS diagnostics</i>)	Total cholesterol, HDL, triglycerides, glucose, LDL, Ketones, Creatinine	Optical (absorbance)	2 min	T: £ 7.50 R: £ 700
Cholestech LDX (<i>Alere</i>)	Cholesterol, HDL, glucose, triglycerides, LDL, ALT , AST and hs-CRP	Optical (absorbance)	5 min	T: £ 8.50 R: £ 950
DCA Vantage (<i>Siemens Healthineers</i>)	HbA, HbF, HbS, HbC, HbE in urine	Immunological	-	T: £ 9.11 R: £ 4000
In2it (<i>Provalis</i>)	HbS and HbD	Boronate affinity	-	T: £ 6 R: £ 1500
Q-POC (<i>Quantum DX</i>)	HPV or Tuberculosis or STI	Functionalised Nanowire FET	20 min	T: \$ 10 R: \$ 1000



1397

1398 *Figure 2.16 Reproduced and modified from [16]. (a) i-STAT (Abbott), (b) In2it (Provalis),*
 1399 *(c) coagmax (Microvisk), (d) Q-POC (Quantum Dx), (e) Cholestech (Alere), (f) Optium*
 1400 *(Abbott), (g) Genome sequencer (Ion torrent), (h) DCA Vantage (Siemens), (i) Contour*
 1401 *(Bayer), (j) MiniOn (Nanopore technology), (k) CardioChek PA (PTS diagnostics), (l)*
 1402 *Prototype from DNA electronics, (m) Accutrend Plus (Cobas-Roche).*

1403

1404 Therefore, similar costs requirement can also be set. Specifically, maximum target costs for
 1405 the reader and cartridge were assumed to be £5200 and £10, respectively.

1406 The cost of the reader can be easily met by using off-the-shelf electrical components.
 1407 However, the maximum target price of the cartridge is a challenging requirement. This is
 1408 because the disposable cartridge integrates CMOS sensors, biological reagents, and
 1409 microfluidic systems. The requirement can potentially be met when cartridges are mass-
 1410 produced but, in this project, cartridges were not mass-produced. However, the methods and
 1411 procedures developed in this project must be suitable for mass-production.

1412 The cost of the cartridge could be reduced by integrating reusable sensors in the reader rather
 1413 than in the cartridge. However, with reference to the versatility requirement, a reduction of
 1414 the functionalities of the platform is not advised at this stage. It is also worth outlining that
 1415 the platform can be used for many applications, meaning that only one reader can be used
 1416 for several applications. This can produce additional cost savings.

1417 Thus, the cartridge was developed with integrated CMOS sensors. Optimisation strategies
 1418 aiming to reduce the cost for specific applications can be investigated as part of future works.

1419 **2.7. Summary of the Chapter**

1420 In conclusion, the quantitative requirements of the POC platform have been discussed and
 1421 set in this chapter. Strategies required to meet the requirements have also been identified.

1422 Table 2.11 summarises the discussion.

1423

1424 *Table 2.11 Summary of the quantitative requirements of the platform. The strategies*
 1425 *identified to address the requirements are also summarised.*

Requirement	Criterion	Strategy
Affordability	- Reader cost < £5200 ¹ . - Test cost < £10 ¹ .	- Use well-established techniques for sensors and readout. - Use processes suitable for mass-scale production (e.g. CMOS, moulding, enzyme printing). - Use colorimetry
Sensitivity	- Ischemic stroke: results comparable to NHS standard. - PCa: specificity ≥ 0.32 [18] ² . - Relative error of the measurement in the order of 15-20% ³ .	- Use well-established detection methods. - Optimise the platform to achieve the requirement. - Evaluate the platform with clinical samples.
Specificity	Develop a biomarker panel specific to PCa and ischemic stroke	- Identify and use multiple biomarkers. - Discuss biomarkers with experts. - Test the biomarker with clinically sourced samples.
User-friendly	- Use blood/plasma/serum ^{1,2} . - Minimal sample pre-processing ^{1,2} . - Low sample volume (tens of μL) ^{1,2} . - Plug and play device ¹ .	- Integrate sensors, fluidics and biological reagents. - Use blood/serum/plasma. - Develop the platform to be used with a small volume. - Develop an intuitive user interface. - Minimise user operations.
Rapid	- Complete test in minutes ¹ .	- Estimate substrate from initial reaction rate.
Robust	- Compensation of sample-to-sample and device-to-device variations. - Capable of detecting failure ¹ .	- Develop a solution to standardise the measurement (controls). - Develop strategies for the safe failure of the platform (e.g. invalidate result).
Equipment-free	- No other external equipment required for running the test.	- Embed all the required equipment into the platform.
Delivered	- Reagents must have shelf-life in the order of weeks/months ¹ .	- Develop established strategies for reagent stabilisation and storage (lyophilisation).
Multi-analyte capability	- Measure 2 or more metabolites at the same time ^{1,2} .	- Use multiple sensors (array). - Develop a sample handling system (microfluidics).
Versatility	- Demonstrate multiple biomarker detection. - Potential use of other sensors.	- Use custom CMOS chip. - Integrate fluidics monolithically. - Beware of other possible use of the platform (e.g. use ISFET). - Demonstrate platform usage with multiple biomarkers.
¹ Assumed from market review. ² Assumed from the literature review. ³ Assumed from glucose meters guidelines.		

1426 Chapter 3: Embedded Platform Development

1427 3.1. Introduction

1428 The present chapter describes the development of the proposed embedded platform.
1429 Requirements, simulations, fabrication, and design consideration are also discussed. Table
1430 3.1 illustrates the contribution to each activity discussed in this chapter.

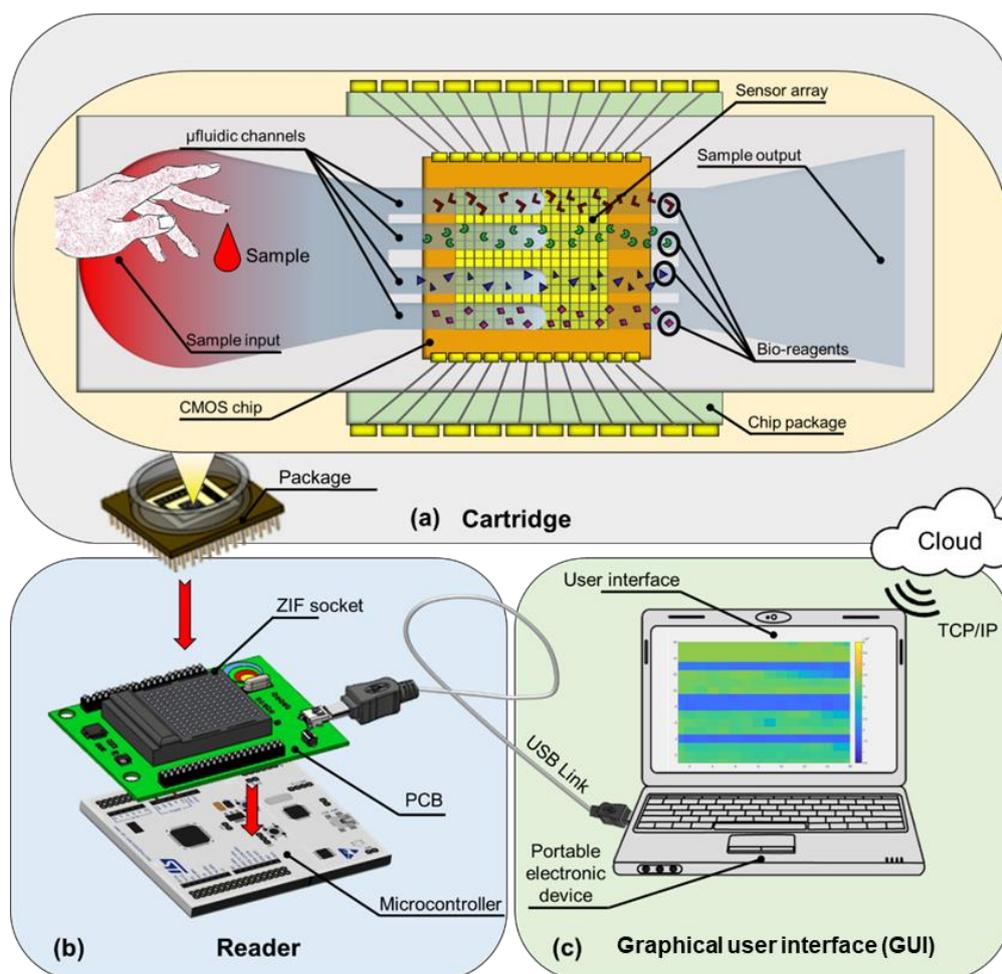
1431 The platform is composed of a cartridge, a reader, and a graphical user interface (GUI) – see
1432 Figure 3.1. The cartridge is the core of the platform. It is meant to be disposable when mass-
1433 produced, but it has been reused in this project due to limited resources. It integrates the
1434 CMOS chip, passive microfluidics, and on-chip reagents onto a ceramic package. In this
1435 chapter, the sensing platform is illustrated. Microfluidics and bioreceptors integration is
1436 illustrated in the next chapter. The cartridge is designed for the colorimetric detection of
1437 multiple metabolites. This raises the question of whether the cartridge requires a single
1438 sensor or more sensors organised into an array format.

1439 Typically, a biosensor with one transducer provides a single result. An apparatus containing
1440 multiple sensors can deliver multiple or single results. Image sensors, for example, provide
1441 multiple readings. Multiple readings can be combined for providing a lower number of
1442 readings.

1443

1444 *Table 3.1 Table of contributions for the activity presented in this chapter.*

Task / Activity presented in Chapter 3	Main investigators
Identification of a potential metabolic biomarker panel for prostate cancer	- Valerio F. Annese (literature survey) - Prof. Rob Jones ² (discussion/validation)
Identification of a potential metabolic biomarker panel for ischemic stroke	- Valerio F. Annese (literature survey) - Dr Samadhan Patil ¹ (discussion/validation)
Design of the CMOS chip	- Dr Mohammed Al-Rahawani ¹ - Dr Christos Giankulovitch ¹ - Dr James Beeley ¹
Fabrication of the CMOS chip	- Outsourced (Austriamicrosystems)
Development of the reader (hardware)	- Dr Mohammed Al-Rahawani ¹ - Dr Christos Giankulovitch ¹ - Dr Claudio Accarino ¹
Development of the reader (software)	- Valerio F. Annese
Development of the graphic user interface for both acquisition and data analysis	- Valerio F. Annese
Enzymatic reactions modelling and simulations	- Valerio F. Annese
Platform testing	- Valerio F. Annese
Affiliation at the time of completion of the activity: ¹ Microsystem Technology Group, James Watt School of Engineering, University of Glasgow. ² Institute of Cancer Sciences, University of Glasgow, Beatson West of Scotland Cancer Centre, Glasgow.	



1445

1446 *Figure 3.1 The overall architecture and components of the developed platform: (a) the*
 1447 *cartridge, (b) the reader, and (c) the GUI. This is a high-level diagram and it is not in scale.*

1448

1449 When combined altogether, data coming from multiple sensors can be used to provide a
 1450 single output. Microstructures, such as microfluidic channels, can provide physical
 1451 separations allowing to confine target reactions in different zones of a sensing area. For
 1452 example, authors in [240] use a microfluidics-based device for simultaneous testing of a
 1453 plurality of separate nucleic acids in a barcode-like layout. Also, authors in [241] disclose
 1454 an apparatus capable of performing test and controls at the same time from the same sample.
 1455 The developed platform uses an array of optical detectors. Similarly to [240] and [241], this
 1456 platform aims to perform multiple simultaneous measurements. Thus, the use of an array of
 1457 optical detectors is the most suitable configuration for this platform. The use of multiple
 1458 independent sensors has also the potential to reduce the fixed-pattern-noise of the array and
 1459 improve the overall SNR of the measurement [242].

1460 The optical detectors used in this work were custom developed. Arguably, the use of a
1461 commercial camera chip for this project would have also been possible. However, it is worth
1462 stressing once again that this work is part of a larger vision aiming to develop a multimodal
1463 platform. As such, the use of a commercial camera chip would have reduced the
1464 functionalities of the platform to optical detectors only and would have not satisfied the
1465 versatility requirement. The use of a custom sensing platform enabled the integration of other
1466 sensors (i.e. ISFET) to be used in conjunction with optical sensors. The use of
1467 electrochemical and optical sensors at the same time on this platform has been demonstrated
1468 by other members of my research group [243]. This would not have been possible with a
1469 commercial camera chip.

1470 The cartridge connects to the reader through a zero-insertion force (ZIF) socket. The reader
1471 is composed of a custom printed circuit board (PCB) and a commercial microcontroller
1472 board. It is employed for sensors addressing and data digitisation. It also handles raw data
1473 and sends them in real-time to the GUI through USB link.

1474 The GUI is a software running on a portable electronic device. It allows user interaction as
1475 well as data visualisation, analysis, and storage. The platform can also take advantage of the
1476 TCP/IP capability of the portable electronic device for uploading the result of the test onto a
1477 cloud-based storage platform.

1478

1479 **3.2. The Cartridge**

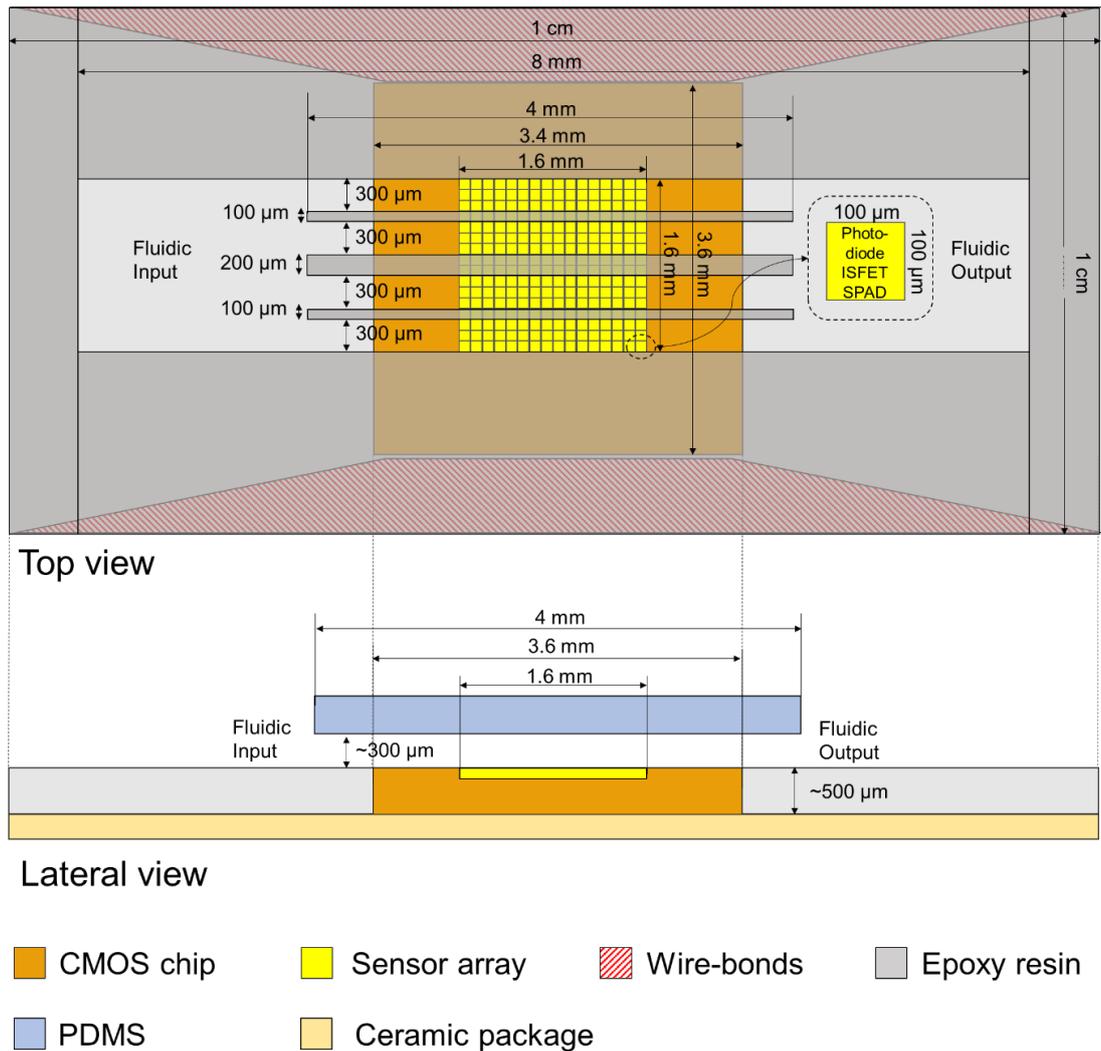
1480 The cartridge integrates the CMOS chip, one or more biorecognition elements and the
1481 passive microfluidics (illustrated in the next chapter). All the parts are integrated onto a
1482 ceramic chip package. Figure 3.2 shows a diagram of the cartridge with four microfluidic
1483 channels.

1484

1485 **3.2.1. Target applications**

1486 The platform is meant to be versatile and capable of adapting to a wide range of biological
1487 assays with no or minimal modifications. However, two case studies have been selected to
1488 demonstrate the diagnostic capability of the platform.

1489 The first proposed application of the platform is PCa diagnosis. This application aims to
1490 demonstrate the potential of POC platforms for early diagnosis of deadly diseases, especially
1491 for use where the current standard lacks reliability.



1492

1493

1494 *Figure 3.2 Top view (top) and later view (bottom) of the cartridge. Biological reagents have*
 1495 *been omitted in the schematic for clarity. The diagram is in scale. Further microfluidic*
 1496 *structures have been analysed and developed in this project.*

1496

1497 As introduced in Chapter 2, the current standard alone, PSA blood testing, is not reliable
 1498 enough, and invasive methods are usually used in conjunction with the blood test. In this
 1499 frame, the proposed platform is suggested for the quantification of metabolic biomarkers to
 1500 be used in conjunction with the PSA testing for non-invasive improved diagnosis. Four
 1501 analytes have been selected for this application, namely total LAA, glutamate, choline, and
 1502 sarcosine. The selection of the metabolites panel is based on the literature review presented
 1503 in Chapter 2. Subsequently, the metabolites review has been discussed with a team of cancer
 1504 researchers, led by Prof. Robert Jones, professor of clinical cancer research at the University
 1505 of Glasgow. The team of cancer researchers have recognised that there is merit in the selected
 1506 metabolites panel, although metabolomics is still a relatively unexplored field in PCa. The

1507 relation between LAA, glutamate, choline, and sarcosine and PCa are well-known to the
 1508 research community. The correlation between sarcosine and the disease is still controversial,
 1509 and this study can shed light on the contentious matter. The development of such a platform
 1510 has the potential to provide additional information which, together with PSA testing, can
 1511 improve the early diagnosis of PCa.

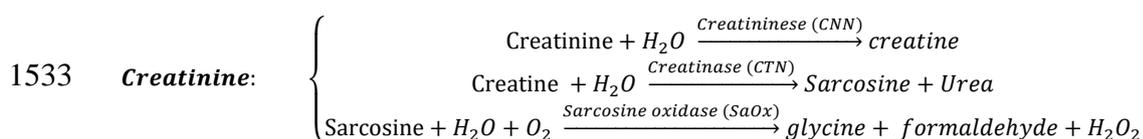
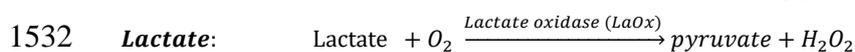
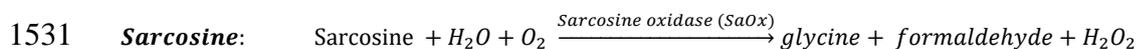
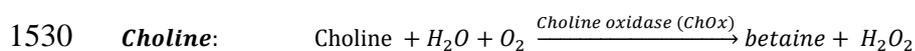
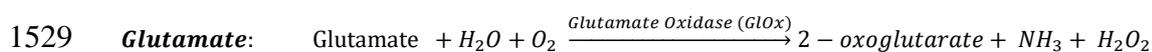
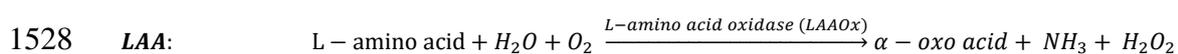
1512 The second proposed application of the platform is the diagnosis of ischemic stroke. With
 1513 this application, the aim is to highlight the potential of POC platforms for acute medicine,
 1514 where timing is vital. Two metabolites have been selected for this application, namely
 1515 creatinine and lactate. The selection of the metabolites is based on a similar procedure
 1516 involving literature review and discussions with experts in the field including Dr Samadhan
 1517 Patil, lecturer of medical engineering at the University of York, and Prof Jesse Dawson,
 1518 professor of stroke medicine at the Institute of Cardiovascular & Medical Sciences,
 1519 University of Glasgow.

1520 In summary, six tests have been selected for this research project, LAA, glutamate, choline,
 1521 sarcosine, lactate, and creatinine. It should be clarified that the total profile of LAA is not a
 1522 single metabolite but, throughout this work, it will be referred to as a metabolite.

1523

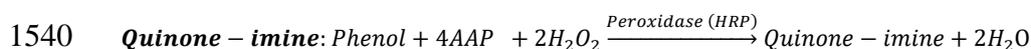
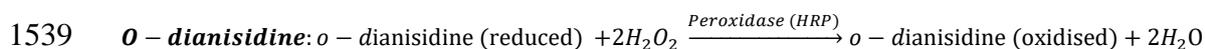
1524 3.2.2. Detection strategy for the target metabolites

1525 All the selected metabolites were detected with a colorimetric approach using specific
 1526 enzymes interacting with the target analytes for producing hydrogen peroxide. The adopted
 1527 enzymatic reactions are reported in the following [49]:



1534 The produced H_2O_2 is proportional to the concentration of the analyte of interest. The
 1535 production of H_2O_2 was monitored by a colorimetric probe which changes its absorbance
 1536 property depending on the H_2O_2 level. Two different probes were employed, namely

1537 *o*-dianisidine and the system phenol/4-aminoantipyrine (4AAP). The target reaction for
 1538 H_2O_2 are reported below:



1541 Thus, for each selected test, at least two enzymatic reactions are required. However, the ratio
 1542 of the concentration of the enzymes within the same reaction chain can be tuned. In this
 1543 work, an increased level of HRP was adopted. According to the Michaelis-Menten model,
 1544 this ensures that when H_2O_2 is produced, it is promptly used for the oxidation of the probe.
 1545 Consequently, the reaction rate of the entire reaction chain can be approximated to the slower
 1546 reaction, i.e. the one leading to the production of hydrogen peroxide. There are two main
 1547 parameters to be considered in the selection of the hydrogen peroxide probe, namely the
 1548 extinction coefficient and the wavelength absorbance range. Commercially sourced *o*-
 1549 dianisidine and quinone imine have extinction coefficients of $7.5 \text{ mM}^{-1}\text{cm}^{-1}$ and
 1550 $12 \text{ mM}^{-1}\text{cm}^{-1}$ at 500 nm, respectively [222]. The effective extinction coefficient for this
 1551 platform has been measured and reported in Figure 4.13. Table 3.2 summarises the selected
 1552 panel of metabolites together with their physiological range, the enzymes employable for
 1553 their colorimetric determination, and related kinetics constants.

1554

1555 3.2.3. Simulations of colorimetric reactions

1556 **Method.** A Matlab-based model for the simulation of a generic colorimetric assay was
 1557 developed and used for preliminary assessment of the platform requirements. The
 1558 simulations aimed to identify critical parameters in the development of the platform.

1559 The implemented simulation employed the Michaelis-Menten model and rate-equations to
 1560 simulate the enzymatic-reaction.

1561

1562 *Table 3.2 Summary of the target metabolites to be measured by colorimetric method.*

Analyte	Physiological range (μM)	Application	Enzyme	Km (mM) [49]
LAA profile	1700 - 4600 [244]	↑ in PCa	LAAOx	0.17 - 116.5
Glutamate	40 - 150 [244]	↑ in PCa	GLOx	0.15 - 10
Choline	10 - 40 [245]	↑ in PCa	ChOx	0.05 - 213
Sarcosine	0 - 20 [246]	↑ in PCa	SaOx	0.01 - 142.3
Lactate	300 - 2000 [247]	↑ in stroke	LaOx	0.039 - 103
Creatinine	100 - 150 [248]	↑ in stroke	CNN	0.17 - 350
			CTN	0.034 - 53.2
			SaOx	0.01 - 142.3

1563 Beer-Lambert's law was then applied for estimating light absorbance and light
 1564 transmittance. Michaelis-Menten equation and Beer-Lamber law are reported here for ease
 1565 of reading:

$$\frac{d[P]}{dt} = \frac{V_{\max}}{1 + \frac{K_m}{[S]}} \quad (3.1)$$

$$A = -\log T - \log \frac{I}{I_0} = \varepsilon \cdot L \cdot [P] \quad (3.2)$$

1566 Where [P] is the concentration of the product, V_{\max} is the maximum rate of the reaction, K_m
 1567 is the Michaelis-Menten constant, [S] is the concentration of the substrate, A is the light
 1568 absorbance, T is the light transmission, I_0 is the light intensity from the light source, I is the
 1569 light intensity transmitted from the sample, ε is the extinction coefficient, L is the optical
 1570 length (in this work L coincide with the height of the microfluidic channel). Numeric values
 1571 used in the simulations are summarised in Table 3.3.

1572 The simulation assumed that light with constant power and fixed wavelength is shone onto
 1573 an ideal photodetector (i.e. one with unity quantum efficiency). The wavelength was in the
 1574 absorbance range of the H_2O_2 probe (i.e. around 500 nm) and adequate for the maximum
 1575 responsivity of the ideal photodetector. The model also did not include any source of noise.
 1576 The implemented Matlab model is reported in Appendix A.

1577 **Results.** Figure 3.3 summarises the primary simulated outcomes. The results of the
 1578 simulations led to several design considerations. Primarily, it is clear from Figure 3.3(a) that
 1579 the trend of light transmission over time is not linear. Substrate concentration is the unknown
 1580 parameter that the system aims to quantify.

1581 Generally, the reaction rate increases with the substrate concentration. As shown in Figure
 1582 3.3(b), the reaction rate is the highest at the beginning of the reaction, and it progressively
 1583 decreases until the end of the reaction. The reaction duration is not known apriori and
 1584 depends on all the platform variables.

1585

1586

Table 3.3 Simulation parameters.

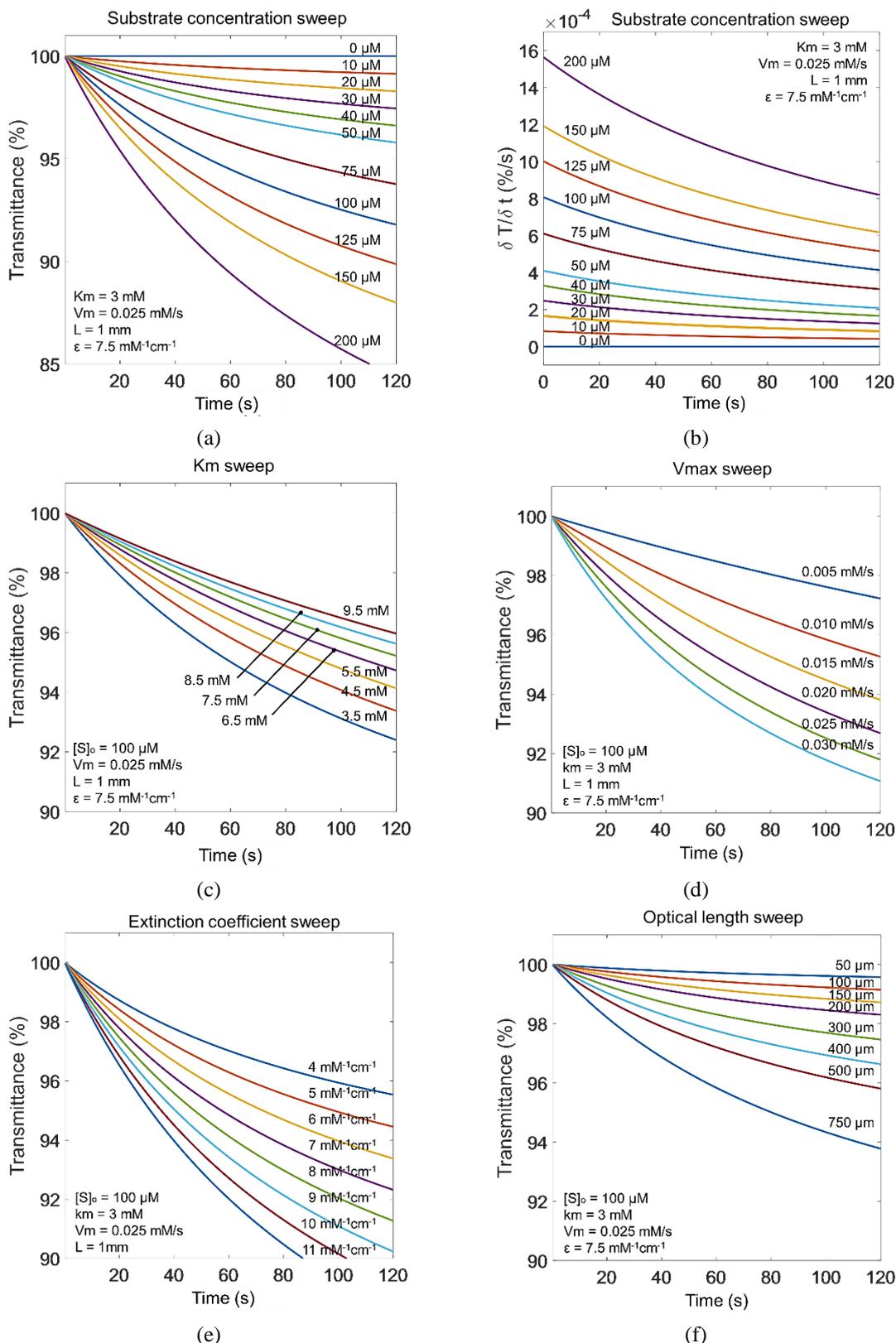
Parameters	Simulation value /range	Reference
[S]	0 – 200 μM	Target range – worst case (see Table 3.2)
K_m	3.5 – 9.5 mM	Typical values for oxidation enzymes [49]
V_{\max}	5 - 30 μMs^{-1}	Typical values for oxidation reactions [49]
ε	4 - 11 $\text{mM}^{-1}\text{cm}^{-1}$	Typical values of commercial colorimetric probes [222]
L	50 - 750 μm	Typical heights of microfluidic channels [249]

1587 Kinetics constants, namely K_m and V_{max} , also have a significant impact on the system
1588 response. Specifically, the reaction rate increases when K_m is reduced, or V_{max} is increased.
1589 K_m and V_{max} typically depend on the selected chemistry and the concentration of the
1590 individual reagents employed. Generally, K_m depends on the specific enzyme and cannot be
1591 easily modified. However, V_{max} can be adjusted by varying the concentration of the enzymes.
1592 The rate of light transmittance is also higher when increasing the extinction coefficient,
1593 which depends on the selected light-absorbing species and the working wavelength chosen.
1594 With all the kinetics variables fixed, the light transmittance trend and the estimated reaction
1595 rate are also strongly affected by the optical length of the system.

1596 The following design considerations can be made, based on the results of the simulations:

- 1597 • A rate-analysis approach for the estimation of the substrate concentration is viable with
1598 the adopted chemistry since different levels of the substrate correspond to different initial
1599 reaction rates. This method was then selected.
- 1600 • ϵ , K_m and V_{max} have to be tuned when designing the optimal reaction to avoid saturation
1601 and match the range of the analyte to be measured.
- 1602 • Strictly from the reaction point of view, the optical length L has to be maximised to
1603 ensure the sensor can easily detect the drop in absorbance. However, there is a trade-off
1604 between maximising L and microfluidic performance, which will be discussed later.

1605



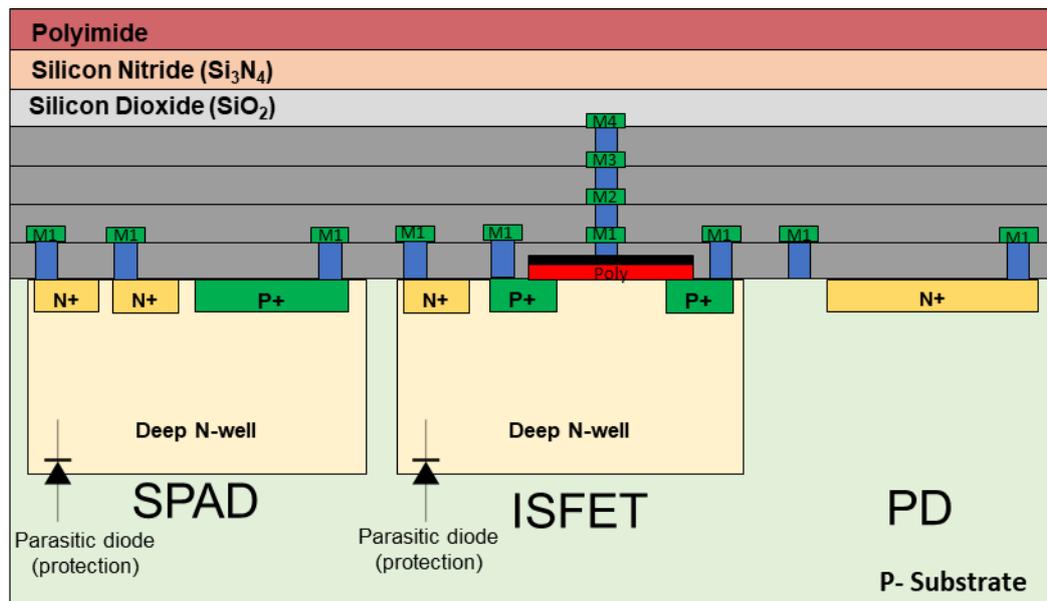
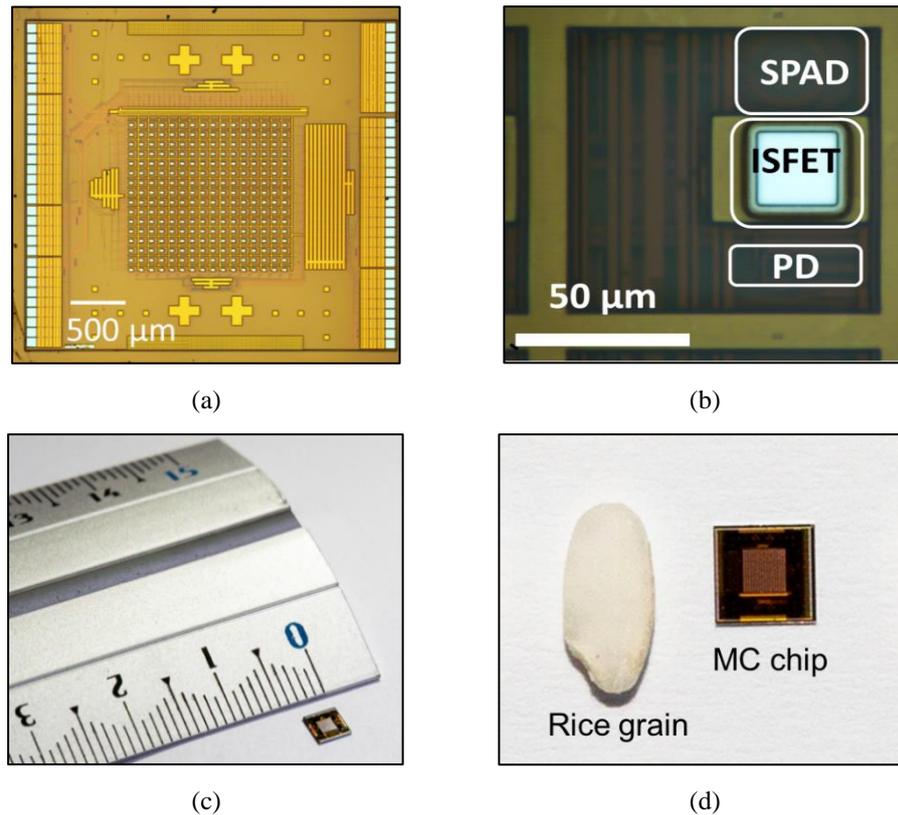
1606 Figure 3.3 Simulated colorimetric assays. (a) Transmission and (b) reaction rate with
 1607 substrate concentrations sweeping from 0 μM to 200 μM . (c) K_m sweep from 3.5 mM to
 1608 9.5 mM. (d) V_{max} sweep from 5 $\mu\text{M}\text{s}^{-1}$ to 30 $\mu\text{M}\text{s}^{-1}$. (e) Extinction coefficients sweep from 4
 1609 to 11 $\text{mM}^{-1}\text{cm}^{-1}$. (f) Optical length sweep from 50 μm to 750 μm . Simulations parameters are
 1610 shown in Table 3.3

1611 **3.2.4. The Multicorder chip**

1612 This research project is part of the project Multicorder project. The Multicorder project led
1613 to the development of several CMOS-based chips for measuring the personal metabolome.
1614 A particular version of the developed chip herein referred to as the CMOS chip, has been
1615 employed in this project. The CMOS chip was designed by a group of researchers from the
1616 Microsystem Technology (MST) group at the University of Glasgow. Dr M.A. Al-Rawhani
1617 was the principal designer [85].

1618 The CMOS chip, presented in Figure 3.4(a), is a 16x16 array of multi-sensors elements,
1619 herein also referred to as pixels or clusters. Each multi-sensor element integrates a
1620 photodiode, an ISFET and a SPAD. Within the cluster, sensors are aligned in the north-south
1621 direction, as shown in Figure 3.4(b). The interface electronics can address sensors
1622 individually or simultaneously [85]. Each cluster has a size of $100 \times 100 \mu\text{m}^2$. Thus, the whole
1623 array occupies a total area of approximately $1.6 \times 1.6 \text{ mm}^2$, in the centre of the chip. The
1624 entire chip occupies an area of $3.4 \times 3.6 \text{ mm}^2$ (see Figure 3.4(c),(d)). The electronic circuitry
1625 embedded into the cluster is mainly located on the west side of the sensors. Sixty-four pads
1626 are equally distributed on the west and east side of the chip. Alignment marks (crosses and
1627 squares) are symmetrically placed on the north and the south side of the multi-sensor array.
1628 The CMOS process selected for the design of the chip was the $0.35 \mu\text{m}$ high voltage process
1629 with four metal layers ('H35B4' technology). The constraints leading to the selection of this
1630 technology are linked to the presence of SPADs on-chip, requiring a high reverse bias
1631 voltage. Mainly, the H35B4 process enables the use of a deep n-well that allows the SPADs
1632 to operate at a high breakdown voltage with minimal interference with other close devices.
1633 A schematic representation of the cluster manufacture with the selected technology is
1634 presented in Figure 3.4(e). The schematic representation is not in scale (information about
1635 layer thickness is confidential), and some design structures have been omitted for the sake
1636 of clarity. The fabrication of the chip was outsourced to Austriamicrosystems (a different
1637 company for manufacturing the CMOS chip might be used in future). After the manufacture,
1638 bare chips were diced and sent to the MST group.

1639 The CMOS chip and different iterations of the chip within the same project have been
1640 employed in related works. The ISFET array of the CMOS chip has been employed to
1641 quantify on-chip urea [243], [250], and glucose [243], [251]. However, many challenges
1642 associated with the use of the ISFET arrays had to be addressed by additional post-
1643 fabrication of the chip [252].



1644 Figure 3.4 (a) Micrograph of the CMOS chip. The multi-sensor array is located at the centre
 1645 of the CMOS chip. 64 pads are equally distributed on the west and the east side of the chip.
 1646 Alignment markers are located on the north and south side of the sensor array. (b)
 1647 Micrograph of a single multi-sensor element of the CMOS chip. Sensors are located on the
 1648 east side of the cluster. Electronic interfaces are mainly located on the west side of the
 1649 cluster. (c), (d) The size of the CMOS chip compared to a ruler and a rice grain. (e)
 1650 Schematic representation of the multi-sensor element fabricated with CMOS technology.
 1651 Schematic is not in scale, and some components are omitted for clarity. Reproduced and
 1652 modified from [85]. PD: photodiode.

1653 The SPAD array of the CMOS chip has also been adopted for chemiluminescence
1654 experiments, leading to the quantification of urate [250]. The fabrication of resonant
1655 nanostructures enabled the capability of performing local surface plasmon resonance
1656 experiments [250]. The photodiode array has been used for immunoassays [216]. In [84], by
1657 fabricating micro-well on top of the active area, the photodiode array was also used to
1658 simultaneously determine with colorimetric assay choline, xanthine, sarcosine and
1659 cholesterol. Remarkably, the ISFET and the photodiode arrays have been used to perform
1660 chemical multiplexing and quantify cholesterol and glucose simultaneously without any
1661 physical separation [243].

1662

1663 **3.2.5. The photodiodes array**

1664 In this project, only photodiodes were employed. Accordingly, this paragraph describes the
1665 aspects of the CMOS chip relevant to this work. The reasons leading to the use of
1666 photodiodes are discussed here. According to the strategy previously described, an optical
1667 sensor must be used. Thus, the use of the ISFET is excluded. Potentially, both SPAD and
1668 photodiode could have been employed for colorimetric assays. They mainly differ in their
1669 dynamic range, with the SPAD being able to detect light with lower intensity. However, in
1670 this application, the device aims to measure the variation in the transmittance of light shown
1671 onto the device with tuneable initial light intensity. It is more convenient to use high light
1672 intensity for two reasons. First, high-intensity light creates a more substantial absolute
1673 transmittance drop. Secondly, the system is more stable to environmental noise. Both factors
1674 contribute to the increase in SNR. Photodiodes also did not require large reverse bias and
1675 showed excellent reliability in a real-life scenario.

1676 The photodiode employed in this project is a p-n junction. As shown in Figure 3.5(a), the n-
1677 layer has a polygonal shape, designed to optimise the area considering both the surrounding
1678 electronics and the design rules. The total area of the n-layer is approximately $38.4 \mu\text{m}^2$. The
1679 n-layer was diffused directly in the p-substrate, thus creating a p-n junction.

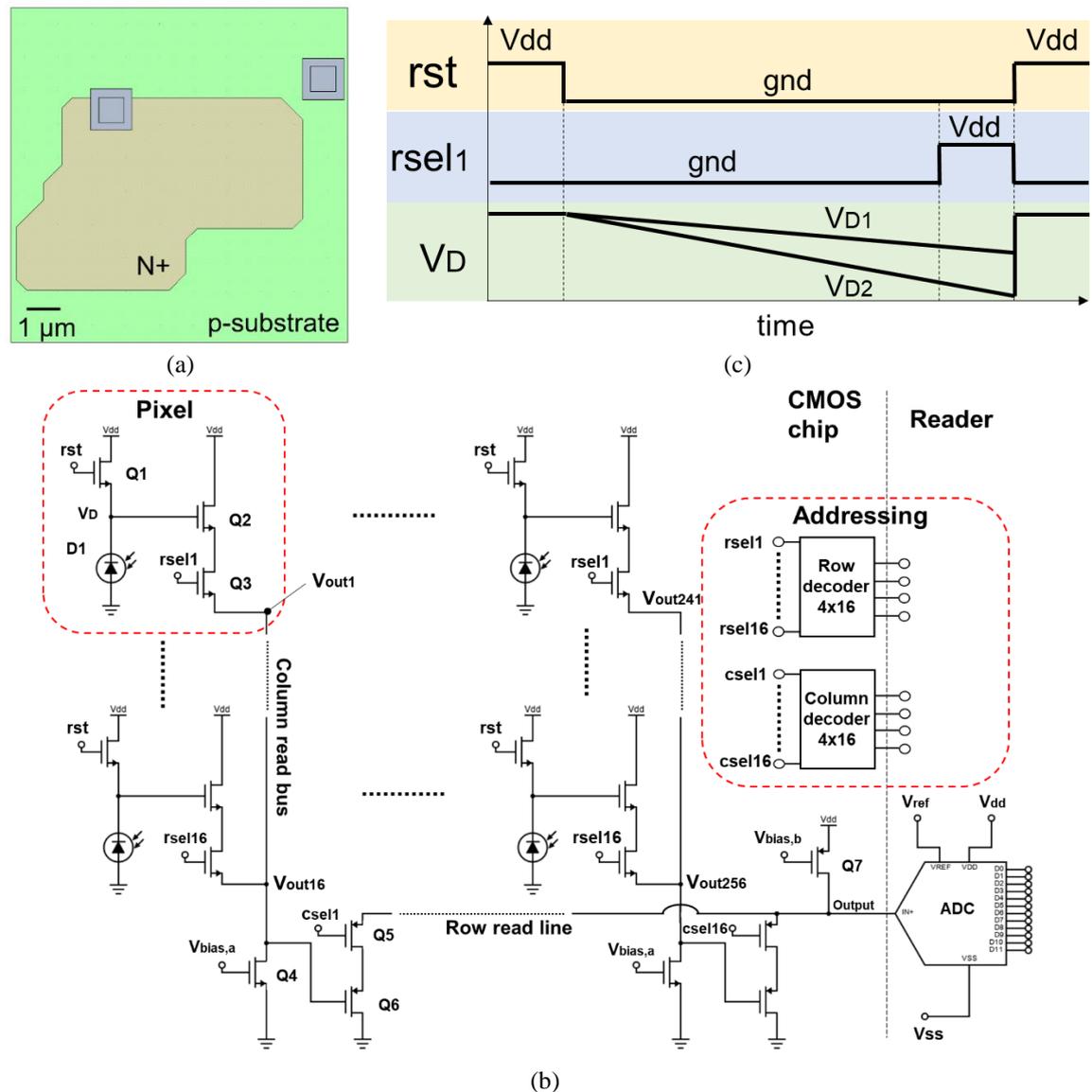
1680 Photodiodes are organised in a 16×16 array format, according to the schematic in Figure
1681 3.5(b). The addressing of the appropriate pixel in the array is performed by using row and
1682 column addressing signals, $rsel_i$ and $csel_i$ - respectively. 16 $rsel$ signals ($rsel_1, \dots, rsel_{16}$) and
1683 16 $csel$ signals ($csel_1, \dots, csel_{16}$) are provided by two 4×16 decoders, embedded in the CMOS
1684 chip (addressing block shown in Figure 3.5(b)). Both the decoders are operated using four
1685 digital control signals, delivered to the CMOS chip by the reader. For each couple of $rsel_i$

1686 and $csel_i$ signals, a single pixel is uniquely addressed. Each pixel integrates one photodiode
1687 and its respective readout electronics. The proposed readout method, usually referred to as
1688 accumulation mode, is provided by three transistors, namely Q_1 , Q_2 and Q_3 [71].

1689 Here the pixel circuit behaviour will be explained. Each of the pixels and their respective
1690 voltages, as described below for one pixel, are independent. The reading cycle starts with a
1691 reset pulse ($rst = V_{dd}$), bringing the node V_D of each pixel to a charged state by charging the
1692 parasitic capacitances of transistors Q_1 and Q_2 . When $rst = 0$ V, Q_1 is off, and there is a
1693 direct path from V_D to ground through the photodiode. In the presence of light, the
1694 photogenerated current flows from V_D to ground, consequently discharging the parasitic
1695 capacitances. The discharge of V_D is buffered using a source follower configuration to the
1696 column read bus (V_{out1}), when the gate Q_3 is selected for the whole row of pixels with an
1697 external addressing signal (e.g. $rsel_1$). Only one row is activated at a time, using the row
1698 select ($rsel$) addressing signal.

1699 In this implementation, the voltage V_D is inversely proportional to the detected light
1700 intensity. Thus, with reference to Figure 3.5(c), V_{D1} represents a situation where the detected
1701 incident light was less intense than for the pixel with V_{D2} . However, to have a more intuitive
1702 reading, the GUI numerically inverts data so that low values of voltage correspond to low
1703 light intensity. This is described in detail in the section dedicated to the GUI. The time
1704 between $rst = 0$ V and the reading of V_{out1} is generally referred to as integration time.
1705 Integration time must avoid the full discharge of V_D . In this implementation, the reset signal
1706 is a global signal but the readout is designed to give a rolling shutter output, as described in
1707 the next paragraph.

1708 The output of the array does not use the bus signals (V_{out1} , ..., V_{out16}) directly. An additional
1709 buffer stage was added in order to isolate the internal pixel circuits, raise the offset voltage
1710 of the output and dedicate only one output pad to connect to external circuitry. The output
1711 voltage (e.g. V_{out1}) of the pixel is buffered to the row read line, using a PMOS source follower
1712 configuration, composed by transistors Q_4 , Q_5 , Q_6 . There is one PMOS source follower block
1713 for every array column. Only one column is activated at a time, using the column select
1714 ($csel$) addressing signals. One current source (Q_7) is used for all column select source
1715 followers. When a row and column select signals are enabled, a buffer path is forged to the
1716 output of the array, allowing for all the pixels to use the same output node sequentially. The
1717 output of the sensor array is then digitised using a 12-bit ADC embedded into the reader.
1718 A comprehensive description of the CMOS chip can be found in [250], [253].

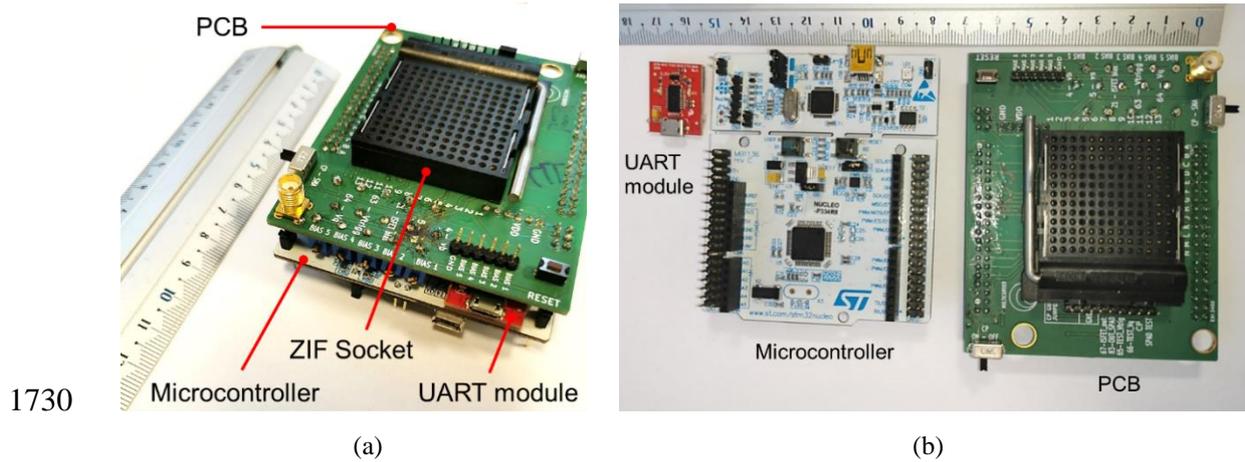


1719 *Figure 3.5 (a) Layout of the active area of the photodiode. (b) Schematic of the 16x16*
 1720 *photodiode sensor array. (c) Time diagram for the operation of a single pixel.*

1721

1722 3.3. The Reader

1723 The reader is composed of a PCB (designed by Dr Claudio Accarino) and a microcontroller
 1724 board. The PCB measured a compact 8.5x7.5 cm. It allowed connecting the cartridge in a
 1725 very user-friendly way by employing a ZIF socket. The PCB was also used for voltage
 1726 supply interface, testing and calibration. The PCB performed all the signal conditioning
 1727 needed to interface the microcontroller board. The microcontroller board was dedicated to
 1728 the addressing of the array, data digitisation and data transmission to the GUI. The USB link
 1729 also provided power for the chip and the Mbed processor.



1730

1731 *Figure 3.6 (a) View of the reader in the final configuration, with individual components*
 1732 *stacked together. (b) Components of the reader (UART module, Microcontroller board and*
 1733 *PCB) shown individually.*

1734

1735 The ST Nucleo F334R8 board, programmed with custom firmware [254], was selected
 1736 because with a total of 51 general-purpose input-output (GPIO) ports was capable of
 1737 accommodating all the required interconnections in an affordable (about £10) and user-
 1738 friendly way. It integrates a 32-bit ARM Cortex-M4 microcontroller unit working at a
 1739 maximum frequency of 72 MHz, which can be programmed with the on-board debugger
 1740 [255]. The board also has a 64kb flash memory and a 12kb static random-access memory.
 1741 Among all the capabilities of the board, the onboard 12-bit analogue-to-digital converter
 1742 (ADC) was used for data digitisation. The PCB and the microcontroller board were stacked
 1743 together, as shown in Figure 3.6(a). The communication between reader and GUI was
 1744 achieved through the universal asynchronous receiver/transmitter (UART) communication.
 1745 UART is a widespread standard for serial interfaces. However, the maximum baud rate
 1746 supported by the microcontroller board is 115200. To increase the communication rate, an
 1747 external module, the FT231X module by Sparkfun electronics, was plugged into the PCB.
 1748 The use of the external UART module enabled a higher baud rate of 921600. The PCB board,
 1749 the UART module and the microcontroller board are individually shown in Figure 3.6(b).
 1750 The microcontroller supports the use of custom firmware, which was developed on the
 1751 ‘mbed’ online compiler using C++[256]. The full C++ code is reported in Appendix B.
 1752 The firmware begins with an initialisation phase. During this phase, a first-in-first-out
 1753 register is initialised for the UART communication. The register is shared by both the
 1754 transmitter (the UART module in this case) and the receiver (the GUI). The transmitter
 1755 sequentially writes the register. In parallel, the receiver can asynchronously access the

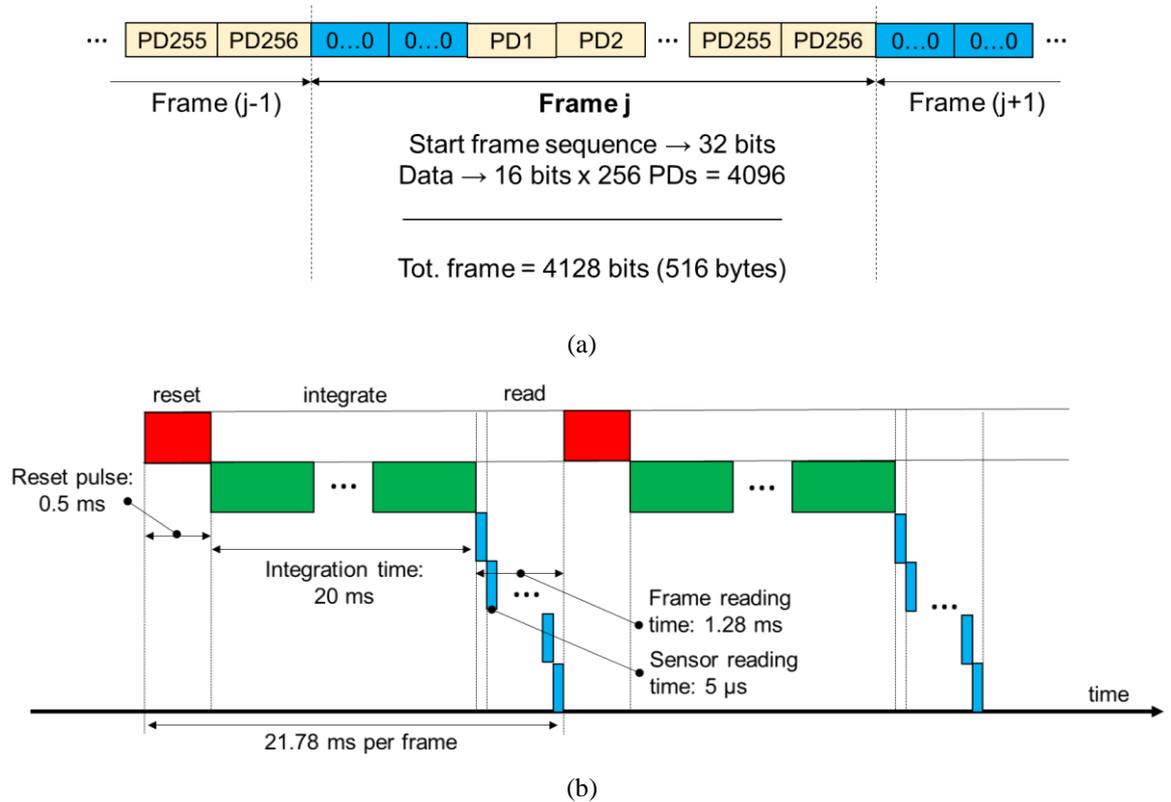
1756 register and read binary values sent from the transmitter. During initialisation, GPIOs are
1757 also defined. Specifically, eight pins are used for chip addressing, four of which are
1758 dedicated to row selection, whereas the remaining four are for column addressing. One
1759 analogue input is dedicated to data digitisation. After initialisation, a loop is adopted for
1760 continuous data acquisition.

1761 Data reading consists of three steps: reset, integration and reading. In the first step,
1762 addressing is disabled, and a reset pulse with a $500\ \mu\text{s}$ width is delivered to all the
1763 photodiodes. The integration time, here set at 20 ms, is a waiting time accordingly to the
1764 adopted approach, previously described. The integration time has been selected to be much
1765 higher than the reading time and to provide a frame rate comparable to standard imaging
1766 techniques, usually providing about 30 frames per second (fps).

1767 After the integration, a starting frame sequence is first sent to inform the GUI that a frame
1768 data is about to start. The starting sequence is a double zero encrypted with 32-bits in total.
1769 It must be pointed out that it was experimentally verified that the digitised output of the
1770 sensors never reached a perfect zero. Subsequently, the first row is addressed by the four
1771 digital output pins. The first column address is also delivered to the cartridge: a single pixel
1772 is then identified. A waiting time of $5\ \mu\text{s}$ is adopted to make sure all the electronic transient
1773 effects are discharged. The analogue output of the sensor is then read with the embedded
1774 12-bits ADC of the board. Digitised data is converted into a 16-bits value and sent to the
1775 GUI. The conversion is necessary since UART communication works using bytes. Once data
1776 is sent, a new column address is delivered to the cartridge, and further reading is performed.
1777 When all the columns have been read, a new row address is provided. The process is iterated
1778 till all the array has been scanned.

1779 As mentioned in the previous paragraph, pixels in the same column share the same output
1780 line. Thus, from a data integrity viewpoint, it is safer to read different columns sequentially.
1781 From a data transfer viewpoint, an entire frame contains 4128 bits (516 bytes). This includes
1782 32 bits (4 bytes) for the start frame sequence and 4096 bits (512 bytes) of data, where each
1783 pixel is sent with a 16-bits binary code (2 bytes). Frames are continually sent on the GUI.
1784 So, the necessity of the starting frame sequence is here demonstrated. Representation of data
1785 packing is provided in Figure 3.7(a).

1786 From a timing viewpoint, the time needed from the reader to read and send an entire frame
1787 is 21.78 ms. The total time is composed of $500\ \mu\text{s}$ for reset, 20 ms for the integration, and
1788 1.28 ms for the frame reading.



1789 *Figure 3.7 (a) Representation of data packing for serial transmission. (b) Timing diagram.*

1790

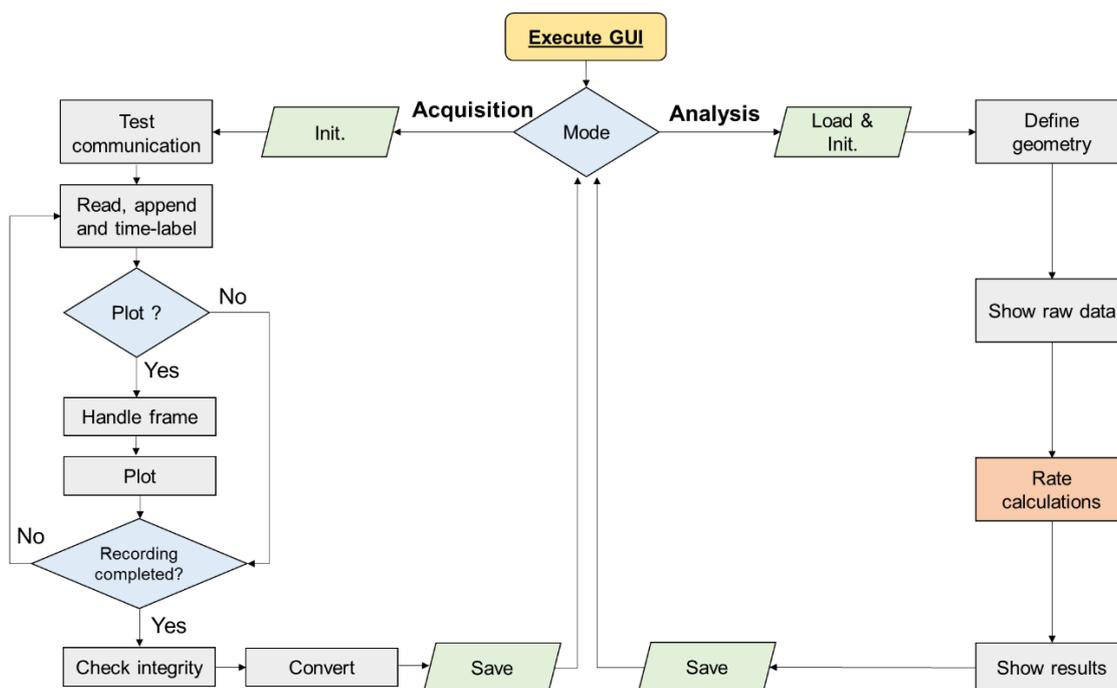
1791 The time needed for the reading of a single pixel was approximately 5 μs. A timing diagram
 1792 of data reading is provided in Figure 3.7(b). Altogether, the reader sends about 185,760 bits
 1793 (23.2 kbytes) per second. This means that the approximate size of a 5-minute data recording
 1794 is approximately 55,728,000 bits (6.9 Mbytes).

1795

1796 **3.4. The Graphical User Interface (GUI)**

1797 The GUI interface is a software developed using the Matlab-based graphical user interface
 1798 development tool. It was exported as a standalone application and can run on any portable
 1799 device running a Microsoft Windows operating system. In this work, a PC (Dell Optiflex
 1800 7050), a laptop (HP EliteBook 830 G5) and a tablet (HP Pavillion x2) have all been
 1801 successfully employed to host the GUI. A simplified android version of the GUI, currently
 1802 available on the Google App Store, was developed by Bence Nagy but has not been used in
 1803 this work.

1804 The GUI connected to the reader by USB link. The USB link provided the 5V power supply
 1805 to the microcontroller.



1806

1807

Figure 3.8 Flow chart of the GUI operation.

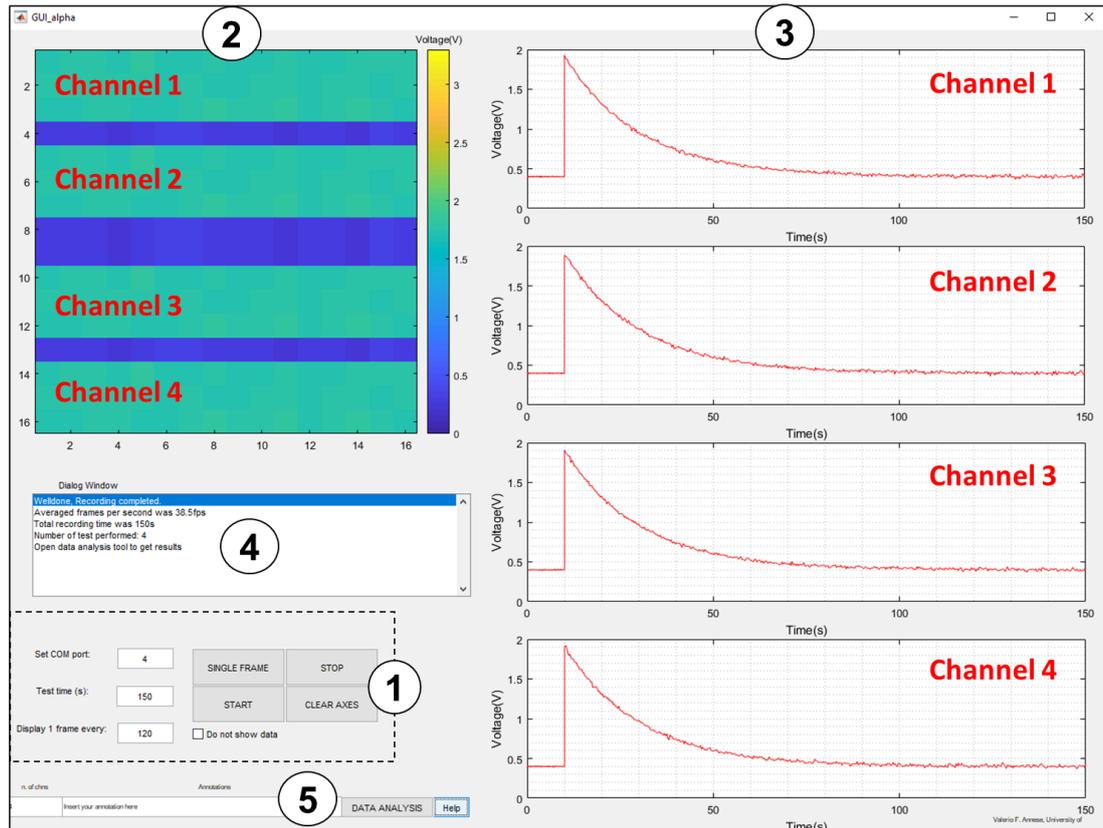
1808

1809 In turn, the reader provided the 3.3 V required for the cartridge to work through a linear
 1810 voltage regulator. The GUI received binary data from the reader, and it was employed for
 1811 data collection, visualisation, processing, and analysis. A flow chart of the primary
 1812 operations performed by the GUI is reported in Figure 3.8. The GUI worked in two different
 1813 modalities: data-acquisition mode and data-analysis mode. When working in data
 1814 acquisition mode, the GUI was used in conjunction with the reader and the cartridge to
 1815 collect, represent and save data. This is the modality employed for monitoring colorimetric
 1816 reactions. The data analysis mode was instead used to process data once the experiment was
 1817 completed. Both processing branches are described in the next sections.

1818

1819 3.4.1. Data acquisition

1820 When working in data acquisition mode, the GUI executes the operation on the left-hand
 1821 side of the flow chart reported in Figure 3.8. A demonstrative screen-print of the GUI
 1822 working in data-acquisition mode is presented in Figure 3.9. Before running the test, the user
 1823 can modify default parameters such as communication port, test duration time, and the frame
 1824 per second to be represented (panel (1) in Figure 3.9). The communication port mainly
 1825 depends on the physical USB port, where the reader has been plugged in. The test duration
 1826 time is the time interval in which the GUI saves data.



1827

1828 *Figure 3.9 GUI in data-acquisition mode. 1) Control panel; 2) Frame visualisation;*
 1829 *3) Single-pixel representation; 4) Dialog window; 5) Go to data analysis.*

1830

1831 In this section, it is also possible to decide how many frames to represent per second. The
 1832 biological reaction is very slow so it might not be necessary to visualise in real-time each
 1833 recorded frame. Data representation takes time and resources so overplotting should be
 1834 minimised. Experiments showed that reducing the number of frames shown in real-time
 1835 increased the recorded frames per second. In other words, the system is faster when no or
 1836 minimal data is presented in real-time. The user expresses the will to start the test by clicking
 1837 on 'start'. Immediately, the user is prompted with a window where he can graphically select
 1838 four different pixels to be shown in real-time - section (3) in Figure 3.9. After the selection,
 1839 the GUI automatically records for a fixed time-period data coming from the cartridge. The
 1840 user is meant to insert the sample in the cartridge at this stage. Data recording can be stopped
 1841 at any time by selecting 'stop'. For each recorded frame, a time-label is saved. While
 1842 recording, real-time data is shown. Referring to Figure 3.9, the entire frame is shown in
 1843 section (2), and single-pixel data is instead shown in section (3).

1844 Once the recording is completed, data is handled for a more convenient subsequent
 1845 processing. First, frames are identified and isolated. The entire recorded data is scanned for

1846 the presence of double zeros, the starting frame sequence. Data between the two starting
 1847 sequences are saved as single frames. Frames with an unexpected number of data, due to any
 1848 communication error, are discarded together with their time label. Frames are organised in a
 1849 2D matrix with dimensions 256xM, where M is the number of frames in the recording. Thus,
 1850 each row of the 2D matrix represent data coming from a single pixel over time. Time labels
 1851 are also compressed into 1xM vectors. After frame handling, data needs to be converted into
 1852 the original photodiode voltage value. The software interprets incoming single bytes as
 1853 decimal values. Thus, first, the incoming decimal value is converted back to binary with 8-
 1854 bits precision. This represents the most significant byte (MSB) of the reading. The
 1855 subsequent decimal value, which represents the least significant byte (LSB), is also
 1856 converted into a binary string with the same precision and appended to the MSB. The so
 1857 created 16-bits string is now converted into decimal, providing a value in the range 0 -
 1858 $2^{16}=65536$. Data is also flipped for a more intuitive reading, so that a high output
 1859 corresponding to high light intensity. Afterwards, the numerical decimal values are
 1860 converted into a voltage value by employing the following formula:

$$V_{\text{out}} [\text{V}] = \frac{V_{\text{out}} [\text{dec}] \cdot V_{\text{dd}}}{2^N - 1} \quad (3.3)$$

1861 Where V_{dd} is the voltage range of the ADC used (3.3 V in this case), and N the number of
 1862 bits used to digitise the analogue signal (16 in this case).

1863 At the end of the process, the recording is composed of a 256xM matrix containing the value
 1864 in the range 0 – 3.3 V and a 1xM vector containing time labels in seconds, with M being the
 1865 number of frames in the recording. The process concludes with data storage, eventually onto
 1866 a cloud-shared folder when TCP/IP communication is available.

1867 The GUI is meant to work in a real-time scenario and, for this reason, must be able to detect
 1868 failures and ‘fail safely’. For this aim, if any communication error occurs (for example the
 1869 cartridge is disconnected while the GUI is recording), an error is reported to the user, and
 1870 only data collected till the error occurs is saved. Data integrity checks, consisting in verifying
 1871 that each frame has the expected number of elements with numerical values included in the
 1872 expected range, are also in place.

1873 Collected data is now ready to be processed using the GUI in the data analysis mode. To
 1874 switch to this modality, the user can press the ‘data analysis’ button (panel (5) in Figure 3.9).
 1875 Otherwise, the system is ready for a new recording. An extract containing an essential
 1876 section of the Matlab code used for the acquisition of data is reported in Appendix C.

1877 **3.4.2. Data analysis**

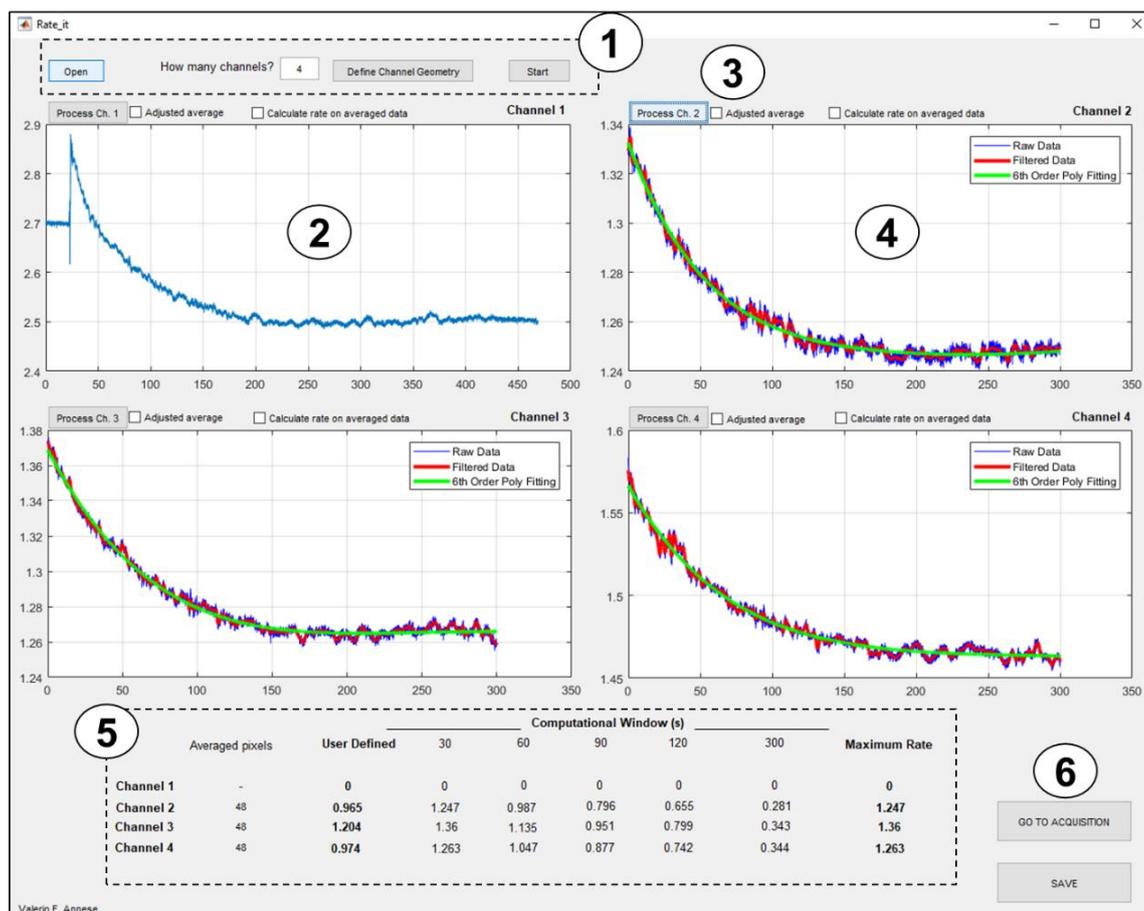
1878 When working in data analysis mode, the GUI executes the operation on the right-hand side
1879 of the flow chart reported in Figure 3.8. A demonstrative screen-print of the GUI working in
1880 data-analysis mode is presented in Figure 3.10. The present tool was developed for use by
1881 several researchers within the MST group and, for this reason, it allows customisation of a
1882 wide range of settings. First, the user loads the dataset to be analysed (panel (1) in Figure
1883 3.10). Then, the user specifies how many reaction zones are present on the cartridge and
1884 defines their geometry by clicking on the dedicated button and following the guided
1885 procedure. In this project, each microfluidic channel is a reaction zone. By clicking the start
1886 button, raw data is averaged in the selected microchannels and plotted as panel (2) in Figure
1887 3.10. At this stage, the user can analyse the data within the microchannel chosen with the
1888 user panel (3) always in Figure 3.10, which will be referred to throughout the following text.
1889 By clicking the ‘process’ button in (3), the user initiates a process leading to the calculation
1890 of the initial rate of the reaction. Results are then graphically shown in (4) and numerically
1891 reported in (5). Results can be saved through a dedicated button in panel (6).

1892 The process leading to the estimation of the initial reaction rate from raw data is described
1893 in Figure 3.11 and can be divided into three sub-routines, namely data preparation, noise
1894 reduction and rate calculation.

1895 In the first processing step, data is prepared for the analysis. The process makes sure data is
1896 converted into a voltage value; the number and geometry of pixels included in the channel
1897 to be processed are defined. Also, the starting point of the reaction is defined and validated
1898 by the user. Usually, this is visible from raw data due to the sudden transmittance variation
1899 induced by the sample introduction onto the platform, as shown in the next chapter. Data is
1900 cropped to 5 minutes (300 s) segment starting from the starting point of the reaction, even if
1901 data is recorded for longer than that. At this stage, eventual unresponsive pixels and pixels
1902 presenting strong artefacts (e.g. air bubble) are excluded after visual inspection. At the end
1903 of this process, the data which has been handled is composed of an $N \times L$ matrix containing
1904 the value in the range 0–3.3 V and a $1 \times M$ vector containing time labels in seconds and a $1 \times L$
1905 vector. N is the number of pixels contained in the microfluidic channel after visual
1906 inspection, L is the number of frames in the 300 s recording.

1907 In the second stage, data analysis aims to reduce expected noise. The primary noise sources
1908 in CMOS sensor arrays are temporal noise and fixed pattern noise (FPN) [80].

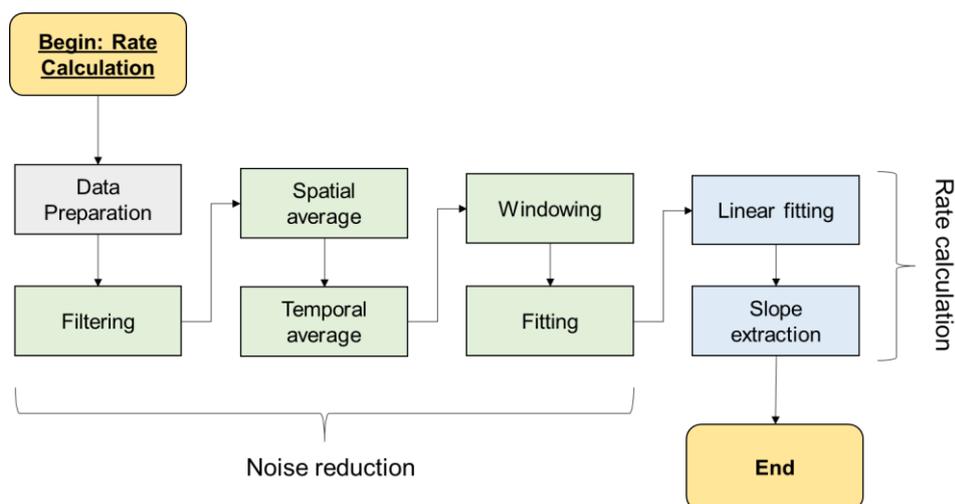
1909



1910

1911 *Figure 3.10 GUI in data-analysis mode. 1) Control panel; 2) Raw data visualisation;*
 1912 *3) Start processing button for single-channel; 4) Processed data visualisation; 5) Rates*
 1913 *(mVs⁻¹); 6) Save and go to data-acquisition mode.*

1914



1915

1916 *Figure 3.11. Flow chart of the process adopted for the estimation of the initial reaction rate*
 1917 *from the raw data.*

1918

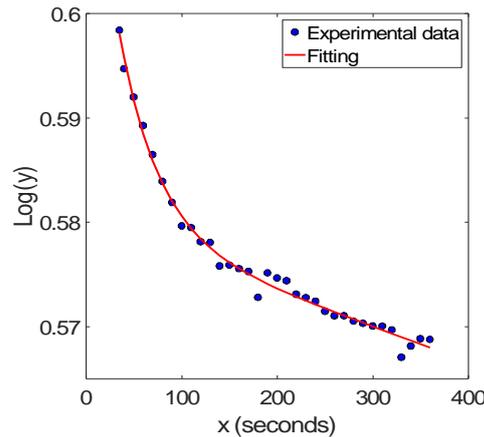
1919 Temporal noise is a combination of pixel noise components (thermal, shot and flicker),
 1920 addressing circuit noise, ADC noise. FPN is the variation of the output among pixels when
 1921 the same input is applied. Data is filtered with an 8th order low pass filter to reduce the
 1922 standard deviation of temporal noise. The biological reaction is usually slow, as
 1923 demonstrated in the simulation proposed in the initial section of this chapter. So, a low
 1924 normalised cut-off frequency, namely 0.1, is selected. Precaution is taken to avoid any signal
 1925 distortion at the borders. Next, data is averaged in time (usually 1-second information).
 1926 However, temporal averaging does not affect the FPN. The spatial average reduces the
 1927 standard deviation of the FPN over the entire channel. Pixels offset before the spatial average
 1928 is compensated by aligning the starting point of the reaction to the same reference. Over the
 1929 assumption that both the noise of a single sensor and of the entire array has a Gaussian
 1930 distribution, the averaging process reduces the standard deviation of a factor \sqrt{N} , where N
 1931 is the number of population in the average [242]. The time vector is similarly averaged. So,
 1932 at the end of the process, two 1x300 vectors are created containing respectively averaged
 1933 data from the channel and time. At this stage, the vector containing data is segmented using
 1934 five different time windows, namely 0–30s, 0–60s, 0–90s, 0–120s, 0–300s. The user can
 1935 introduce an additional time window by custom selection. Consequently, these lead to six
 1936 different vectors containing voltage data with variable length. Those signals can be here
 1937 converted into transmittance and absorbance to undergo the same following processing. Data
 1938 from each vector is fitted using the following double exponential model:

$$y = a \cdot e^{b \cdot x} + c \cdot e^{d \cdot x} \quad (3.4)$$

1939 Where the four numerical parameters a, b, c, and d have been optimised using Matlab-based
 1940 tools for the minimisation of the root mean square error (RMSE). The proposed model
 1941 experimentally showed to be the most suitable method for data fitting. Figure 3.12 shows
 1942 an example of data fitting from experimental data.

1943 In the third stage of signal processing, the initial reaction rate is estimated from the fitted
 1944 signals. Reaction rates are calculated by linearisation of the fitted signals in time windows.
 1945 The extracted initial reaction rate is the highest rate calculated onto all the versions of the
 1946 windowed signal. The decomposition of the signal in different time windows allows the
 1947 automatic calculation of the reaction. It is not known apriori which window is the best for
 1948 the calculation of the reaction rate. Thus, the algorithm tries several fixed windows and
 1949 selects the optimal one based on the maximisation of the reaction rate.

1950



1951

1952 *Figure 3.12 Example of data fitting according to Equation (3.4). Data from LAA assay in*
 1953 *diluted serum (LAA concentration: 1mM). The blue markers indicate experimental data*
 1954 *points. The red line represents the double exponential fitting.*

1955

1956 When using the method on voltage, transmittance and absorbance data, the algorithm
 1957 provides rate information in mV/s, %/s, a.u./s, respectively. A per minute-rate can also be
 1958 supplied by multiplying for a factor of 60. When using a device with variable geometry, it
 1959 is convenient to convert the rate in μMs^{-1} by using the following formula:

$$P(t) = \frac{A(t)}{\varepsilon h} = \frac{\log_{10} \frac{1}{T(t)}}{\varepsilon h} = \frac{\log_{10} \frac{V(0)}{V(t)}}{\varepsilon h} \quad (3.5)$$

1960 Where $P(t)$ is the concentration of the product, $A(t)$ is the absorbance, ε is the extinction
 1961 coefficient of the light-absorbing species, h is the microchannel height, $T(t)$ is the
 1962 transmittance, and $V(t)$ is the sensor output in voltage. This representation is convenient
 1963 because normalised to any variation due to the extinction coefficient and the optical length.
 1964 Whatever the measurement units adopted for the rate representation, the initial concentration
 1965 of the substrate can be estimated by using the Michaelis-Menten model or by using a
 1966 previously calculated calibration curve. An extract containing the essential sections of the
 1967 Matlab code used for the data analysis is reported in Appendix D.

1968

1969 **3.5. Connectivity**

1970 The connectivity diagram of the platform is shown in Figure 3.13. It should be noted that the
 1971 CMOS chip integrates other sensors besides the one used for this project. However, this
 1972 section only reports the connections required for this project.

1973 The CMOS chip connects to the ceramic package by 18 wire bonds. In turn, the ceramic
 1974 package connects to the PCB through a ZIF socket. The same 18 connections are thus routed
 1975 to the PCB. The PCB connects to the microcontroller through 16 bits. The PCB is also
 1976 connected to the UART/USB module through 6 additional pins. The UART/USB module
 1977 connects to the portable electronic device via USB. The GUI, running on the portable
 1978 electronic device, handles and saves data.

1979 Table 3.4 provides a description of the functionalities of the connections.

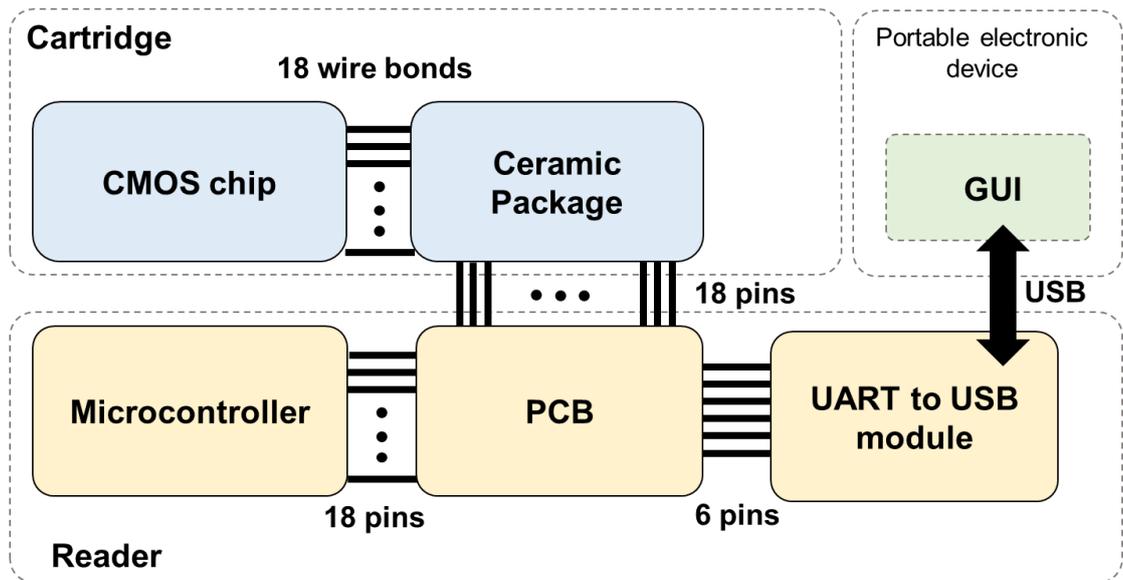
1980

1981

Table 3.4 Connection list of the platform.

	N° of Pins	Type	Function
CMOS chip from/to Package (wire bonds)	6	Power	Biasing and reference voltages
	2	Power	ground
	1	Analogue	Photodiode data
	1	Analogue	Photodiode reset
	4	Digital	Column addressing
	4	Digital	Row addressing
	18	Total	
Package from/to PCB	6	Power	Biasing and reference voltages
	2	Power	ground
	1	Analogue	Photodiode data
	1	Analogue	Photodiode reset
	4	Digital	Column addressing
	4	Digital	Row addressing
	18	Total	
PCB from/to Controller	4	Power	Biasing
	2	Power	ground
	1	Analogue	Photodiode data
	1	Analogue	Photodiode reset
	4	Digital	Column addressing
	4	Digital	Row addressing
	1	Digital	Transmit (TX)
	1	Digital	Receive (RX)
18	Total		
PCB from/to USB/UART module	1	Power	Biasing
	1	Power	Ground
	1	Digital	Transmit (TX)
	1	Digital	Receive (RX)
	1	Digital	Data Terminal Ready Control
	1	Digital	Clear To Send Control
	6	Total	

1982



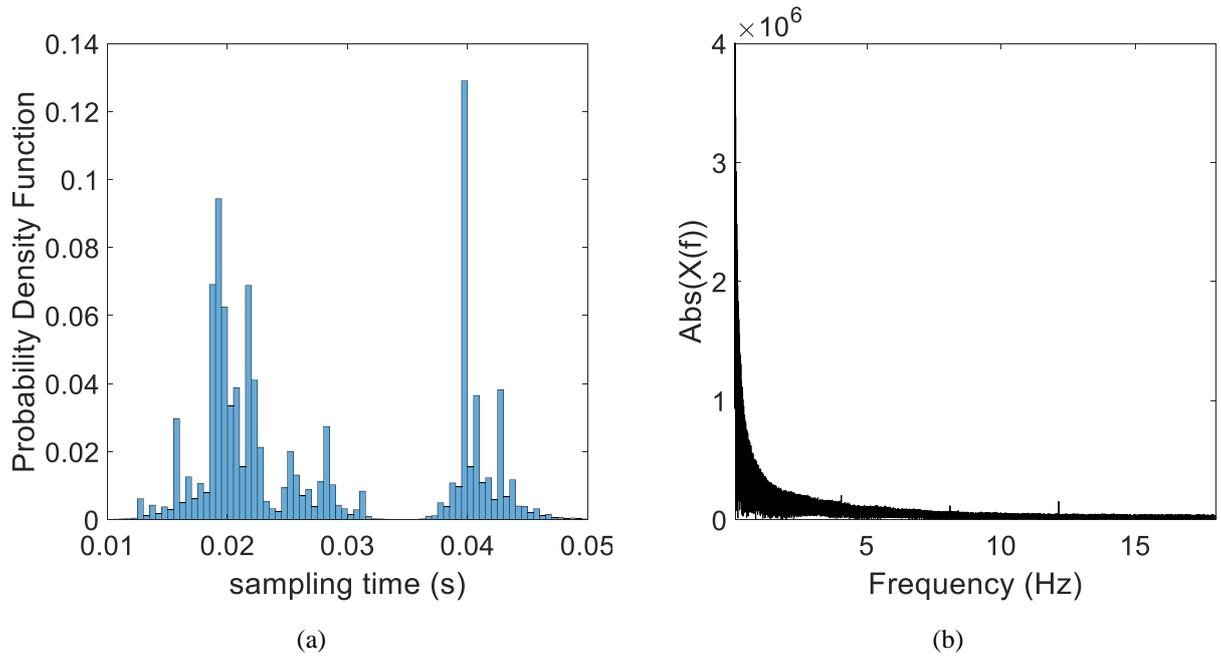
1983

1984

1985

1986 **3.6. Graphical User Interface Benchmark**1987 **3.6.1. Data acquisition mode**

1988 The GUI in data acquisition mode was tested using a laptop as the portable electronic device
 1989 (HP Elitebook 840). The sampling time for data acquisition was analysed over twenty
 1990 independent measurements, each with a 5-minute duration. The probability density function
 1991 of the sampling time was obtained by calculating the derivative of the time vectors, counting
 1992 the recurrence into defined bins, and dividing by the total number of samples (around 260k
 1993 in this analysis). The obtained probability density function is reported in Figure 3.14(a). The
 1994 average and standard deviation of the sampling time was 27.4 ± 9.7 ms. When converted into
 1995 frame per seconds (fps), the average fps was 36.5 ± 9.5 fps. However, the probability density
 1996 function seems composed of two different components which might be approximated with
 1997 Gaussian distributions. The right Gaussian behaviour was attributed to the additional time
 1998 required for graphic representation of the samples. Signal integrity was analysed to detect
 1999 any systematic source of noise in the platform. The spectra of the data from different
 2000 independent recordings with a fixed optical power were analysed. Figure 3.14(b) shows one
 2001 spectrum of an entire recording from one randomly selected pixel. Harmonics at 4, 8 and 12
 2002 Hz appeared to be systematically introduced in the system.

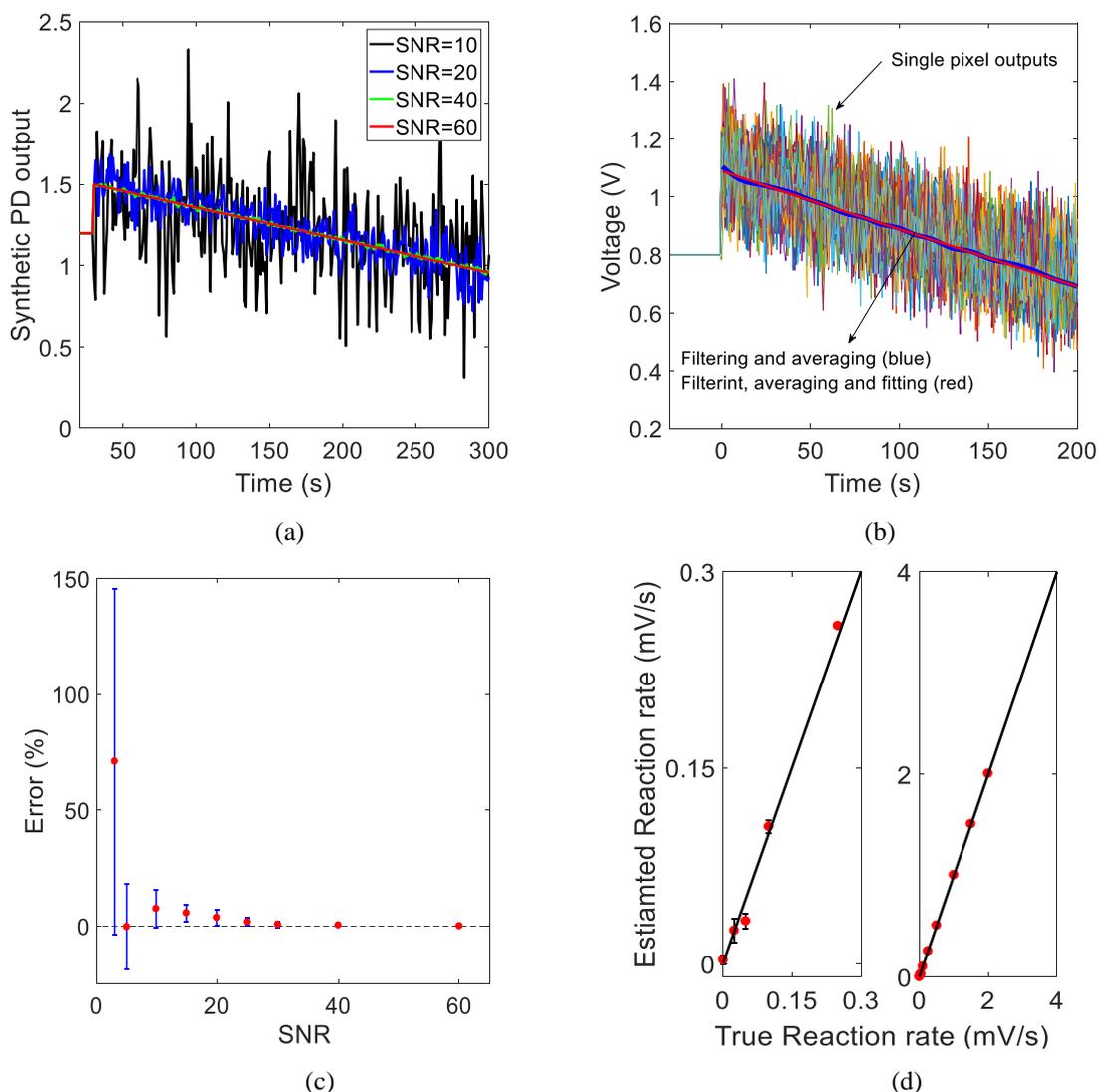


2003 *Figure 3.14 (a) Probability density function of the sampling time. The analysis was obtained*
 2004 *from 20 different measurements, each with a 5-minute duration. The total number of samples*
 2005 *was around 260k. (b) Spectrum of the recordings.*

2006

2007 **3.6.2. Data processing mode**

2008 The GUI in data analysis mode was also tested. The signal processing algorithm was tested
 2009 on computer-generated signals with the same characteristics as the expected experimental
 2010 ones. The synthetic recording simulated a reaction with a constant reaction rate. The
 2011 synthetic dataset had 256 pixels, a 5-minute and sampled at 36.5 fps. The presence of
 2012 microfluidic channels and the spike in the signal output due to sample introduction was also
 2013 emulated. White Gaussian noise was added to the synthetic signals to mimic a real-life
 2014 scenario. A synthetic dataset was obtained by sweeping the reaction rate and the SNR. To
 2015 simplify the study, the reaction rate was kept constant for each synthetic signal. Figure
 2016 3.15(a) shows a set of synthetic signals with different SNR levels. The developed algorithm
 2017 was used to estimate the reaction rate throughout the dataset. The results were then compared
 2018 with the true rate. Figure 3.15(b) goes through all the main processing steps leading to the
 2019 final reaction rate estimation for a single microchannel, as already described in Chapter 3.
 2020 Data from all the available pixels in the channel were filtered and averaged. An additional
 2021 time averaging step was employed to average all the samples within a one-second time
 2022 window, reducing the fps to 1. The resulting curve was used to produce a double exponential
 2023 fitted curve.



2024 *Figure 3.15 (a) Testing synthetic signals with different level of SNR. Constant reaction rate:*
 2025 *2 mVs^{-1} . (b) Data from 48 synthetic pixels was used (SNR=20). Data was first filtered and*
 2026 *averaged from the reaction starting point (blue line). Data was then fit to a double*
 2027 *exponential model (red curve) used for rate, transmittance, and absorbance evaluation. (c)*
 2028 *Relative error of the reaction rate determination with different levels of noise. Testing*
 2029 *signals had a fixed rate of 2 mVs^{-1} but different additive noise levels. (d) Estimated reaction*
 2030 *rate vs. true reaction rate with reaction rate sweeping in the expected region from 0.001*
 2031 *mVs^{-1} to 4 mVs^{-1} . Noise was kept constant to SNR = 30.*

2032

2033 The resulting curve was finally used to calculate rates, absorbance, and transmittance. Figure
 2034 3.15(c) quantifies the effect of the noise magnitude when calculating the reaction rate. The
 2035 estimation of the reaction rate by the algorithm showed a negligible error when the SNR is
 2036 higher than 30. The performance of the algorithm gradually degraded when the SNR was
 2037 decreased. The degradation of the performance was verified by increased values of both error
 2038 and standard deviation. The performance of the algorithm was no longer acceptable with

2039 SNR ≤ 3 . Figure 3.15(d) shows the reliability of the algorithm in the evaluation of different
2040 reaction rates with SNR = 30. The algorithm showed excellent capability in reconstructing
2041 the reaction rate, even for reaction rate as small as 0.001 mVs^{-1} . The performance of the
2042 reconstruction algorithm was not affected by the speed of the reaction, when the level of
2043 noise was in the acceptable range.

2044

2045 **3.7. Summary of the Chapter**

- 2046 • The platform is composed of three units: the cartridge, the reader, and the GUI.
- 2047 • The cartridge is composed of three sub-units: the CMOS chip, the microfluidics and the
2048 bioreagents.
- 2049 • The CMOS chip, developed within the Multicorder project from the MST group,
2050 University of Glasgow, integrates a 16×16 array of multi-sensing elements which
2051 comprise photodiodes. The integration of the CMOS chip with microfluidics and
2052 bioreceptors is discussed in the next chapters.
- 2053 • The platform was designed for the quantification of four potential metabolic biomarkers
2054 for PCa (LAA, glutamate, choline and sarcosine) and two potential metabolic biomarkers
2055 for ischemic stroke (lactate and creatinine) using a colorimetric approach. Reagents were
2056 selected accordingly.
- 2057 • The reader, composed of a custom PCB and a microcontroller board, was used for sensor
2058 addressing and data digitisation. The cartridge slots into the reader through a dedicated
2059 user-friendly socket.
- 2060 • The GUI, a custom software running on a portable electronic device such as a laptop, is
2061 dedicated for data acquisition and processing. Data processing focused on estimating the
2062 initial rate of the reaction, which is related to the concentration of the target analyte by
2063 the Michaelis-Menten model.
- 2064 • Reader and GUI were tested. The average fps was 36.5 ± 9.5 fps, with variations due to
2065 real-time graphic representation settings. The algorithm performing the rate estimations
2066 was also tested using a synthetic dataset with different SNRs. The algorithm could
2067 reconstruct the synthetic reaction rate with a negligible error when SNR ≥ 30 . The
2068 reduction of the SNR degraded the performance of the algorithm. Noise levels producing
2069 SNR ≤ 3 were considered unacceptable.

2070 Chapter 4: Microfluidic System

2071 4.1. Introduction

2072 The integration of microfluidics and ICs is a major challenge for point-of-care devices [257],
 2073 [258]. In this work, microfluidics is required to address the specification of multi-analyte
 2074 testing (see Table 2.11). The microfluidics integration with the CMOS chip is required to be
 2075 monolithic to address the versatility requirement. Specifically, although they were not used
 2076 in this work, the CMOS chip also integrates an ISFET array, which requires to be directly
 2077 exposed to the solution to be analysed. Therefore, microfluidics is required to be integrated
 2078 in such a way that the sensor array is in contact with the sample. Monolithic integration is
 2079 also required for application aiming to detect a weak signal [259]. The integration eliminates
 2080 any superfluous signal path, which can additionally deteriorate the signal quality and
 2081 introduce additional noise [259]. Monolithic integration also reduces parasitic capacities and
 2082 minimises the footprint associated with sensing [259].

2083 The present chapter illustrates the design, manufacturing, and characterisation of the
 2084 microfluidic system. The chapter begins discussing the relevant state of the art on
 2085 microfluidics manufacturing and integration. The design of the passive microfluidic system
 2086 is then illustrated through prototypal fabrication and simulations. Subsequently, the
 2087 fabrication of the microfluidic system and the CMOS chip is described. Analysis and
 2088 characterisation of the manufactured cartridge conclude the chapter. Table 4.1 illustrates the
 2089 contribution to each activity discussed in this chapter.

2090

2091 *Table 4.1 Table of contributions for the activity presented in this chapter.*

Task / Activity presented in Chapter 4	Main investigators
Microfluidics design and modelling	- Valerio F. Annese
Integration of capillary microfluidics on the CMOS chip	- Valerio F. Annese
Packaging for multiplexed wet assays	- Valerio F. Annese
Characterisation of the microfluidic structures	- Valerio F. Annese
Spectral characterisation of the photodiode array	- Valerio F. Annese - Dr Mohammed Al-Rahawani ¹ - Dr Christos Giankulovitch ¹
Characterisation of the cartridge	- Valerio F. Annese
Characterisation of sample flow in the microfluidic system	- Valerio F. Annese
Affiliation at the time of completion of the activity: ¹ Microsystem Technology Group, James Watt School of Engineering, University of Glasgow.	

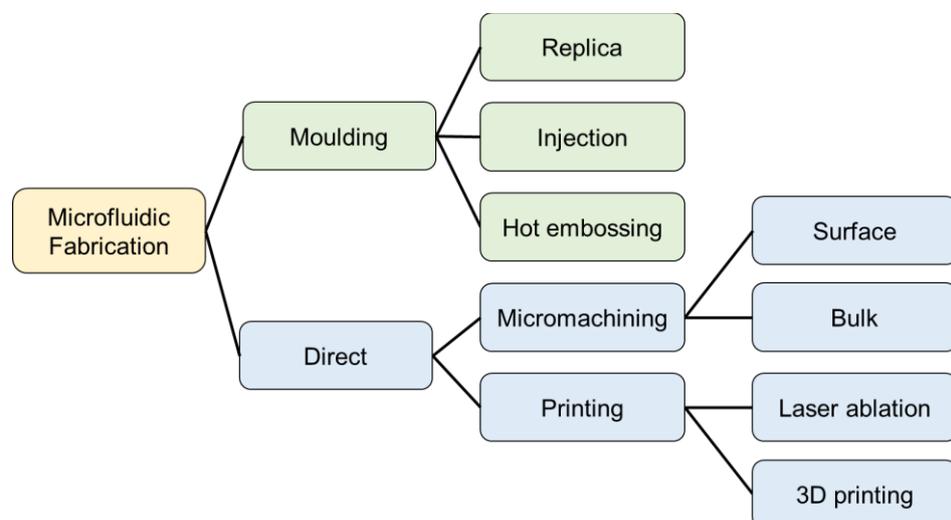
2092 4.2. Microfluidic Fabrication Techniques

2093 The most commonly used techniques for microfluidics fabrication can be grouped into two
 2094 categories: direct fabrication and moulding [206], [260] (see Figure 4.1). Further methods
 2095 have been employed for the fabrication of microfluidics devices but not included in this
 2096 discussion. Additional reading in [260], [261] is suggested for a more detailed review.

2097 **Direct fabrication.** Direct fabrication groups all the method used to manufacture
 2098 microfluidics directly on top of the substrate. There are two main techniques used for direct
 2099 fabrication, namely micromachining and printing.

2100 Surface micromachining refers to all the techniques allowing to fabricate microscale and
 2101 nanoscale structures by sequential deposition and removal of structural layers on a substrate.
 2102 Photolithography is probably the most commonly used method for micromachined
 2103 microfluidics [262]. Other lithographic technique, such as e-beam lithography, are also
 2104 commonly used [262]. Micromachined devices fabricated with the lithographic method are
 2105 generally referred to as surface micromachined. The use of photoresist is widespread for
 2106 surface micromachined devices [262]. SU-8 is probably the most commonly used photoresist
 2107 for surface micromachined microfluidic devices [260]. SU-8 is a common negative
 2108 photoresist performing high resolution, durability and capacity for high aspect ratio
 2109 structures [260]. Micromachined microfluidics device can also be fabricated using etching
 2110 techniques. This category of devices is usually referred to as bulk micromachined [257],
 2111 [263]. This fabrication usually involves etching steps aiming to remove material from a bulk
 2112 substrate, such as a silicon wafer [263].

2113



2114

2115

Figure 4.1 Main methods used for the manufacturing of microfluidic systems.

2116 Several materials can be used as substrates, including silicon [262], glass slides [262],
2117 polymers for micromachined devices [264]. The resolution of micromachined microfluidics
2118 depends on the technique used for its fabrication [260], [262], [263]. The fabrication of
2119 microfluidic structure with photolithography is typically in the order of a few micrometres.
2120 However, micromachined structures suffer the need for cleanroom facilities. Materials and
2121 methods employed for the fabrication of these devices are sometimes costly and time-
2122 consuming.

2123 Printed microfluidics refers to all the techniques allowing the direct deposition or removal
2124 of material from a substrate. Popular writing techniques include laser ablation and 3D
2125 printing [260]. Laser ablation is used for the direct removal of material from the substrate.
2126 Microfluidics devices fabricated by stacking independently cut layers bonded together are
2127 generally referred to as laminated devices [260]. A wide range of material has been used as
2128 a substrate for direct fabrication, including paper (for chromatography strips) [199], glass
2129 slides, polymers (e.g. PMMA, polycarbonate) and tapes [260]. In this category, the depth of
2130 the microfluidic channel can be tuned by controlled the thicknesses of the layers. The layers
2131 composing the laminated structure are typically bonded by thermal or adhesive bonding.
2132 Laminated devices offer several advantages, including rapid and straightforward process
2133 steps, no need for cleanroom facilities, low-cost, versatility and scalability [260]. The main
2134 disadvantages of this technique are the difficulty in aligning the individual layers and the
2135 lower resolution when compared to alternative methods [260]. Laser-cut laminated
2136 microfluidic devices typically offer a resolution of tens of micrometres [260]. Recently 3D
2137 printed microfluidic devices are also getting progressively popular thanks to their low-cost
2138 and rapid fabrication times [265]. Printing also usually does not require cleanroom facilities.

2139 **Moulding fabrication.** Moulding fabrication refers to all the method that can be used to
2140 manufacture microfluidics by mean of a mould. The mould can be fabricated in many ways,
2141 including all the methods illustrated for direct fabrication [260]. The resolution of the device
2142 usually depends on the technique adopted for mould fabrication [260]. Arguably,
2143 photolithography is the most commonly used method for mould fabrication. [260].

2144 Moulded devices can be further divided into three categories: replica moulding, injection
2145 moulding and hot embossing [260]. They all have an initial stage of mould manufacturing
2146 [260]. Microfluidic devices fabricated by replica moulding employ a liquid polymer to be
2147 poured into the mould and subsequently cured. The cured polymer is then peeled from the
2148 mould and bonded onto a glass slide or a substrate [260]. This process is also generally

2149 referred to as soft lithography [260]. Among the polymers employed for the fabrication of
2150 replica moulded devices, Polydimethylsiloxane (PDMS) is probably the most popular [260].
2151 PDMS is a polymer structure with the repeating monomer units of $\text{SiO}(\text{CH}_3)_2$. It exhibits
2152 some advantages with respect to other materials used for microfluidic (e.g. PMMA,
2153 Polycaprolactone) [257]. PDMS is transparent from 240 nm to 1100 nm, elastic, permeable
2154 to oxygen and easy to use and to manipulate. When freshly plasma-oxidised, it can be sealed
2155 to itself and other materials without any adhesive layer. Under the exposure to oxygen
2156 plasma, the methyl groups Si-CH_3 on PDMS surfaces are attacked by reactive oxygen
2157 radicals and substituted by unstable silanol groups Si-OH which can permanently attach to
2158 the ionic group on different plasma-oxidised substrates [266]. This property enables PDMS
2159 bonding directly on the target substrate without any intermediate adhesive layer. PDMS
2160 functionalisation techniques are also robust and well-known [214], [257], [267]–[273].
2161 Injection moulded microfluidic devices are fabricated by injecting a melted thermoplastic (
2162 liquid form) into the mould [260]. Usually two halves of the mould are used to create a cavity
2163 [260]. Once the thermoplastic is cooled, the cast is removed from the mould [260]. Similarly,
2164 in microfluidic devices fabricated using hot embossing moulding, a thermoplastic film is
2165 shaped onto the mould by applying pressure and heat [260].
2166 Moulded microfluidic devices share similar limitations to direct writing methods. Expensive
2167 and time-consuming methods might be required for the fabrication of the mould. However,
2168 moulding is more suitable for large scale production. The mould can be reused many times.
2169 Furthermore, the mould can also produce more than one pattern in the same processing steps.
2170 These advantages yield to time and costs reduction when producing a high number of
2171 devices. Evidence of this is shown by large scale use of moulding processing in commercial
2172 devices [260]. Direct writing techniques are instead typically used for prototyping or small
2173 scale production [260].
2174 The platform developed in this work is meant to be affordable and suitable for large scale
2175 production. Accordingly, a moulding process was adopted. A comparison between three
2176 widely adopted fabrication techniques for microfluidic systems (i.e. photolithography,
2177 printing and moulding) is shown in Table 4.2.
2178
2179
2180

2181 *Table 4.2 Comparison between widely adopted fabrication techniques for microfluidic*
 2182 *systems.*

	Photolithography	Printing	Moulding
Resolution	μm	tens of μm	Down to μm scale (depending on the technique used for the fabrication of the mould)
Time to manufacture	<ul style="list-style-type: none"> - From hours to days - Several fabrications steps - Cleanroom facility needed 	<ul style="list-style-type: none"> - From minutes to hours - Largely automatised - One device is fabricated at one time - No cleanroom facility needed 	<ul style="list-style-type: none"> - Minutes¹ - Several devices are fabricated at one time - Can be automatised - No cleanroom facility needed¹
Adaptability	<ul style="list-style-type: none"> - Wide range of substrates and structural materials - Channels have a rectangular cross-section 	<ul style="list-style-type: none"> - Wide range of substrates and structural materials - 3D structures - Highly customisable 	<ul style="list-style-type: none"> - Wide range of substrates and structural materials - Network topology depends on the technique used for the fabrication of the mould
Cost per device	High	Low	Low ²
Suitable for large scale production	No (expensive and slow process)	No (slow process, lower resolution)	Yes
¹ After mould fabrication ² When manufacturing a large number of devices			

2183

2184 **4.3. Microfluidic integration with CMOS technology**

2185 Integrated platforms are significantly complicated to implement [259]. Generally, printed
 2186 devices are very difficult to monolithically integrate due to alignment problems [260][263].
 2187 Recently, printing techniques have been used to print structural materials, such as SU-8, on
 2188 top of a CMOS device to achieve monolithic integration [274]. For instance, authors in [274]
 2189 demonstrated the integration of a CMOS device with microfluidics through direct writing.
 2190 In this work, an organic ink is firstly deposited on top of the CMOS chip [274].
 2191 Subsequently, an optically clear epoxy resin is used to encapsulate the ink filaments and the
 2192 CMOS device [274]. Finally, the ink filaments are extracted by applying heat and pressure,
 2193 leaving epoxy-based microchannels on top of the CMOS chip [274].

2194 Micromachined devices have higher integration capability compared to printing methods
 2195 [263]. A CMOS chip can be employed as a substrate and monolithically integrate the
 2196 fluidics on top of the device [263]. In [275], for instance, the authors demonstrate a CMOS
 2197 compatible microfluidic technology by integrating a microfluidic network on top of optical
 2198 biosensor devices. In [275], the microfluidics is integrated by using SU-8 in a

2199 photolithography process. A polymer slab is finally bonded onto the SU-8 microstructure to
2200 enclose the microchannel [275].

2201 Integration of microfluidic networks fabricated with moulding techniques has also been
2202 reported in the literature. Authors in [276], for instance, adopt soft lithography to integrate a
2203 CMOS chip and microfluidic in a flexible package.

2204 There are mainly three challenges to be addressed when integrating CMOS chip with
2205 microfluidics: size compatibility, process compatibility and economic considerations [203].

2206 **Size compatibility.** The CMOS chip price is proportional to its area, so designers usually
2207 try to minimise the area [277]. Although fluidic channels have a compatible size with CMOS
2208 elements, fluidic input/output (I/O) ports need to be large enough (in the order of hundreds
2209 of micrometres) to allow practical operation. Increasing the area of CMOS to accommodate
2210 fluidic I/O in the design phase is possible. However, this typically requires an additional area
2211 which yields to an increased cost of the chip. The increase of the cost cannot be acceptable
2212 with the respect to the affordability requirement. Furthermore, when the photoresist is
2213 applied by spin-coating on a millimetric area, surface tension creates an unwanted thicker
2214 ‘edge bead’ around the perimeter of the IC [259]. On millimetre-scale ICs, the bead can
2215 occupy the majority of the area and can pose a significant problem [259].

2216 Size compatibility can be addressed by planarization [203]. Planarization allows integrating
2217 the CMOS chip into a larger substrate. Typically, fluidic I/O are incorporated onto the larger
2218 substrate rather than onto the CMOS chip [203]. This technique has the potential to avoid
2219 increasing the area of the CMOS chip for microfluidic constraints which, in turn, would
2220 increase the cost of the CMOS chip. Notably, authors in [278]–[280] employ planarization
2221 before integrating the microfluidic network on top of the CMOS platform.

2222 **Process compatibility.** This includes the necessity of a set of processes which demand new
2223 practical solutions [203]. Chip packaging is probably the most prominent complication to
2224 be overcome [203]. CMOS chips are usually connected to a chip package to be operated,
2225 and flip-chip bonding and wire-bonding are probably the two most reliable techniques for
2226 metallic interconnections [203]. Interconnects also require insulation and encapsulation
2227 [203]. Unlike traditional electronic packaging, fluidic packaging has not been standardised
2228 by industry [259]. Thus, the approach to accommodate fluidics on CMOS is either to modify
2229 a pre-existing standard package or develop a custom package [259]. If wire-bonding is used
2230 for packaging, the fluidic network must avoid the bond-pads [259]. Consequently, the area
2231 the microfluidics network can occupy is largely decreased, and the geometry also

2232 constrained. Passivation of the wire-bonds can also be challenging in these conditions [259].
2233 Remarkably, authors overcome the problem of wire bonds and metal interconnects by using
2234 liquid metal interconnects [276]. Thus, in [276] microfluidics ensures both sample handling
2235 and electrical connections. However, the approach has practical limitations and not easily
2236 repeatable. Alternative techniques have also been adopted in literature, such as screen-
2237 printing and additive manufacturing [203].

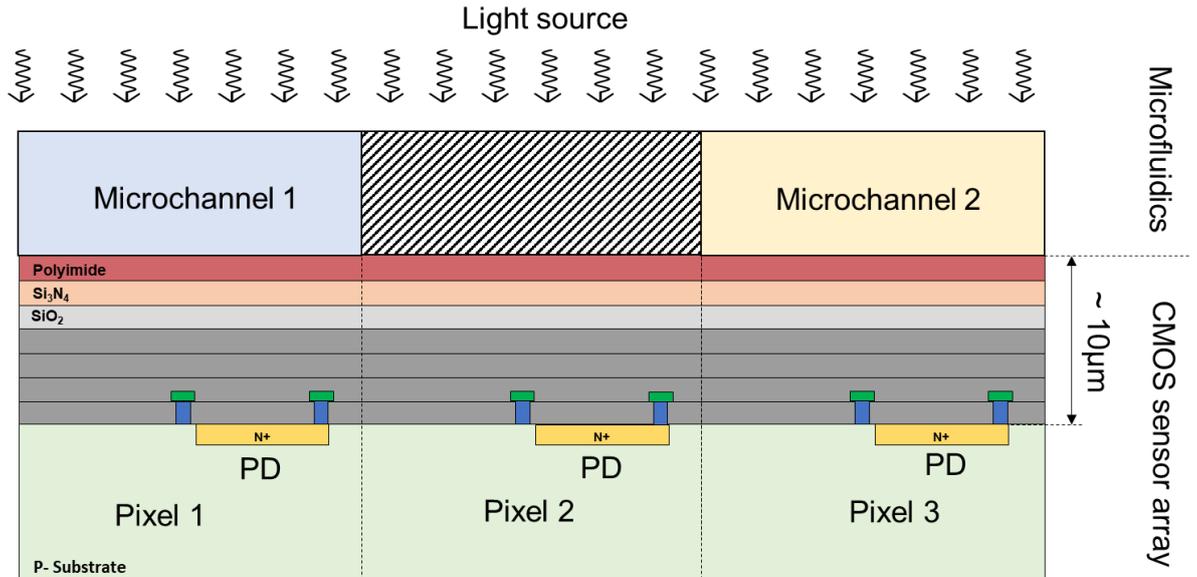
2238 Material selection also poses a challenge to be addressed. Employed materials must be inert
2239 during the biological reaction and must not interfere [259]. The development of a reliable
2240 sterilisation and cleaning method is also essential [259]. The use of materials such as PDMS
2241 and SU-8, which deteriorates over 200°C, reduces the maximum temperature to which the
2242 platform can be exposed [259]. Furthermore, the wettability of materials needs also to be
2243 considered for the optimal flow and reduction of the evaporation [259]. Further
2244 complications about process compatibility also come from the topology of the IC, the
2245 alignment and functionalisation [203], [259].

2246 **Economic considerations.** Microfluidics integration requires additional fabrication steps.
2247 However, CMOS-based microfluidic systems can be justified only when the production cost
2248 of the integrated system is low [203]. Consequently, this excludes several solutions which
2249 are not economically viable.

2250

2251 Monolithic integration with CMOS has the potential to minimise the crosstalk between
2252 adjacent channels for multi-analyte measurements [259]. However, it is worth noting that
2253 although microfluidics can be fabricated on top of CMOS chips, sensors are still separated
2254 by the microfluidic channels due to the presence of passivation layers (see Figure 4.2). The
2255 separation between a microchannel and sensor is typically in the order of 10µm. Therefore,
2256 for optical measurements (i.e. colorimetric detection) photons transmitted through the
2257 microfluidic channels need to pass through several material interfaces before reaching the
2258 sensor. Transmitted photons can experience reflection, diffraction, and resonance effects
2259 before reaching the sensor. These unwanted optical effects can be a source of noise and
2260 contribute to crosstalk between adjacent sensors. Adequate separation between different
2261 channels might be effective in reducing the crosstalk. Table 4.3 discusses some of the
2262 integration works reported in the literature, underlining materials and techniques employed.
2263 [257], [261], [281] are suggested for an extensive review on the field.

2264



2265

2266 *Figure 4.2 Diagram illustrating the separation between CMOS-based optical sensors and*
 2267 *microfluidic channels for colorimetric detection. Transmitted photons pass through several*
 2268 *layers of materials before reaching the sensor. This can cause unwanted optical effects,*
 2269 *leading to sensor-to-sensor crosstalk.*

2270

2271

Table 4.3 Integration of ICs with microfluidics.

Target Substrate	Channels	Intermediate layer	Distance ⁽¹⁾	Material	Technique	Ref.
CMOS chip	n.d.	Yes (ONO)	300 μm	SU-8, glass	Micromachining (planarization, photolithography)	[278]
IC and flexible PCB	n.d.	Yes (PDMS)	120 μm	glass	Micromachining (laser engrave)	[282]
CMOS and flexible PCB	4	Yes (Polyimide)	85 μm	PDMS	Replica moulding and adhesive bonding	[283]
CMOS chip	n.d.	Yes (photoresist)	1.8 μm	PMMA	Micromachining (planarization, laser engrave)	[279]
IC chip	1	No	0	PDMS	Replica moulding and plasma bonding	[284]
CMOS chip	1	No	0	Epoxy	Direct writing	[274]
CMOS chip	n.d.	No	0	SU-8	Micromachining (photolithography) and plasma bonding	[275]
CMOS chip	1	No	0	SU-8, PDMS	Micromachining (planarization, photolithography) and plasma bonding	[280]
CMOS chip	n.d.	No	0	PDMS	Replica moulding and encapsulation	[276]

⁽¹⁾ Distance between the sample and the external passivation layer of the IC.

2272 **4.4. Microfluidics Design**

2273 The process leading to the fabrication of microfluidic system can be divided into three
2274 stages: (i) design considerations, (ii) preliminary active microfluidics development and (iii)
2275 passive microfluidics development. The manufacturing has been subjected to a trial-and-
2276 error process for continuous optimisation and different stages of design, development, and
2277 testing.

2278

2279 **4.4.1. Design considerations**

2280 For the integration of microfluidics with the CMOS sensor array, several design
2281 specifications were considered.

2282 **Distance to the sensor array.** The microfluidics was required to be in direct contact with
2283 the sensor to avoid any additional signal path which can decrease the SNR. As anticipated
2284 in the introduction, this design strategy was chosen for two reasons: monolithic integration
2285 addresses the versatility requirement of the platform and eliminates any superfluous signal
2286 path, which can introduce additional noise [259].

2287 **Manufacture technique.** Soft lithography and micromachining were selected as
2288 employable technique. This choice was made mainly for three reasons: (i) availability of the
2289 bare chip to be processed, (ii) access to the cleanroom facility of the James Watt
2290 Nanofabrication Centre (JWNC) at the University of Glasgow, (iii) availability of well-
2291 established procedure for microfluidics fabrication in the literature. The selection of the
2292 manufacturing technique implicitly also contains the selection of the material to be
2293 employed, such as Polydimethylsiloxane (PDMS) and photoresists.

2294 **Number of fluidic channels.** The optimal number of channels was four, so that all the
2295 metabolomics marker identified for PCa can be simultaneously measured. The maximum
2296 number of microchannels which can realistically be manufactured is 16, with each column
2297 of the sensor array hosting a single microfluidic channel. Identical microchannel geometry
2298 was also required.

2299 **Geometry.** According to the selected manufacture technique, microchannels were
2300 developed with a rectangular section. Thus, designing parameters were microchannel width
2301 w , height h and length L . The active area exposed to the liquid is to be maximised to extract
2302 as much significant data as possible from the chip. However, the contact area between fluidic

2303 walls and chip also needs to be optimised to ensure proper adhesion. The maximisation of
2304 both active and contact areas are thus opposite design requirements.

2305 **Fluidic inputs and outputs (I/Os).** Ideally, the microfluidic network should have only one
2306 fluidic input and multiple fluidic outputs. For preliminary active microfluidics, I/Os were in
2307 the form of a hole where a needle was inserted. For passive microfluidics, a single sample
2308 input was required. Fluidic outputs for the passive microfluidics were in the form of an
2309 aperture/ventilation.

2310 **Constraints.** The chip required to be wire-bonded onto a chip package. The fluidics had to
2311 avoid areas dedicated to wires. Pads are 100 μm wide and located on the west and east sides
2312 of the chip. A tolerance gap of 200 μm was needed to ensure proper wire-bonding of the
2313 CMOS chip. The location of the pad limited the orientation of the microchannel that had to
2314 have its length L parallel to the north-south direction. Additionally, the wire-bonds required
2315 encapsulation to ensure electrical insulation and mechanical strength.

2316 Eventually, the process for the fabrication and integration of microfluidics on the CMOS
2317 chip had to consider real-life scenario constraints, including economic and usability
2318 considerations.

2319

2320 4.4.2. Preliminary active microfluidics

2321 The initial active microfluidics development aimed to (i) verify the suitability of the selected
2322 manufacture techniques; (ii) determine critical dimensions for the development of the
2323 passive microfluidics; (iii) develop knowledge and practical experience needed for the
2324 development of passive microfluidics.

2325 Twenty-four different networks with several channels ranging from 1 to 6 were designed
2326 with software Tanner L-Edit from Mentor Graphics, and fabricated using soft-lithography
2327 (see Figure 4.3). Networks had different microchannel width and different I/O
2328 configurations. A custom figure of merit (FoM) was identified for comparing various
2329 networks. The FoM was defined as the mathematical average between normalised active
2330 area (A_{act}), normalised contact area (A_{con}) and normalised liquid volume per channel (V_{chn}),
2331 according to the following equation:

$$\text{FoM} = \frac{1}{3} (A_{act} + A_{con} + V_{chn}) \quad (4.1)$$

2332 A_{act} represents the area exposed to the liquid sample normalised by the total active area; A_{act}
2333 represents the area covered by microfluidic walls therefore not exposed to the liquid sample

2334 normalised by the total active area; V_{chn} represent the volume of the channel normalised to
2335 the maximum achievable volume (i.e. the volume of a single channel covering the entire
2336 active area).

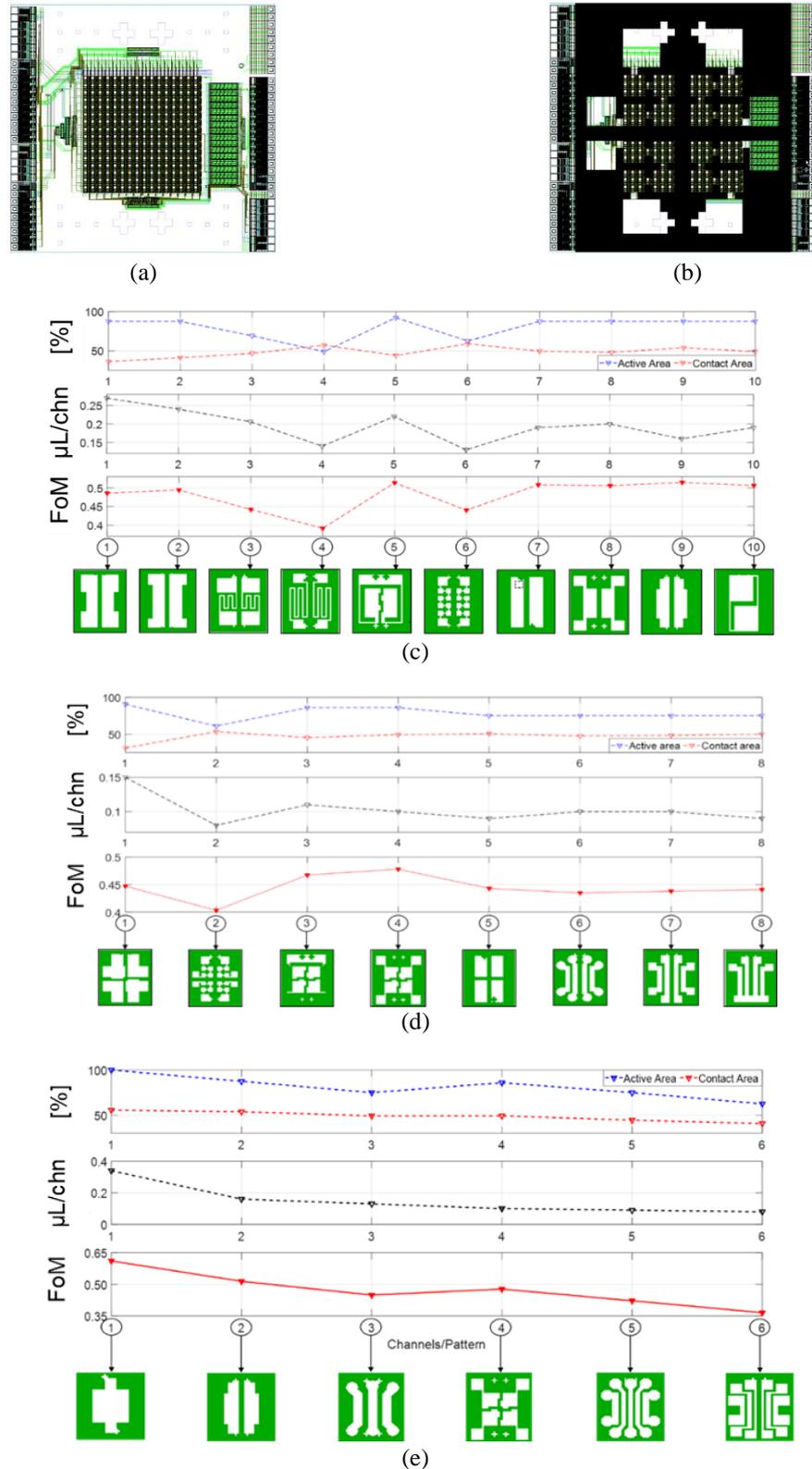
2337 The fabrication of the PDMS active microfluidics was performed at the JWNC. It employed
2338 a photolithographic process for the manufacturing of a mould and soft lithography for the
2339 manufacture of the PDMS structure. Figure 4.3(a)-(d) presents the full set of designs for 2
2340 and 4 channels networks. Figure 4.3(e) shows that by reducing the number of channels, the
2341 FoM gradually reduces meaning that bonding strength and employed sensing area are both
2342 reduced. The measurements of the moulds by contact profilometer (Veeco Dektak) and
2343 optical profiler confirmed that:

- 2344 • Channels were successfully patterned on the silicon wafer.
- 2345 • The achievable depth of the microchannels was approximately 130 μm when using a
2346 single layer of SU-8 onto a silicon wafer.
- 2347 • The profile of the mould was smooth and flat, particularly crucial for high bonding
2348 strength.

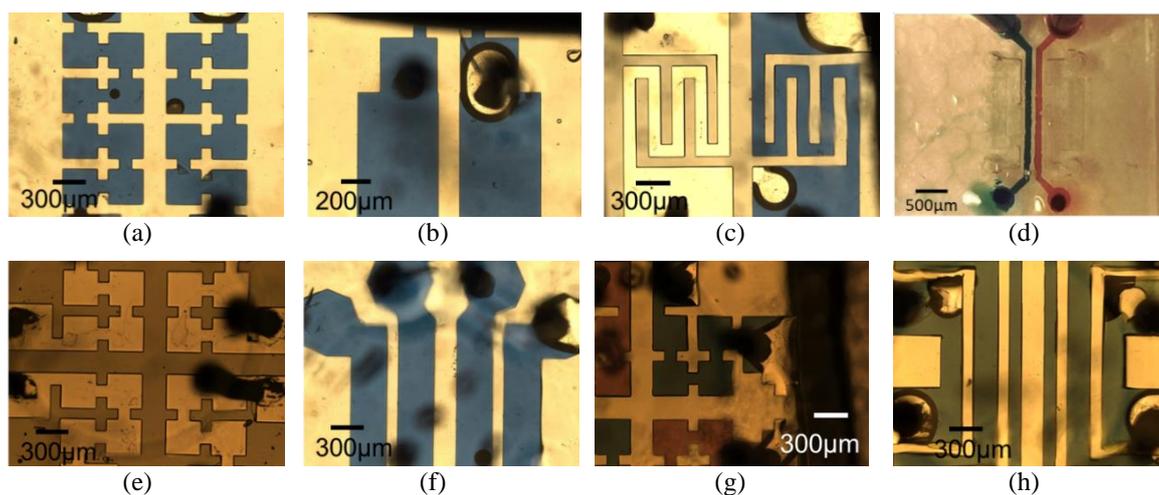
2349 For testing the flow in the microfluidic structures, PDMS structures were bonded to glass
2350 and silicon substrates. Testing structure bonded onto the glass substrate are reported in
2351 Figure 4.4. The flow in the whole set of designs was tested using coloured dyes to emulate
2352 the presence of samples. The entire collection of designs was successfully bonded to the
2353 substrate. The flow was forced into the channels with a syringe pump and a 300 μm needle.
2354 The whole set of designs performed physical separation of the flow without any detectable
2355 leakage.

2356 After testing on the glass slide, the PDMS structures were then flip-chip bonded onto the
2357 CMOS chip after exposure to oxygen plasma. PDMS active microfluidic structures bonded
2358 onto the CMOS are reported in Figure 4.5.

2359

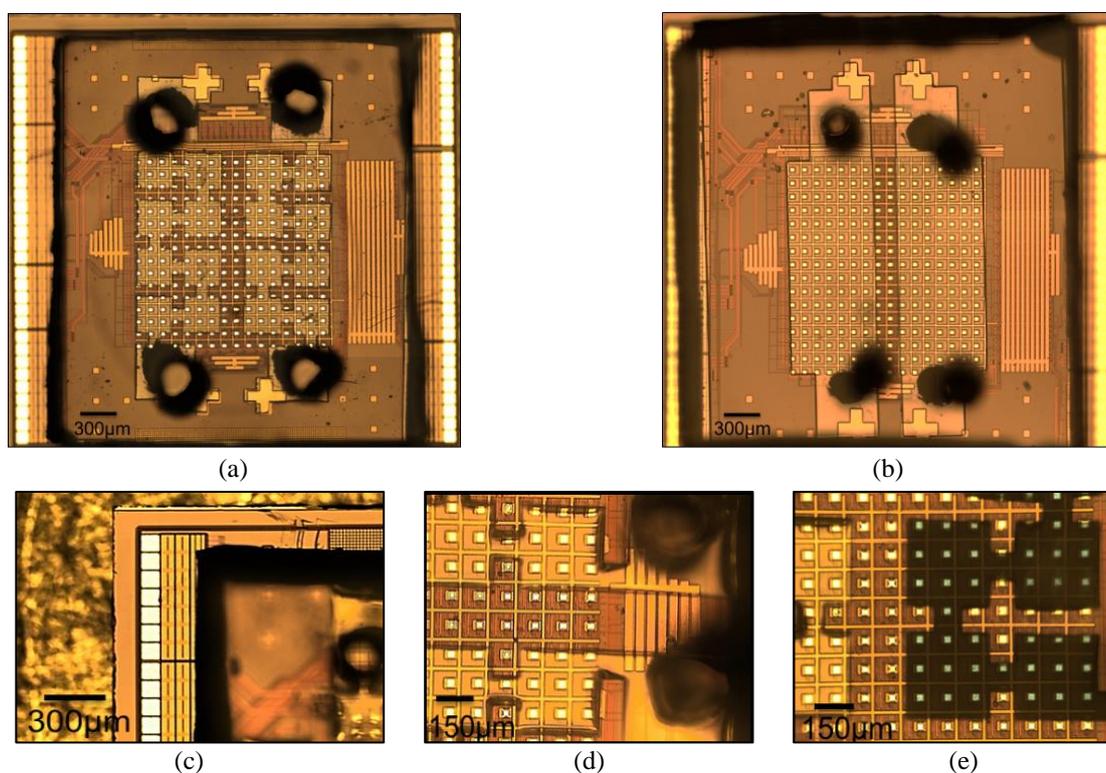


2360 *Figure 4.3 Design of an active microfluidic network by using the (a) CMOS CHIP layout*
 2361 *and (b) overlapping it with the fluidics 2nd four-channel layout (b) Comparison of all the 2-*
 2362 *channel active microfluidic networks designed and fabricated. (c) Comparison of all the 4-*
 2363 *channel active microfluidic networks designed and fabricated. (d) Comparison of the active*
 2364 *area, contact area, volume/channel and FoM for different active networks.*



2365 *Figure 4.4 Experimental results on solution confinement in PDMS active microchannels,*
 2366 *tested with blue and red dye. (a) 2 microchannels with microwells. (b) 2 straight*
 2367 *microchannels. (c) The 2-microchannel design was capable of confining solution in only one*
 2368 *channel. (d) Two parallel microchannels with 100 μm fluidic wall were enough to confine*
 2369 *two different solutions with no apparent leakage. (e) 4-channel active microfluidic network.*
 2370 *(f) 4-channel active microfluidic network with straight channels filled with testing dye. (g)*
 2371 *4-channel active microfluidic network was capable of confining different solutions. (h)*
 2372 *6-channel active microfluidic network with straight channels filled with testing dye.*

2373



2374 *Figure 4.5. (a), (b) Active microfluidic network with two microfluidic channels bonded onto*
 2375 *the CMOS chip. (c) Bonding pads are left exposed. (d) Detail of the fluidic I/O. (e) The liquid*
 2376 *was confined in the microfluidic channel also when bonded onto the CMOS chip.*

2377 The preliminary active microfluidics development and testing allowed to gather information
2378 relevant to the manufacture of the passive microstructure. Specifically:

- 2379 • Photolithography and soft lithography were able to produce microstructures with
2380 dimension suitable for the application.
- 2381 • 100 μm wide walls could provide physical separation of two parallel channels. The
2382 absence of crosstalk was preliminarily demonstrated by visual inspection when flowing
2383 two different dyes into two adjacent channels.
- 2384 • Active fluidic I/Os was not a viable solution. I/O management for the 4-channels network
2385 was difficult, for the 6-channels network was very challenging, due to their high density.
2386 Additionally, a syringe pump was required, which is not ideal in a real-life scenario.
2387 Another issue with external pumping also was the formation of air bubbles.
- 2388 • No capillary action was detected when the sample was introduced using vertical via
2389 holes. However, the capillary effect was observed when I/Os were on the side of the
2390 structure (the same plane of the substrate).
- 2391 • Microfluidics could have been extended on the north and south side of the CMOS chip
2392 using a planarization step.

2393

2394 **4.4.3. Passive Microfluidics**

2395 Although active fluidic was successful in confining multiple solutions on the CMOS chip,
2396 the use of syringes and pumps was not adequate for the application when considering real-
2397 life constraints. It was then necessary to adapt the active microfluidics to work passively.

2398 The main problem related to fluidic I/O management was the compatibility with the wire-
2399 bonds encapsulation. The encapsulation step was necessary for the proper functioning of the
2400 device. However, despite numerous approaches, the epoxy resin used in the encapsulation
2401 step kept leaking into the passive fluidics because of its capillary effect. After several
2402 attempts, it was decided to change the approach entirely and, instead, take advantage of this
2403 effect. Therefore, epoxy resin was used as structural material moulded by the PDMS
2404 microstructure. Besides being compatible with the chip packaging, the functionalisation of
2405 the epoxy resin also enables planarization without adding any processing step. The detailed
2406 procedure for the fabrication of passive microfluidics is reported in Paragraph 4.5.

2407 The maximisation of the capillary effect was achieved by optimising dimensions and
 2408 materials employed. Passive fluidics design was mainly based on theoretical equations,
 2409 already discussed in the chapter, and reported here again for convenience:

$$\Delta p = \gamma \left(\frac{\cos\Theta_b + \cos\Theta_t}{h} + \frac{2\cos\Theta_s}{w} \right) = R_h Q = \frac{12\eta L}{\left\{1 - 0.63\left(\frac{h}{w}\right)\right\}h^3 w} Q \quad (4.2)$$

$$l(t) = h \sqrt{\frac{\Delta p}{6\eta L} \left(1 - 0.63 \frac{h}{w}\right) t} \quad (4.3)$$

2410 Where Δp is the pressure gradient, Θ denotes the contact angle of the different materials
 2411 employed, γ the surface tension, h and w denote the height and the width of the channel, R_h
 2412 is the hydraulic resistance ($\text{kg/m}^4\text{s}$), Q is the flow rate (m^3/s), η is the dynamic viscosity of
 2413 the fluid, L is the total length of the channel, $l(t)$ defines the position of the advancing
 2414 meniscus in the channel.

2415 Equations (4.2) and (4.3) highlight that there are three main aspects to be evaluated, namely
 2416 (i) liquid properties, (ii) geometry of the network, (iii) materials adopted.

2417 **Liquid properties.** The two main parameters of interest are dynamic viscosity (η) and
 2418 surface tension (γ) of the liquid sample. The platform is meant to work with blood or
 2419 processed blood, such as plasma or serum. Blood and derived human samples have different
 2420 fluidic characteristics. Fluidic characteristics relevant to the present work have been
 2421 summarised in Table 4.4

2422 **Geometry of the microchannel.** When designing a single straight microchannel with
 2423 rectangular cross-section, there are mainly three parameters to be considered, i.e. width w ,
 2424 height h , and length L of the channel. The minimum width w of the channel can be set to
 2425 correspond to the pixel size of the CMOS chip: $100 \mu\text{m}$. The maximum channel width
 2426 depends on how many channels are laid on the top of the sensor array. According to the
 2427 proposed application where multiple metabolites are meant to be measured simultaneously,
 2428 a fluidic network containing four identical channels is adequate for this work. In this case,
 2429 the maximum width for a microfluidic channel was $300 \mu\text{m}$. Minimum width of $w = 100 \mu\text{m}$
 2430 was dedicated to fluidics wall on the sensing area. According to the Beer-Lambert law, it is
 2431 essential to maximise the height h of the microchannel. But increasing h yields to a reduction
 2432 of the capillary pressure, as reported in Equation (4.2). h is also linked to w since a structure
 2433 with high aspect ratio could easily collapse. A target height between $100 \mu\text{m}$ and $300 \mu\text{m}$
 2434 was thus chosen to keep the height to width ratio (h/w) below 3. As previously mentioned,
 2435 the area of the CMOS chip is $3.6 \times 3.4 \text{ mm}$, and the pads are $100 \mu\text{m}$ wide and located on the

2436 west and east sides of the chip. A tolerance gap of 200 μm was adopted in accordance with
2437 the tolerances of the wire-bonding equipment used. Thus, the maximum width of the entire
2438 microfluidic network was set to 2.9 mm. The minimum length L of the microchannel is the
2439 length of the active area, i.e. 1.6 mm. Thanks to planarization techniques, the length of the
2440 microchannel can be increased (in the north and south side of the chip). A great extension of
2441 the length of the channel, however, is undesirable since it would cause an increase in fluidic
2442 resistance and a decrease of the flow rate in turn. The length of the microchannel was thus
2443 set to 4 mm. The microchannel covered the CMOS chip completely (3.4 mm) with 0.3 mm
2444 tolerance on each side for convenient handling of the sample.

2445 **Materials.** Aiming to maximise the capillary pressure reported in Equation (4.2),
2446 hydrophobic and hydrophilic materials can both be employed, as long as their contact angle
2447 is as far as possible from 90° . A custom setup for contact angle measurements was utilised
2448 for estimating the wettability of untreated PDMS, PVA-modified PDMS according to the
2449 recipe in [285], epoxy resin and the CMOS chip. Measured and assumed contact angles
2450 values used for the simulations are reported in Table 4.4. Appendix E describes the
2451 procedure for contact angle measurements.

2452 **Simulations.** Designing equations, fluid properties, geometric constraints and wettability
2453 properties of the adopted materials have been used to simulate the behaviour of fluidic
2454 structures and to verify capillary action. Simulations analysed the behaviour of the
2455 microstructure when using different specimens (i.e. water, serum, plasma, blood), and when
2456 modifying its width, height, and top contact angle. The custom Matlab model developed to
2457 simulate the capillary effect in a single channel with a rectangular section together with a
2458 more detailed description of the results is reported in Appendix F. Simulations indicated that
2459 a microfluidic channel manufactured with $w = 300 \mu\text{m}$, $h = 300 \mu\text{m}$, $L = 4 \text{ mm}$, $\theta_b = 78.2^\circ$,
2460 $\theta_s = 98.4^\circ$, and $\theta_t = 32.5^\circ$ minimised the time required for the liquid to cover the sensing area
2461 entirely. In these conditions, the estimated time required for water, serum, plasma, and blood
2462 to reach and cover the sensing area are 1.7s, 10.6s, 18.1s, and 23.3s, respectively. Figure 4.6
2463 provides a comparison of flowing simulations for different liquids into the optimised
2464 structure.

2465

2466

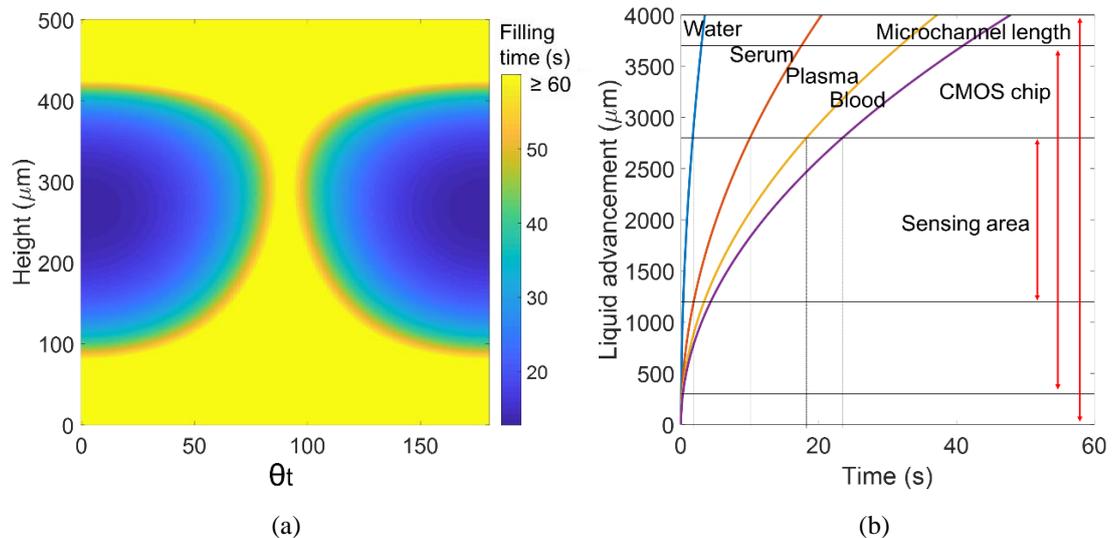
2467

2468

2469

Table 4.4 Simulation parameters.

Fluid Properties		
Liquid	Dynamic Viscosity (η) [mPa/s]	Surface tension (γ) [N/m]
Water	0.84 [286]	0.073 [286]
Serum	1.4 [287]	0.050 [288]
Plasma	1.7 [287]	0.045 [288]
Whole Blood	2.4 [287]	0.056 [289]
Geometry constraints		
Variable	Min	Max
w	100 μm	300 μm (4-channel network)
h	\downarrow to increase Δp	\uparrow to increase absorbance
L	1.6 mm (active area)	none
Materials		
Material	Static water contact angle	Behaviour
PDMS (θ_t)	100° - 110° [285] 107° (measured)	Slightly hydrophobic
Plasma treated PDMS (θ_t)	< 10° (temporarily) [285]	Super hydrophilic
PVA-coated PDMS (θ_t)	20° - 40° (permanent) [285] 32.5° (measured)	Hydrophilic
Epoxy resin (θ_s)	75°-100° [290] 98.4° (measured)	Slightly hydrophobic/hydrophilic
CMOS Chip (θ_b)	78.2° (measured)	Slightly hydrophilic



2470

2471 Figure 4.6 (a) Time required for the sample to cover the sensing area (i.e. filling time)
 2472 against microchannel height and top contact angle, assuming blood flow. Other simulation
 2473 parameters: $w = 300 \mu\text{m}$, $\theta_s = 98.4^\circ$, $\theta_b = 78.2^\circ$, $L = 4 \text{ mm}$. (b) Simulations of water, serum,
 2474 plasma, and blood flowing into the optimised microstructure.

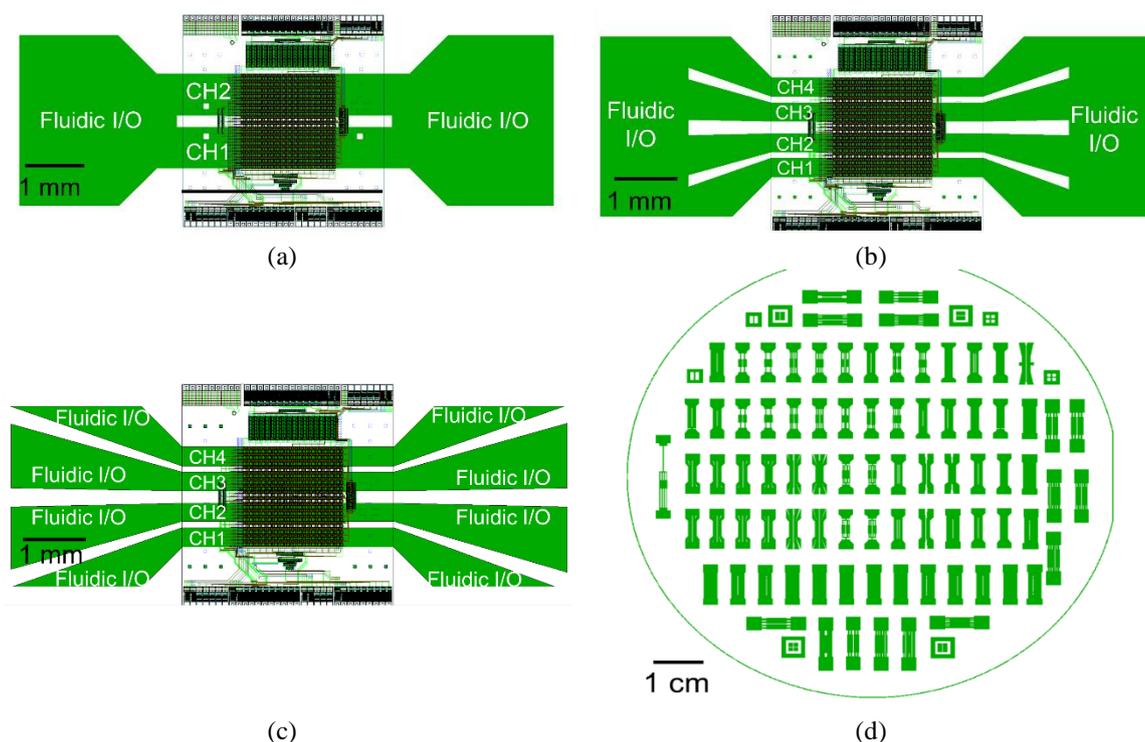
2475

2476 **Fluidic Input/output.** Having identified the optimised geometry, fluidic I/Os were defined.
 2477 Experimental studies on the active microfluidics demonstrated that capillary effect was
 2478 observed only when the fluidic I/Os of the network were on the same plane of the
 2479 microchannel. No capillary action was observed when fluidic I/Os were fabricated in the

2480 form of holes running perpendicularly to the plane of the microchannel. Fluidic I/Os were
 2481 located on the north and south side of the chip, on the epoxy planarized area and designed
 2482 as microwells, to which microchannels were connected. Besides the numerically optimised
 2483 microchannels, several passive microfluidic patterns were designed and fabricated with
 2484 channels ranging from 2 to 16 and different configurations for fluidic I/O. The design of the
 2485 passive patterns was also performed using the Tanner L-EDIT tool from Mentor Graphics.
 2486 Among all produced patterns, the most successful designs are the ones reported in Figure
 2487 4.7. It must be highlighted that the length L of the microchannel corresponds to the length
 2488 of the PVA-modified PDMS slab to be bonded onto the epoxy structure. The designs
 2489 reported in Figure 4.7(a) and (b) have a single common input and a common output.
 2490 Differently, the design in Figure 4.7(c) has independent fluidic I/O. The designed photomask
 2491 for passive microfluidics, shown in Figure 4.7(d), included a multitude of patterns to be
 2492 manufactured altogether onto a 4 inches silicon wafer.

2493

2494



2495 *Figure 4.7. Designs of (a) passive 2-channel network, and (b), (c) passive 4-channel*
 2496 *networks. (d) The photomask designed for the fabrication of passive microfluidics included*
 2497 *many patterns with different configurations.*

2498

2499 **4.5. Microfluidics Fabrication**

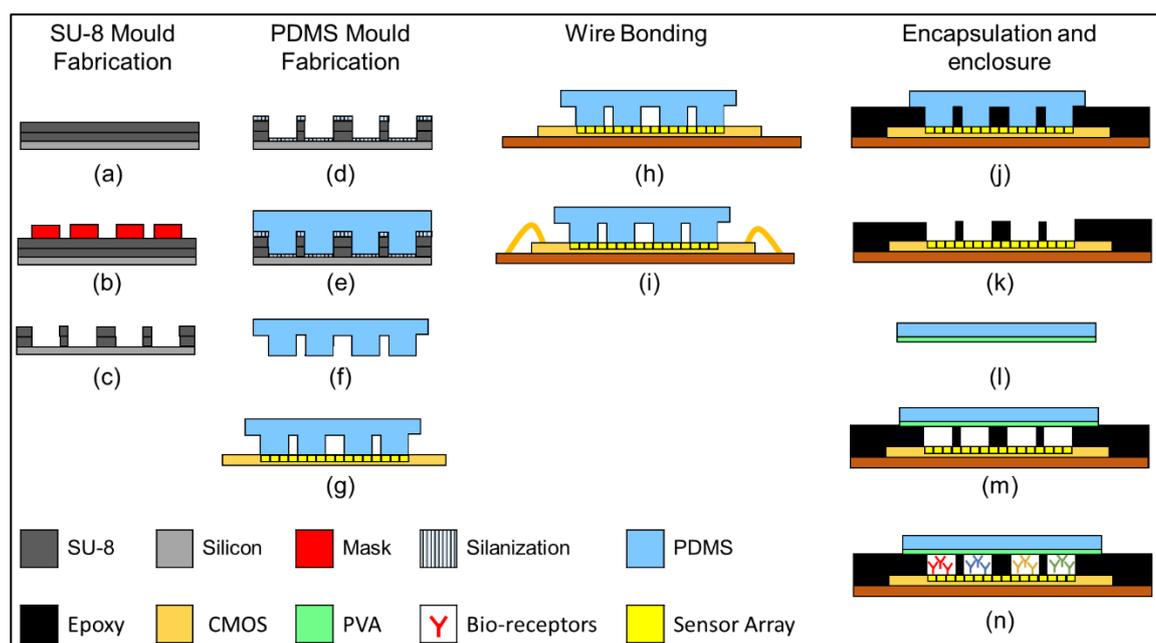
2500 The development of the microfluidics on top of the CMOS chip was achieved with the
2501 combination of replica and injection moulding. The integration was carried out through the
2502 following processing stages: (i) SU-8 mould fabrication, (ii) PDMS mould fabrication, (iii)
2503 wire-bonding, (iv) epoxy encapsulation, and (v) channel enclosure.

2504 First, a PDMS microstructure was fabricated from a SU-8 mould through replica moulding.
2505 The PDMS microstructure was then temporarily bonded onto the CMOS chip. CMOS chip
2506 and PDMS structure were subsequently bonded onto the chip package, and the CMOS chip
2507 was wire bonded. Next, the wire-bonded microstructure was encapsulated with black
2508 biomedical epoxy. The liquid epoxy, on the one hand, encapsulated the wire-bonds, and, on
2509 the other hand, filled the microchannels provided by the PDMS microstructure. Once cured,
2510 the PDMS microstructure was removed, leaving the epoxy microchannels exposed. Epoxy
2511 microchannels were sealed with a planar slab of PVA-coated PDMS.

2512 The recipe was modified over time to increase the height of the microfluidic channel. In
2513 early attempts, a single SU-8 layer was spun onto the silicon wafer, resulting in a
2514 microchannel with an approximate expected height of 130 μm [291]. A double SU-8 layer
2515 was therefore adopted to bring the expected microchannel height to 260 μm [291].
2516 Throughout the present work, it is clearly stated if the recipe employed a single or double
2517 SU-8 layer. The main process steps leading to the integration of the microfluidics on-chip
2518 are discussed in the next sub-sections and summarised in Figure 4.8.

2519 **SU-8 mould fabrication.** The fabrication of the SU-8 mould was performed using a
2520 photolithographic process in the JWNC, University of Glasgow. A silicon wafer was cleaned
2521 with standard procedures, soaking it while sonicated in the following succession of solvents:
2522 isopropyl alcohol (IPA), acetone, and finally deionised (DI) water for rinsing. A 10-minute
2523 dehydration step at 90°C in a convection oven under standard atmosphere followed, and
2524 immediately before spinning the sample was oxidised under oxygen plasma for 2 minutes in
2525 an ET340 PlasmaFab oxygen barrel asher with an RF power of 120W. Plasma exposure just
2526 before spinning was effective in providing a more uniform photoresist coat. The photoresist
2527 adopted in this work is the negative resist SU-8 3050. For a negative photoresist, the area of
2528 the photoresist exposed to UV light becomes insoluble to the developer. The selected is
2529 widely used for MEMS fabrication and is suitable for applications in which high film
2530 thickness is needed [291].

2531



2532

2533 *Figure 4.8 (a) Spin-coating of SU-8 3050 onto a silicon wafer. (b) Photolithography process.*
 2534 *(c) Development and final SU-8 microstructure. (d) Silanisation of the surface of the mould.*
 2535 *(e) Cast of PDMS onto the mould. (f) Curing of PDMS and removal of the mould. (g)*
 2536 *Temporary bond of the PDMS microstructure onto the CMOS chip. (h) Permanent mounting*
 2537 *of the chip on the chip package. (i) Wire-bonding of the chip. (j) Fabrication of epoxy*
 2538 *channels through injection moulding, with epoxy also encapsulating the wire bonds. (k)*
 2539 *Removal of the PDMS microstructure. (l) PVA-coating of a PDMS slab. (m) Bonding of the*
 2540 *PVA-coated PDMS slab onto the epoxy microstructure. (n) Loading of the bioreceptors into*
 2541 *the microchannels.*

2542

2543 SU-8 3050 was spin-coated on the wafer for 30s at 1000 rpm and sequentially baked for
 2544 1min at 65°C, 90min at 90°C and 1min at 65°C on a vacuum hotplate. A second SU-8 3050
 2545 was spin-coated and baked with the same recipe on the top of the first SU-8 layer. The second
 2546 layer aims to increase the total height of the SU-8 film. A slower spin speed (e.g. 500 rpm)
 2547 resulted in an unacceptably non-uniform surface, and therefore this option was excluded.
 2548 Subsequently, the substrate with the double SU-8 layer was exposed twice to UV using a
 2549 Karl Suss MA6 photolithography mask aligner for 70s each time. A 15s wait time between
 2550 the two exposures was used to avoid overheating of the photoresist. The sample and the
 2551 photomask were in hard contact. After the exposure, the sample was baked for 2min at 65°C,
 2552 10min at 90°C and 2min at 65°C on a vacuum hotplate. Following exposure, the pattern was
 2553 developed using EC solvent (development time 28 min) and rinsed with IPA. The mould
 2554 fabrication is concluded by hard baking the wafer for 30min at 180°C in a convection oven
 2555 under standard atmosphere.

2556 **PDMS mould fabrication.** The SU-8 mould was silanised by exposure for 30 mins to
2557 Trichloro (1H,1H,2H,2H-perfluorooctyl) silane into a vacuum chamber. The silanisation
2558 process aided with the subsequent removal of PDMS from the mould itself. The wafer was
2559 subsequently placed into a petri dish, and 25 g of a mixture of PDMS and curing agent (1:14
2560 weight ratio) was poured onto the mould and degassed for 1 hour into a vacuum chamber to
2561 remove air bubbles. The process continued with PDMS curing by baking the sample for 2h
2562 at 70°C. When cured, the PDMS was released from the SU-8 mould, placed on a clean
2563 substrate, and cut with a sharp knife. The PDMS mould was then temporarily bonded to the
2564 CMOS chip using a flip-chip bonder.

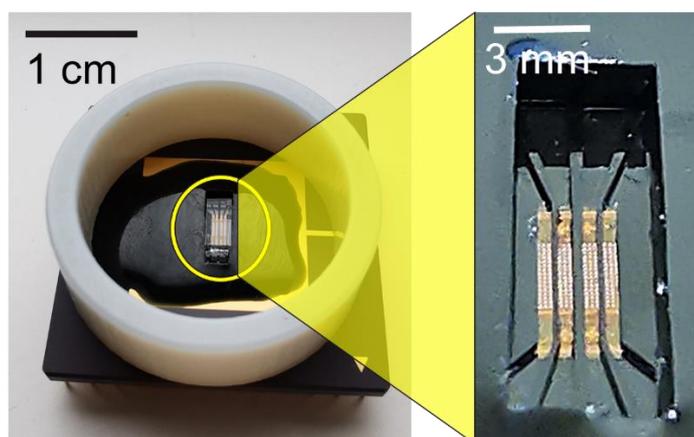
2565 Flip-chip bonding was performed in the cleanroom facility of the JWNC using the ‘flip-chip
2566 placement system model 850’ by Semiconductor Equipment Corporation. For flip-chip
2567 bonding, the CMOS chip was placed on the movable stage of the tool and held in place by a
2568 vacuum system. The PDMS mould was flipped and secured by a vacuum system to the tip
2569 of the bonder, located above the stage. A movable camera, together with a beam splitter,
2570 situated between the stage and the tip, provided the user with an overlapped picture of both
2571 the substrates to be bonded. Light intensity, focus and other optical parameters were tuned
2572 to improve the quality of the provided image. The stage was moved in the x, y and z
2573 directions to align the CMOS chip with the PDMS mould. The alignment marks on both the
2574 chip and the PDMS microstructure enabled alignment with a tolerance of tens of μm that is
2575 negligible for this work. Once the alignment was achieved, the camera was removed, and
2576 the tip was brought in contact with the stage. The bonding strength was increased by heating
2577 both the stage and the tip for 10min at 90°C under a constant pressure of 5 psi. Subsequently,
2578 the vacuum systems were disabled, and the tip raised, leaving the chip and the flipped mould
2579 structure bonded together. The PDMS was not exposed to any plasma, and there was no
2580 adhesive coating on the CMOS chip. Thus, the bonding was only temporary, and the PDMS
2581 mould could be easily peeled off from the chip. The use of PDMS in a weight ratio of 1:14
2582 with the curing agent showed better adherence to the CMOS chip with respect to the more
2583 commonly used 1:10 ratio [292].

2584 **Wire bonding and packaging.** The CMOS chip with the PDMS microstructure was bonded
2585 to a ceramic pin grid array (CPGA) package with 120 pins purchased from Europractice
2586 [293]. This was achieved by using the EPO-TEK H74 epoxy from Epoxy Technology Inc
2587 [294]. The overall size of the selected CPGA package was 3.3x3.3 cm, with an 8.3x8.3 mm
2588 cavity accommodating the structure to be wire-bonded.

2589 Wire bonding was performed in the cleanroom facility of Glasgow Laboratory for Advanced
2590 Detector Development (School of Physics and Astronomy, University of Glasgow) using the
2591 Hesse and Knipps Bondjet 710). The detailed procedure for wire bonding and packing has
2592 been reported in Appendix G.

2593 **Epoxy microfluidics.** The microchannels fabrication was performed using injection
2594 moulding. Initially, a mixture of black epoxy resin (302-3M 1LB by Epoxy Technology Inc.)
2595 and curing agent (weight ratio 1: 45) was flown into the PDMS microstructure [295]. Epoxy
2596 was also used for the encapsulation of the wire bonds. It provided both mechanical strength
2597 and electrical insulation to the device. The epoxy resin was then cured for 48 hours at room
2598 temperature. After curing, the PDMS structure was removed from the CMOS chip. As
2599 previously mentioned, the geometry of the wire bonding diagram allowed taking advantage
2600 of the absence of wire bonds at the north and south side by extending the microchannels in
2601 those directions. Once cured, the epoxy planarized the surface and created more available
2602 space for sample handling and delivery. For PVA-coating and channel enclosure, a plain
2603 slab of PDMS was cut with a sharp knife (5mm x 3mm), cleaned and exposed to oxygen
2604 plasma for 1min at 80 W in an ET340 PlasmaFab oxygen barrel asher. After the plasma
2605 oxidation, PDMS was immersed in the PVA solution (1 wt%) [285]. The PVA-modified
2606 PDMS slab can be permanently bonded to the epoxy microstructure by plasma activation.
2607 For the PDMS permanent bond, both PDMS and epoxy microchannel were exposed to O₂
2608 plasma at 80W for 45s and baked after being brought in contact for 15 min at 90°C. A figure
2609 of the cartridge at this stage is reported in Figure 4.9.

2610



2611

2612 *Figure 4.9 Cartridge with four microchannels on top of the CMOS chip (left) and close-up*
2613 *of the cartridge (right). The top PDMS lid on the right figure was removed.*

2614

2615 **4.6. Microchannel Functionalisation**

2616 As introduced in Chapter 2, there are many ways of coupling a biorecognition element
2617 together with a sensor for biosensing purposes. In this work, two different approaches were
2618 adopted, namely off-chip mixing and lyophilisation. Off-chip mixing was utilised for
2619 multiple independent assays on the same metabolite. Lyophilisation was used for
2620 multiplexed assays. The reasons leading to this approach are discussed here.

2621 Off-chip mixing means that the bioreagents in the liquid state are mixed with the sample
2622 immediately before performing the test. Thus, both sample and bioreagents are introduced
2623 in the system at the same time. This approach is commonly used in both experimental and
2624 commercial POC devices currently available [296]. There are two major drawbacks for this
2625 method: firstly, off-chip processing is acceptable for in-laboratory based POC devices, but
2626 should be minimised for in-home POC platforms; secondly, since the passive microfluidics
2627 network has only one fluidic input, the same mixture flows in all the identical channels.
2628 Thus, this method is suitable for simultaneously repeated measurements but does not support
2629 analyte multiplexing.

2630 Both limitations can be overcome with lyophilisation. Among the different techniques
2631 available for receptors integration, lyophilisation has been selected because it is versatile,
2632 well-demonstrated and potentially suitable for mass production. Freeze-drying can improve
2633 the stability of the biological sample over temperature, pH and time. When freeze-dried
2634 inside the microfluidic channels, the bioreceptor is confined, trapped in a solid and dry state
2635 into the microstructure. The reagents are then re-hydrated by the sample itself once
2636 introduced. In this project, enzymatic solutions were deposited into the microchannel. The
2637 deposition was performed by pipetting (when the dimension of the microchannel was large
2638 enough) or by drop-on-demand inkjet printing using the Jetlab II by Microfab. The sample
2639 was then lyophilised using the Lyotrap by LTE scientific. The procedure mentioned above
2640 has been performed on both open and enclosed channels, i.e. both before and after the PDMS
2641 bonding to enclose the channels. Quicker freeze-drying was recorded when the reagents were
2642 loaded before the enclosure of the channels. However, since the chip was routinely re-used,
2643 the bio-reactive solutions were also introduced after the channel enclosure using syringes.
2644 Freeze drying of reagents in enclosed channels proved to be just as effective as the same
2645 process on open channels since the same set of results was produced on both cases.
2646 Bioreceptors lyophilisation overcomes the limitation of off-chip mixing. Reagents are

2647 already available on-chip. Thus, no additional sample pre-processing step is needed.
2648 Additionally, a different reaction mix can be deposited/inserted into the different
2649 microchannel, and multiplexed assays can be simultaneously performed. However, there
2650 was a drawback of lyophilisation: the CMOS chip became unresponsive after 3 – 4 freeze-
2651 drying cycles, probably because of the thermal and mechanical shock. This is not a problem
2652 for a CMOS-based disposable cartridge. However, in this project, the number of chips and
2653 resources were limited, and it was not possible to use such a large amount of CMOS chips.
2654 Thus, as initially mentioned, off-chip mixing was adopted for multiple independent assays
2655 on the same metabolite. Lyophilisation was instead used for multiplexed assays. A detailed
2656 description of the printing and lyophilisation of bioreceptor is provided in Chapter 5.

2657

2658 **4.7. Fabrication Results**

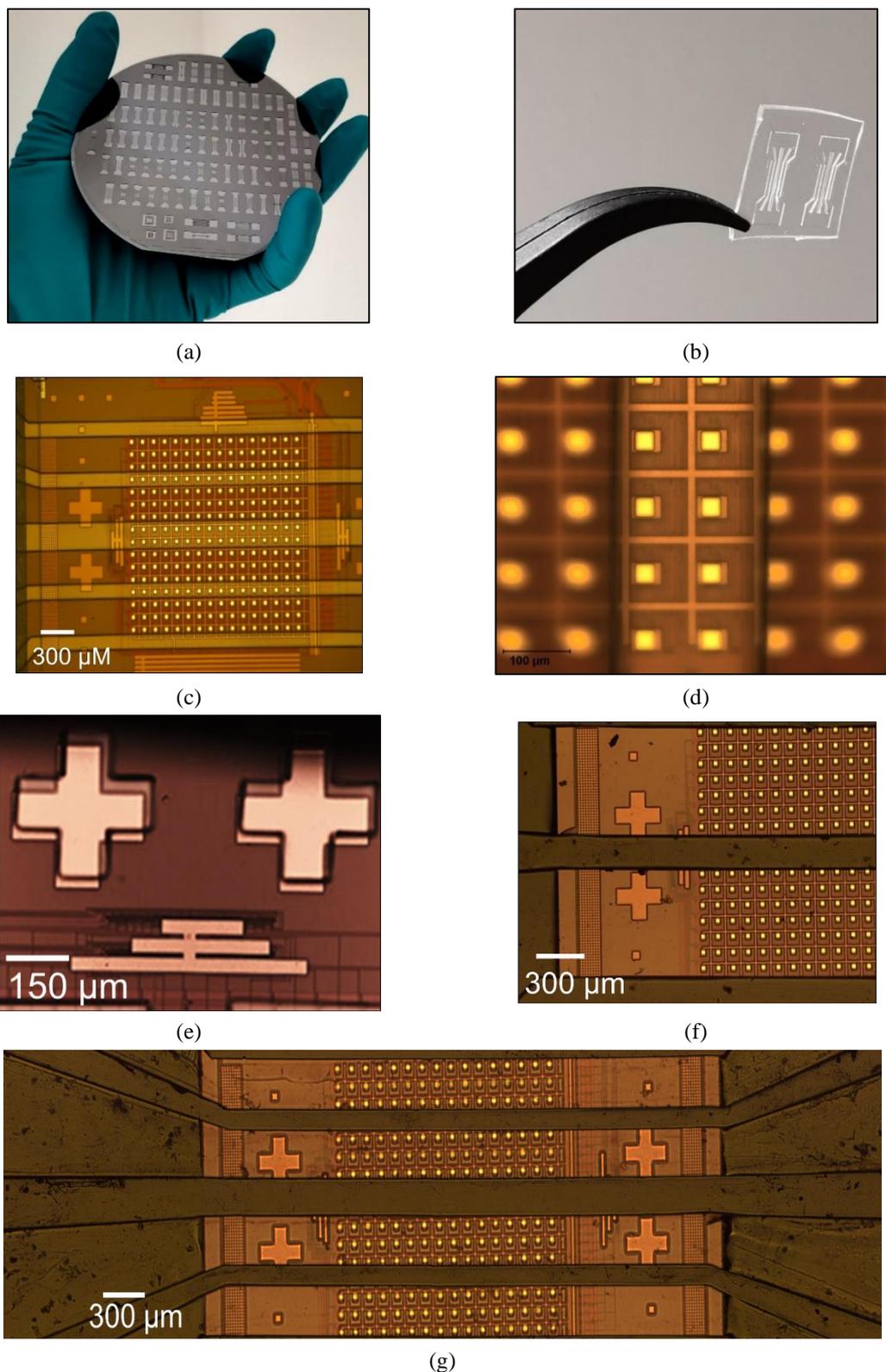
2659 Figure 4.10 demonstrates the main manufacturing steps of the cartridge. A set of SU-8
2660 patterns were fabricated altogether on a silicon wafer, as shown in Figure 4.10(a). The height
2661 of the microchannel was related to the SU-8 layer thickness. The SU-8 microstructures were
2662 used as a mould for the fabrication of PDMS microstructures. PDMS microstructures were
2663 then temporarily bonded on top of the CMOS chip. The misalignment of the flip-chip
2664 bonding process, evaluated over three different samples, was estimated to be, on average,
2665 less than 50 μm on both the axis, an example is shown in Figure 4.10(e). The misalignment
2666 did not appear to be systematic and therefore could not be compensated. However, the
2667 precision of the method adopted was suitable for the feature size of interest and did not affect
2668 the proper functioning of the device. Consequently, epoxy resin was flown into the PDMS
2669 structure, which was subsequently removed, leaving the epoxy microstructure on the CMOS
2670 chip, forming the microchannels as originally fabricated on the SU-8 resist layer. As shown
2671 in Figure 4.10(f) and (g), the adopted manufacturing method allowed to effectively fabricate
2672 a relatively planar microstructure surface and provided an additional off-chip area for fluidic
2673 inputs and outputs, forming a uniform rigid structure that encapsulated the CMOS chip. The
2674 final step was to cover microchannels with a flat PDMS lid, cut to measure, and create
2675 microfluidic channels on-chip.

2676 Figure 4.11(a) quantifies the flatness degree for the planarized surface. Measurements were
2677 performed in the cleanroom facility of the JWNC, University of Glasgow, using the Contour
2678 GT-X 3D Optical Profiler by Bruker. The top PDMS lid of the microfluidic channels had

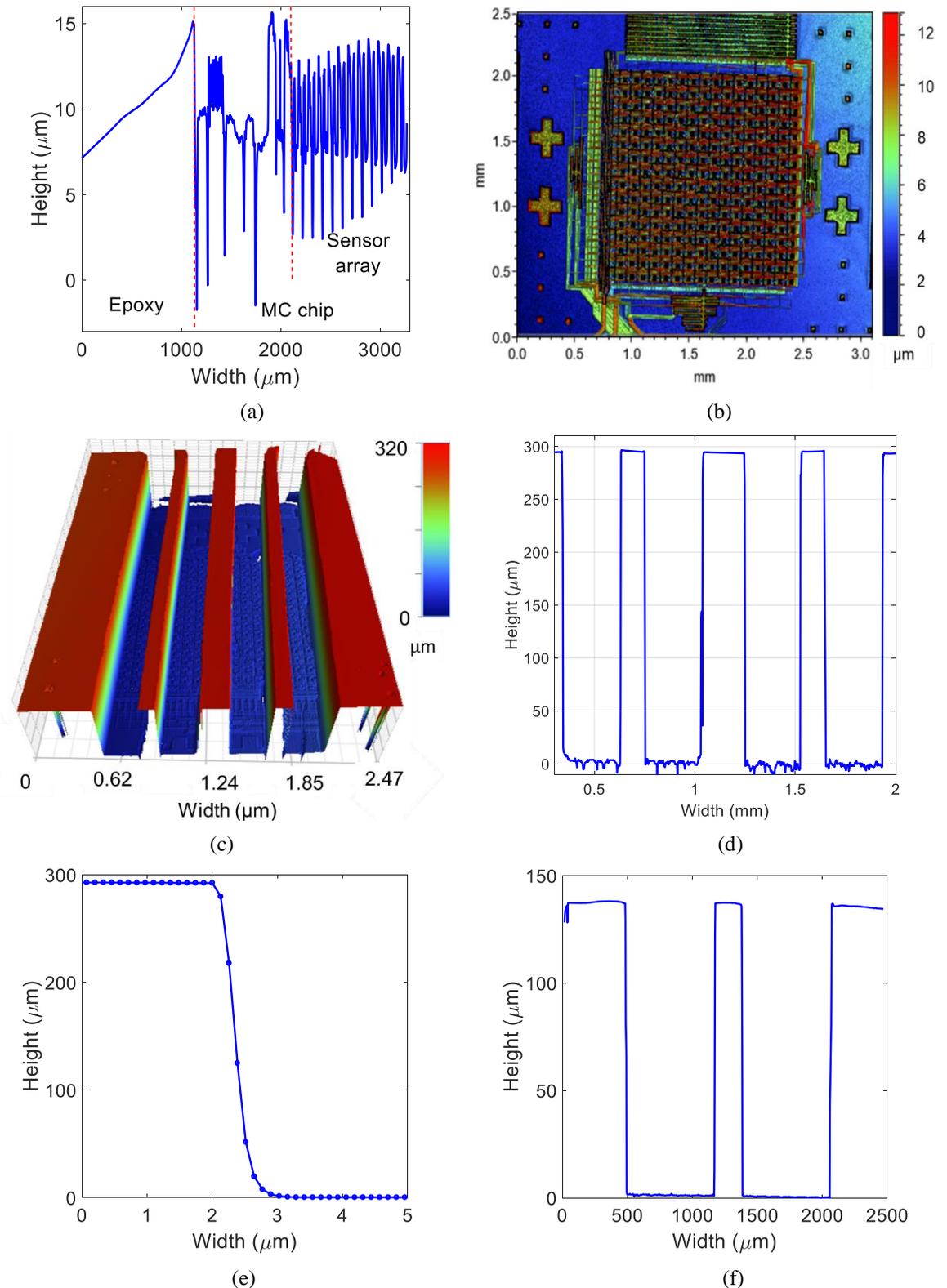
2679 been removed to accommodate the optical measurement. The epoxy surface area converged
2680 with the CMOS chip with an average slope of $0.007 \mu\text{m}/\mu\text{m}$. The slight incline of the epoxy
2681 surface region is negligible when compared to the CMOS chip surface, shown in Figure 4.11
2682 (a) and (b). The inhomogeneous surface of the chip is derived from the CMOS
2683 manufacturing of different layers by the foundry. The surface profile of the chip is
2684 particularly uneven on the active area, where the device's top metal layer density is higher.
2685 Another factor that contributes to the uneven surface is that this chip also exhibits openings
2686 on the passivation/polymer layer above the ISFETs. The inhomogeneities of the surface of
2687 the chip led to peaks of the height of $13 \mu\text{m}$.

2688 Figure 4.11(c) shows the result from a surface measurement of a cartridge using the
2689 aforementioned optical equipment. Four identical microfluidic channels traversed the
2690 CMOS chip from the north to the south side, crossing the sensing area of the chip. Apart
2691 from creating channels, the casted epoxy was also used to form lateral walls that encapsulate
2692 pads and wire-bonds, providing both mechanical strength and resistance to aqueous
2693 environments. As expected, the top of the epoxy walls appeared smooth and flat, especially
2694 when compared to the CMOS chip surface. The smoothness and flatness of the epoxy walls
2695 were fundamental for achieving a robust bonding strength with the PDMS top lid.

2696 A section of the cartridge of interest is reported in Figure 4.11 (d). The heights and widths
2697 of the manufactured microchannels were, on average, $291.95 \pm 6.44 \mu\text{m}$ and
2698 $300.87 \pm 0.86 \mu\text{m}$, respectively. The profile of a single microfluidic wall is shown in Figure
2699 4.11(e). The trench had a deep slope of approximately $929 \mu\text{m}/\mu\text{m}$. The length of the channel
2700 was, on average, $4.0 \pm 0.1 \text{ mm}$. The manufactured patterns showed features that were
2701 expected, and the resulting microfluidic channels were compliant to the design
2702 specifications. In addition to the analysed microfluidic design, further patterns and recipes
2703 were manufactured. On this note, it is also relevant to report the height of microfluidic
2704 channels achieved using a single layer of SU-8. Expectedly, the height of the microchannels
2705 reached with only one SU-8 layer was lower. More precisely, the average height of
2706 $137.14 \pm 3.1 \mu\text{m}$ was measured. Figure 4.11 (f) reports the section of a microfluidic network
2707 composed of two channels with reduced height. For this pattern, the width of the
2708 microchannels was, on average, $693.65 \pm 3.3 \mu\text{m}$.



2709 *Figure 4.10 (a) Silicon wafer patterned with SU-8 microstructures. (b) Two identical PDMS*
 2710 *microstructure for microchannel fabrication. (c) PDMS microstructure was temporarily*
 2711 *placed onto the CMOS. (d) Close-up of the PDMS microstructure on-chip. (e) PDMS and*
 2712 *CMOS chip misalignment. (f) A 2-microchannel microfluidic network on chip (top PDMS*
 2713 *lid removed). (g) A 4-microchannel microfluidic system on chip (top PDMS lid removed).*
 2714 *Multiple micrographs have been merged to produce this figure.*

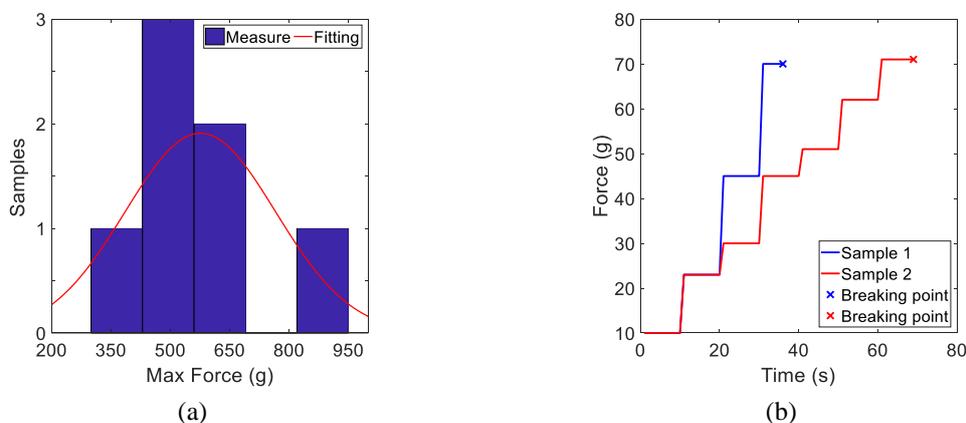


2715 *Figure 4.11 (a) Surface analysis of the flat epoxy area encapsulating the CMOS chip. (b)*
 2716 *Surface measurement of the CMOS chip with an optical profiler. (c) Optical profile of a 4-*
 2717 *microchannel pattern fabricated on the chip. (d) Cross-section of a 4-microchannel pattern*
 2718 *fabricated on-chip. (e) Close up of a microfluidic wall measured using optical profiling. (f)*
 2719 *Cross-section of a 2-microchannel pattern made on-chip using an alternative recipe*
 2720 *involving only one SU-8 layer.*

2721 Mechanical strength of the microfluidic structure was quantified using two methods, namely
 2722 shear testing and pull testing. Shear testing was carried using the DAGE 4000HS bond tester
 2723 in the cleanroom facility of the Glasgow Laboratory for Advanced Detector Development
 2724 (School of Physics and Astronomy, University of Glasgow) with the help of the staff. Testing
 2725 was performed on seven dummy structures (PDMS structure bonded to a 3.4x3.4 mm silicon
 2726 substrate with a 500 nm coating of silicon nitride to emulate the surface characteristic of the
 2727 CMOS chip). An increasing lateral force was applied to the PDMS top lid using a piston
 2728 while the structure was held still. Consequently, the PDMS structure was stressed, deformed,
 2729 and then peeled off from the substrate (the test was destructive). The maximum shear force
 2730 that the structures tolerated before permanently getting damaged was evaluated by analysing
 2731 the force diagram.

2732 Results are reported in Figure 4.12(a). The shear test showed that the bonding could tolerate
 2733 a maximum lateral force of 576 ± 190.2 g (applied on a surface circa 2.9x2 mm wide).
 2734 However, the surface of the CMOS chip is not as flat as one of the testing devices, so it is
 2735 expected that the final device can tolerate a lower shear force.

2736 Pull tests were performed over two cartridges. The tested cartridges had been extensively
 2737 used for other biological experiments before the pull testing. Thus, the bonding strength
 2738 might have deteriorated. Pull testing was carried out in the electronics testing laboratory,
 2739 Rankine Building University of Glasgow. The cartridges under test were glued onto a custom
 2740 weight holder. The weights in the holder were progressively increased. For each newly
 2741 introduced weight, the cartridge was lifted for 10 seconds by the PDMS block with tweezers.
 2742 The total lifted weight was recorder before lifting using a precision scale. For both samples,
 2743 PDMS damage started when applying a force around 70 g. Results for the pull testing are
 2744 reported in Figure 4.12(b).



2745 *Figure 4.12 (a) Results of the shear testing. (b) Results of the pull testing.*

2746 **4.8. Spectral Analysis**

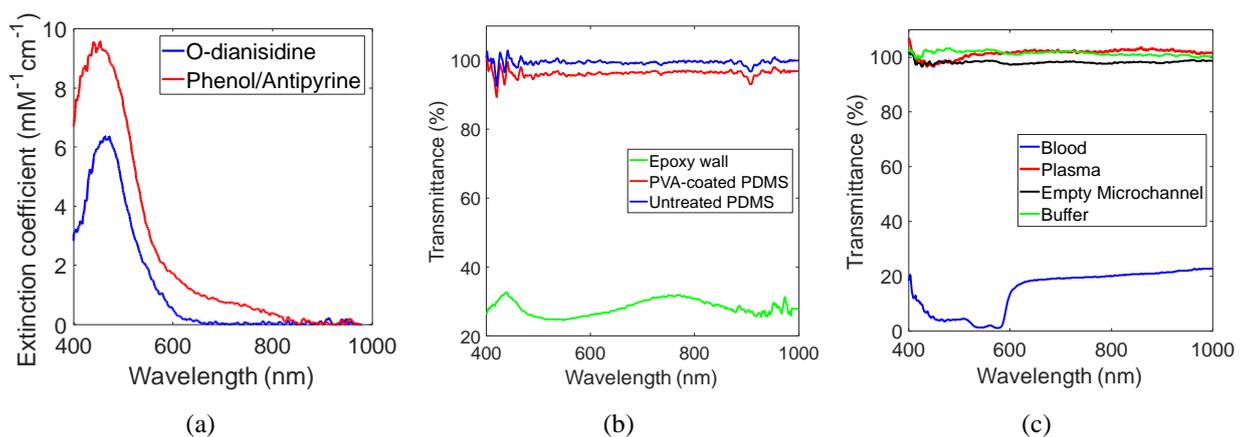
2747 Preliminary optical testing was performed using the micro-spectrometer ffTA-1 from Foster
2748 and Freeman. Spectrophotometric analysis was performed on three aspects of the platform,
2749 namely the colorimetric reagents, the material used for microfluidic and the type of human
2750 specimen to be tested with the platform. Dedicated test samples were fabricated to study the
2751 perform transmission mode analysis. The test devices were manufactured with the same
2752 materials and methods presented in the previous chapter, but a glass slide was used as a
2753 substrate instead of the CMOS chip. The height of the test microchannels was, on average,
2754 137 μm . For all the measurements, the analyses were performed for wavelengths in the range
2755 of 400 – 1000 nm with 1 nm step. The calibration was performed using measurements on an
2756 empty channel and in dark conditions. For each reported spectrum, three measurements were
2757 recorded and averaged.

2758 The analysis of the colorimetric agents aimed to quantify the extinction coefficients and the
2759 wavelength range according to the relevant light absorption. The extinction coefficient was
2760 measured in the microchannels using testing solutions of H_2O_2 . For this analysis H_2O_2 ,
2761 o-dianisidine, phenol, 4AAP and HRP were purchased from Sigma Aldrich. Two different
2762 solutions with the same total H_2O_2 concentration of 1 mM were produced. For the first
2763 solution, 30 μL of 2 mM H_2O_2 , 5 μL of 41 mM o-dianisidine, 10 μL of 10 U/mL of HRP
2764 and 15 μL of DI water were mixed together. For the second solution, 30 μL of 2 mM H_2O_2 ,
2765 5 μL of 44.5 mM phenol, 5 μL of 10.5 mM 4AAP, 10 μL of 10 U/mL of HRP and 10 μL of
2766 DI water were mixed together. Both the solutions were incubated for 1 h at room
2767 temperature. Subsequently, they were introduced into 137 μm high microchannels, and the
2768 transmittance spectra were recorded. The transmittance spectra were then numerically
2769 converted into absorbance and, finally, into the extinction coefficients for different
2770 wavelengths using the Beer-Lambert's law. The extinction coefficient against the
2771 wavelength for both the colorimetric methods for H_2O_2 quantification are reported in Figure
2772 4.13(a). The trend of o-dianisidine extinction coefficient shows a maximum of
2773 $6.37 \text{ mM}^{-1}\text{cm}^{-1}$ at 463 nm. The FWHM for o-dianisidine was 112 nm. The extinction
2774 coefficient when using phenol/4AAP had a similar trend, with a maximum of $9.54 \text{ mM}^{-1}\text{cm}^{-1}$
2775 at 440 nm and FWHM of 180 nm. For both the colorimetric methods, the results agree with
2776 the scientific literature [49].

2777 The analysis of the materials used for cartridge manufacturing aimed to quantify the related
 2778 transmission losses. Figure 4.13(b) reports the spectra for untreated PDMS, PVA-coated
 2779 PDMS and epoxy microfluidic walls. No liquid was introduced in the microchannel during
 2780 these measurements. Untreated PDMS had a transmittance of 98.85% at 500 nm. At the same
 2781 wavelength, the PVA-coated PDMS had a slightly lower transmittance of 95.29%. Epoxy
 2782 walls also showed light transmittance, although with a highly reduced value. In this case, at
 2783 500 nm the light transmittance of a 137 μm microchannel was approximately 25.28%.
 2784 However, such a low transmittance was acceptable since the epoxy walls only served as
 2785 liquid barriers to form the microfluidic channels and no measurement was performed in those
 2786 areas.

2787 The analysis of the target human body fluids aimed to quantify the sample-specific
 2788 transmission loss when introduced into a microchannel so that it can then be isolated from
 2789 changes in transmission due to metabolomic reactions. Figure 4.13(c) reports the spectra of
 2790 the human body fluid of interest. When the buffer, tris hydrochloride (Tris HCl), was only
 2791 added in the microchannel, a small increase of transmittance for all the wavelengths of
 2792 interest was measured. The increase of the transmittance is related to the reduced reflection
 2793 with respect to an empty channel. Assuming perpendicular light, according to Snell's
 2794 equation, the power light reflectivity R of an interface with refractive indexes n_1 and n_2 is
 2795 given by [297]:

$$R = \left| \frac{n_1 - n_2}{n_1 + n_2} \right|^2 \quad (4.4)$$



2796 *Figure 4.13 Measured spectra of different samples introduced into a microchannel. Spectra*
 2797 *were measured using the micro-spectrometer ffTA-1 from Foster and Freeman. Spectra are*
 2798 *averaged over three different measurements. Wavelength range: 400 – 1000 nm. Wavelength*
 2799 *step: 1 nm. The spectra represent: (a) The extinction coefficients of oxidised o-dianisidine*
 2800 *and phenol/4AAP, (b) transmittance through untreated PDMS, PVA-coated PDMS and the*
 2801 *epoxy walls, and (c) transmittance through different media and air.*

2802 Thus, considering PDMS ($n_1 = 1.4$ [298]) and air ($n_2 \sim 1$), $R = 0.0278$. Differently, when a
2803 water-based solution is introduced ($n_2 = 1.33$ [299]), $R^* = 6.39 \cdot 10^{-4} < R$. The expected
2804 increase of the transmission spectrum is therefore justified.

2805 Expectedly, the light transmission when introducing human plasma into the microchannel
2806 decreased to 97.7% at 500 nm. This reduction owes to the different optical properties of the
2807 samples. This effect is more prominent in whole human blood where light transmittance is
2808 drastically reduced to 4.2% at 500 nm as there has been no filtering of the thick nature of
2809 whole blood.

2810

2811 **4.9. Sensor Array Characterisation**

2812 **4.9.1. Photodiode spectral analysis**

2813 Spectral response of the photodiodes was characterised in collaboration with Dr Mohammed
2814 Al-Rawhani and Dr Christos Giagkoulovits, in the electronic labs of the Rankine Building,
2815 University of Glasgow. To test the spectral response of the optical devices, a monochromator
2816 (DTMS300 from Bentham) was used as the light source and it was attached to an integrating
2817 optical sphere to ensure uniform light distribution. A calibrated photodiode (DH_Si Silicon
2818 photodiode from Bentham) was fitted to one exit port to measure the light intensity.

2819 The CMOS chip was placed at another exit port. The light source was used to measure the
2820 sensor output at different wavelengths, in the range of 350 – 1000 nm with a 5 nm step. The
2821 average power level was adjusted to avoid sensor saturation at the peak wavelength. All
2822 experiments were performed in dark conditions. Data from 25 randomly selected
2823 photodiodes in the sensor array were collected and averaged. The average voltage output
2824 was then divided by the recorded reference power to calculate the CMOS photodiode array
2825 responsivity in V/W.

2826 Figure 4.14(a) shows the average spectral response of the photodiodes. The responsivity was
2827 normalised to its maximum, which was 0.25 V/ μ W at 575 nm. The responsivity graph
2828 exhibits a second peak at 620 nm. We can, therefore, assume that there was a sensor-to-
2829 sensor variability from the responsivity point-of-view. For each photodiode, we can
2830 understand the wavelength where the responsivity is maximised is in the range of 565 –
2831 630 nm. The full width half maximum (FWHM) of the photodiode responsivity was 405 nm.
2832 When comparing the spectral response of the photodiodes with the absorbance spectrum of
2833 the H₂O₂ probe (reported in the previous section), the responsivity peak did not coincide

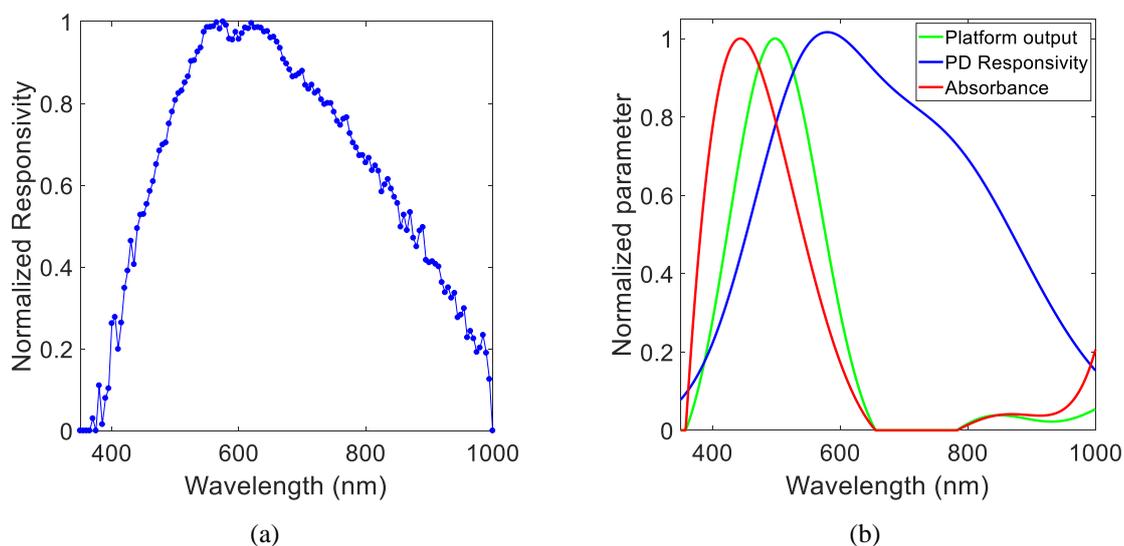
2834 with the absorbance maximum. Thus, the working wavelength of the device was selected to
 2835 be a trade-off of the two spectra. The optimal wavelength was calculated using a custom
 2836 Matlab-based algorithm computing the variation of the platform output when varying the
 2837 wavelength. The model was trained using the experimental spectra of both the photodiode
 2838 responsivity and the absorbance of the H₂O₂ probes. The experimental H₂O₂ absorbance
 2839 spectrum and the photodiode responsivity were fit with polynomial (6th order) and a double
 2840 Gaussian model, respectively. The result of the analysis is reported in Figure 4.14(b).
 2841 Accordingly, the optimal working wavelength was 498 nm, and the optimal working range
 2842 was 480 – 520 nm. When confronting these results with commercial LED choices by
 2843 Thorlabs [64], a 490 nm LED with a 20 nm FWHM was selected. Among all the commercial
 2844 LED available, this device was the most suitable in terms of optical power and required
 2845 power supply (3 mW at 20 mA), wavelength range (480 – 500 nm) and package type [64].

2846

2847 4.9.2. Photodiode output characteristic

2848 After the working wavelength was selected, the sensor output was characterised at the
 2849 specific wavelength of 490 nm using the selected LED. For this characterisation, a cartridge
 2850 with four microfluidic channels was used. The platform characterisation was performed in
 2851 dark conditions.

2852

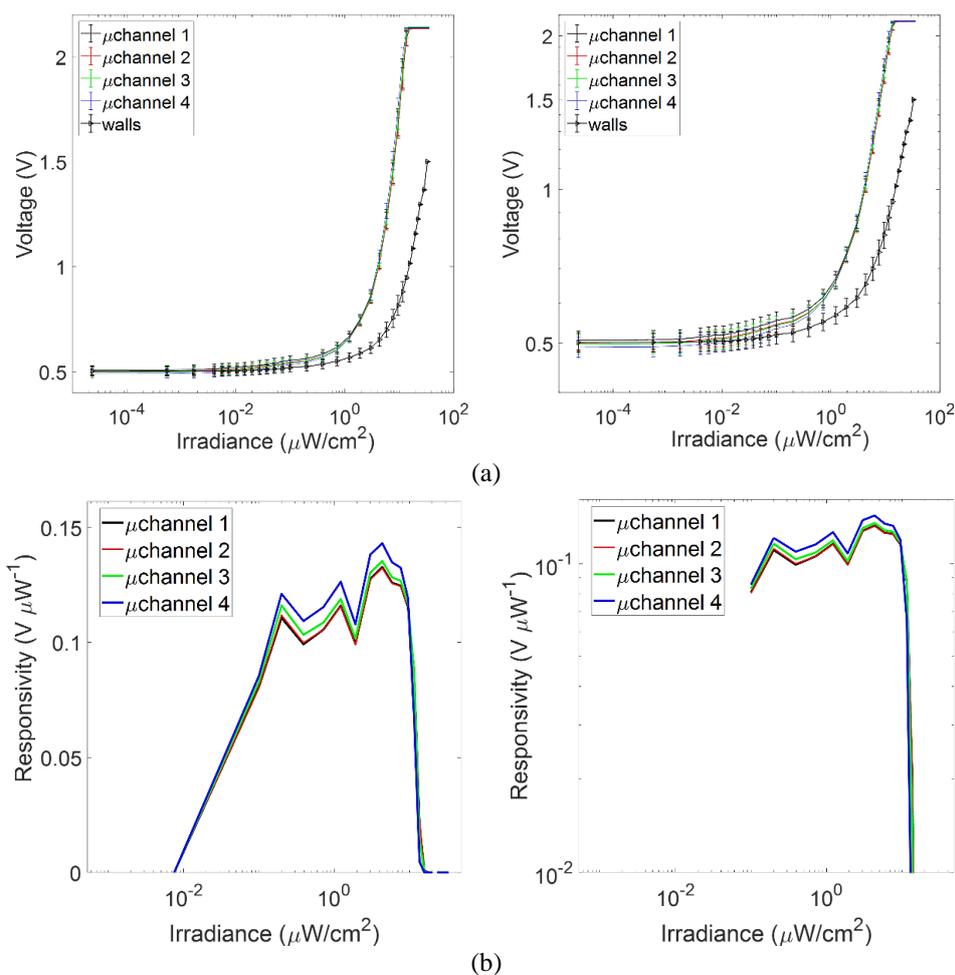


2853 *Figure 4.14 (a) Average spectral response from 25 randomly selected pixels in the sensor*
 2854 *array. The responsivity was normalised to its maximum. (b) The estimated best response of*
 2855 *the platform (green) taking into account photodiode responsivity (blue) and absorbance*
 2856 *spectrum of the H₂O₂ probe (red). The optimal wavelength was in the range 480 – 520 nm*
 2857 *with a peak at 498nm.*

2858 The 490 nm LED from Thorlabs was used as the light source. An optical lens was used
2859 (AC254-035-A-ML BBAR Coating $f = 35\text{mm}$ lens from Thorlabs) to provide collimated
2860 light. The current supply to the LED was swept across its range. The light intensity was first
2861 measured with the cartridge in each of its four microchannels. The reference light intensity
2862 was also measured with a power meter (1936-R power meter with silicon photodetector 818-
2863 SL/DB, Newport) and expressed as irradiance in μWcm^{-2} [300]. The area of the reference
2864 photodetector was 1 cm^2 . The average outputs of pixels enclosed in the microchannels and
2865 the ones covered by fluidic walls versus the power recorded by the benchtop equipment are
2866 reported in Figure 4.15. The outputs of the microchannels were obtained by averaging the
2867 enclosed pixels in time (1000 frames) and space (48 pixels per channel). The output of the
2868 active area covered by microfluidic structures was obtained by averaging both in time (1000
2869 frames) and in space (64 pixels in total) the output of the sensors covered by the epoxy walls.
2870 Reference readings from the power meter were obtained as average over 1000 samples. The
2871 output signals from the microchannels were almost identical. Considering that a 12-bit ADC
2872 was used for data digitisation on a dynamic range of 3.3V, data from each pixel had a
2873 resolution of 0.0504 mV.

2874 In dark conditions, the average output signal reported for the microchannels was 498.97 ± 22
2875 mV. LOD and LOQ, according to the IUPAC definition [58], were 571.57mV and 718.97
2876 mV – respectively. When converted into irradiance using the characteristic, they correspond
2877 to $0.39\ \mu\text{Wcm}^{-2}$ and $1.9\ \mu\text{Wcm}^{-2}$, in the same order. From $1.9\ \mu\text{Wcm}^{-2}$ to $11.5\ \mu\text{Wcm}^{-2}$, the
2878 platform showed a linear response. Sensor output signals started saturating at around
2879 $15.6\ \mu\text{Wcm}^{-2}$. Average responsivity values in the linear range were 0.116, 0.116, 0.118 and
2880 $0.119\ \text{V}\mu\text{W}^{-1}$, from channel 1 to channel 4 respectively. Pixels covered by fluidic walls
2881 showed less sensitivity to light. There are many factors which can create small fluctuations
2882 in the output of the microchannels. These include device-to-device variability, fabrication
2883 impurities, noise and variability in the read-out and biasing circuitry. Since the platform was
2884 used for rate estimation of enzymatic reactions, sensors drift in dark and condition of
2885 constant illumination of $9\ \mu\text{Wcm}^{-2}$ were also estimated over 5 minutes measurements.
2886 Average drifts over triplicates measures within the microchannels were $0.0014 \pm 0.001\ \text{mVs}^{-1}$
2887 and $0.0009 \pm 0.001\ \text{mVs}^{-1}$, respectively.

2888



2889 *Figure 4.15 (a) Sensor output (V) vs irradiance (μWcm^{-2}) at 490nm. Voltage is shown in*
 2890 *linear (left) and logarithmic scale (right). Irradiance is shown in logarithmic scale. The*
 2891 *outputs from pixels enclosed in each microchannel were averaged over time (1000 frames)*
 2892 *and space (48 pixels). The outputs from pixels covered by epoxy microstructure – ‘walls’–*
 2893 *were similarly averaged over time and space (64 pixels). (b) Responsivity of the*
 2894 *microchannel vs irradiance at 490nm. Responsivity is shown with linear (left) and*
 2895 *logarithmic scale (right). Irradiance is shown in logarithmic scale.*

2896

2897 **4.9.3. Sensor array characterisation**

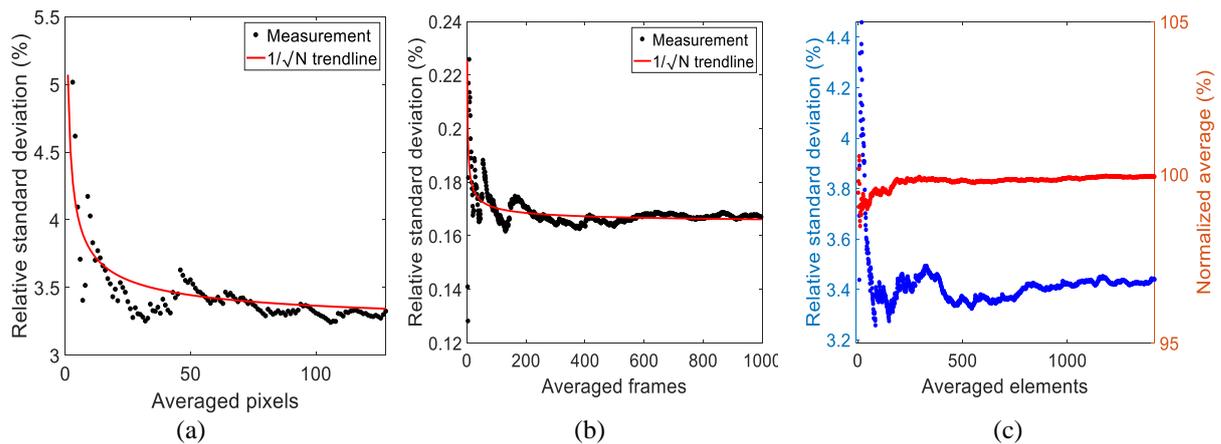
2898 The improvements of the signal quality when using multiple sensors and oversampling are
 2899 quantified. In this study, the sensor array was illuminated with a constant optical intensity
 2900 of $9 \mu\text{Wcm}^{-2}$ at 490 nm. To study the behaviour of standard deviation when increasing the
 2901 number of averaged pixels, pixels in a single frame were randomised, and sub-groups of the
 2902 array were averaged.

2903 Figure 4.16(a) demonstrates that the standard deviation of the measurement is reduced by a
 2904 factor of $1/\sqrt{N}$ when averaging N different pixels. This analysis is particularly critical when
 2905 considering that the microfluidic channel encloses several pixels. Increasing the number of

2906 microfluidic channels decreases the number of pixels enclosed in each microstructure.
 2907 Therefore, it can be assumed that increasing the amount of the microfluidic channels and,
 2908 accordingly, the number of metabolites to be simultaneously tested, degrades the
 2909 performance of the platform. For the implemented 4-channel network, each microchannel
 2910 encloses 48 pixels. This corresponds to an average reduction of the standard deviation of the
 2911 measurement by a factor 6.93.

2912 Similarly, the trend of the standard deviation when oversampling on the same sensor was
 2913 analysed (time averaging). Figure 4.16(b) shows that the standard deviation reduction can
 2914 also be achieved by averaging multiple measurements from the same sensor. By comparing
 2915 Figure 4.16(a) and Figure 4.16(b), it is possible to conclude that the standard deviation
 2916 related to space averaging is higher than the one obtained with temporal averaging. However,
 2917 time averaging was particularly useful in eliminating high-frequency noise.

2918 The combined effect of time and space averaging is analysed in Figure 4.16(c). Here, the
 2919 array was divided into sub-groups and their time and space samples were randomised
 2920 altogether. Then, the random space-time samples were averaged. The graph demonstrates
 2921 that the reduction of the standard deviation is verified regardless of the nature of the sample
 2922 population. Also, averaging allows the output to converge to its final stable value. In this
 2923 case, the convergence of both standard deviation and mean value was achieved by averaging
 2924 more than 500 samples. Additional averaging does not further increase the performance of
 2925 the system.

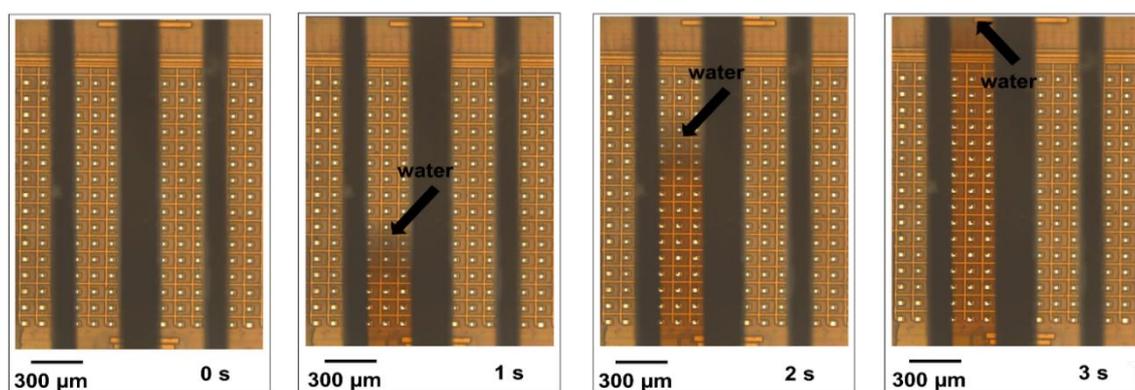


2926 *Figure 4.16 (a) Relative standard deviation decreases with a $1/\sqrt{N}$ trend when averaging*
 2927 *different pixels. (b) Relative standard deviation also decreases likewise when averaging*
 2928 *different frames (average over time). (c) Averaging in both space and time is effective in*
 2929 *reducing the standard deviation and reaching a convergence to a stable value.*

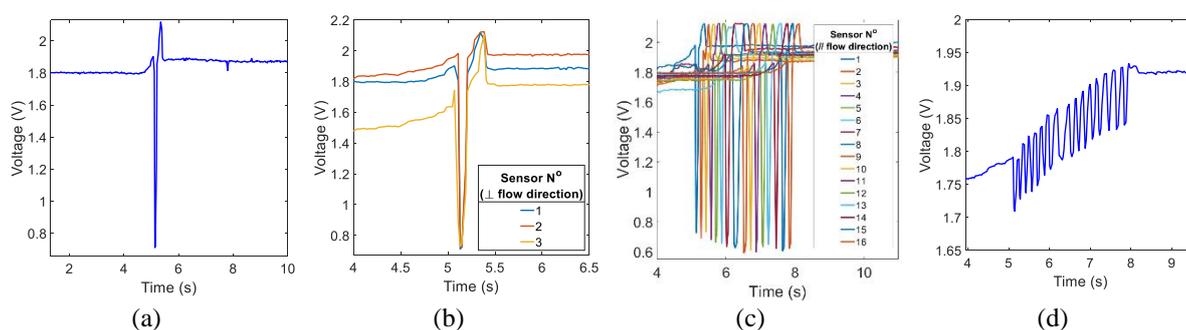
2930 **4.10. Capillary Flow Characterisation**

2931 Capillary flow was experimentally verified on test samples and on the cartridge using visual
2932 inspection. Figure 4.17 reports a proof-of-concept image, composed of a sequence of
2933 micrographs. In these experiments, recorded with a microscope, the capillary effect when
2934 introducing water into a microchannel can be observed. After its introduction, water
2935 travelled from the south to the north side of the device, completely covering the sensing area.
2936 In this experiment, water covered the sensing area of the CMOS chip in less than 3 seconds.
2937 The sample flow stopped once the microchannel was filled. Another key information the
2938 figure shows is that the microstructure was successful in containing the liquid only in the
2939 microchannel, and there was no evident leakage of introduced samples in adjacent channels.
2940 The flow rate of the introduced sample was quantified using the sensor array. The frames
2941 per second rate (approximately 36.5 fps) ensured a temporal resolution of 27.4 ms, suitable
2942 for the expected flow rate of the sample. It has already been demonstrated that the
2943 introduction of a liquid sample into the microstructure creates a detectable increase in the
2944 light transmittance. Raw data reported in Figure 4.18(a) corroborate that the photodiodes
2945 embedded in the sensor array were capable of detecting the arrival of the advancing
2946 meniscus. In particular, the photodiodes recorded a voltage spike and a sudden increase of
2947 transmittance once covered with the inserted liquid. The spike was very pronounced (~ 1.2
2948 V) and clearly detectable. Pixels enclosed into microchannel and aligned in the perpendicular
2949 direction with respect to the flow responded with simultaneous voltage spikes, as shown in
2950 Figure 4.18(b). This demonstrated that the meniscus advanced with a linear front inside the
2951 microstructure. Pixels enclosed into the microchannel and aligned in the parallel direction
2952 with respect to the flow, responded with sequential spikes, effectively recording the
2953 advancement of the meniscus. Figure 4.18(c) shows an example of 16 pixels sequentially
2954 sensing the arrival of the introduced sample. When the pixels inside the microchannel were
2955 averaged, a single signal with 16 spikes was typically obtained, as shown in Figure 4.18(d)
2956 Despite the less pronounced voltage spike, it allowed the quantification of the flow rate from
2957 a single signal. In the data-analysis phase, the mentioned signal was used to verify the correct
2958 filling of the microstructure. The above-mentioned data demonstrated that the sensor array
2959 could detect the liquid flowing on the sensing area. This capability has been used to quantify
2960 the filling time of the device, i.e. the time required for the sample to completely cover the
2961 sensing area. In the design stage, several simulations were presented to show the parameter

2962 optimisation and estimate the expected performance of the device. Ultimately, a conservative
 2963 approach was adopted, and the system was designed to provide a filling time of maximum
 2964 30s when using whole blood as a fluid of interest. By using the aforementioned approach,
 2965 the flow rate, and the filling time of diluted serum (1:10), diluted plasma (1:1) and whole
 2966 blood were quantified over triplicates. Serum and plasma were purchased from Sigma
 2967 Aldrich while whole blood was purchased from Cambridge Bioscience. Plasma and serum
 2968 were diluted in DI water. A cartridge embedding four microfluidic channels with height and
 2969 width of approximately $290\ \mu\text{m}$ and $300\ \mu\text{m}$, respectively, were employed. For diluted
 2970 serum, the time required for the sample to reach the first and the last pixel (filling time)
 2971 of the array were $2.48\pm 0.06\ \text{s}$ and $4.58\pm 0.129\ \text{s}$. The same figures increased to $2.44\pm 0.009\ \text{s}$
 2972 and $7.67\pm 0.005\ \text{s}$, respectively, for diluted plasma (1:1).
 2973

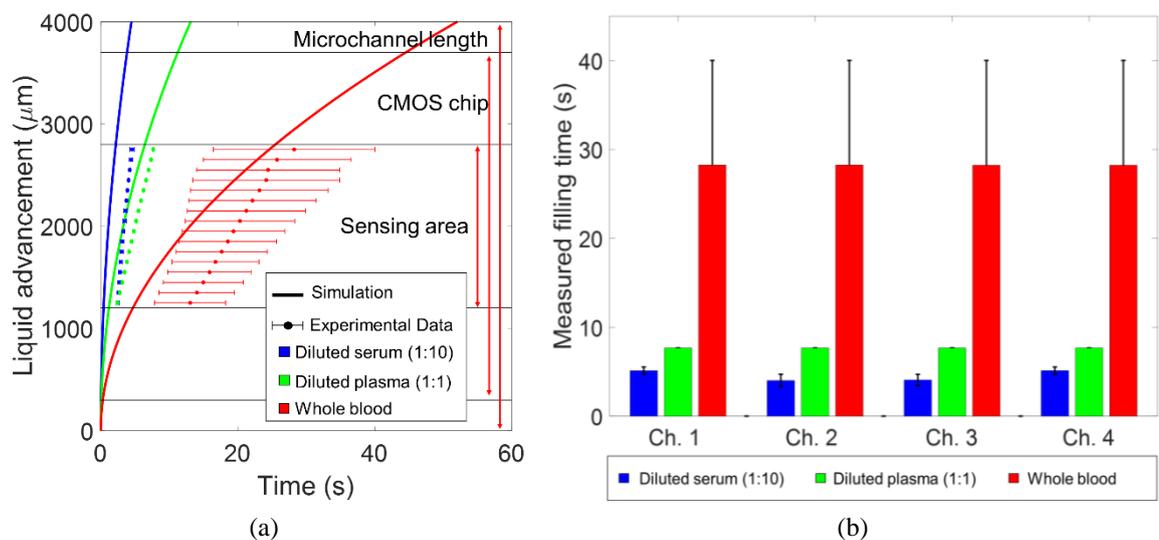


2974
 2975 *Figure 4.17 Water flowing into a microchannel fabricated on chip. The sample covered*
 2976 *completely the sensing area of the CMOS chip in approximately 3 seconds. The micrographs*
 2977 *also show a leakage-free flow.*



2978 *Figure 4.18 Raw data from the sensor array when a sample (water) was introduced into a*
 2979 *microchannel ($h\sim 290\ \mu\text{m}$). (a) Voltage spike induced by the arrival of the meniscus onto a*
 2980 *photodiode. (b) Advancing meniscus covering sensors aligned in the perpendicular*
 2981 *direction of the flow simultaneously. (c) Advancing meniscus covering sensors aligned in the parallel*
 2982 *direction of the flow sequentially. (d) When averaging the pixels of a microchannel, the*
 2983 *advancement of the meniscus over the sensing area produced sequential spikes.*

2984 Expectedly, the flow was slower when using whole blood. Precisely, in this case, the time
 2985 required for the blood to reach the first and the last pixel of the array were 13.05 ± 5.20 s and
 2986 28.23 ± 11.77 s. The standard deviation of the flow was also higher when using blood,
 2987 suggesting that the results are less repeatable when using this specimen. Experimental data
 2988 were compared with the simulation model used for the design of the device. Simulations
 2989 were repeated with adjusted parameters, including microchannels geometry and contact
 2990 angles. Physical properties of the diluted specimens were assumed using linear regression.
 2991 Experimental data, together with simulations, are represented in Figure 4.19(a). For all the
 2992 analysed specimens, the correlation between experimental and simulated data was high
 2993 ($R^2 > 0.98$). However, the model seemed to be affected by a small bias of 3.36 s against the
 2994 experimental data. The bias was calculated as the average over the absolute measurement
 2995 error, as per definition. The flow in parallel microchannels was also analysed and reported in
 2996 Figure 4.19(b). Regardless of the nature of the sample introduced in the microstructure, the
 2997 flow in the channel was virtually identical. Identical channels were another design
 2998 specification which was therefore met.
 2999



3000 *Figure 4.19 The advancement of the meniscus in a four-microchannel cartridge (height ~*
 3001 *290 μm) was recorded with the sensor array for diluted serum (1:10) diluted plasma (1:1)*
 3002 *and whole blood. Data is reported as the average \pm standard deviation over three replicates*
 3003 *and over all the microchannels. (a) Data compared to simulations. Simulations were*
 3004 *adjusted using measured values of width, height, length, and contact angles. Sample*
 3005 *parameters for diluted samples were assumed using a linear regression. As per design, all*
 3006 *the introduced liquids completely covered the sensor array in less than 30s on average. (b)*
 3007 *For all the introduced samples, microchannels had an identical filling time.*

3008

3009 4.11. Summary of the Chapter

- 3010 • A passive microfluidics network was integrated on top of the sensing area with no
3011 intermediate layer using a combination of soft lithography and injection moulding.
- 3012 • Bioreceptors were introduced in the fluidics by off-chip mixing or preloaded using
3013 lyophilisation.
- 3014 • The fabrication procedure was suitable for planarization, with a slope of $0.007 \mu\text{m}/\mu\text{m}$,
3015 which was negligible when compared to the roughness of the CMOS chip. The heights
3016 and widths of the microchannels were, on average, $291.95 \pm 6.44 \mu\text{m}$ and
3017 $300.87 \pm 0.86 \mu\text{m}$, respectively. Mechanical strength of the structure was also evaluated
3018 through shear and pull testing (maximum lateral force: $576 \pm 190.2 \text{ gr}$; maximum pulling
3019 force: 70 gr).
- 3020 • Optical spectral testing showed that o-dianisidine and phenol/4AAP are both suitable
3021 H_2O_2 probes with experimental extinction coefficients of $6.37 \text{ mM}^{-1} \text{ cm}^{-1}$ at 463 nm
3022 (FWHM: 112 nm) and $9.545 \text{ mM}^{-1} \text{ cm}^{-1}$ at 440 nm (FWHM: 180 nm).
- 3023 • The photodiodes have a maximum responsivity at 575 nm (FWHM: 405nm).
- 3024 • The optimized working wavelength, considering H_2O_2 probes properties, sensors
3025 responsivity and commercially available LEDs was 490 nm.
- 3026 • The sensors at 490 nm had a linear response with optical intensity in the range
3027 $1.9 - 11.5 \mu\text{Wcm}^{-2}$, showing a responsivity of $0.117 \pm 0.001 \text{ V}\mu\text{W}^{-1}$. Averaging
3028 photodiodes within the same microchannel and averaging oversampled reading from the
3029 same photodiode were effective in the reduction of the noise: the standard deviation of
3030 the measurement was reduced by a factor of $1/\sqrt{N}$ by averaging N different
3031 measurements.
- 3032 • The capillary flow of different samples (i.e. diluted serum, diluted plasma and whole
3033 blood) was also tested. Visual inspection also demonstrated that the microfluidic was
3034 successful in providing passive flow and confining the liquid sample. As per the design,
3035 all the samples covered the active area within 30 seconds after their introduction in the
3036 fluidic input without any externally applied pressure. The time required for whole blood
3037 to completely cover the sensing area was $28.23 \pm 11.77 \text{ s}$ (worst-case scenario).
3038

3039 Chapter 5: Metabolomics-on-CMOS

3040 5.1. Introduction

3041 The present chapter focuses on biological experiments for the quantification of the six
 3042 metabolites of interest: LAA, glutamate, choline and sarcosine for PCa and lactate and
 3043 creatinine for ischemic stroke. Metabolites are first quantified in diluted human serum
 3044 samples. Subsequently, multiplexed testing is demonstrated in different configurations.
 3045 Procedures for reagents immobilisation are also illustrated. Proof-of-concept experiments
 3046 with whole blood conclude this chapter. Table 5.1 illustrates the contribution to each activity
 3047 discussed in this chapter.

3048

3049 5.2. Experimental Setup

3050 The setup for the biological experiments henceforward used is described here. A schematic
 3051 of the experimental setup is shown in Figure 5.1. All the optomechanical components were
 3052 purchased from Thorlabs. The reader of the platform was secured to an optical aluminium
 3053 breadboard using two screws with the ZIF socket facing up.

3054

3055 *Table 5.1 Table of contributions for the activity presented in this chapter.*

Task / Activity presented in Chapter 5	Main investigators
Development of the experimental setup	- Valerio F. Annese
Assay formulations	- Well established in the literature
Assay optimisations for this platform	- Valerio F. Annese
Characterisation of the platform when measuring PCa-related metabolites in diluted serum	- Valerio F. Annese
Characterisation of the platform when measuring ischemic stroke-related metabolites in diluted serum	- Valerio F. Annese
Quantification of the test duration	- Valerio F. Annese
Reagents printing for microchannel functionalisation	- Valerio F. Annese
Reagents lyophilisation for microchannel functionalisation	- Valerio F. Annese
Quantification of the reagents shelf-life after lyophilisation	- Valerio F. Annese
Multiplexed assays in human plasma (1 metabolite + control)	- Valerio F. Annese
Multiplexed assays with paper microfluidics (2 metabolites)	- Dr Chunxiao Hu ¹ (designed the work and performed experiments) - Dr Srinivas Velugotla ¹ (developed the paper strips) - Valerio F. Annese (developed and applied functionalisation method of the paper strips)
Whole blood experiments	- Valerio F. Annese
Affiliation at the time of completion of the activity: ¹ <i>Microsystem Technology Group, James Watt School of Engineering, University of Glasgow.</i>	

3056 The size of the optical breadboard was 15 x10 x1.2 cm. Exposed microcontroller pins were
3057 electrically isolated with rubber tape. A cartridge, whose geometry and characteristics are
3058 specified for each set of experiments, was inserted into the ZIF socket. Accordingly, the
3059 sensing area of the CMOS chip was parallel to the optical breadboard and facing up.

3060 An optical post with an approximated height of 30 cm was vertically fixed to the same optical
3061 breadboard. Two T-junction connectors were mounted onto the vertical post, and two new
3062 transversal optical posts were fitted into the setup. The top transversal optical post
3063 accommodated a LED holder. A 3mW LED working at 490 nm (FWHM 20 nm) was
3064 mounted inside the holder and orientated with the emitting junction facing straight down
3065 towards the reader. The light source was power supplied by an external power supply (HP
3066 E3631A). The lower transversal optical post accommodated a lens holder, where an
3067 achromatic collimating lens (AC254-035-A-ML BBAR Coating $f = 35$ mm) was mounted.
3068 The height and the orientation of the two optical posts were adjusted so that the active area
3069 of the chip could receive perpendicular collimated light. The setup mounted onto the optical
3070 breadboard was enclosed into a cardboard box, externally coated with a blackout cloth made
3071 of nylon and polyurethane. The coating was essential to ensure that the experiments were
3072 performed in a dark environment. Only a small aperture was left open to accommodate
3073 connection wires and undertake on-chip sample delivery. The enclosing box was internally
3074 coated with aluminium, to reduce any eventual environmental electrical interference. The
3075 reader inside the enclosed dark environment was connected to an external laptop (HP
3076 EliteBook i7-8650u 16 GB) through a USB cable. A ferrite adapter was used to reduce any
3077 eventual interference noise affecting data travelling through the USB cable. The Matlab-
3078 based user interface was running on the laptop. During the work, the GUI evolved in several
3079 different versions. However, the modifications were mainly graphical, therefore did not
3080 substantially affect the format of the recorded data. The USB link also provided power
3081 supply to the reader (5V). Data was recorded with an average frame rate of 36.5 fps and a
3082 resolution of 12-bit. Typically, the duration of a single experiment was 5 minutes
3083 (approximately 11000 frames).

3084

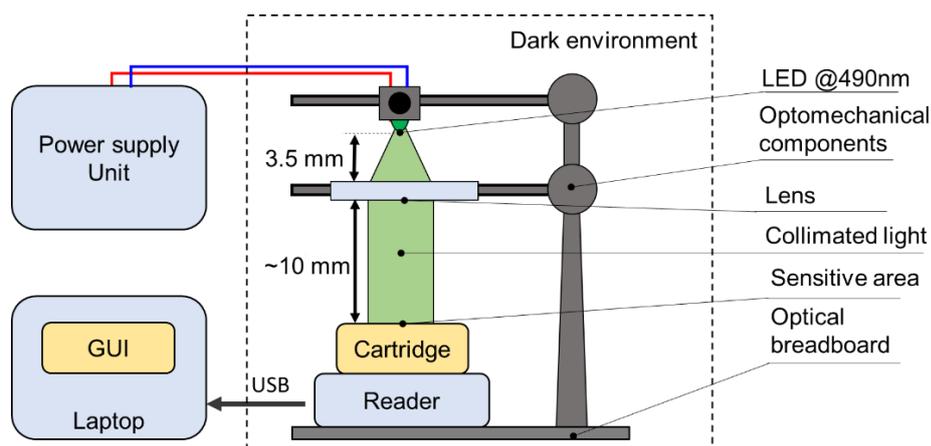


Figure 5.1 Experimental setup for biological experiments.

3085

3086

3087

3088 5.3. Metabolomics-on-CMOS in Diluted Serum

3089 The capability of the platform in quantifying the target metabolites was first assessed in
 3090 diluted serum. Human serum was modified with known concentrations of metabolites of
 3091 interest to determine the calibration curves of the platform.

3092

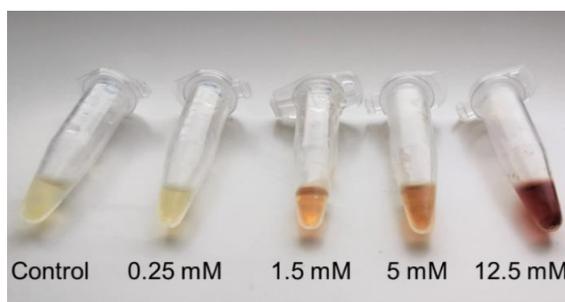
3093 5.3.1. Materials and Methods

3094 **Assay formulation.** All the chemicals were purchased from Sigma Aldrich. Dehydrated
 3095 human serum was also obtained from Sigma Aldrich and reconstituted with DI water
 3096 following the recommended protocol. The reconstituted human serum was further diluted
 3097 with additional DI water for a volume ratio of 1:10. All the reagents were prepared using 0.1
 3098 mM Tris HCl buffer (pH 8). Modified serum samples were freshly prepared before each test.
 3099 Biochemical protocols for the preparation of reagents used for diluted serum experiments
 3100 are detailed in Appendix H.

3101 The formulations of the assays were optimised using a trial-and-error approach. The
 3102 optimisation aimed to create a detectable colour change in the physiological range of the
 3103 target metabolite within a few minutes. The procedure was first performed off-chip. Fine-
 3104 tuning was subsequently performed on-chip. The assay formulation led to the
 3105 determination of desired concentrations for enzymes and reagents. Expectedly, by increasing
 3106 the level of the enzymes in the formulation, the reactions had a higher reaction rate.
 3107 Similarly, the colour change of the solution was more accentuated by increasing the
 3108 concentration of the substrate in the testing solution. Figure 5.2 shows demonstrative

3109 solutions for the LAA assay. The colour change of the reagents increased when increasing
 3110 the level of the substrate in the test. Similar results were obtained off-chip before running
 3111 the assay on-chip. Assay formulations for metabolites sensing in diluted human serum are
 3112 summarised in Table 5.2 (for PCa) and Table 5.3 (for ischemic stroke).

3113



3114

3115 *Figure 5.2 Demonstration of the colour changes due to different concentrations of the*
 3116 *substrate (LAA assay). The picture was taken 30min after the assay was started.*

3117

3118 *Table 5.2 Assay formulations for PCa-related metabolites sensed in diluted human serum*
 3119 *using the developed platform.*

	LAA	Glutamate	Choline	Sarcosine
Cartridge	Four parallel and identical microchannels (h ~ 137 μ m)			
Microchannel volume	0.158 μ L			
Light source	LED @ 490nm (3 mW, FWHM = 20 nm)			
Total Volume	50 μ L			
Sample Volume	25 μ L			
Reagent mix volume	25 μ L			
Reagent buffer	0.1 Tris HCl			
1st reaction stage	LAAOx (10 μ L, 4U/mL)	GlOx (10 μ L, 4U/mL)	ChOx (10 μ L, 150U/mL)	SaOx (10 μ L, 200U/mL)
2nd reaction stage	10 μ L HRP 65.5U/ml 5 μ L o-dianisidine 41mM		10 μ L HRP 300U/ml 5 μ L o-dianisidine 41mM	
Negative control	1st reaction stage was substituted with 10 μ L of DI water			

3120

3121 *Table 5.3 Assay formulations for ischemic stroke-related metabolites sensing in diluted*
 3122 *human serum using the developed platform.*

	Lactate	Creatinine
Cartridge	Two parallel and identical microchannels (h ~ 137 μ m)	
Microchannel volume	0.316 μ L	
Light source	LED @ 490nm (3 mW, FWHM = 20 nm)	
Total Volume	60 μ L	60 μ L
Sample Volume	30 μ L	24 μ L
Reagent mix volume	30 μ L	36 μ L
Reagent buffer	10 mM PBS	
1 st reaction stage	LaOx (10 μ L, 4U/mL)	CNN (6 μ L, 200U/mL) CTN (6 μ L, 200U/mL) SaOx (6 μ L, 150U/mL)
2 nd reaction stage	10 μ L HRP 150U/ml 5 μ L 4-Aminoantipyrine 10.5 mM 5 μ L Phenol 44.5 mM	6 μ L HRP 150U/ml 6 μ L 4-Aminoantipyrine 10.5 mM 6 μ L Phenol 44.5 mM
Negative control	1 st reaction stage was substituted with 10 μ L of DI water	CNN was substituted with 6 μ L of DI water

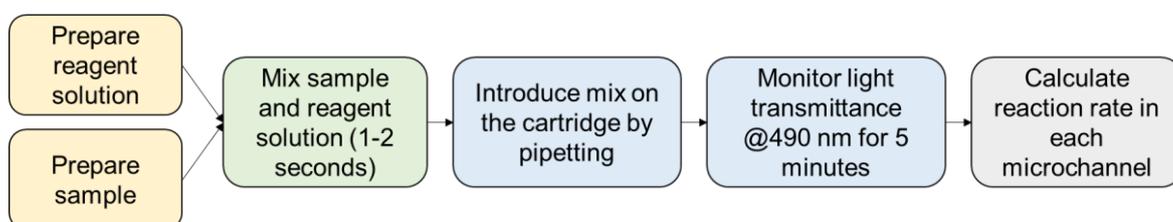
3123 **Procedure.** Experiments were conducted at room temperature in the laboratories of the MST
 3124 group, Rankine Building, University of Glasgow. Metabolites were tested individually.
 3125 Reagents were off-chip mixed with the sample and immediately introduced into the cartridge
 3126 within a few seconds. Sample introduction was achieved by pipetting the total testing volume
 3127 onto the fluidic input. The sample flowed into the microstructure and over the sensing area
 3128 by capillary effect. A schematic representation of the adopted protocol is shown in Figure
 3129 5.3. Cartridges with four microchannels were used for PCa-related metabolites. Cartridges
 3130 with two microchannels were used for PCa-related ones. In both cases, the height of the
 3131 microchannel was, on average, $137.14 \pm 1.1 \mu\text{m}$.

3132 **Data handling.** For each concentration, the assay was performed in triplicates, herein
 3133 referred to as biological replicates. Since each cartridge had multiple microchannels, each
 3134 biological replicate had several readings, herein indicated as technical replicates. After data
 3135 collection, measurements were offline processed using the developed GUI. Technical
 3136 replicates with unexpected behaviour were excluded. Examples of readings with unexpected
 3137 were:

- 3138 • Readings where the rate of the reaction accelerated over time.
- 3139 • Readings where transmittance increased over time.
- 3140 • Readings where the noise level was excessive with respect to the standard measures.
- 3141 • Measurements affected by air bubbles or other strong artefacts.
- 3142 • Readings affected by microfluidics failure, including underfilling of the microstructure.
- 3143 • Measurements considered outliers.

3144 Data from technical replicates were independently analysed using the developed GUI, and
 3145 the results were averaged. Thus, for each biological replicate, only one result was obtained.
 3146 The result for each concentration was obtained as the average and standard deviation over
 3147 the biological replicates.

3148



3149

3150 *Figure 5.3 Protocol adopted for metabolomics experiments in diluted serum.*

3151 **Cartridge reuse.** Cartridges were cleaned and re-used. Ten cartridges were used for PCa-
3152 related experiments. Three cartridges were employed for ischemic stroke experiments. A
3153 cleaning procedure after each measurement was adopted to avoid cross-contamination. The
3154 cleaning recipe involved subsequent rinse in DI water, IPA, ethanol, and nitrogen blow-dry.
3155 Cleaning the cartridge with more aggressive solvents, such as piranha, was attempted.
3156 However, it was avoided because the solvent also etched the epoxy microchannels. Cross-
3157 contamination minimisation was also achieved by optimising the testing sequence. For each
3158 metabolite, a negative control (control measurement) was first recorded. Then, the
3159 colorimetric estimation was performed in triplicates.

3160

3161 **5.3.2. PCa Metabolites**

3162 Calibration curves for LAA, glutamate, choline and sarcosine in diluted human serum are
3163 reported in Figure 5.4. The complete characterisation of the platform for the analytes of
3164 interest is discussed in Table 5.4. An example of raw data for LAA and sarcosine, the tests
3165 with respectively the highest and lowest physiological ranges, are shown in Figure 5.5.
3166 Typically, increased concentrations of the substrate created increased transmittance drop,
3167 measured by a reduction of the voltage output of the photodiodes. Transmittance drop was
3168 nonlinear and is in line with the Michaelis-Menten model. Other metabolites showed
3169 analogue behaviours.

3170 Kinetics constants (K_m) were estimated by fitting data to the Michaelis-Menten model. K_m
3171 results for all the metabolites were comparable with the values reported in the literature [49].
3172 The discrepancies are related to the different materials, methods, and conditions of the tests.
3173 For all the metabolites, the fitting of the experimental data with the Michaelis-Menten model
3174 was satisfactory with R^2 values ≥ 0.98 .

3175 A subset of the collected data (low concentrations) was also fitted using a linear model.
3176 Herein, linear range is defined as the range of measurement reporting $R^2 \geq 0.90$ when a linear
3177 fit is performed. Linear ranges were covering the physiological ones. The sensitivity of the
3178 assays was increased when the physiological range of the target analyte decreased. This was
3179 expected and reflected the choice of enzyme concentrations in the formulation of the tests
3180 described previously. Relative standard deviations of the measurement in the linear range
3181 were in between 12.7% and 19.8%.

3182 LOD and LOQ were quantified using the respective control. LOD and LOQ expressed in
3183 mVs^{-1} were then converted in μM by using the estimated Michaelis-Menten for each

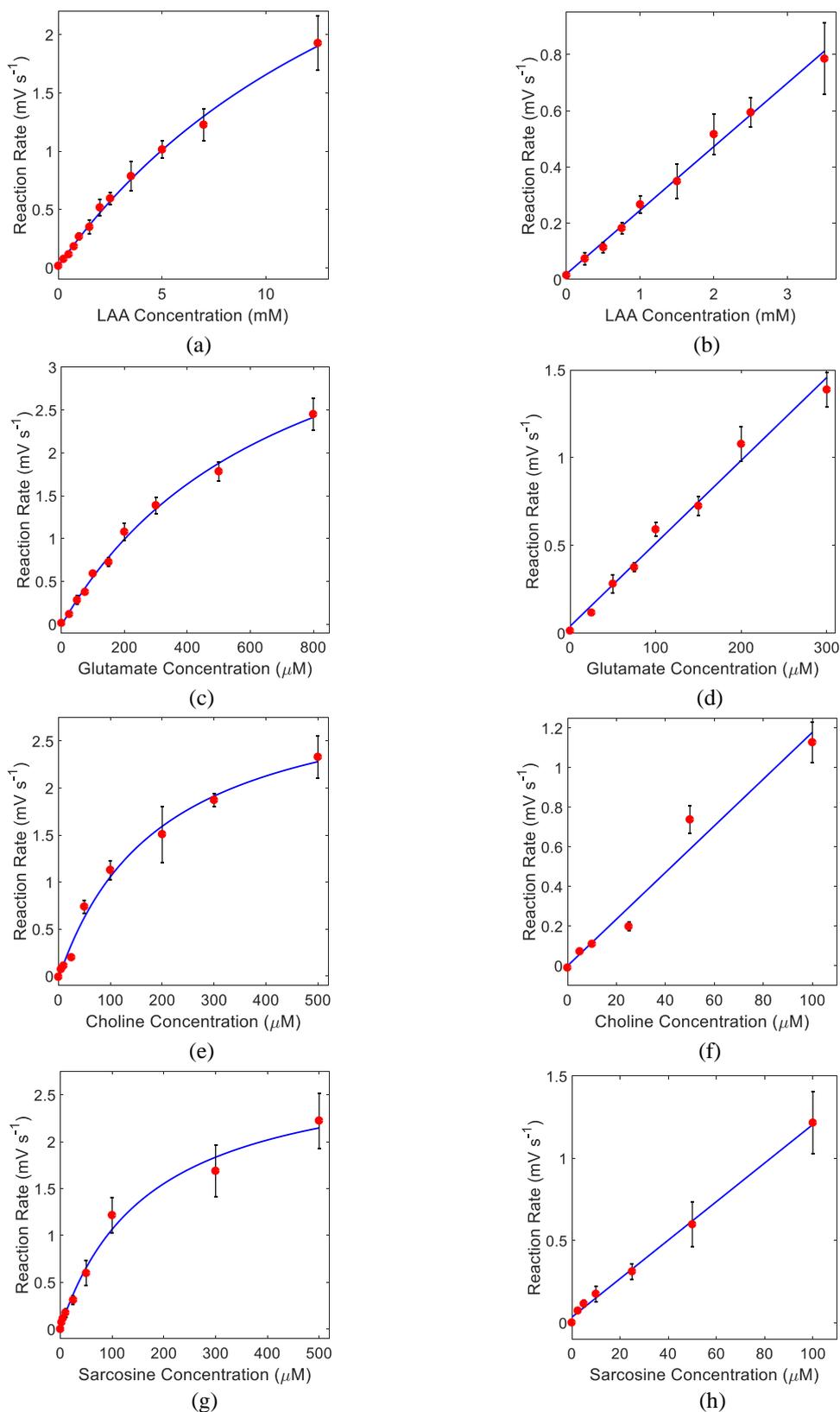
3184 metabolite. Thus, LOD for LAA, glutamate, choline and sarcosine were 69.01 μM , 6.86 μM ,
 3185 3 μM and 0.26 μM , respectively. Similarly, LOQ values for the metabolites in the same
 3186 order were 218.3 μM , 12.04 μM , 4.22 μM , 2.13 μM . LOD and LOQ results demonstrated
 3187 the suitability of the platform for the measurements in the target range in diluted human
 3188 serum.

3189

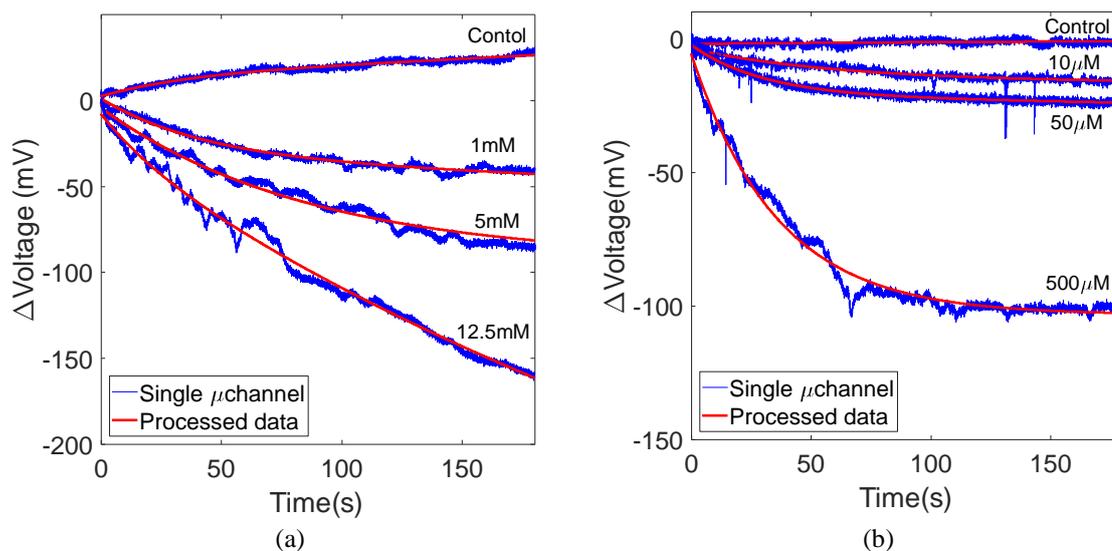
3190 *Table 5.4 Platform Characterisation in diluted human serum for PCa-related metabolites.*
 3191 *V_m , c and K_m are calculated using the Michaelis-Menten model. Metrics have been defined*
 3192 *in Table 2.3.*

	LAA	Glutamate	Choline	Sarcosine
Physiological Range	1.7 – 4.6 mM	40 – 150 μM	10 – 40 μM	0 – 20 μM
Test Range	0 – 12.5 mM	0 - 800 μM	0 – 500 μM	0 – 500 μM
Relation with PCa	↑	↑	↑	↑
Model	$y = \frac{V_m \cdot x}{K_m + x} + c$			
V_m (mVs^{-1}) (95% coefficient bounds)	4.70 (3.68, 5.71)	4.60 (3.61, 5.59)	3.219 (2.62, 3.82)	2.874 (2.297, 3.45)
c (mVs^{-1}) (95% coefficient bounds)	0.016 (-0.027, 0.058)	-0.014 (-0.115, 0.088)	-0.029 (-0.166, 0.108)	0.012 (-0.123, 0.146)
K_m (μM) (95% coefficient bounds)	18610 (12280, 24940)	715.1 (411.9, 1018)	197 (95.77, 298.1)	172.9 (70.45, 275.4)
SSE	0.010	0.0284	0.049	0.059
RMSE	0.034	0.064	0.091	0.099
R^2	0.997	0.995	0.992	0.989
Linear Model	$Y = S \cdot x + C$			
Linear Range ¹	0 – 3.5 mM	0 – 300 μM	0 – 100 μM	0 - 100 μM
Analytical Sensitivity (S) ($\text{mVs}^{-1}\text{mM}^{-1}$) (95% coefficient bounds)	0.226 (0.210, 0.243)	4.72 (4.15, 5.30)	11.79 (8.77, 14.82)	11.72 (11.0, 12.44)
C (mVs^{-1}) (95% coefficient bounds)	0.02 (-0.009, 0.049)	0.003 (-0.317, 0.324)	$7.8 \cdot 10^{-4}$ (-0.143, 0.143)	0.034 (0.003, 0.065)
SSE (linear)	0.004	0.023	0.034	0.003
RMSE (linear)	0.023	0.062	0.093	0.025
R^2 (linear)	0.993	0.985	0.967	0.997
Precision ²	17.8%	12.7 %	13.4%	19.8%
LOD (mVs^{-1})	0.033	0.030	0.019	0.017
LOQ (mVs^{-1})	0.070	0.063	0.039	0.047
LOD (μM) ³	69.01	6.86	3.00	0.26
LOQ (μM) ³	218.3	12.04	4.22	2.13
Resolution (μM) ⁴	24.52	1.03	0.48	0.4
¹ Linear range is defined as the measurement range were the linear model had $R^2 > 0.9$. ² Calculated as the average of the relative standard deviation of the measurements in the linear range. ³ Converted from mVs^{-1} to μM using the Michaelis-Menten model. ⁴ Calculated as the ratio between the standard deviation of the control measurements and the sensitivity in the linear range [58].				

3193



3194 *Figure 5.4 Calibration curves obtained by fitting data with Michaelis-Menten in the*
 3195 *extended range (left) and with a linear model (right) for (a)(b) LAA, (c)(d) glutamate, (e)(f)*
 3196 *choline and (g)(h) sarcosine in diluted human serum. Concentrations refer to the total*
 3197 *reaction volume.*



3198 *Figure 5.5 Averaged raw data from single microchannel (blue) and processed data (red) for*
 3199 *LAA (a) and sarcosine (b).*

3200

3201 **5.3.3. Ischemic Stroke Metabolites**

3202 Calibration curves for lactate and creatinine in diluted human serum are shown in Figure 5.6
 3203 while the complete characterisation of the platform for the analytes of interest is reported in
 3204 Table 5.5. Like the analysis performed for PCa-related metabolites, Kinetics constants were
 3205 estimated by data fitting to the Michaelis-Menten model. Also for lactate and creatinine, K_m
 3206 results are comparable with the values reported in the literature [49]. For both the
 3207 metabolites, the fit with the Michaelis-Menten model was satisfactory with R^2 values ≥ 0.96 .
 3208 Also in this case, a subset of data points with lower concentrations was fitted using a linear
 3209 model.

3210 As shown in Table 5.5, the linear range for lactate was smaller than the physiological one.
 3211 This suggests the need for sample dilution when testing lactate. The linear range for
 3212 creatinine was suitable for determination in the physiological range. The average standard
 3213 deviations of the measurement in the linear range for lactate and creatinine were 17.5% and
 3214 25.1%, respectively. LOD and LOQ were also quantified using the respective control
 3215 measurements. The LOD for expressed in μ M for lactate and creatinine were 31.85 μ M and
 3216 5.21 μ M, respectively. The LOQ for both the metabolites were 64.38 μ M and 36.55 μ M.
 3217 The performance of the platform in the quantification of lactate and creatinine indicates that
 3218 it is suitable for the determination of the two metabolites in the physiological range.

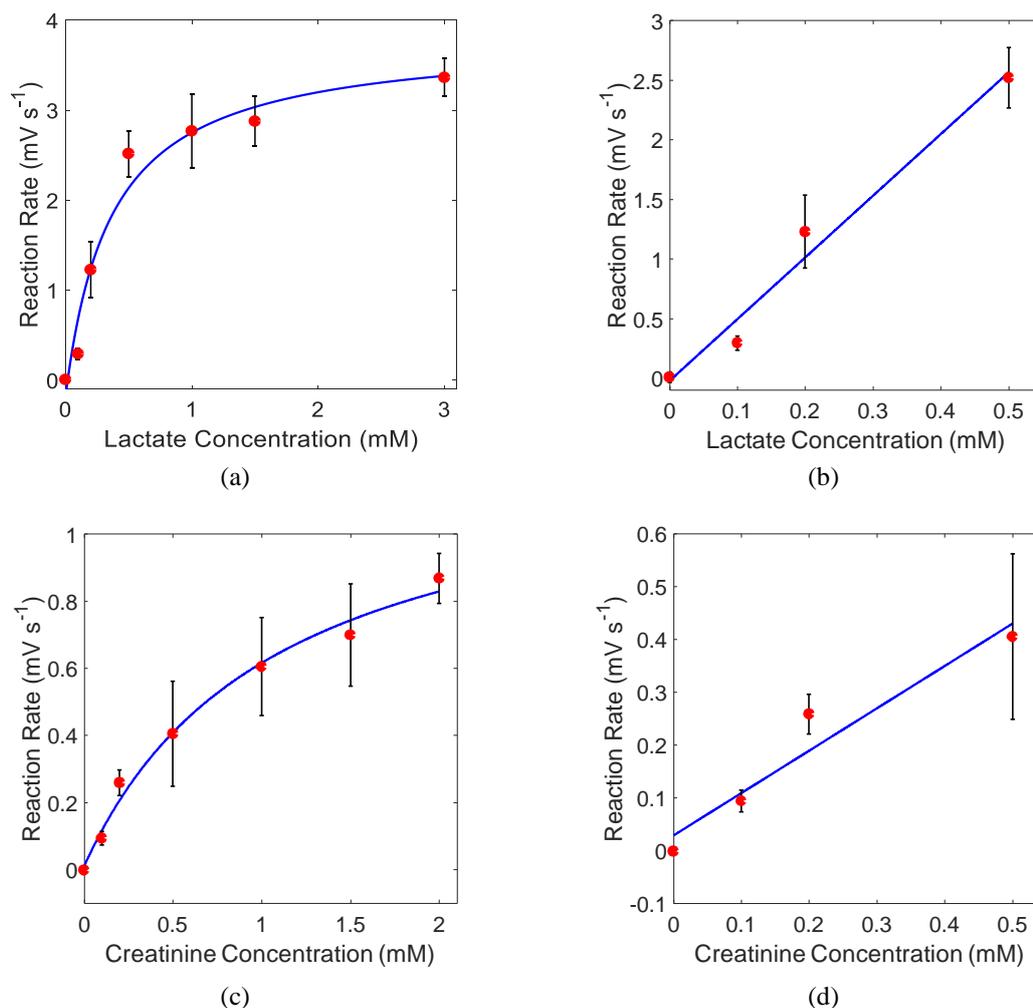
3219

3220 *Table 5.5 Platform Characterisation in diluted human serum for ischemic stroke related*
 3221 *metabolites. V_m , c and k_m are calculated using the Michaelis-Menten model. Metrics have*
 3222 *been defined in Table 2.3.*

	Lactate	Creatinine
Physiological Range	0.3 – 2.0 mM	100 – 150 μ M
Test Range	0 – 3 mM	0 – 2 mM
Relation with ischemic stroke	↑	↑
Model	$y = \frac{V_m \cdot x}{K_m + x} + c$	
V_m (mV s ⁻¹) (95% coefficient bounds)	3.99 (2.90, 5.08)	1.263 (0.818, 1.708)
c (mV s ⁻¹) (95% coefficient bounds)	-0.177 (-0.954, 0.601)	0.010 (-0.086, 0.106)
K_m (μ M) (95% coefficient bounds)	362 (260, 751)	1085 (807, 2089)
SSE	0.360	0.0069
RMSE	0.300	0.042
R ²	0.967	0.998
Linear Model	$Y = S \cdot x + C$	
Linear Range ¹	0 – 0.5 mM	0 – 0.5 mM
Analytical Sensitivity (S) (mV s ⁻¹ mM ⁻¹) (95% coefficient bounds)	5.175 (2.738, 7.612)	0.803 (0.143, 1.462)
C (mV s ⁻¹) (95% coefficient bounds)	-0.023 (-0.690, 0.644)	0.028 (-0.152, 0.209)
SSE (linear)	0.090	0.007
RMSE (linear)	0.212	0.057
R ² (linear)	0.977	0.932
Precision ²	17.5%	25.1%
LOD (mV s ⁻¹)	0.146	0.016
LOQ (mV s ⁻¹)	0.425	0.051
LOD (μ M) ³	31.85	5.21
LOQ (μ M) ³	64.38	36.55
Resolution (μ M) ⁴	7.92	39.76
¹ Linear range is defined as the measurement range were the linear model had R ² > 0.9. ² Calculated as the average of the relative standard deviation of the measurements in the linear range. ³ Converted from mV s ⁻¹ to μ M using the Michaelis-Menten model. ⁴ Ratio between the standard deviation of the control measurements and the sensitivity in the linear range [58].		

3223

3224



3225 *Figure 5.6 Calibration curves obtained by fitting data with Michaelis-Menten in the*
 3226 *extended range (left) and with a linear model (right) for (a)(b) lactate and (c)(d) creatinine.*

3227

3228 5.3.4. Discussion

3229 The biological experiments in diluted serum showed that the platform is suitable for the
 3230 quantification of LAA, glutamate, choline, sarcosine, lactate, and creatinine with
 3231 physiological concentrations. Experimental data were in agreement with the Michaelis-
 3232 Menten model. All the metabolites, except for lactate, showed a linear response within the
 3233 expected physiological concentration levels. For lactate, it is suggested the use of diluted
 3234 body fluid to take advantage of the linear response of the platform.

3235 The precision of the measurements, calculated as the average standard deviations, was in the
 3236 range 12.7 % - 25.1%, that is comparable to the precision of the glucose meters currently on
 3237 the market [237]. LODs and LOQs were lower than the expected physiological levels.
 3238 Additionally, for the selected applications, increased levels of analytes are expected.

3239 Therefore, the LOD and LOQ values do not impose any limitation on the selected
3240 applications.

3241 The analytical sensitivity of the platform was variable in relation to the metabolite under
3242 test. Analytical sensitivity ranged from was $0.226 - 11.79 \text{ mVs}^{-1}\text{mM}^{-1}$. A correlation was
3243 identified between the analytical sensitivity and the concentrations of the enzymes used for
3244 the assays. Assays formulated with a higher level of enzymatic solutions were more sensitive
3245 towards the lower concentration of the substrate and had a higher sensitivity. However,
3246 creatinine sensitivity was low despite the high concentrations of the enzymatic solution. In
3247 this specific case, it is worth underlining that the first reaction stage leading to H_2O_2 was
3248 made up of three different enzymatic reactions. Thus, this assay is not easily comparable to
3249 all the other ones. Creatinine assay was, in fact, expectedly slower than the other tests, where
3250 only one enzymatic reaction led to H_2O_2 . Despite the decreased sensitivity, creatinine testing
3251 demonstrated that the platform could also support more complicated enzymatic systems and
3252 that the suggested metabolites could be considered as a proof-of-concept of the platform.

3253 Regarding the versatility of the platform, it is should be emphasised that the same hardware
3254 with no modification was used for the measurements of six different metabolites linked to
3255 different diseases. This was achieved by minimal modification of the assay formation only.
3256 Aguably, the platform might be suitable for the quantification of substrates where a
3257 respective oxidase enzyme exists and a similar chemistry can be deployed. This might
3258 include the use of up to 350 oxidase enzymes and respective substrate reported in the enzyme
3259 database BRENDA [49]. Additional substrates could also be quantified using a series of
3260 multi-step reaction leading to the production of H_2O_2 (e.g. creatinine assay).

3261 There were some limitations to these experiments. Firstly, the sample composition was
3262 simplified. From a microfluidic point of view, the diluted serum (1:10) ensured a quick and
3263 reliable filling of the microcavities. Also, the sample was modified with a pure and freshly
3264 introduced substrate. The high dilution ratio of the serum simplified the composition of the
3265 sample by decreasing the concentration of both endogenous substrate and interfering
3266 substance. This scenario simplifies in many ways, the functioning of the platform in a real-
3267 life environment. A thicker whole plasma or blood sample has a much slower flow rate, and
3268 the filling of the microchannel is, therefore, less repeatable, as experimentally demonstrated
3269 in the previous chapter. Undiluted samples also contain impurities which degrade the signal
3270 to noise ratio of the recorded signal, consequently affecting the test result. From an organic
3271 point of view, an undiluted sample also contains thousands of additional molecules which

3272 can potentially interfere with the developed assay. Experiments with clinically source
3273 undiluted human plasma are illustrated in the next chapter.

3274

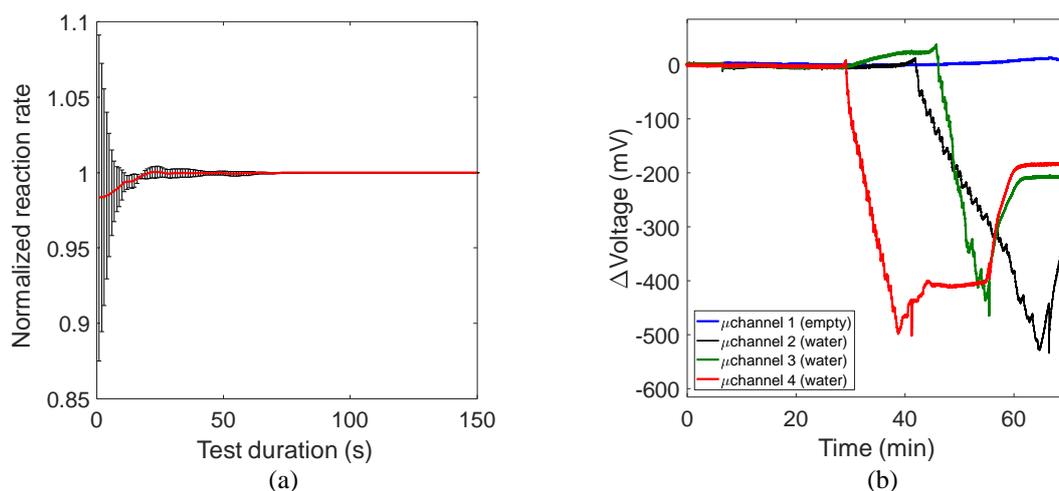
3275 **5.3.5. Test Duration**

3276 Some considerations can be done about the time that the platform requires to estimate the
3277 reaction rate. Only the initial reaction rate is important for the estimation of the substrate
3278 level. Thus, recording only the first part of the reaction is enough. This raises the question
3279 about the minimum time required for the platform to estimate the reaction rate.
3280 Experimentally, it was observed that tests with higher substrate concentrations required a
3281 shorter test duration. This was expected because the high substrate concentration created a
3282 rapid transmittance drop and a short recording was enough to determine the initial reaction
3283 rate. On the contrary, tests with lower substrate concentrations required a longer test duration
3284 to provide a reliable result. This was also expected since the additional data collected due to
3285 the increased time duration allowed a better estimation of the reaction rate. However, in a
3286 real-life scenario the substrate concentration is not known.

3287 To answer this question, additional data processing was performed. All the biological
3288 experiments recorded had a duration of 5 minutes. Three recordings from the glutamate
3289 dataset were used for this analysis. Conservatively, glutamate test with a substrate
3290 concentration of 50 μM was selected. The duration test of the recordings was gradually
3291 reduced by 1 second. Recording truncation was purely numerical. For each single shortened
3292 fragment of data, the reaction rate was calculated and normalised against the reaction rate
3293 obtained with the 5 minutes test. The results of the analysis are proposed in Figure 5.7(a). It
3294 shows that when using only 60 seconds of data from the reaction starting point, the algorithm
3295 was able to calculate the reaction rate with an error $< 1\%$ with respect to the full-length
3296 duration. The error then stabilised to zero for test length longer than 60 seconds. Thus, one
3297 minute can be considered as the minimum test duration required to the platform for the
3298 substrate quantification. For a conservative approach, one additional minute can be added to
3299 the previous amount as a tolerance factor.

3300 Arguably, evaporation can potentially pose a problem when handling liquid in the microliter
3301 scale. This raises the question of whether the drying of the sample in the microchannel is
3302 quick enough to interfere with the assay. To address the question, microchannels were filled
3303 with water, and sensor data were collected until the full evaporation of the sample.
3304 Experiments were performed at room temperature. Results are reported in Figure 5.7(b). For

3305 all the three channels analysed, no evaporation effect was observed in the first 27 minutes.
 3306 Subsequently, evaporation effects were evident and profoundly affected the signal.
 3307 Precisely, during the evaporation of the sample, the trend of the average signal of the
 3308 microchannel resembled the voltage spikes observed when the channel was filling. This
 3309 showed that the sample inside the microchannel was progressively evaporating, from the
 3310 more external pixels to the internal ones. After approximately 1 hour, the water sample was
 3311 evaporated entirely. This is a crucial figure for reagents loading into the microchannels,
 3312 where drying methods have been employed. Therefore, despite the volume of the sample,
 3313 the confinement of the liquid into the microstructure sensibly increased its evaporation time.
 3314 In summary, we can therefore conclude that a two-minute test duration is adequate for the
 3315 quantification of the metabolites of interest. A test with such duration can be considered
 3316 unaffected by the process of the evaporation of the sample, which started to be evident only
 3317 after 27 minutes.
 3318



3319 *Figure 5.7 (a) Normalised reaction rate calculated for different test durations. Test duration*
 3320 *was numerically reduced, and the reaction rate iteratively recalculated. Rate is normalised*
 3321 *to the rate calculated when using the full-length data (5 minutes). (b) Effects of water*
 3322 *evaporation on the platform. Evaporation effects start to be relevant after 27 minutes. The*
 3323 *test, whose duration was 5 minutes, can be considered unaffected by evaporation effects.*

3324

3325

3326

3327

3328 **5.4. Microchannel Functionalisation**

3329 For multiplexed assays, biological reagents need to be preloaded into the different
3330 microchannels with each channel acting as an individual reaction zone. The present section
3331 also focuses on the procedures for reagents lyophilisation, is a well-established and versatile
3332 procedure commonly used in the biotechnology industry for the production and storage of
3333 commercial products or reagents. The entrapment of the bioreagents was achieved by two
3334 processing steps: (i) deposition and (ii) freeze-drying.

3335

3336 **5.4.1. Deposition and Regents Printing**

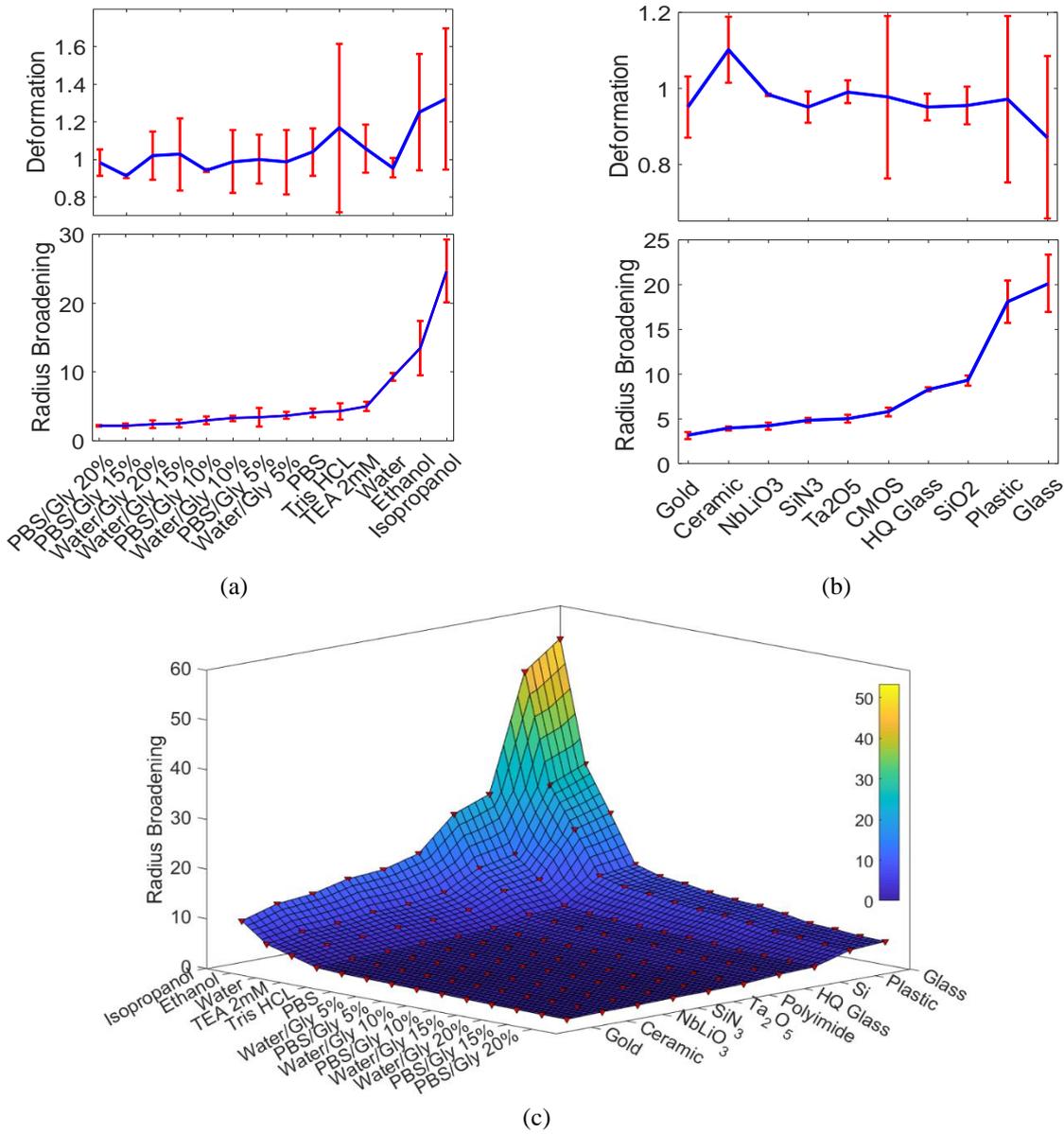
3337 Bioreagents deposition was mostly achieved by manual pipetting in the microchannel by
3338 micropipetting under the microscope. However, this method is not suitable for mass-
3339 production. Thus, a scalable approach for the functionalisation of the platform is illustrated
3340 here. In the following experimental study, the suitability of the printing techniques for the
3341 deposition of bioreagents on the chip is demonstrated. This was achieved by quantifying
3342 printing performance when using materials commonly employed in enzyme-based solutions.
3343 The Jetlab® II piezoelectric drop-on-demand inkjet printer was used in this experimental
3344 study. The printer was connected by serial ports (RS232 and 2xUSB 2.0) to a desktop
3345 computer (Advantech PPC-157T, Window 7 Pro, 32bit, Intel® Core Duo Processor,
3346 2.00GHz, 1GB RAM). By scaling down the orifice size to few micrometres (70 μm used in
3347 this experimental study), the process of drop ejection becomes very dependent on the
3348 operating conditions, and the jetting parameters need to be empirically tuned [301]. Here,
3349 jetting parameters were optimised according to a ‘trial and error’ process based on literature
3350 references and experimental evidence [301], [302]. The Jetlab II has eleven jetting
3351 parameters to be tuned, including stimulation wave shape, amplitude and frequency,
3352 backpressure of the print head, the temperature of the print head. The optimal jetting
3353 parameters allowed having picolitre droplets with no satellites, almost no solid angle, speed
3354 lower than 2m/s (to avoid splash) and high repeatability over time. However, for a specific
3355 ink, the set of parameters could not be unique [301], [302]. Parameter optimisation and
3356 analysis of the printed droplets was achieved using custom Matlab algorithms performing
3357 automatic drop recognition and image-processing tools. The radius of each drop,
3358 deformation and position were quantified. Since the printed droplets were not perfect circles
3359 for physical reasons, ‘drop radius’ is used to refer to as the radius of a circle approximating

3360 the printed drop. The deformation of the drop is the ratio between the effective area of the
3361 drop and the area of the perfect circle. The automatic drop recognition was performed using
3362 the Hough circle transform [302], a widely used technique for facial recognition in image
3363 processing [303].

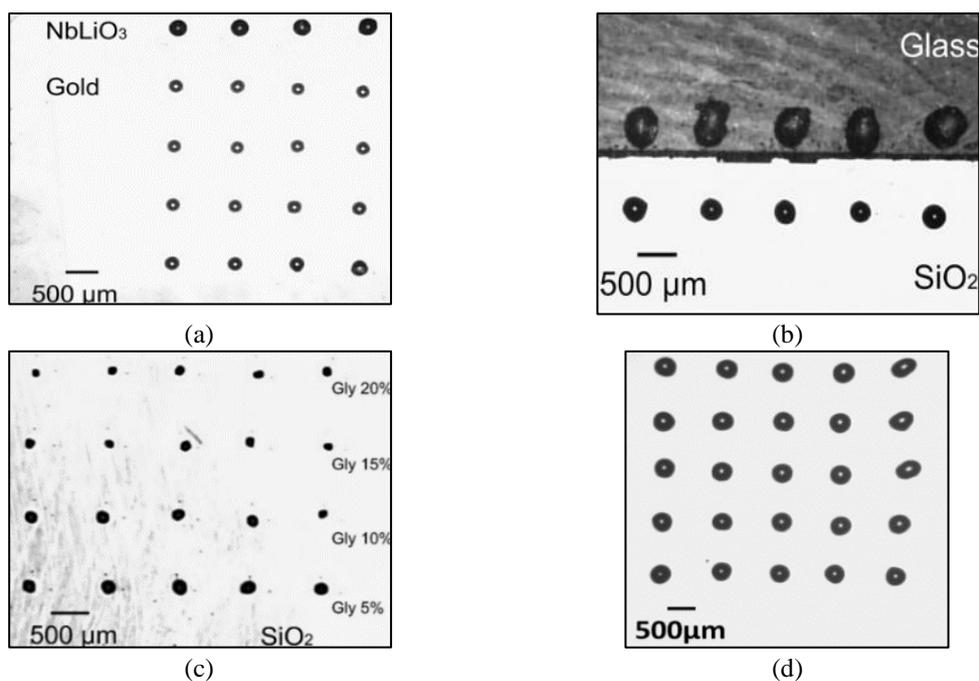
3364 The experimental study using 14 different inks and 10 different substrates showed that the
3365 printing performance depends on the materials employed in the process. The quantification
3366 of the printing performance in terms of drop deformation and radius broadening using
3367 different inks on silicon and using DI water on various substrates are presented in Figure
3368 5.8(a) and (b), respectively. Assuming that the effects of inks and substrates are independent,
3369 a numerical interpolation shown in Figure 5.8(c) highlights the printing performance for all
3370 the different combinations of ink and substrate. Demonstrative pictures are shown in Figure
3371 5.9. Printing performance was also quantified on Polyimide, the outer layer of high-voltage
3372 0.35 CMOS technology. Specifically, the use of a solution made by PBS buffer and Glycerol
3373 20% on polyimide showed a radius broadening of 1.96. By delivering several piezo
3374 stimulations, it was possible to print a desired amount of ink. However, the evaporation of
3375 the printed droplets was observed to be rapid. Figure 5.10(a) shows the reduction in the
3376 radius of the droplets over time while printing with different volume of a solution of
3377 PBS/glycerol 20% printed on silicon. The experimental analysis demonstrated that in the
3378 first 10 minutes after printing, part of the printed drop spontaneously evaporates (Figure 5.10
3379 (b)). Expectedly, the evaporation process was dependant on the type of ink used and the
3380 environmental condition.

3381 After having demonstrated that bio-printing is capable of depositing patterns with a size
3382 comparable to the CMOS chip, two different enzymatic solutions (cholesterol oxidase and
3383 glucose oxidase) were successfully deposited on the top of a CMOS chip. Post fabricated
3384 microstructure on the CMOS chip also helped improve the printing process performance.
3385 Figure 5.11 reports some optical microscope images of printed patterns on different
3386 substrates with and without microchannels. Figure 5.11(a) shows a picture of the Jetlab II
3387 inkjet printer used in this study. Figure 5.11(b) illustrates the shape and the volume of the
3388 ejected droplets. Figure 5.11(c) demonstrates that it is possible to print into a microfluidic
3389 channel 200 μm wide. Figure 5.11(d)-(g) demonstrate that the printing technique provides
3390 adequate deposition accuracy that can potentially allow the deposition of different inks into
3391 microstructures. The volume of the droplet can be controlled according to requirement.
3392 Figure 5.11(g) experimentally demonstrated that inkjet printing could be used for the direct

3393 deposition of bio-inks on CMOS. In the pictures, glucose oxidase was printed on the CMOS
 3394 chip. The printing time was less than 20 seconds. Patterning the surface of the chip can help
 3395 improving accuracy.
 3396

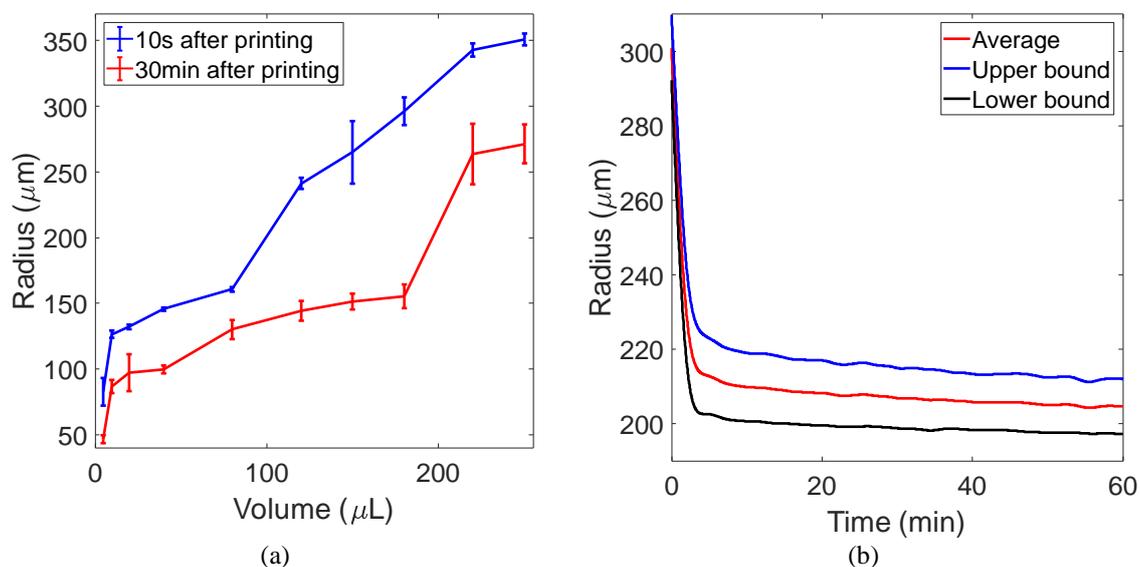


3397 *Figure 5.8 (a) Deformation (top) and radius broadening (bottom) of printed droplets using*
 3398 *14 different inks on a silicon substrate. (b) Deformation (top) and radius broadening*
 3399 *(bottom) of DI water on ten different substrates, including polyimide, the outer layer of*
 3400 *standard 0.35 CMOS technology. (c) Radius broadening numerical interpolation for 140*
 3401 *combinations of ink and substrate.*



3402 *Figure 5.9 (a) DI water printed on NbLiO₃ and gold. (b) DI water printed on glass and SiO₂.*
 3403 *(c) Different solutions containing glycerol on SiO₂. (d) Array of DI water droplets on silicon.*

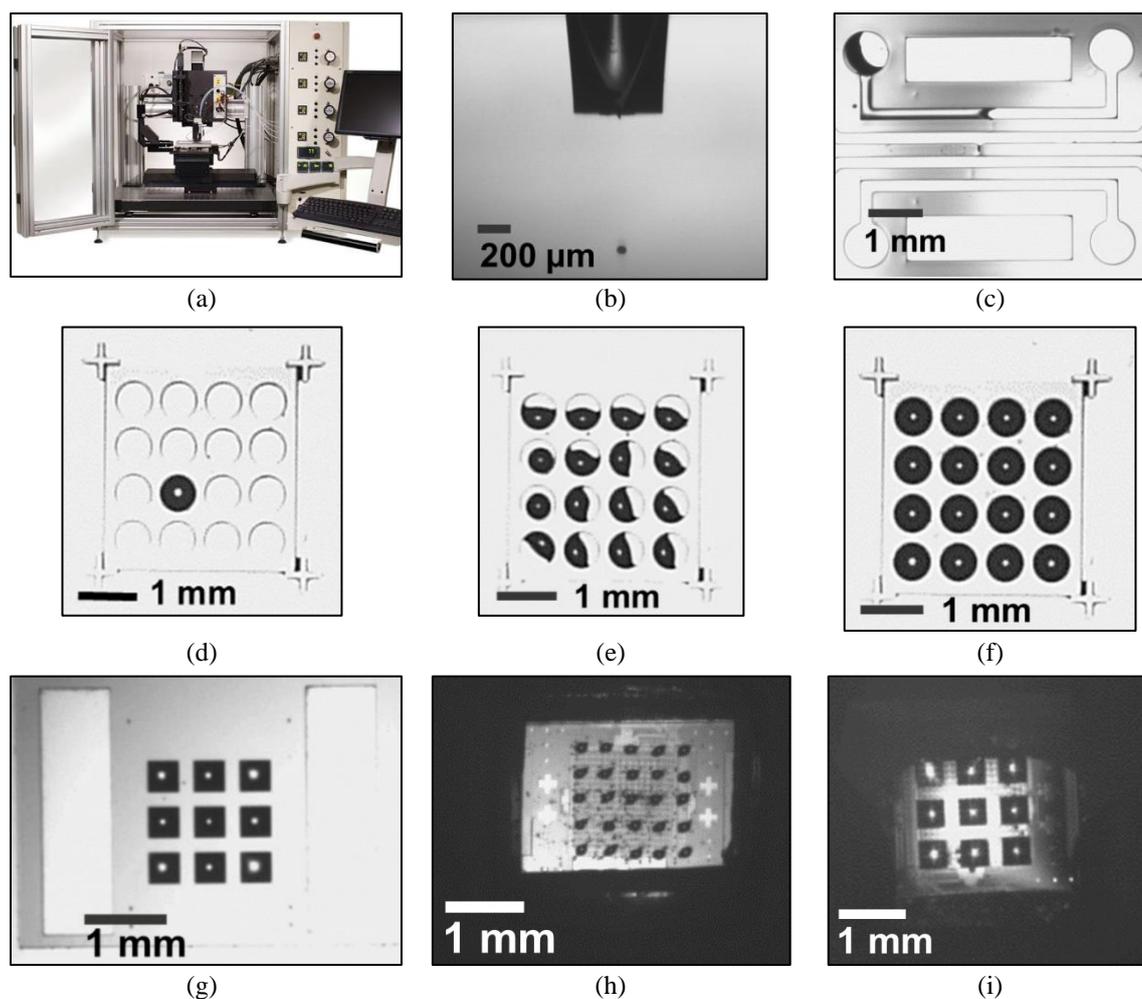
3404



3405 *Figure 5.10 (a) Evaporation dynamics of a solution of PBS/Glycerol 20% on a silicon*
 3406 *substrate: Volume vs Radius. (b) Short-term evaporation dynamics: radius vs. time. PBS on*
 3407 *silicon. Droplet volume was ~180μL.*

3408

3409



3410 *Figure 5.11 (a) Ejection of a picoliter droplet from a 70 μm print head. (b) Printing in a 200*
 3411 *μm wide open microchannel. (c)-(g) Printing into a SU-8 microstructure with different*
 3412 *positions and volume. (h) Direct enzyme printing (GOX) in an array format on the*
 3413 *Multicorder chip. (i) Multi-enzyme printing (GOX and ChOX) into a SU-8 structure*
 3414 *fabricated on top of the Multicorder chip.*

3415

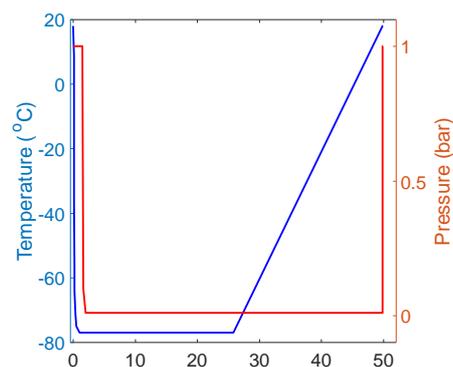
3416 **5.4.2. Freeze-drying**

3417 Lyophilisation was achieved by using a benchtop freeze-dryer - the Lyotrap by LTE
 3418 Scientific in Figure 5.12(a) - with a cylindrical condenser chamber (diameter: 20 cm, depth:
 3419 35 cm). The size of the chamber allowed the parallel processing of multiple cartridges. For
 3420 this model, the minimum temperature that can be reached in the chamber is -85°C , which
 3421 was suitable for this application where reagents are in an aqueous environment. The typical
 3422 drying cycle adopted in this work is shown in Figure 5.12(b). Samples with liquid reagents
 3423 to be lyophilised were loaded into the chamber at room temperature and atmospheric
 3424 pressure. After the Lyotrap was loaded, the top lid of the chamber was closed, and the
 3425 freezing cycle was activated. Typically, the chamber reached a temperature of -77°C in

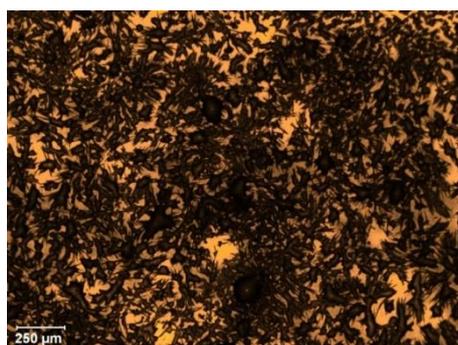
3426 approximately 30 minutes. Once reached a stable temperature, the sample was left in the
 3427 chamber for 1 hour at atmospheric pressure. In this phase, the functionalisation solution is
 3428 expected to freeze rapidly. Subsequently, the chamber was pumped down to pressure
 3429 typically in the range of 0.02 – 0.05 mbar. Generally, the chamber reached the target pressure
 3430 in about 15 - 30 minutes. The sample was left in this condition for 24 hours. After 24 hours,
 3431 the chiller of the unit was switched off, and the temperature of the chamber gradually
 3432 increased. The pressure of the chamber was kept in the same range. After a further 24 hours,
 3433 the temperature of the chamber was proximal to the ambient temperature. The chamber was
 3434 then slowly brought to atmospheric pressure in about a few minutes through a dedicated
 3435 valve. At this phase, the samples were unloaded from the unit and ready to be stored or used
 3436 for testing. Temperature, pressure, and timing of the processing were empirically tuned. The
 3437 temperature and pressure typically depend on the composition of the solution to be
 3438 lyophilised. Timings usually depend on the volume of the solution.



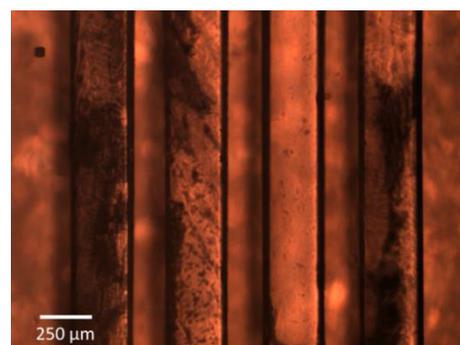
(a)



(b)



(c)



(d)

3439 *Figure 5.12 (a) The Lyotrap freeze-dryer from LTE Scientific. (b) Typical drying cycle used*
 3440 *in this work. (c) Reagents required for choline oxidase lyophilised onto a petri-dish*
 3441 *(stabiliser: 1% glycerol (w:w)). (d) Reagents required for choline oxidase lyophilised into*
 3442 *three PDMS microchannels. One channel was deliberately left unmodified to demonstrate*
 3443 *channel-specific capabilities.*

3444 The process of lyophilisation was successful for reagents deposited on both glass substrates
3445 (e.g. petri dish and well plates) and into microfluidics structures. Figure 5.12(c) shows the
3446 result of the lyophilisation process into a 385-well plate using reagents for choline assay (i.e.
3447 ChOx, HRP and o-dianisidine). Successful lyophilisation was also obtained when the
3448 reagents were inserted into microchannels. As shown in Figure 5.12(d), different
3449 microchannels were loaded with application-specific reagents. Therefore, the process
3450 enables multiplexed testing. Reagents were also successfully freeze-dried on the chip.
3451 However, the process of lyophilisation was found to be affecting the CMOS chip, which
3452 usually became unresponsive after undergoing this process multiple times. This is not an
3453 issue for an application where the CMOS chip is meant to be disposable.

3454

3455 **5.4.3. Reagents stability**

3456 The stability of the reagents over a period of time after the lyophilisation was experimentally
3457 assessed using for the choline reagents as a case study.

3458 **Materials and methods.** The activity of the reagents was evaluated by the micro-
3459 spectrometer fFTA-1 from Foster and Freeman using a 384-wells clear plate. Experiments
3460 were performed in triplicates, and the results of this study are summarised in Figure 5.13.
3461 First, the initial reaction rate was estimated using reagents in solution (Figure 5.13(a)). The
3462 reaction rate was measured by mixing 50 μ L of a test solution containing 1 mM of choline
3463 in 0.1 Tris HCl (pH 8) and 50 μ L of a reacting solution composed of 20 μ L of ChOx
3464 (150 U/mL), 20 μ L of HRP (300 U/mL) and 10 μ L of 41 mM o-dianisidine. Subsequently,
3465 50 μ L of reacting solutions were freeze-dried into different wells of the 384-wells plate using
3466 the Lyotrap by LTE scientific. There is evidence in the scientific literature that
3467 cryoprotectant substances (stabilisers) can increase the stability over time of the lyophilised
3468 substances [304]. Thus, the reacting solutions were freeze-dried with and without potential
3469 stabiliser solutions (see Figure 5.13). Four different types of stabiliser solution combinations
3470 were used: (i) the addition of glycerol with 1% and (ii) 2% w:w ratio, (iii) and (iv) the
3471 addition of the commercial stabilizers STKES by SunChemicals, in two different
3472 formulations. The composition of the commercial stabiliser was not known, due to copyright
3473 reason. However, no interference with the colorimetric reaction was expected, according to
3474 the company guidelines.

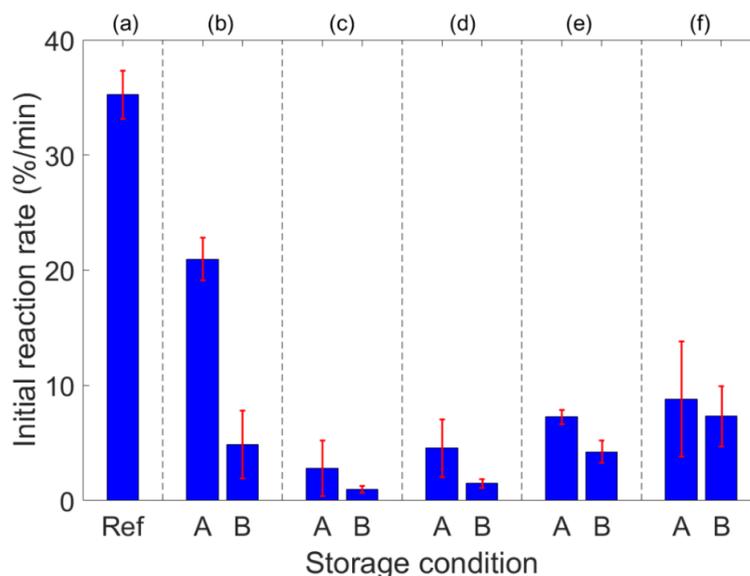
3475 After the lyophilisation, the stability of the reagent was tested using a solution by mixing
3476 50 μ L of a test solution containing 1mM of choline in 0.1 Tris HCl (pH 8) and additional

3477 50 μ L of the buffer. The reagents were tested within 2 hours after the completion of the
3478 lyophilisation process (storage condition: A) and after seven days storage at 20°C into a
3479 vacuum-sealed plastic bag under dark conditions (storage condition: B).

3480 **Results.** For all the formulations and conditions, the freeze-drying process was observed to
3481 affecting the activity of the reagents. By observing the results in condition 'A', it can be
3482 assumed that the lyophilisation process created an inherent loss of the activity of the reagent.
3483 Among all the formulations, the one with no additive retained most of the activity when
3484 tested in storage condition A. However, the loss of activity due to the lyophilisation process
3485 can be compensated by increasing the enzymatic units and the concentration of the reagents
3486 to be freeze-dried. The stability of the lyophilised reagents over time is expressed by storage
3487 condition B. After seven days of storage, the formulation with no additive reported the most
3488 significant drop in activity: -76.8%. The formulation containing glycerol improved the
3489 stability, with approximately a -67% drop for both the conditions. The stability was further
3490 enhanced using the commercial stabiliser kit, with an average decrease in the activity of -
3491 29% in 7 days. Reagents stored with no vacuum-sealed bag (i.e. exposed to open-air)
3492 reported inconsistent results due to partial rehydration, due to ambient humidity. Therefore,
3493 storage under vacuum condition is recommended.

3494 **Discussion.** Based on this data, reagent stability can be estimated in different storage
3495 conditions using the standard model for accelerated ageing (American Society for Testing
3496 and Materials, standard F1980-02) [305]. The standard for accelerated ageing is based on
3497 the Arrhenius' law. Typically, reducing the storage temperature of 10°C increases the shelf
3498 life of a multiplication factor Q_{10} . Q_{10} is set to 2 for most of the applications [305]. The shelf-
3499 life is defined as the time required for a property to be lower than a certain threshold [305].
3500 For enzymatic stability, such as in this case, we can define the shelf-life of the reagents as
3501 the storage time producing an enzyme activity decrease more than 10%. The shelf-life
3502 estimations of the lyophilised reagents for choline assay in different storage conditions are
3503 summarised in Table 5.6. In summary, the use of stabiliser for the lyophilisation process has
3504 the potential to increase the shelf-life of the reagents. The best-case-scenario obtained in this
3505 work is a shelf-life of more than 2 months when freeze-drying the reagents with the
3506 commercial stabiliser STKES by SunChemicals and storing the sample at -20°C. It is
3507 expected that the shelf-life of the lyophilised reagents for all the other assays are like the one
3508 estimated for choline.

3509



3510

3511

Figure 5.13 Assessment of the stability of the reagent after freeze-drying for choline. Storage

3512

condition: Ref = reference (no lyophilisation); A: freeze-dried reagents tested within 2 hours

3513

after the completion of the process. B: freeze-dried reagents tested after 7 days of storage at

3514

20°C in a vacuum-sealed plastic bag and in dark conditions. (a) Reaction in solution.

3515

Reagents were freeze-dried with (b) no additive, (c) with 1%, (d) 2% glycerol, (e),(f) with

3516

two different formulations of the commercial stabiliser STKES by SunChemicals.

3517

3518

Table 5.6. The shelf life of the lyophilised reagents for choline assay.

Storage temperature (°C)	Shelf life (reduction of 10% of reaction rate) in days				
	No additive	1% glycerol	2% glycerol	Commercial stabilizer (1)	Commercial stabiliser (2)
20*	0.92	1.08	1.04	1.7	4.21
10**	1.83	2.17	2.08	3.41	8.42
0**	3.67	4.33	4.16	6.83	16.83
-10**	7.33	8.67	8.33	13.67	33.67
-20**	14.66	17.33	16.67	27.33	67.33

* Shelf-life calculation based on the data
 ** Shelf-life estimation using accelerated ageing model [305]

3519

3520

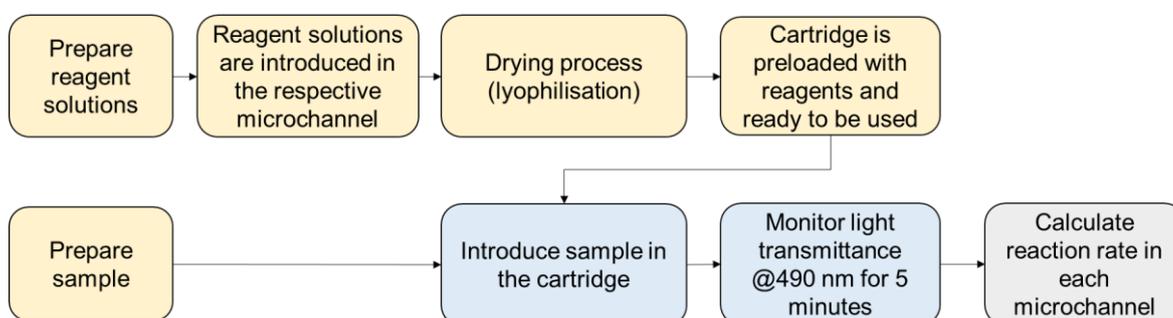
3521 5.5. Multiplexed Assays

3522 5.5.1. Multiplexed Assays in Human Plasma

3523 The capability of the platform working with preloaded reagents in the dry state was verified
3524 with glutamate assay and controls performed simultaneously in human plasma.

3525 **Materials and methods.** A cartridge with four microchannels ($h \sim 290 \mu\text{m}$) was
3526 functionalised with three channels dedicated to glutamate assay and one channel left for the
3527 negative control. Accordingly, two solutions were prepared for the microchannel
3528 functionalisation: a control solution and a glutamate assay solution. The former solution was
3529 used to functionalise microchannel dedicated to negative control testing. The latter was used
3530 to functionalise microchannels allocated for metabolite assays. $1 \mu\text{L}$ of the solution was
3531 deposited in the respective microchannel. The protocol for solution preparation is reported
3532 in Appendix I. The deposition was obtained both by pipetting and printing. Same results were
3533 obtained, regardless of the deposition method. After the deposition, solutions were
3534 lyophilised. No stabiliser was used during the lyophilisation process. Cartridges were used
3535 for experiments immediately after the completion of the lyophilisation process. Cleaning
3536 procedures and setup of the experiment were identical to the one previously described.
3537 Human plasma was purchased from Sigma Aldrich and reconstituted following the
3538 manufacturer instructions. It is expected that human plasma had an endogenous
3539 concentration of glutamate. The sample was then spiked with additional known
3540 concentrations of glutamate. A volume of $20 \mu\text{L}$ of the sample was introduced into the
3541 cartridge with no further dilution. Experiments were performed in triplicates. A schematic
3542 representation of the adopted protocol is shown in Figure 5.14.

3543



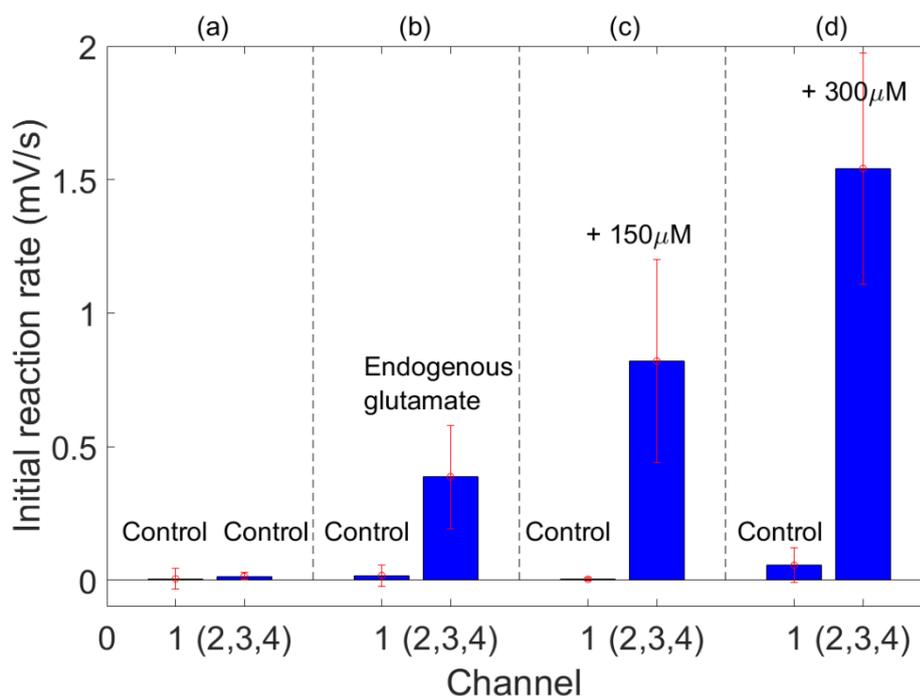
3544

3545

Figure 5.14 Protocol adopted for multiplexed assays in human plasma.

3546 **Results.** Results of the experiments are presented in Figure 5.15. Expectedly, channels
 3547 allocated for control measurements provided a minimum measurable signal, with an average
 3548 rate of $0.031 \pm 0.03 \text{ mVs}^{-1}$. However, for the channels functionalised with the solution
 3549 containing GLOx, the rate of the reaction, using the same unmodified plasma sample,
 3550 increased of more than 10 folds to $0.394 \pm 0.188 \text{ mVs}^{-1}$. Accordingly, rates increased further
 3551 when the plasma sample was spiked with $150 \mu\text{M}$ and $300 \mu\text{M}$, respectively. Excluding the
 3552 measurements on the unmodified plasma sample, data points had high linearity ($R^2 = 0.977$).
 3553 The linearity justified the estimation of the endogenous concentration of the unmodified
 3554 sample using the auto-controlled approach, adopting the two spiked samples as positive
 3555 controls. Thus, the glutamate level was estimated to $108.4 \mu\text{M}$. Under this assumption, a
 3556 calibration curve was obtained using a linear model and shown in Figure 5.16(a). The
 3557 sensitivity of the platform (slope of the linear model) in these experiments was 3.3
 3558 $\text{mVs}^{-1}\text{mM}^{-1}$. Averaged and filtered data and signal after curve fitting are shown in Figure
 3559 5.16(b).

3560



3561

3562

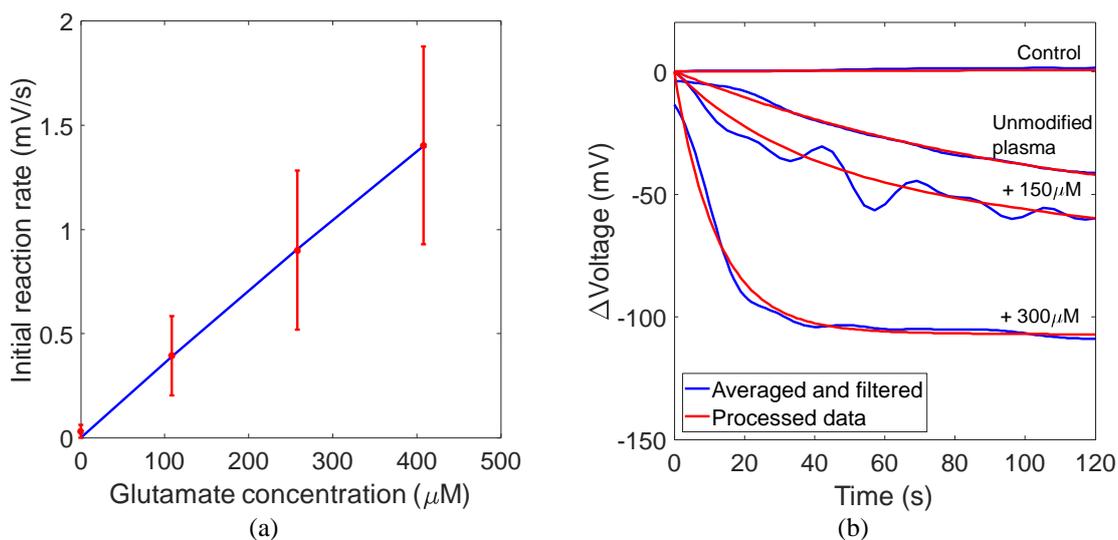
3563

3564

3565

3566

Figure 5.15 Glutamate experiments in undiluted human plasma with preloaded dry reagents. (a) All channels were functionalised for control measurements. The introduced sample was unmodified plasma. (b)-(d) Channel 1 was functionalised for control measurement, the remaining for glutamate assay. The introduced sample was (b) Unmodified plasma; (c) plasma spiked with $150 \mu\text{M}$ of glutamate; (d) plasma spiked with $300 \mu\text{M}$ of glutamate.



3567 *Figure 5.16 (a) Calibration curve of glutamate assay with preloaded reagents. (b) Average*
 3568 *and filtered data (blue) and processed data (red) for different samples.*

3569

3570 **Discussion.** It is not possible to directly compare the rates calculated from the lyophilised
 3571 reconstituted reagents on-chip with the rates obtained from wet assays for several reasons
 3572 explained below:

- 3573 • Microchannels were functionalised with a different number of units with respect to the
 3574 units used in wet experiments.
- 3575 • During the drying process activity loss is expected.
- 3576 • Plasma introduced in the platform had no further dilution.
- 3577 • The process of rehydration of the reagents could produce systematic modification on the
 3578 light absorbance drop.

3579 Although a direct comparison is not suitable, there have been several positive outcomes of
 3580 this work. This set of experiments is the first of the multiplexed assays performed on the
 3581 CMOS chip, with 1 channel always dedicated to the control measurement and the others
 3582 performing the actual measurements. An optical inspection confirmed that channels were
 3583 successful in confining the liquid, and no leakage was observed. Nevertheless, crosstalk
 3584 between two adjacent channels is still possible. This is due to optical effects of reflection
 3585 and dispersion taking place in the platform since there are multiple optical interfaces: air-
 3586 PDMS, PDMS-sample, sample-passivation layers, passivation layers-doped region. Thus, a
 3587 crosstalk quantification can be computed using the following approach [45]:

$$\text{Crosstalk}_{\%} = \frac{\sum_{i=1}^N \frac{|r_{c,i} - \mu_c|}{|r_{t,i} - \mu_c|}}{N} \cdot 100 \quad (5.1)$$

3588 Where $r_{c,i}$ is the generic rate in the control channel when the adjacent channel is performing
3589 a metabolite assay, $r_{i,i}$ is the generic rate in the assay channel when the adjacent channel is
3590 performing a control measurement, μ_c is the average rate in the control channel when the
3591 adjacent channel is performing a control measurement, N is the number of averaged
3592 experiments. Accordingly, average channel-to-channel crosstalk of 2.59 ± 0.8 % was
3593 quantified in these set of tests.

3594 From a fluidic point of view, optical inspection showed that the layer of powdered reagents
3595 within the microchannels promoted a reliable and stable flow.

3596 In conclusion, these experiments exhibited that this platform could perform simultaneous
3597 assays for glutamate and related control, using on-chip preloaded reagents. However, the
3598 loss of activity of the reagent was observed due to the functionalisation process, and the
3599 additional noise introduced by the reagents' rehydration has the potential to degrade the
3600 performance of the platform.

3601

3602 **5.5.2. Paper Microfluidics: An Alternative Approach**

3603 On-chip multiplexed assays have also been demonstrated by using an alternative method
3604 based on paper-microfluidics. This work has been carried out in collaboration with Dr
3605 Chunxiao Hu and Dr Srinivas Velugotla [306]. Dr Chunxiao Hu and Dr Srinivas Velugotla
3606 designed the concept idea and developed prototypal paper microfluidics. I have completed
3607 the paper-microfluidic manufacturing by appropriate functionalisation. Dr Chunxiao Hu
3608 performed biological experiments. I also offered technical support to all the phases of the
3609 processing. The reader and GUI, as developed in this PhD research project, were also
3610 employed. A detailed report of this work has been published [306]. In this section, an
3611 overview of the work is presented to demonstrate the versatility of the platform.

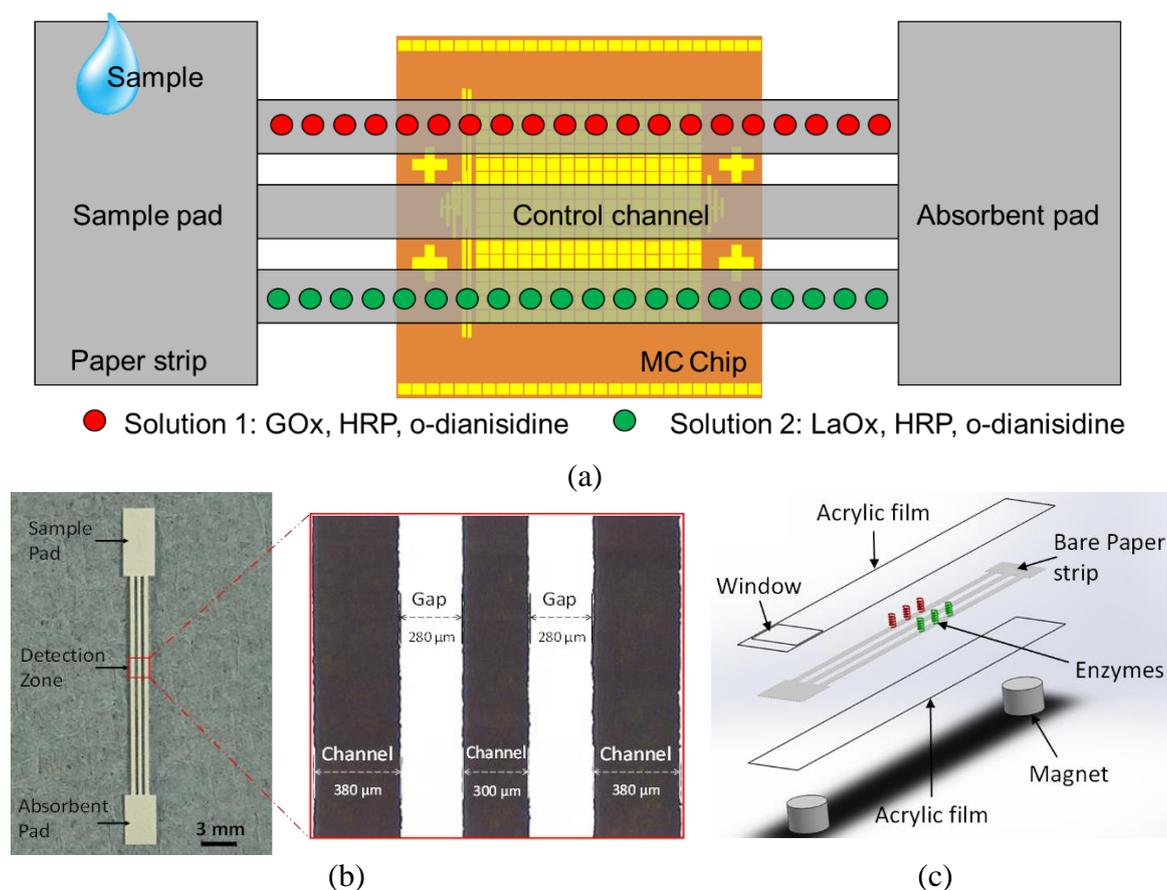
3612 The paper-strip based platform is schematically represented in Figure 5.17(a).
3613 Functionalised paper microchannels were placed on top of the active area of the CMOS chip.
3614 Once the sample was introduced on the fluidic input, it flowed through the paper substrate
3615 due to capillary effect and split into three microchannels where the colorimetric reaction was
3616 triggered. The platform was designed for the simultaneous colorimetric determination of
3617 glucose and lactate on cellulose, which is partially permeable to visible light. A CMOS chip
3618 was glued to a chip carrier and wire bonded. No microfluidics was fabricated on top of the
3619 CMOS. Reader and GUI were unchanged.

3620 **Materials and methods.** A paper-microfluidics strip to be placed on top of the sensing area
3621 was separately fabricated. A Grade 1 Cellulose Chromatography Paper (thickness: 0.18 mm;
3622 water linear flow rate: 130 mm/30 mins) was purchased from GE Healthcare Life Sciences
3623 to be used as the substrate for the paper microfluidics. The paper microfluidics was
3624 fabricated using laser micromachining (CO₂ laser cutting machine by Laser Micromachining
3625 Ltd.). Laser micromachining had a few advantages than other commonly used techniques,
3626 including wax printing and photolithography. It required only a single step of fabrication
3627 with no need of cleanroom facilities. It was a flexible process with good reproducibility,
3628 high throughput, and low cost. The paper strip, as shown in Figure 5.17(b) had a size of
3629 30 × 2.8 mm. It was composed of (i) sample pad (ii) detection zone and (iii) absorbent pad.
3630 The sample pad (length: 5 mm) was used for sample loading. The detection zone (2 × 2 mm)
3631 had approximately the same size of the active area of the CMOS chip. The absorbent pad
3632 (length: 4 mm) was in place to absorb overflowed liquid. Three microfluidic channels
3633 were fabricated. Lateral channels were 380 μm wide. The central channel, which was used
3634 for negative control measurements, had a width of 300 μm. Two 280 μm wide gaps between
3635 the channels prevented crosstalk.

3636 Two different solution inks containing reagents for the lactate assay and glucose assay were
3637 printed on the specific paper microfluidic channels using the Jetlab II printer (see Appendix
3638 J for protocol). The freeze drier (Lyotrap by LTE Scientific) was used to store freeze-dried
3639 paper strips right after the enzyme printing. No noticeable signal drop was observed after
3640 two weeks of storage in the fridge at 4 °C.

3641 To increase mechanical strength, reduce sample evaporation and reduce contamination, the
3642 paper strip was sandwiched in two transparent acrylic films (3MTM 9969 Diagnostic
3643 Microfluidic Adhesive Transfer Medical Tape), as shown in Figure 5.17(c). A laser
3644 micromachined aperture in the top acrylic film was used for exposing the sample pad. The
3645 acrylic films provided excellent support to the bare paper strip so that it could be easily
3646 folded to accommodate the chip surface. Preliminary experiments were performed to prove
3647 that the acrylic film had no discernible effect on the biological reaction. The paper strip was
3648 kept in place on top of the CMOS chip by magnet bases.

3649



3650 *Figure 5.17 (a) Schematic of the paper strip based platform. (b) Fabricated paper strip and*
 3651 *size of the paper microchannels. (c) Encapsulation of the paper strip into acrylic films [306].*

3652

3653 **Results.** Analyte solutions containing glucose and lactate were measured in a buffer solution
 3654 simultaneously with the photodiode array. The total volume of the solution was 6 μL, which
 3655 was large enough to wet the channels in a relatively short time, but not too large to cause an
 3656 overflow. A preliminary analysis showed that no obvious crosstalk was observed [306]. In
 3657 total, three concentrations of lactate (0.5, 1, 2 mM) and glucose (2.78, 5.55, 11.1 mM) were
 3658 measured. Lateral channels were dedicated to the quantification of lactate and glucose,
 3659 where a signal decrease was observed. The central channel was used as a control channel
 3660 where no signal drop was observed.

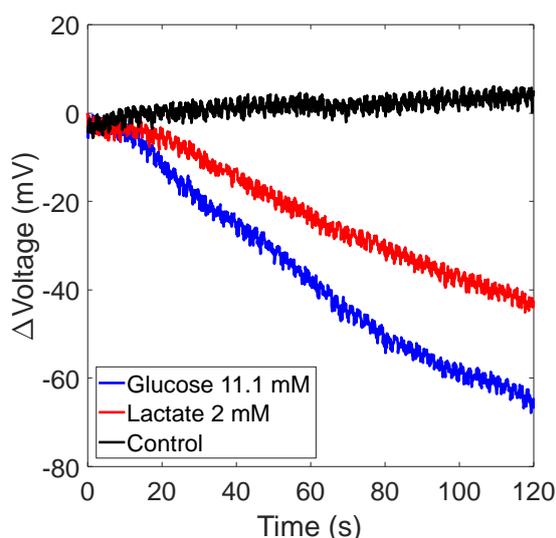
3661 All the three microfluidic channels were wet simultaneously, which gave a good comparison
 3662 of the reactions occurring on the three individual channels. Both enzymatic reactions
 3663 produced a colour change from clear to brownish, which absorbed the green LED light,
 3664 therefore decreasing the amount of light getting to the photodiode and therefore decreasing
 3665 the voltage signal. A new paper-strip was used for each measurement. No washing step of

3666 the chip was required due to the encapsulation of the paper strip. The change in photodiode
 3667 voltage for different channels is plotted Figure 5.18. Initial reaction rates were calculated,
 3668 and calibration curves were obtained [306]. The Michaelis constant K_m values were
 3669 estimated and found to be 33 ± 13 mM for glucose-glucose oxidase and 1655 ± 527 μ M for
 3670 lactate-lactate oxidase, respectively. The LOD was 520 μ M for glucose and 110 μ M for
 3671 lactate. Detailed results have been published in [306].

3672 **Discussion.** There are three main advantages of using paper strips rather than on-chip
 3673 integrated microfluidics. Firstly, paper strips can be easily disposed of and incinerated.
 3674 Secondly, the use of paper strip implies the re-use of the CMOS chip leading to a lower cost
 3675 per test. Thirdly, an inherent capability of the passive flow of the paper strip dramatically
 3676 simplifies the platform.

3677 This approach has some limitations. The alignment of the paper strip to the sensing area is,
 3678 in fact, crucial and needs to be supported by an additional mechanical structure in a real-life
 3679 scenario. Also, the paper strips can accommodate a limited number of microfluidic channels
 3680 because laser patterning has a lower resolution than photolithography. Thirdly, the sample
 3681 is not directly integrated onto the sensing area, which can potentially reduce the sensitivity
 3682 towards low concentrations of the substrate. In conclusion, the versatility of the platform
 3683 allows its use in different configurations which can satisfy different application-specific
 3684 requirements.

3685



3686

3687 *Figure 5.18 Real-time recording of the reactions detected by the three paper channels. Data*
 3688 *shown is the average over the channel. Lateral channels were functionalised for glucose and*
 3689 *lactate assays. Central channels were used for blank measurements (control).*

3690

3691 5.6. Whole Blood Experiments

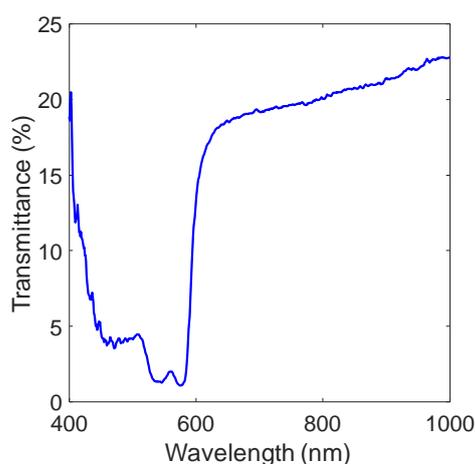
3692 In a real-life scenario, sample processing steps need to be minimised or eliminated. This rise
 3693 the question if the developed platform is suitable for metabolite quantification with no or
 3694 integrated sample processing. The use of whole blood in optical measurements it is
 3695 challenging because of the reduction in the light transmission. The spectrum reported in
 3696 Figure 5.19 shows the light transmittance of whole human blood inserted in a microfluidic
 3697 channel ($h \sim 290\mu\text{m}$) obtained using a micro-spectrometer (ffTA-1 from Foster and
 3698 Freeman).

3699 The light absorbance is also particularly high in the range of wavelength where the platform
 3700 operates. The light transmission of the whole blood is around 4% at 490 nm. However, a
 3701 sharp increase in the transmission is observed for wavelength higher than 600 nm, with a
 3702 20% transmittance at 800 nm. Besides the low light transmission, the whole blood is also
 3703 viscous and contains many impurities. It is therefore expected a further decrease in the SNR
 3704 for experiments performed in whole blood. To assess the possibility of the use of whole
 3705 blood on the platform, two different strategies have been implemented: (i) direct assay in the
 3706 whole blood and (ii) on-chip blood filtration.

3707

3708 **Direct assay on whole blood.** Preliminary experimental studies demonstrated that the
 3709 change in absorbance was detectable also in whole blood as the sample, with no pre-
 3710 processing. One sample of human blood was purchased from Cambridge bioscience.

3711



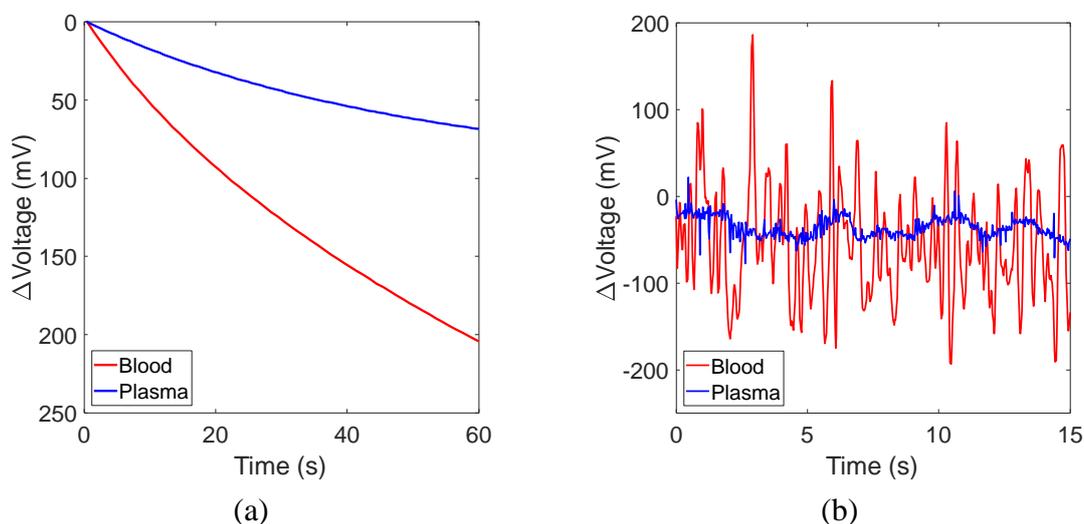
3712

3713 *Figure 5.19 Light transmittance spectrum for whole blood in a microfluidic channel with*
 3714 *$h \sim 290\mu\text{m}$. The curve is an average over three measurements.*

3715 Half of the sample was centrifuged, and plasma was extracted. Both plasma and blood from
 3716 the same sample were spiked with an additional LAA concentration of 3.75 mM. The
 3717 resulting samples were tested using the same protocol adopted for the experiments with
 3718 diluted serum. For the testing in whole blood, the light intensity of the LED was increased
 3719 to keep the working point in the same range as previous experiments.

3720 Despite the low transmittance, an increase in absorbance was also observed when blood was
 3721 used as the sample under test, as shown in Figure 5.20(a). When comparing the rate of the
 3722 reaction in blood and plasma from the same sample, a higher initial rate was observed when
 3723 using blood. It is not completely clear the reasons leading to increased rate from this
 3724 preliminary study. Probably, the process of centrifugations filters out compounds that are
 3725 catalysing the reaction. Also, whole blood might contain a higher concentration of free
 3726 oxygen, which also takes part in the colorimetric reaction. However, when considering the
 3727 system noise, the presence of unprocessed blood degraded the quality of the signal (see
 3728 Figure 5.20(b)). High-frequency noise was introduced when using unprocessed blood, with
 3729 peak-to-peak spikes reaching 200 mV. The high-frequency noise was probably related to the
 3730 presence of agglomerates of molecules free to move on the top of the sensors. In conclusion,
 3731 direct assay on whole blood was possible, but additional work is needed to reduce or
 3732 minimise the noise introduced by the impurities in the sample.

3733

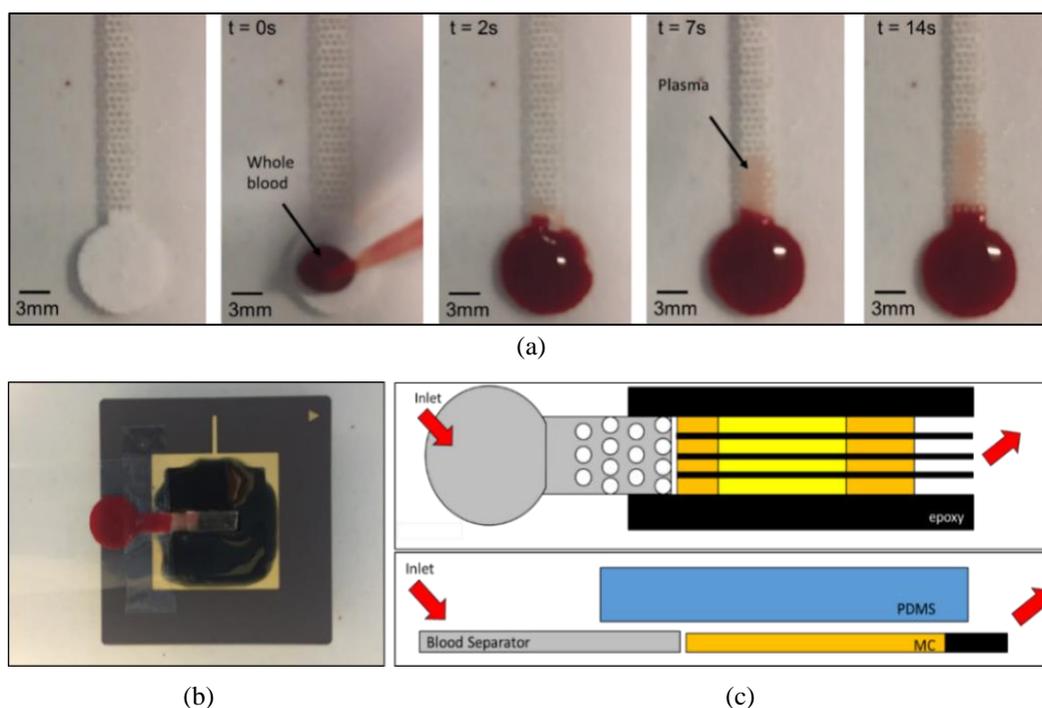


3734 *Figure 5.20 (a) Processed output for LAA assay in blood and plasma. Both blood and plasma*
 3735 *were modified with 3.75mM of LAA. (b) Unprocessed data from a single-pixel selected into*
 3736 *a microchannel. LAA assay in blood and plasma, both modified with 3.75mM. The noise*
 3737 *level when testing LAA in the blood was substantially higher than when testing LAA in*
 3738 *plasma.*

3739

3740 **On-chip blood filtration.** Integration of a blood filter for on-chip sample preparation has
3741 the potential to increase the practical use of the platform. Integrating commercially available
3742 passive blood filters with custom microfluidics platform has already been reported in the
3743 scientific literature [307], [308]. Thus, several passive commercial blood filters were
3744 purchased and tested for their integration with the cartridge. Glass fibre blood separator LF1,
3745 MF1, VF2 and GF/DVA were purchased from GE Healthcare. The Vivid™ plasma
3746 separation membrane was also obtained from PALL Corporations. Blood filtration devices
3747 were tested using whole blood commercially sourced from Cambridge Bioscience. The
3748 blood sample was not subjected to any freezing step since freezing modifies the shape and
3749 the properties of red cells. All the commercially sourced filters use porous materials (with
3750 variable porous size) to trap red cells during the passive flow of the sample. Among the
3751 filters commercially sourced, the glass fibre blood separator LF1 was adopted because it
3752 provided more reliable results according to the target sample volume (10 – 20 μL). The LF1
3753 blood separator has a thickness of 247 μm , wicking rate of 35.6 s/4cm, and water absorption
3754 of 25.3 mg/cm^2 . Thus, the LF1 glass fibre blood separator was shaped using a laser cutter
3755 (CO_2 laser cutting machine by Laser Micromachining Ltd). A circular pad with a 1 cm
3756 diameter was used as a sample pad. From the sample pad, a straight 3 mm wide glass fibre
3757 strip was used to converge the plasma flow in the preferred direction. The strip was also
3758 patterned with laser-cut perforation to physically reduce the absorbance of the substrate and
3759 facilitate the flow for plasma.

3760 Figure 5.21(a) demonstrates the process of blood filtration on the laser-cut device. 15 μL of
3761 blood inserted on the sample pad and plasma was extracted in the glass fibre strip after a few
3762 seconds by capillary action. The passive filter was then integrated with a cartridge - see
3763 Figure 5.21(b). For its integration, part of the epoxy on the side of the CMOS chip was
3764 removed to create a slot for the insertion of the glass fibre filter. The blood filter was then
3765 slotted in the cavity in immediate contact with the microfluidic channels - Figure 5.21(c).
3766 The strategy was successful, and plasma entered the microfluidic channels after separation.
3767 However, the process was not easily repeatable with many underfilling or no-filling of the
3768 microchannels recorded. After inspection using a microscope, it was clear that the interface
3769 between the blood filter and the microchannel is crucial since the plasma was reluctant to
3770 leave the blood filter. In summary, the strategy of integrating the blood filter with the
3771 developed cartridge was promising, but the results were difficult to replicate and very
3772 unreliable, suggesting the need for optimisation.



3773 *Figure 5.21 (a) Passive blood filtration using the GE glass fibre filter. (b) Integration of the*
 3774 *filter into the cartridge. (c) Strategy for the integration of the filter.*

3775

3776 5.7. Summary of the Chapter

- 3777 • The platform was successful in quantifying six target metabolites, namely LAA,
 3778 glutamate, choline, sarcosine, lactate, and creatinine, in diluted human serum (ratio
 3779 1:10). Table 5.7 summarised the main findings.
- 3780 • Inkjet printing has the potential to be used for the deposition of enzymatic solutions on
 3781 top of the CMOS and microstructures for the immobilisation of reagents.
- 3782 • Lyophilisation was successful in trapping reagents in the solid-state within the
 3783 microchannel. The process also increased the shelf-life of the reagents, estimated to be
 3784 more than 60 days for choline-related chemicals when freeze-dried and stored at -20°C
 3785 in a vacuum-sealed package.
- 3786 • The capability of the platform working with preloaded reagents in the dry state was
 3787 verified with glutamate assay in modified human plasma. For all the measurement, one
 3788 channel was used for control measurement, demonstrating that the platform can run
 3789 different assays at the same time. The crosstalk between adjacent channel was quantified
 3790 to be 2.59%.

- 3791 • An alternative approach based on paper microfluidics was also demonstrated to be
 3792 capable of performing three measurements at the same time, i.e. glutamate, negative
 3793 control, and lactate.
- 3794 • Preliminary testing demonstrated that the platform could be used for metabolomics
 3795 assays using whole blood by both using it without any processing and by integrating a
 3796 commercial passive blood filter into the cartridge.

3797

3798

Table 5.7 Summary of on-chip metabolites quantification in diluted serum.

	LAA	Glutamate	Choline	Sarcosine	Lactate	Creatinine
Cartridge type	4 microchannels on CMOS				2 microchannels on CMOS	
Microchannel height	h ~ 137.14 μm					
Sample volume	25 μL				30 μL	24 μL
Application	PCa				Ischemic stroke	
Physiological Range	1.7 - 4.6 mM	40 - 150 μM	10 - 40 μM	0 - 20 μM	0.3 - 2.0 mM	100 - 150 μM
Test Range	0 - 12.5 mM	0 - 800 μM	0 - 500 μM	0 - 500 μM	0 - 3 mM	0 - 2 mM
Linear Range	0 - 3.5 mM	0 - 300 μM	0 - 100 μM	0 - 100 μM	0 - 0.5 mM	0 - 0.5 mM
Linearity (R^2)	0.993	0.985	0.967	0.997	0.977	0.932
K_m (μM)	18610	715.1	197	172.9	362	1085
Analytical Sensitivity ($\text{mVs}^{-1}\text{mM}^{-1}$)	0.226	4.72	11.79	11.72	5.175	0.803
LOD (μM)	69.01	6.86	3.00	0.26	31.85	5.21
LOQ (μM)	218.3	12.04	4.22	2.13	64.38	36.55
Resolution (μM)	24.52	1.03	0.48	0.4	7.92	39.76

3799

3800

3801 Chapter 6: Clinical Evaluation

3802 6.1. Introduction

3803 A clinical evaluation of the platform was performed for both prostate cancer and ischemic
3804 stroke. Multiplexed assays were also demonstrated with clinically source human plasma
3805 samples. Table 6.1 illustrates the contribution to each activity discussed in this chapter.

3806 The objective of this evaluation was to determine the analytical accuracy of the device with
3807 respect to the state of the art using clinically sourced samples. This was achieved by
3808 comparing results obtained using this platform with results obtained using standard
3809 measuring methods. Lactate is already a well-established biomarker for ischemic stroke, so
3810 the diagnostic accuracy of this metabolite is not under analysis. However, the diagnostic
3811 accuracy of the proposed metabolomic biomarkers for prostate cancer is unknown. As such,
3812 the secondary objective was to provide a scientific evaluation linking the candidate
3813 metabolic biomarkers to prostate cancer.

3814

3815 6.2. Platform Optimisation for Clinical Evaluation

3816 Transitioning from diluted samples to undiluted biological required significant
3817 modifications of the platform. The main problem encountered was the drastically reduced
3818 colour change when using o-dianisidine in undiluted samples. The possible explanation to
3819 this phenomenon was the interference with other substances in the undiluted sample, whose
3820 concentrations were negligible when heavily diluted. Specifically, the degradation of
3821 performance was attributed to a specific enzyme naturally present in the blood: catalase.

3822

3823 *Table 6.1 Table of contributions for the activity presented in this chapter.*

Task / Activity presented in Chapter 6	Main investigators
Optimisation for clinical evaluation	- Valerio F. Annese
Clinical evaluation with PCa samples	- Valerio F. Annese
Clinical evaluation with ischemic stroke samples	- Valerio F. Annese
Multiplexed assays with PCa samples	- Valerio F. Annese

3824

3825 Blood is structured to be very stable and integrates several substances to preserve its stability,
3826 including catalase an enzyme which catalyses the decomposition of free hydrogen peroxide
3827 to water and oxygen [49]. Catalase also has one of the highest turnover numbers among all
3828 the enzymes and, therefore, it is one of the most efficient catalysts [49]. Therefore, it was
3829 hypothesised that catalase was interfering with the designed assays by decomposing
3830 hydrogen peroxide faster than the colorimetric probe. The introduction of a catalase inhibitor
3831 was initially considered. Among the inhibitors, hydroxylamine was selected, and
3832 preliminary tests were carried out. Nevertheless, hydroxylamine also appeared to
3833 undesirably reduce the activity of HRP. Preliminary experiments showed that assays using
3834 phenol/4AAP instead of o-dianisidine were working correctly. This corroborated the
3835 hypothesis of catalase interaction, as both phenol and 4AAP are also catalase inhibitors [49].
3836 Regarding the fluid properties, undiluted samples contained impurities which led to a
3837 decreased SNR. This was expected because of larger particles free to move on top of optical
3838 sensors. In addition, higher fluidic density due to undiluted solutions led to higher filling
3839 times.

3840 In order to mitigate the above-mentioned challenges, the platform was modified as follows:

- 3841 • All experiments were performed using phenol/4AAP as H₂O₂ probe in substitution to o-
3842 dianisidine. Formulations were modified accordingly.
- 3843 • HRP concentration was increased to compensate for potential activity loss due to
3844 interferences.
- 3845 • Channels with increased height ($h \sim 290 \mu\text{m}$) were employed to speed-up the liquid flow
3846 and provide more substantial transmittance drop.

3847

3848 **6.3. Research Ethics and Data Protection**

3849 Samples were clinically sourced under ethical approved. For cancer samples, the ethical
3850 approval was issued by the West of Scotland Research Ethics Service with reference number
3851 10/S0704/18. For ischemic stroke samples, the ethical approval was issued by the West of
3852 Scotland Research Ethics Service with reference number 17/WS/0252. Ethical approval
3853 letters are reported in Appendix K. Samples were anonymised and randomised within the
3854 relative group, in accordance with the General Data Protection Regulation. No personal data
3855 which could have undermined the anonymity of the sample was requested or recorded.
3856 Numeric IDs were assigned to the samples.

3857 6.4. Prostate Cancer Clinical Evaluation

3858 The POC testing for PCa diagnosis was performed in three stages: calibration, validation,
 3859 and clinical evaluation. In the first stage, calibration curves were obtained using a single
 3860 human plasma sample modified with a known concentration of metabolites of interest.
 3861 Validation was performed by two methods: (i) by testing human plasma samples modified
 3862 with different and unknown levels of analytes of interest (blind validation) and (ii) by
 3863 comparing readings from the platform with commercial methods. Clinical evaluation for
 3864 PCa was performed on ten samples from healthy men and sixteen samples from people
 3865 affected by PCa.

3866

3867 6.4.1. Materials and Methods

3868 **Reagents.** All chemicals required for the assays were purchased from Sigma Aldrich unless
 3869 otherwise specified. Plasma samples for calibration and blind validation were purchased
 3870 from Sigma Aldrich. Ambient temperature and humidity were recorded during the clinical
 3871 testing using the Texas Instrument Module HDC 1080EVM. Assay formulations were
 3872 optimised using a trial-and-error approach. Table 6.2 summarises the main aspects of the
 3873 assay formulations for PCa-related metabolites in clinical samples.

3874 **Non-PCa group.** Ten healthy human plasma samples were commercially sourced from
 3875 Cambridge Bioscience. Healthy plasma samples are herein referred to as ‘non-PCa’ and
 3876 constituted the control group. Non-PCa donors were adult males, with diversified ethnicity
 3877 and an average age of 34 ± 10 years. Healthy samples were randomly assigned a numeric ID
 3878 from 1 to 10.

3879

Table 6.2 Assay formulations.

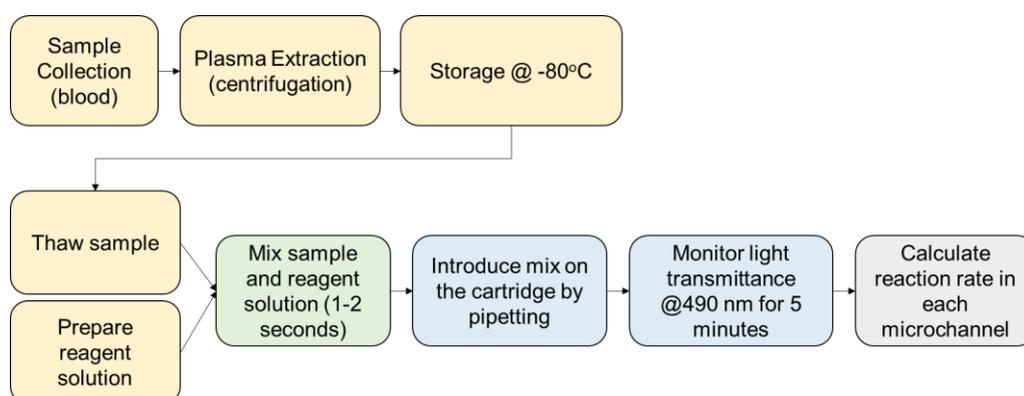
	LAA	Glutamate	Choline	Sarcosine
Cartridge	4 parallel and identical microchannel (h ~ 290 μ m)			
Microchannel volume	0.348 μ L			
Light source	LED @ 490nm (3 mW, FWHM = 20 nm)			
Total Volume	60 μ L			
Sample Volume	30 μ L			
Reagent mix volume	30 μ L			
Reagent buffer	DI water			
1 st reaction stage	LAAOx (10 μ L, 10U/mL)	GIOx (10 μ L, 4U/mL)	ChOx (10 μ L, 150U/mL)	SaOx (10 μ L, 200U/mL)
2 nd reaction stage	10 μ L HRP 300U/ml 5 μ L Phenol 44.5mM 5 μ L 4AAP 10.5mM			
Negative control	1 st reaction stage is substituted with ~10 μ L of DI water			
Positive control	The sample is spiked with a known concentration of the analyte of interest			

3880 **PCa group.** Sixteen human plasma samples from people diagnosed with PCa were sourced
 3881 from the Beatson Cancer Institute, Glasgow, UK, under ethical approval, with the
 3882 collaboration with Dr Robert Jones and Prof Jeff Evans. Donors were selected to be adults
 3883 who had already been diagnosed with PCa. Cancer samples constituted the cancer or PCa
 3884 group. PCa samples were randomly assigned a numeric ID from 11 to 26. Protocols for
 3885 sample collection are reported in Appendix L.

3886 **Procedure.** The setup used for clinical testing was the same as the one used for experiments
 3887 in diluted serum. Reagents were mixed with the sample off-chip and immediately introduced
 3888 into the cartridge within a couple of seconds. Metabolites were tested individually using the
 3889 cartridge with four microchannels. The concentrations of the target metabolites in plasma
 3890 samples were not known when the experiments were performed. A schematic representation
 3891 of the adopted protocol is shown in Figure 6.1.

3892 **Control measurements.** Positive and negative controls were performed. Negative control
 3893 refers to the measurement designed for the quantification of non-specific activity. In this
 3894 case, a reaction was initiated between the sample, HRP and colour-changing reagents
 3895 without substrate-specific enzyme. Thus, a negative control considers the colour change,
 3896 which is not related to the reaction with the specimen under test (non-specific activity). Non-
 3897 specific activity is expected due to the intrinsic complexity of the undiluted sample.
 3898 Positive control indicates the measures designed to create a detectable signal. For this
 3899 purpose, the formulation of the positive control includes the addition of a known quantity of
 3900 analyte under test. The presence of positive controls aims to verify that the assay was
 3901 working as intended.

3902



3903

3904

Figure 6.1 Protocol adopted for clinical evaluation of the platform.

3905

3906 **Cartridge reuse.** Cartridges were cleaned and re-used. Approximately twenty cartridges
 3907 have been used for this set of experiments. Cleaning procedure after every measurement was
 3908 adopted to avoid cross-contamination. Like the experiments performed in diluted serum, the
 3909 cleaning recipe involved subsequent rinse in DI water, IPA, ethanol, and nitrogen blow-dry.
 3910 For the clinical evaluation only, an additional rinsing step with diluted piranha solution was
 3911 used (1:10). Cross-contamination was kept to a minimum by optimising the testing sequence.
 3912 For an individual metabolite, the negative control was first recorded. Then, the colorimetric
 3913 estimation was performed in triplicates, and finally, the measurements for two positive
 3914 controls were carried out.

3915 **Data handling.** Tests were performed in triplicates (biological replicates). Since a four-
 3916 microchannel cartridge was used, each biological replicate had four readings (technical
 3917 replicates). Data was processed according to the same methods used for diluted serum
 3918 experiments.

3919 **Substrate quantification.** The substrate quantification was carried out using two different
 3920 methods. The first method was based on the Michaelis-Menten model and therefore herein
 3921 referred to as ‘model-based estimation’. For this estimation method, Michaelis-Menten
 3922 kinetics parameters extracted during the calibration stage were used to estimate the
 3923 concentration of the analyte of interest according to Michaelis-Menten model - see Eq. (2.4).
 3924 The second method was based on sample-specific control measurements and therefore herein
 3925 referred to as ‘auto-controlled estimation’. In this estimation method, controls were used to
 3926 create a sample-specific calibration. The sample-specific calibration involved the
 3927 determination of (i) baseline and (ii) analytical sensitivity for each sample. The negative
 3928 control was used as a baseline. Let us use r_n and r_t to indicate the initial reaction rates
 3929 resulting from the negative control and from the actual test, respectively. It was, therefore,
 3930 possible to provide an adjusted initial reaction rate r_t^* as follows:

$$r_t^* = r_t - r_n \quad (6.1)$$

3931 The sensitivity was estimated using two different positive controls. Herein, positive control
 3932 A and B refer to controls where an additional known substrate concentration [A] and [B],
 3933 respectively, were added to the undiluted sample. The positive controls A and B provided
 3934 the resulting rates r_a and r_b , respectively. Thus, the additional concentration [A] and [B] and
 3935 the rates r_a and r_b provided the sample-specific sensitivity of the apparatus according to the
 3936 following formula:

$$S = \frac{r_b - r_a}{[B] - [A]} \text{ with } [B] > [A] \text{ and } r_b > r_a \quad (6.2)$$

3937 A and B were selected so that r_a and r_b were in the linear range of the apparatus. [A] and [B]
 3938 were chosen by using the calibration curves. The concentration of the analyte under test [T]
 3939 was then estimated using linear regression, as follows:

$$[T] = \frac{r_t^*}{S} \quad (6.3)$$

3940 Analogously, the sensitivity might also be calculated using the following variants:

$$S' = \frac{r_b - r_t}{[B] - [T]}; S'' = \frac{r_a - r_t}{[B] - [T]} \quad (6.4)$$

3941 Typically, S, S' and S'' had a similar numerical value. Their average was used for the
 3942 substrate quantification using the auto-controlled method.

3943

3944 **6.4.2. Calibration**

3945 A human plasma sample purchased from Sigma Aldrich was modified by adding known
 3946 quantities of analytes of interest. Additional concentration did not consider the unknown
 3947 endogenous level of the substrate of interest in the sample. The endogenous concentration
 3948 was estimated by linearization using the first two points of the characteristic. Thus,
 3949 calibration curves report the total concentration of the substrate in the volume under test.
 3950 Calibration curves for LAA, glutamate, choline and sarcosine in human serum are reported
 3951 in Figure 6.2. The complete characterisation of the platform for the analytes of interest is
 3952 reported in Table 6.3.

3953 Kinetics constants were estimated by data fitting to the Michaelis-Menten model. K_m values
 3954 obtained from the curve for all the metabolites were in line with the values reported in the
 3955 literature [49]. For all the metabolites, fittings to the curve using the Michaelis-Menten
 3956 model were satisfactory with R^2 values ≥ 0.97 . As in the previous chapter, a subset of the
 3957 collected data was also fitted using a linear model. Linear ranges for the measured
 3958 metabolites were covering the physiological concentration ranges. Average standard
 3959 deviations of the measurement in the linear range were in the span 16% - 20%.

3960 LOD and LOQ were also quantified over six control biological replicates. Thus, the average
 3961 reaction rate was $0.005 \pm 0.0027 \text{ mVs}^{-1}$. Consequently, LOD and LOQ were 0.014 mVs^{-1} and
 3962 0.032 mVs^{-1} , respectively. LOD and LOQ expressed in mVs^{-1} were then converted in μM by
 3963 using the estimated Michaelis-Menten for each metabolite. Thus, LOD for LAA, glutamate,

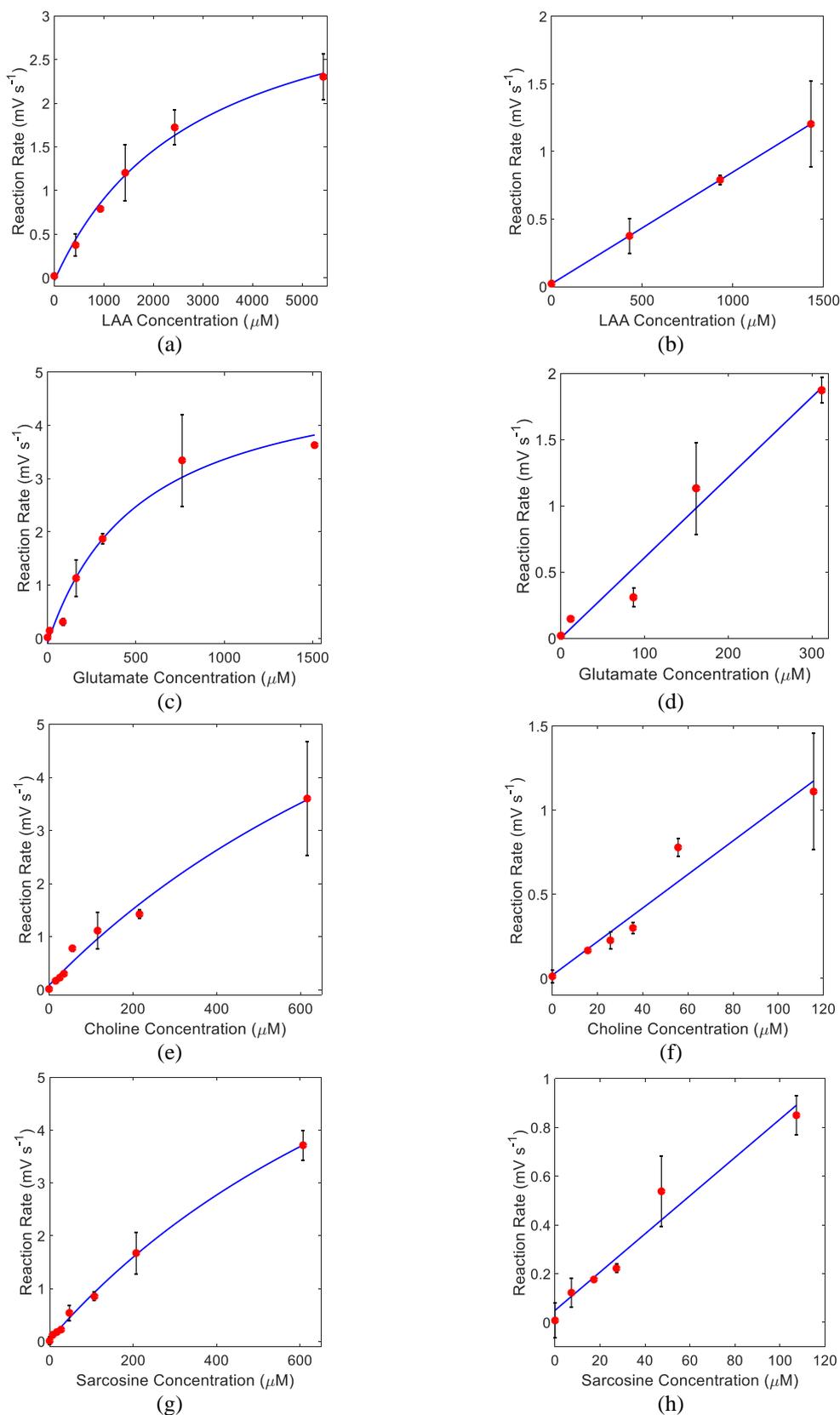
3964 choline and sarcosine were 11.1 μM , 1.4 μM , 1.7 μM and 1.4 μM , respectively. Similarly,
 3965 LOQ values for the metabolites in the same order were 25.5 μM , 3.3 μM , 3.9 μM , 3.5 μM .
 3966 LOD and LOQ results demonstrated the suitability of the platform for the measurements in
 3967 the target range.

3968

3969 *Table 6.3 Platform characterisation in human plasma for PCa metabolites. Metrics have*
 3970 *been defined in Table 2.3.*

	LAA	Glutamate	Choline	Sarcosine
Physiological Range	1.7 – 4.6 mM	40 – 150 μM	10 – 40 μM	0 – 20 μM
Test Range	0 – 5.4 mM	0 - 1500 μM	0 – 600 μM	0 – 600 μM
Relation with PCa	↑	↑	↑	↑
Model	$y = \frac{V_m \cdot x}{k_m + x} + c$			
V_m (mV s^{-1}) (95% coefficient bounds)	3.63 (2.62, 4.63)	5.28 (3.46, 7.10)	11.34 (-2.24, 24.93)	11.03 (6.97, 15.10)
c (mV s^{-1}) (95% coefficient bounds)	-0.032 (-0.280, 0.216)	-0.087 (-0.607, 0.433)	0.082 (-0.172, 0.336)	0.027 (-0.060, 0.115)
K_m (μM) (95% coefficient bounds)	2866 (890, 4842)	529.7 (1.06, 1058)	1382 (-991.1, 3755)	1209 (551.2, 1867)
SSE	0.022	0.283	0.142	0.020
RMSE	0.086	0.266	0.169	0.062
R^2	0.994	0.979	0.985	0.998
Linear Model	$Y = S \cdot x + C$			
Linear Range* ¹	0 - 1500	0 – 320 μM	0 – 120 μM	0 - 120 μM
Analytical Sensitivity (S) ($\text{mVs}^{-1}\text{mM}^{-1}$) (95% coefficient bounds)	0.83 (0.824, 0.830)	6.06 (4.08, 8.04)	9.98 (6.46, 13.5)	7.84 (5.65, 10.03)
C (mV s^{-1}) (95% coefficient bounds)	0.020 (0.017, 0.023)	0.003 (-0.317, 0.324)	0.019 (-0.177, 0.215)	0.050 (-0.059, 0.159)
SSE (linear)	$1.5 \cdot 10^{-06}$	0.076	0.054	0.019
RMSE (linear)	$8.6 \cdot 10^{-04}$	0.159	0.116	0.070
R^2 (linear)	1.000	0.969	0.939	0.961
Precision (linear range) ²	18.3%	17.2 %	16.4%	19.2%
Negative control (mV s^{-1}) ³	0.005 ± 0.0027			
LOD (mV s^{-1})	0.014			
LOQ (mV s^{-1})	0.032			
LOD (μM) ⁴	11.1	1.4	1.7	1.4
LOQ (μM) ⁴	25.5	3.3	3.9	3.5
Resolution (μM) ⁵	3.25	0.45	0.27	0.35
¹ Linear range is defined as the measurement range were the linear model had $R^2 > 0.9$. ² Calculated as the average of the relative standard deviation of the measurements in the linear range. ³ Average over 24 measurements. ⁴ Converted from mV s^{-1} to μM using the Michaelis-Menten model. ⁵ Calculated as the ratio between the standard deviation of the control measurements and the sensitivity in the linear range [58].				

3971



3972 *Figure 6.2 Calibration curves obtained by fitting data with Michaelis-Menten in the*
 3973 *extended range (left) and with a linear model (right) for (a)(b) LAA, (c)(d) glutamate, (e)(f)*
 3974 *choline and (g)(h) sarcosine in human plasma. Concentrations refer to the total reaction*
 3975 *volume.*

3976 **6.4.3. Blind validation**

3977 **Method.** A further human plasma sample was purchased from Sigma Aldrich, aliquoted and
 3978 modified with additional amounts of analytes of interest. Modified plasma samples were
 3979 produced by a different member of the MST group, which disclosed the additional
 3980 concentrations only after the testing was completed. Thus, the modified concentration levels
 3981 were unknown while performing the assays. For each blind sample and metabolite,
 3982 measurements were performed in triplicates. Negative control and two positive controls (A
 3983 and B) were also measured. Controls were repeated in triplicates. The additional
 3984 concentrations for positive controls A for LAA, glutamate, choline and sarcosine were
 3985 500 μM , 100 μM , 100 μM , 100 μM , respectively. The additional concentration for the
 3986 positive control B was $[B] = 2[A]$. The unknown quantity of additional metabolite was
 3987 calculated by performing an additional measurement on the unmodified sample.

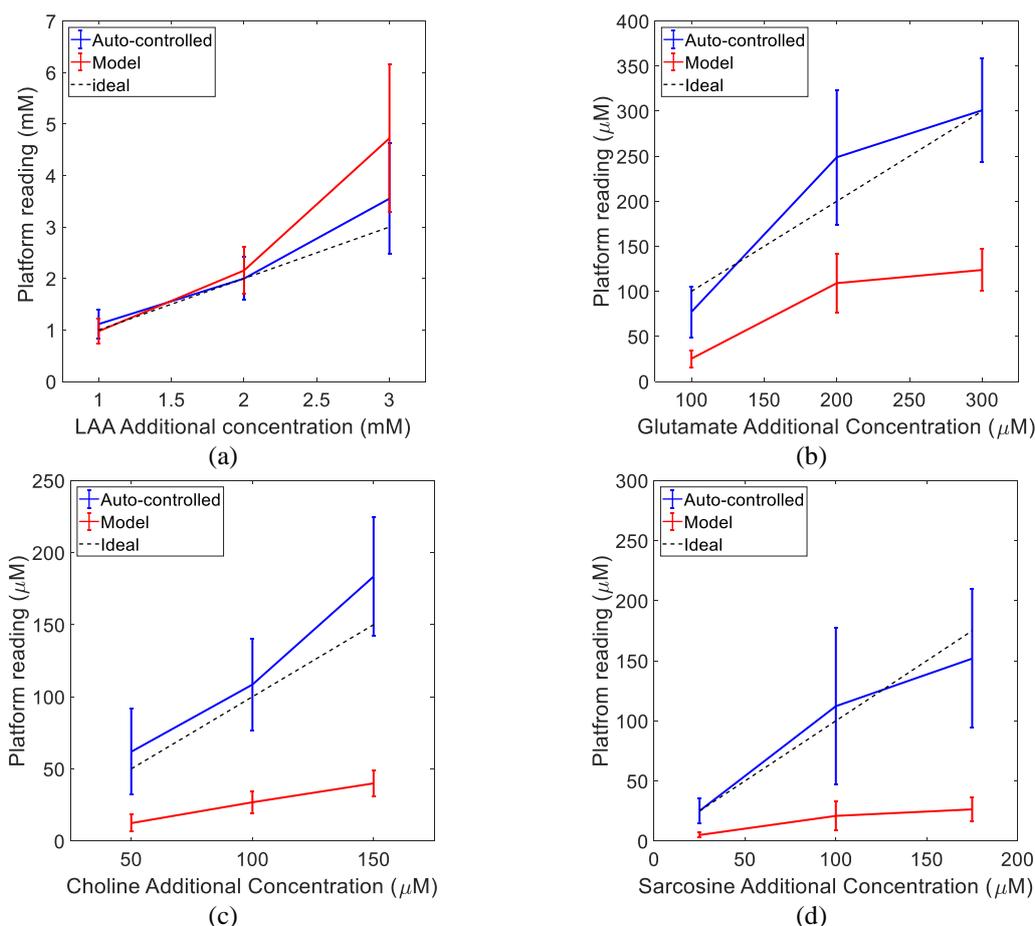
3988 **Results.** Results are reported in Figure 6.3 and Table 6.4. Relative errors were calculated as
 3989 per definition illustrated in Chapter 2, Paragraph 2.2.5. LAA levels estimated with the auto-
 3990 controlled approach had an average relative error of 10%. Data had a high correlation ($R^2 =$
 3991 0.96) with the ideal response, and no relevant bias was observed. A 22.6% error was recorded
 3992 when estimating the same quantities with the approach based on the Michaelis-Menten
 3993 model. The correlation was $R^2 = 0.96$, and a small bias compared to the physiological range
 3994 (620 μM) was observed.

3995 Glutamate levels calculated with the auto-controlled method had an average relative error
 3996 of 15.8%. The correlation with the ideal response and the bias of the estimation was
 3997 $R^2 = 0.92$ and 8.63 μM , respectively. When performing the same determination adopting the
 3998 model-based approach, average error, correlation, and bias were 59.6%, $R^2 = 0.87$
 3999 and -113.9 μM , respectively.

4000

Table 6.4 Characterisation of the blind tests results.

	LAA	Glutamate	Choline	Sarcosine
Auto-controlled estimation method				
Average relative error	10.0%	15.8%	18.2%	8.6%
Correlation coefficient (R^2)	0.96	0.92	0.98	0.96
Bias of the estimation*	0.22 mM	8.63 μM	17.91 μM	- 3.65 μM
Model-based estimation method (Michaelis-Menten)				
Average relative error	22.6 %	59.6%	73.9%	81.4%
Correlation coefficient	0.96	0.87	0.98	0.96
Bias of the estimation*	0.62 mM	- 113.9 μM	-73.61 μM	-82.6 μM
* Calculated as the average of the absolute error.				



4001 *Figure 6.3 Blind validation results when estimating the concentration of the substrate using*
 4002 *the model-based method (red) and the auto-controlled approach (blue) for (a) LAA, (b)*
 4003 *glutamate, (c) choline and (d) sarcosine.*

4004

4005 For choline, average error, correlation, and bias when using the auto-controlled method were
 4006 18.2%, $R^2 = 0.98$ and $17.91 \mu\text{M}$, respectively. When the model-based method was used, the
 4007 average error increased to 73.9%. The correlation remained very high ($R^2 = 0.98$) and the
 4008 bias observed was $-73.61 \mu\text{M}$.

4009 For sarcosine, average error, correlation, and bias when using the auto-controlled method
 4010 were 8.6%, $R^2 = 0.96$ and $-3.65 \mu\text{M}$, respectively. The same quantities were 81.45%, 0.96
 4011 and $-82.6 \mu\text{M}$ when the model based on the Michaelis-Menten equation was used.
 4012 Comparing the two adopted models for substrate quantification, the auto-controlled method
 4013 was more successful in estimating the unknown concentration of analytes for all the
 4014 performed assays.

4015 **Discussion.** For LAA, estimation with the auto-controlled and the model-based methods are
 4016 very similar in the linear range. The model-based approach seems to start failing only for
 4017 higher concentrations of LAA. Low sample-to-sample variability was observed for the LAA

4018 assay. For glutamate, choline and sarcosine determination, the model-based approach
4019 provides results with a high correlation with the ideal response. However, they
4020 systematically provide lower values. Arguably, the sample-to-sample variation was high.
4021 Specifically, these experiments demonstrate that the calibration curve obtained from one
4022 human sample might be not satisfactory for a different one. Probably, this is related to the
4023 composition of the human specimen, which may or may not include molecules interfering
4024 with the developed assay in several concentrations. This is a common problem for POC
4025 diagnostics that many variables and specimens can affect the result. On the contrary, for all
4026 the performed assays, the auto-controlled method provided more reliable results with
4027 estimation errors which are comparable to the glucose meter devices on the market. The
4028 increased reliability of the measurement was achieved by using all the controls to calibrate
4029 the platform on the specific sample. Consequently, the auto-control can compensate for
4030 several variables, including sample-to-sample variation, cartridge-to-cartridge variation,
4031 environmental conditions, and ambient interferences. Drawbacks of this approach include
4032 the need for additional reagents, additional sample volume and further data processing to be
4033 performed. On this basis, the auto-controlled approach was the adopted approach for clinical
4034 evaluation.

4035

4036 **6.4.4. Clinical evaluation**

4037 **Method.** Samples from non-PCa and PCa group were tested for the four metabolites of
4038 interest for PCa diagnosis. The concentration of the metabolites of interest was unknown
4039 during the experiments. The non-PCa group was tested before the PCa group. Within the
4040 group, metabolites were measured in the following order: LAA, glutamate, choline,
4041 sarcosine. For each sample and metabolite, the negative control was first assessed. Then, the
4042 three biological repeats of the assay were performed. Finally, positive controls A and B were
4043 performed. The additional concentrations for positive controls A for LAA, glutamate,
4044 choline and sarcosine were $[A] = 500\mu\text{M}, 100\mu\text{M}, 100\mu\text{M}, 100\mu\text{M}$, respectively. The
4045 additional concentration for the positive control B was $[B] = 2[A]$. To save sample volume,
4046 the total volume of the reaction was reduced from $60\mu\text{L}$ to $40\mu\text{L}$. The amount of the samples
4047 and reagents were proportionally reduced by one third. Thus, the total sample volume used
4048 for each biological replicate was $20\mu\text{L}$. The auto-controlled method was adopted for the
4049 quantification of the analytes. All the errors are expressed as one standard deviation.

4050 **Results.** Results from the clinical evaluation for both non-PCa and PCa groups are reported
4051 in Table 6.5. For LAA, the average over the entire dataset, herein referred to as grand
4052 average, was $2421 \pm 952 \mu\text{M}$. LAA levels were in the range 1213 - 5421 μM for the entire
4053 dataset. Non-PCa samples had an LAA average concentration of $1984 \pm 527 \mu\text{M}$, in the range
4054 from 1213-3167 μM . PCa samples had, on average, an increased level of LAA. The LAA
4055 average level in the PCa group was $2694 \pm 1052 \mu\text{M}$. The range of the measurements in the
4056 PCa group was 1503-5410 μM . Results obtained were in expected physiological ranges for
4057 both non-PCa and PCa groups. The ratio between average LAA in the PCa group and the
4058 non-PCa group was 1.36. The observed average increase in the PCa group was +35.8 %.
4059 When performing a one-tail t-test with homoscedastic variance, a value of $p = 0.03$ was
4060 observed: the increase in the LAA concentration in the PCa group had statistically significant
4061 variation.

4062 The grand average glutamate level was $53.7 \pm 26.4 \mu\text{M}$, with measured values ranging from
4063 6.3 μM to 149.5 μM . The average non-PCa glutamate level was $40.2 \pm 11.2 \mu\text{M}$, in the range
4064 21.9-67.1 μM . PCa samples had, on average, an increased concentration of glutamate. The
4065 average PCa glutamate concentration was $62.2 \pm 29.5 \mu\text{M}$. Measurements in the PCa group
4066 were in the range of 6.3-149.5 μM . Results were compatible with physiological ranges. The
4067 ratio between average glutamate in the PCa group and the non-PCa group was 1.55. The
4068 observed average increase in the PCa group was +54.8 %. The glutamate concentration in
4069 the PCa group had a statistically significant increase ($p = 0.02$).

4070 For choline, the grand average of the entire dataset was $11.7 \pm 7.0 \mu\text{M}$, and the measurements
4071 were in the range 2.3-36.9 μM . The average non-PCa choline level was $9.0 \pm 4.1 \mu\text{M}$. The
4072 range of the non-PCa choline measurements was 2.3-15.4 μM . PCa samples had increased
4073 concentration of choline, with an average of $13.4 \pm 7.9 \mu\text{M}$. PCa results for choline were in
4074 the range of 4.7-36.9 μM . The ratio between average choline in the PCa group and the non-
4075 PCa group was 1.49. The observed average increase in the PCa group was +49.2 %. The t-
4076 test, performed assuming one tail distribution and homoscedastic variance, demonstrated the
4077 statistically significant difference in the average of the two groups ($p = 0.06$).

4078 For sarcosine, clinical evaluation reported a grand average of $10.6 \pm 6.0 \mu\text{M}$ and a range of
4079 1.7- 27.2 μM . The average non-PCa sarcosine level was $11.5 \pm 4.3 \mu\text{M}$, and measurements
4080 were in the range 5.1-18.8 μM . PCa samples had decreased concentration of sarcosine, with
4081 an average of $10.0 \pm 6.8 \mu\text{M}$. The range of sarcosine in the PCa group was 1.7-27.2 μM .
4082 Results were compatible with physiological ranges. The ratio between average choline in the

4083 PCa group and the non-PCa group was 0.87. The observed average decrease in the PCa
4084 group was -13.5 %. The t-test, performed assuming one tail distribution and homoscedastic
4085 variance, demonstrated that this variation was not statistically significant ($p = 0.27$).

4086 Results are presented in Figure 6.4(a) where data has been normalised to the grand average
4087 of the analyte under test. Figure 6.4(b) shows the difference in the statistics of the two groups
4088 for the metabolomics panel. LAA, glutamate and choline showed a statistically relevant
4089 increase in their concentration in the PCa group. Among them, glutamate and choline had,
4090 respectively, the lowest and the highest p-value. Differently, sarcosine concentration in the
4091 PCa group was decreased with respect to the control group but differences were not
4092 considered statistically relevant.

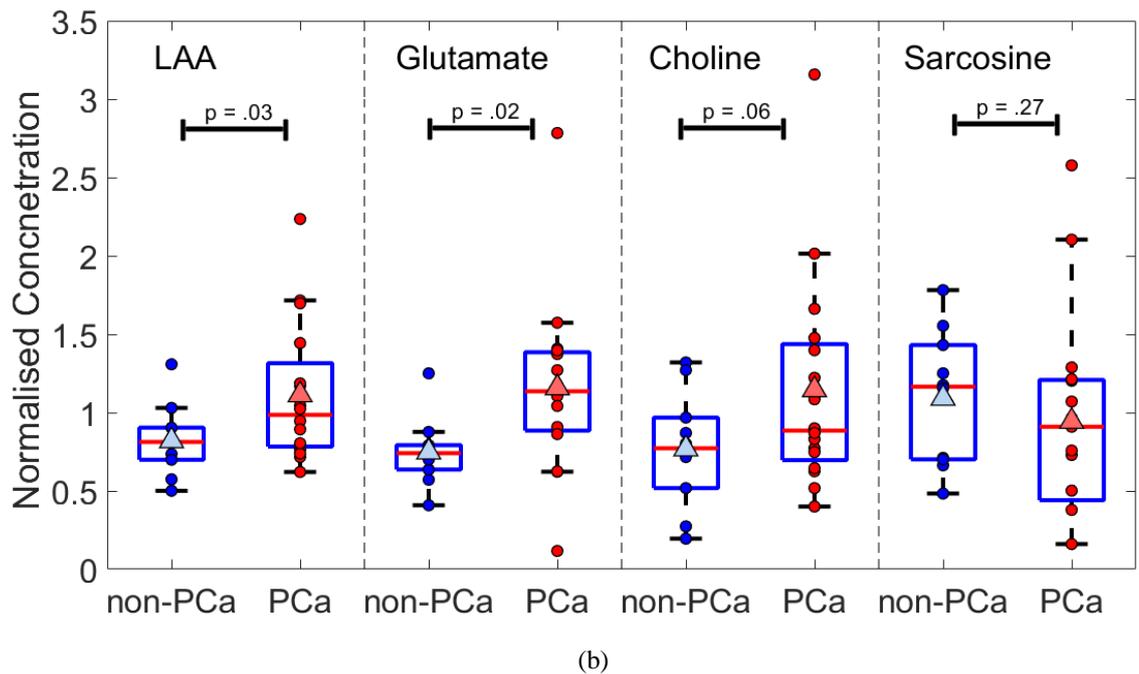
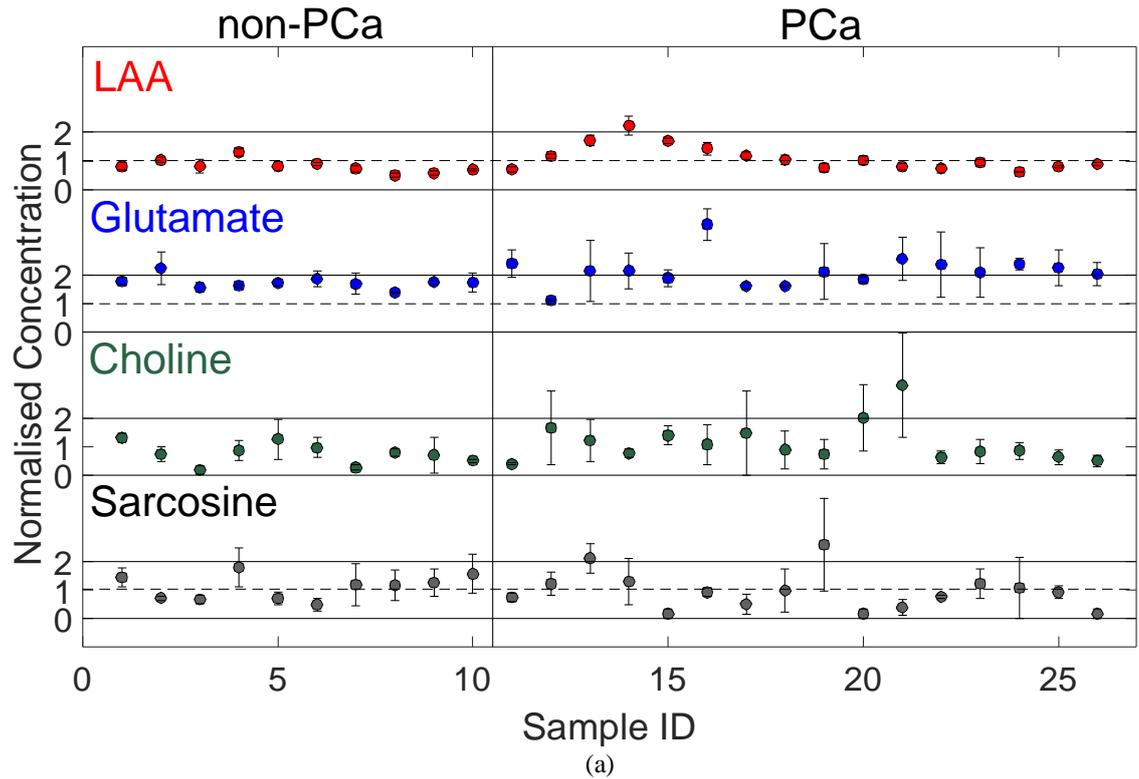
4093 Figure 6.5 suggests that, when used together, metabolites can potentially identify cancerous
4094 conditions. Concentrations of LAA, glutamate and choline seem to be capable of dividing
4095 the two groups in cartesian space. For example, Figure 6.5(b) demonstrate that, for this
4096 population, it is possible to separate the PCa group from the non-PCa group. Cross-
4097 correlation of the profile of the metabolites is also reported in the figure. There is no relevant
4098 cross-correlation among different metabolites (highest recorded cross-correlation was
4099 between LAA and glutamate in the non-PCa group: $R = 0.38$). The study suggests that there
4100 is merit in using the dataset for training a classification model. The research also indicates
4101 that, for this population, LAA, glutamate and choline could be considered metabolic
4102 biomarkers for PCa. On the contrary, for this population, sarcosine could not be regarded as
4103 a metabolic biomarker for PCa.

4104

4105

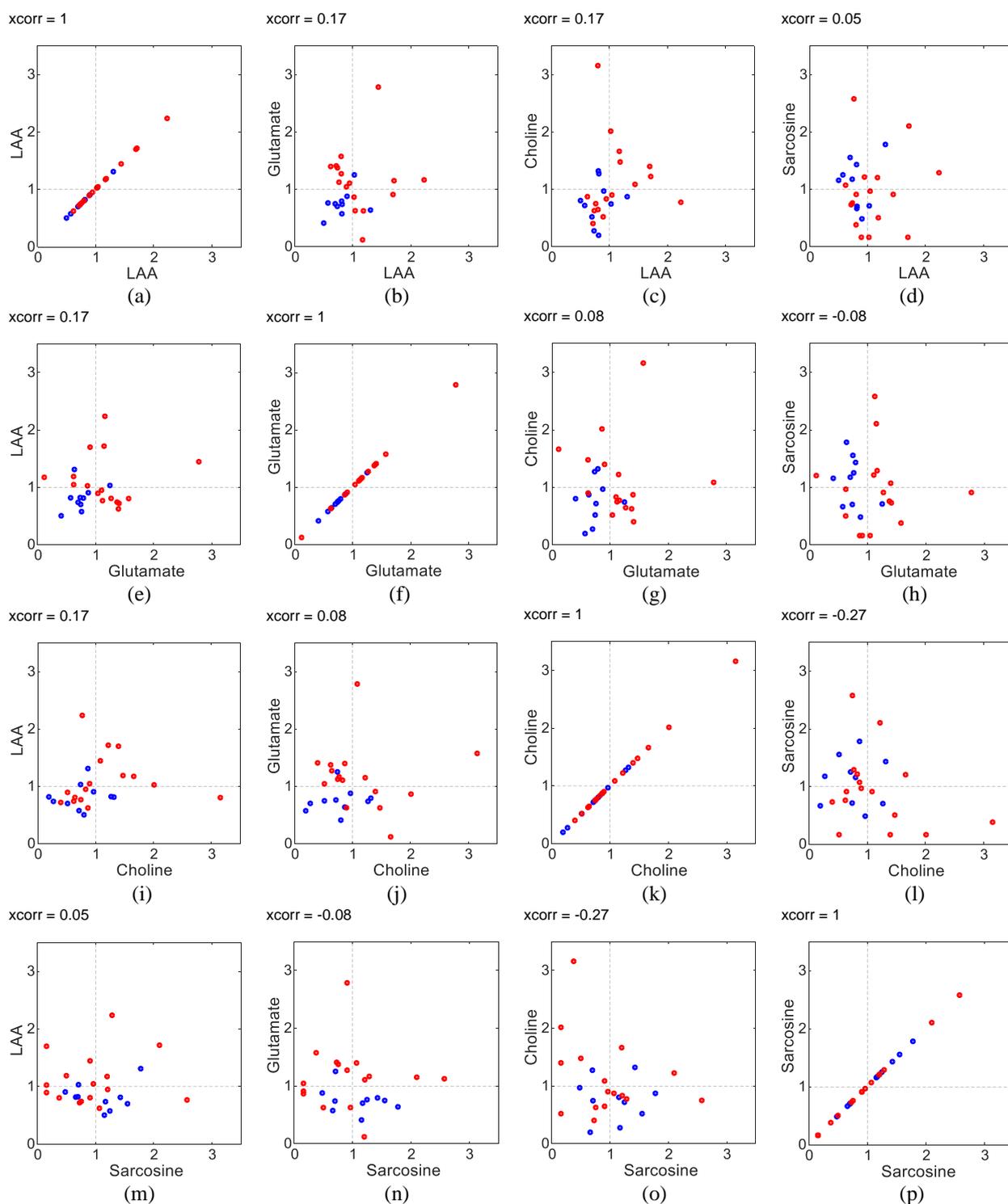
Table 6.5 Clinical evaluation results on control (non-PCa) and cancer (PCa) groups.

Group	Sample ID	LAA		Glutamate		Choline		Sarcosine	
		Avg. μM	Std. %	Avg. μM	Std. %	Avg. μM	Std. %	Avg. μM	Std. %
non-PCa	1	1961	16.2	42.5	16.9	15.4	11.5	15.1	23.5
	2	2493	9.5	67.1	44.7	8.7	34.0	7.5	9.8
	3	1972	29.4	30.7	28.5	2.3 (<LOQ)	78.7	7.0	21.8
	4	3167	10.4	34.2	8.8	10.2	39.9	18.8	38.1
	5	1983	20.8	39.5	14.5	14.8	54.5	7.4	32.2
	6	2187	5.4	47.1	32.0	11.3	36.0	5.1	44.6
	7	1780	15.5	37.6	53.0	3.2 (<LOQ)	32.0	12.4	63.5
	8	1213	13.1	21.9	4.1	9.4	17.5	12.2	45.6
	9	1390	14.4	40.8	8.7	8.4	86.9	13.2	39.5
	10	1693	6.7	40.1	45.0	6.1	9.7	16.4	43.3
PCa	11	1736	13.0	75.6	34.9	4.7	10.5	7.7	20.2
	12	2837	6.2	6.3	25.9	19.4	77.2	12.7	33.8
	13	4152	10.2	61.7	91.9	14.3	59.0	22.2	24.1
	14	5410	14.4	62.5	54.2	9.0	18.5	13.6	63.4
	15	4109	5.7	48.7	32.3	16.3	23.6	< 1.4	100.0
	16	3495	15.4	149.5	20.2	12.7	64.8	9.6	16.7
	17	2872	11.7	33.4	17.9	17.2	100.0	5.3	68.5
	18	2528	16.2	33.5	2.3	10.5	72.8	10.2	78.5
	19	1851	18.9	60.3	87.1	8.7	69.5	27.2	63.0
	20	2479	15.2	46.3	13.5	23.5	58.2	< 1.4	100.0
	21	1940	15.3	84.5	47.3	36.9	58.0	4.0	72.4
	22	1789	20.6	73.8	82.8	7.3	35.5	8.0	6.9
	23	2292	13.1	59.4	77.9	9.7	50.2	12.8	41.6
	24	1503	1.0	75.0	13.8	10.2	33.7	11.3	100.0
	25	1947	6.3	68.2	48.3	7.5	39.2	9.6	25.3
	26	2162	6.7	56.0	38.6	6.1	38.8	< 1.4	100.0
Overall results									
Grand average (μM)	2421		53.7		11.7		10.6		
Grand median (μM)	2072		47.9		10.0		9.9		
Grand std. dev. (μM)	952		26.4		7.0		6.0		
Range (μM)	1213 – 5421		6.3 – 149.5		2.3 – 36.9		1.7 – 27.2		
Avg. env. Temp. ($^{\circ}\text{C}$)	27.3 \pm 1.0		26.4 \pm 1.3		26.3 \pm 0.9		25.9 \pm 1.2		
Avg. env. hum. (%)	52.6 \pm 5.0		49.5 \pm 7.8		44.4 \pm 9.0		42.2 \pm 10.5		
Cross-correlation Matrix (R values)	$\begin{pmatrix} 1.00 & 0.17 & 0.17 & 0.05 \\ 0.17 & 1.00 & 0.08 & -0.08 \\ 0.17 & 0.08 & 1.00 & -0.27 \\ 0.05 & -0.08 & -0.27 & 1.00 \end{pmatrix}$								
non-PCa group									
non-Pca average (μM)	1984		40.2		10.0		11.5		
non-Pca median (μM)	1966		39.8		9.0		12.3		
non-Pca std. dev. (μM)	527		11.2		4.1		4.3		
Range (μM)	1213 - 3167		21.9 – 67.1		2.3 – 15.4		5.1 – 18.8		
Cross-correlation Matrix (R values)	$\begin{pmatrix} 1.00 & 0.38 & 0.17 & 0.09 \\ 0.38 & 1.00 & 0.18 & -0.32 \\ 0.17 & 0.18 & 1.00 & 0.02 \\ 0.09 & -0.32 & 0.02 & 1.00 \end{pmatrix}$								
PCa group									
Pca average (μM)	2694		62.2		13.4		10.0		
Pca median (μM)	2386		61.0		10.4		9.7		
Pca std. dev. (μM)	1052		29.5		7.9		6.9		
Range (μM)	1503 - 5410		6.3 – 149.5		4.7 - 36.9		1.7 – 27.2		
Cross-correlation Matrix (R values)	$\begin{pmatrix} 1.00 & -0.02 & 0.05 & 0.11 \\ -0.02 & 1.00 & -0.08 & 0.01 \\ 0.05 & -0.08 & 1.00 & -0.30 \\ 0.11 & 0.01 & -0.30 & 1.00 \end{pmatrix}$								
Univariate analysis									
Pca/non-Pca (average)	1.36		1.55		1.34		0.87		
Pca/non-Pca (median)	1.21		1.53		1.15		0.79		
t-test (p value)	0.03		0.02		0.06		0.27		



4106 *Figure 6.4 (a) Metabolites quantification in non-PCa (samples 1-10) and PCa group*
 4107 *(samples 11-26). The concentration of the metabolic biomarkers was normalised to the*
 4108 *grand average. From top to bottom, LAA (red), glutamate (blue), choline (green), sarcosine*
 4109 *(black) data. (b) Box plots for the non-PCa group vs the PCa group. Blue and red markers*
 4110 *indicate non-PCa and PCa measurements, respectively. Triangular markers indicate the*
 4111 *average of the group. Concentrations of LAA, glutamate and choline are statistically*
 4112 *increased in PCa group. No statistically significant difference was observed for sarcosine.*

4113



4114 *Figure 6.5 (a)-(p) Scatter plots for all the metabolite combinations. Concentrations are*
 4115 *normalised to the respective grand average. Blue markers: non-PCa samples. Red markers:*
 4116 *PCa samples. Cross-correlation values are referred to the overall dataset.*

4117

4118 **6.4.5. Validation against standard methods**

4119 **Method.** LAA, glutamate, choline, and sarcosine concentrations in the non-PCa group were
4120 independently analysed by Dr Liam Heaney, Lecturer in Bioanalytical Science, School of
4121 Sport, Exercise and Health Sciences, Loughborough University. Plasma samples were
4122 shipped under a specific material transfer agreement. All the metabolites were tested using
4123 commercially available fluorescent plate-based assays following manufacturer instructions
4124 (product codes: ab65347, ab138883, ab219944, ab65338, Abcam, Cambridge, UK). Choline
4125 was also analysed by ultra-performance liquid chromatography-tandem mass spectrometry
4126 (UPLC-MS/MS) using an Acquity liquid chromatography coupled to a Quattro Ultima triple
4127 quadrupole mass spectrometer (Waters, Wilmslow, UK).

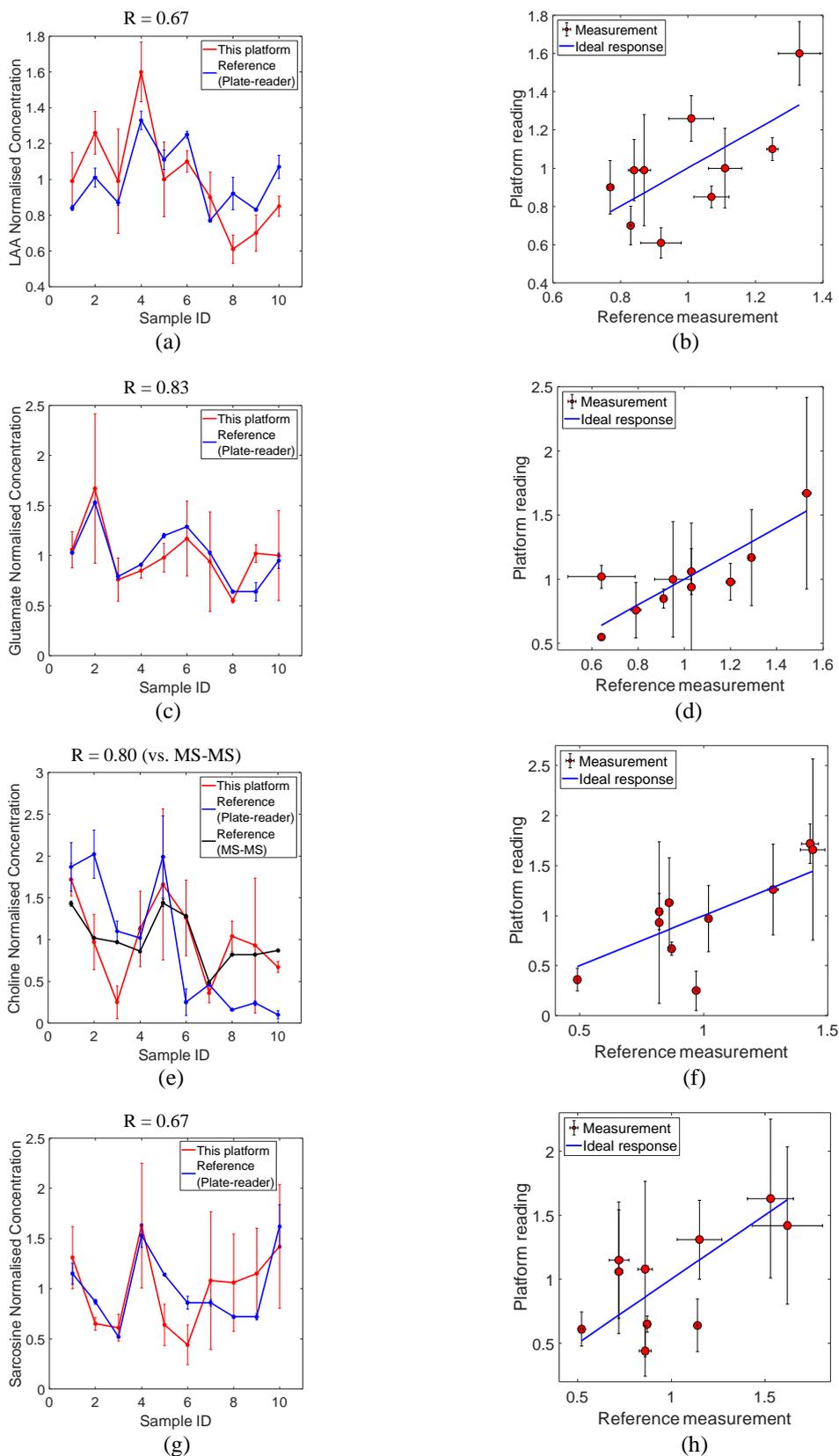
4128 **Results.** Results are shown in Figure 6.6. For each sample, metabolite and testing method,
4129 concentrations were normalised to the group average. All four metabolites had comparable
4130 results with commercial methods. For this population, the average relative errors of the
4131 platform when quantifying LAA, glutamate, choline and sarcosine with respect to the
4132 reference method were 18.5%, 13.81%, 21.37% and 44.4%, respectively. Choline
4133 comparison, shown in Figure 6.6(e), is particularly interesting because data from the
4134 developed platform showed higher correlation with MS-MS measurements ($R=0.8$) rather
4135 than with data obtained with the commercial fluorescent kit ($R=0.5$). It is well-known that
4136 MS-MS provides more accurate results than commercial assay kits. MS-MS analysis for all
4137 the metabolites was not possible due to limited resources. However, data suggests that
4138 measurements with the platform might be more accurate than the commercial kit.

4139 **Discussion.** There are some factors that might have affected the comparison and should be
4140 highlighted. Samples tested in the third-party laboratory went through an additional long-
4141 distance shipping process which might have affected the concentration of the metabolites.
4142 Also, one set of calibration parameters were used for each metabolite using the third-party
4143 method. Concentrations measured with the developed platform were instead estimated using
4144 sample-specific calibration parameters. Furthermore, adopted methods used different
4145 working principles. Authors in [90] warn that serum metabolites measured with different
4146 approaches might have discrepancies due to chemical interferences and therefore exact
4147 match is not expected.

4148

4149

4150



4151 *Figure 6.6 Normalised metabolite levels measured with this platform compared with*
 4152 *commercial standard methods for (a),(b) LAA, (c)(d), glutamate, (e)(f) choline (levels were*
 4153 *measured with fluorescent assay kit used with a benchtop plate reader - solid blue line - and*
 4154 *MS-MS - solid black line) and (g)(h) sarcosine.*

4155 **6.4.6. Classification**

4156 Clinical sensitivity, specificity and accuracy of the platform was quantified by applying
4157 several well-known classification algorithms to the dataset. The comparison of different
4158 classification algorithms was performed using a customised Matlab-based script. Matlab
4159 built-in functions for creating classification models have been used. It was experimentally
4160 verified that sarcosine data was not relevant for data classification, and therefore it was
4161 excluded from this analysis.

4162 **Metrics.** The following metrics have been adopted:

- 4163 • Test outcome is positive/negative if the sample is classified as belonging to the
4164 PCa/control group.
- 4165 • True positives/negatives (TP/TN) are samples correctly classified.
- 4166 • False positives (FP) are negative samples wrongly classified as positive.
- 4167 • False negatives (FN) are positive samples wrongly classified as negative.
- 4168 • Diagnostic (or clinical) sensitivity (S_n), also referred to as true positive rate (TPR), is the
4169 portion of positive samples correctly classified as positives (see Figure 1.1) [17] [18].
- 4170 • Diagnostic (or clinical) specificity (S_p), also referred to as true negative rate (TNR), is
4171 the portion of negative samples correctly classified as negatives (see Figure 1.1) [17] [18].
- 4172 • Diagnostic (or clinical) accuracy (Acc.) of the classification is the sum of true positive
4173 and negatives divided by the entire population (see Figure 1.1) [17].
- 4174 • The area under the curve (AUC) is the area under the receiver operating characteristic
4175 curve (ROC). ROC is a curve created by plotting sensitivity against specificity at various
4176 threshold settings [17], [309]. The scientific community usually adopts the AUC for
4177 comparing different classification algorithm [309].

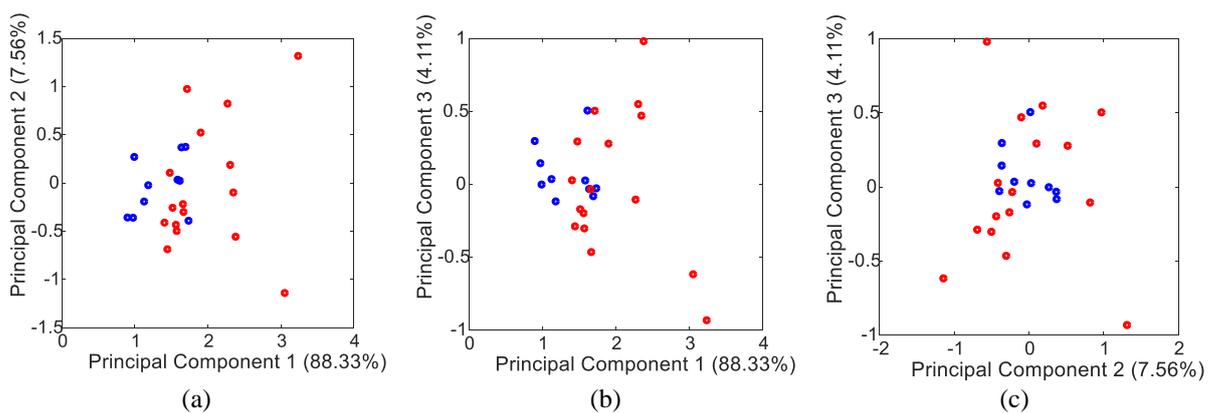
4178 **Methods.** Normalised data of LAA, glutamate and choline were used to train several well-
4179 established classification algorithms. Models were trained using a k-fold cross-validation
4180 approach, which was used to overfitting. In k-fold validation, the dataset was divided into k
4181 sub-groups. The algorithm was then trained using (k-1) sub-groups. The remaining sub-
4182 group was used for validation. The division in sub-group was random. To avoid variation
4183 due to the random process of partitioning the dataset, the process was re-iterated for 500
4184 repetitions where the k sub-groups were randomly re-defined. Considering the population
4185 size, a k value of 5 was selected.

4186 The classifiers were also trained on data processed with the Principal Component Analysis
 4187 (PCA). PCA is a statistical analysis for dimension reduction. It decomposes a dataset with
 4188 N dimension into a new dataset, with the same number of uncorrelated dimensions, called
 4189 components [310]. The components are orthogonal and successively maximise variance
 4190 [310]. The method has been widely used and described in the literature [310]. PCA analysis
 4191 is reported in Figure 6.7. The scores of the PCA analysis are reported in Appendix M.

4192 Algorithms from four different classification classes were adopted:

- 4193 • *Decision trees.* Decision tree-based algorithms define several flow-chart-like decisions
 4194 to reach an outcome. They can have different degrees of complexity and many structures
 4195 have been proposed in the literature [311]. The more sophisticated algorithm here
 4196 adopted is the random forest algorithm, which groups several decision trees were features
 4197 are randomly selected.
- 4198 • *Discriminant analysis.* Algorithm using discriminant analysis develops a discriminant
 4199 function to distinguish between the classes of interest in the feature space [312].
- 4200 • *Support Vector Machines (SVMs).* SVMs derive the hyperplane that maximises the
 4201 distance between the closest negative and the positives [313]. The points defining the
 4202 borders of the hyperplane are called support vectors. Support vector points are then fitted
 4203 using a kernel function for mathematically define the hyperplane [313]. In this work,
 4204 four different kernel functions have been used, namely linear, quadratic, cubic and
 4205 Gaussian. A detailed theoretical description of the method is reported in [313].

4206



4207 *Figure 6.7 (a),(b),(c) Scatter plots for all the combination of the PCA scores. Blue markers:*
 4208 *non-PCa scores. Red markers: PCa scores.*

4209

4210 • *k-nearest neighbours (KNN)*. KNN algorithms use a set of k nearest points in the feature
4211 space to determine the class of the sample under test using a likelihood approach [314].
4212 This class of algorithms can be considered as a voting system based on the closer points
4213 in the feature space [314]. There are many parameters which can be modified to improve
4214 the performance of the decision. The main parameters to be considered are the number
4215 k of nearest point and the type of distance to be used (e.g. Euclidean, correlation, etc.).
4216 The k nearest point can also be weighted when performing the distance [315]. Additional
4217 theoretical knowledge about KNN algorithms can be found in the literature [314], [315].
4218 Other classifiers and training methods are available. However, it was beyond the scope of
4219 this work to identify the ultimate method for classifying the population. Thus, only the most
4220 used algorithms have been trained and validated.

4221 **Results.** Results from all the classifiers are reported in Table 6.6. All the classification
4222 metrics are here reported as the average over 500 iterations. Diagnostic sensitivity and
4223 specificity were calculated in the point of the ROC curve which was the closest to the ideal
4224 condition ($S_n=S_p=1$) [309]. Generally, training the model with the scores of the PCA
4225 analysis only improved the results for discriminant analysis algorithms.

4226 The classification algorithm with the highest AUC was the weighted KNN algorithm, with
4227 an AUC of 0.862. Weighted KNN also showed the highest accuracy: 0.84. The approach
4228 which showed the highest sensitivity was the Gaussian SVM. In this case, sensitivity was
4229 0.90. The method performing the highest specificity was the medium KNN algorithm trained
4230 on PCA scores. In this case, the specificity was 0.83.

4231 The AUC was here used for selecting the algorithm with the best performance, according to
4232 standard procedures [309]. Hence, the weighted KNN algorithm was selected as the optimal
4233 method among the adopted for data classification. Therefore, additional information is here
4234 provided for the developed weighted KNN algorithm.

4235 The model was trained using ten neighbours' samples and evaluating the distance by the
4236 Euclidean definition. The set of weights followed a squared inverse model. When cross-
4237 validating data with the trained KNN, true positive and the true negative were, on average,
4238 13.97 and 7.38, respectively. False positive and false negative were, on average, 2.62 and
4239 2.03. Sensitivity and specificity for this model, as reported in the table, were 0.84 and 0.78,
4240 respectively. The ROC curve for the KNN model is reported in Figure 6.8.

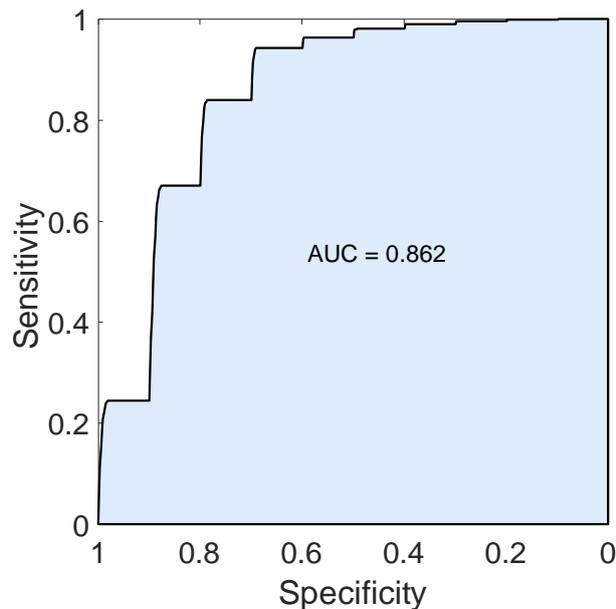
4241

4242 Table 6.6 Diagnostic evaluation of the platform using classification and k-fold validation
 4243 for different methods. Bold values highlight the best value obtained within the classification
 4244 group. Values marked with '*' are the best value among all the adopted classification
 4245 methods.

Method	PCA disabled				PCA enabled			
	AUC	Acc.	Sn	Sp	AUC	Acc.	Sn	Sp
Decision trees								
Fine Tree	0.73	0.80	0.86	0.71	0.73	0.70	0.79	0.54
Medium Tree	0.74	0.80	0.86	0.72	0.73	0.71	0.80	0.55
Coarse tree	0.73	0.80	0.86	0.71	0.73	0.70	0.79	0.55
Boosted tree	0.79	0.81	0.88	0.70	0.79	0.72	0.76	0.66
Random Forest	0.79	0.81	0.88	0.70	0.79	0.72	0.75	0.68
Discriminant analysis algorithms								
Linear	0.76	0.67	0.76	0.53	0.76	0.67	0.76	0.53
Quadratic	0.75	0.76	0.78	0.73	0.76	0.76	0.78	0.73
Logistic Regression	0.75	0.70	0.81	0.53	0.76	0.71	0.82	0.54
SVMs								
Linear	0.78	0.75	0.87	0.54	0.77	0.73	0.86	0.53
Quadratic	0.77	0.74	0.72	0.77	0.81	0.75	0.73	0.79
Cubic	0.74	0.71	0.71	0.73	0.72	0.69	0.65	0.76
Gaussian	0.82	0.81	0.90*	0.66	0.84	0.79	0.86	0.69
KNN algorithms								
Fine	0.78	0.79	0.83	0.73	0.75	0.75	0.77	0.72
Medium	0.73	0.68	0.66	0.70	0.77	0.69	0.60	0.83*
Coarse	0.53	0.62	0.25	0.80	0.53	0.62	0.25	0.80
Cubic	0.77	0.70	0.69	0.73	0.74	0.68	0.61	0.78
Weighted	0.86*	0.84*	0.84	0.78	0.83	0.81	0.84	0.77

*Maximum value among all the adopted methods

4246
 4247



4248
 4249

Figure 6.8 ROC curve for the weighted KNN algorithm.

4250

4251 **6.4.7. Discussion**

4252 The clinical study arises a multitude of discussion points. The first consideration to be
4253 highlighted is that there is merit in using multiple metabolites to create a model for the
4254 discrimination of PCa. However, the selected metabolites must show a correlation with the
4255 disease. Sarcosine in plasma did not show relevant correlation with PCa and it was therefore
4256 concluded that plasma sarcosine was not a metabolic biomarker in this population,
4257 corroborating the reports in the literature [180]. Differently, LAA, glutamate and choline
4258 showed significant correlations and were used as features to train a classification model. The
4259 best classification model here obtained from the AUC viewpoint, was a model based on a
4260 weighted KNN algorithm. However, there are many other classification approaches which
4261 might be adopted for this dataset potentially providing improved performance. It is also
4262 worth stressing that the classification was performed assuming a k-fold validation approach,
4263 and different results might be achieved with varying values of k. More optimistic results
4264 were obtained when no validation was performed. However, model training with no
4265 validation might be affected by overfitting and might not reliable and, as a result, have not
4266 been reported here.

4267 Data was also independently analysed by Dr Ronan Daly, data analysis manager at Glasgow
4268 Polyomics, University of Glasgow. Glasgow Polyomics confirmed the superfluity of
4269 sarcosine data in the classification and the unnecessary of preliminary PCA analysis and
4270 verified that there is merit in the selected metabolic biomarkers. Glasgow Polyomics
4271 suggested the use of a random forest classification algorithm trained using the R packages
4272 ‘randomForest’ and ‘caret’ [316]. The algorithm was set to use 500 trees and try up to three
4273 metabolites at each split. The model was validated using a *leave-p-out* cross-validation
4274 procedure [317], [318]. The resulting cross-validated AUC was 0.8. The ROC showed the
4275 optimal operational point at a sensitivity of 0.93 and a specificity of 0.70. Glasgow
4276 Polyomics also suggested an alternative model based on glutamate measurements only,
4277 which could optimise the sensitivity given a specificity of approximately 0.85.

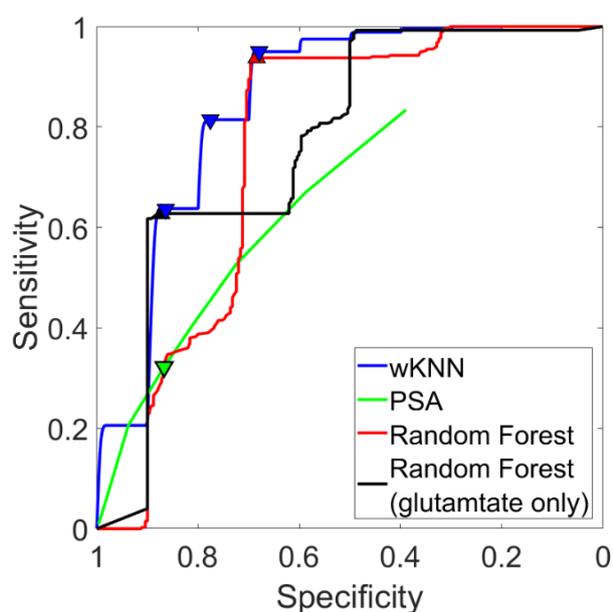
4278 It is interesting to compare the diagnostic capability of the selected metabolites with the
4279 current standard, i.e. PSA testing. Due to ethical reasons, it was not possible to access PSA
4280 data over the studied population. However, PSA testing has been widely characterised in
4281 terms of sensitivity and specificity [18]. In clinical practice, PSA sensitivity and specificity
4282 are 0.32 and 0.87, respectively, for a PSA threshold of 3.1 ng/mL. Sensitivity and specificity
4283 can be tuned by modifying the PSA cut-off [18], [319]. However, the clinical PSA cut-off is

4284 optimised to maximise specificity. This choice is related to the fact that, in order to diagnose
 4285 the highest number of tumours, a relevant number of false positives is acceptable since, in
 4286 these cases, further tests will be in place to confirm or confute the PSA test. Differently,
 4287 people having a false negative result might not immediately undergo further testing, resulting
 4288 in the progression of the disease.

4289 Based on these considerations, the working point of the classifier can be selected to maintain
 4290 the same specificity level of PSA. Figure 6.9 shows a comparison of the potential working
 4291 points for the classifier of interest, together with the PSA ROC curve obtained from [18].

4292 The random forest model based on glutamate only has the potential to increase the sensitivity
 4293 of the diagnosis to 0.63 while maintaining the specificity at 0.87. The random forest model
 4294 based on all the metabolic profiles works just as good as PSA testing with a specificity level
 4295 of 0.87. However, this model has the potential to increase the sensitivity to 0.94 when
 4296 reducing the specificity to 0.68. The weighted KNN algorithm has comparable performance
 4297 to the random forest (glutamate only) with specificity 0.86 and sensitivity of 0.64. This
 4298 model also has a working point comparable to the random forest – all metabolites, with
 4299 specificity and sensitivity of 0.68 and 0.95. A trade-off between the two points can also be
 4300 selected, with specificity of 0.78 and specificity of 0.81.

4301



4302

4303 *Figure 6.9. Comparison of different ROC curves. Weighted KNN ROC, trained and validated*
 4304 *using a k-fold validation approach within this PhD research work, is shown in blue. Random*
 4305 *forest algorithms using all the metabolites and glutamate only, trained and validated by*
 4306 *Glasgow Polyomics, are shown in red and black, respectively. PSA ROC obtained from [18]*
 4307 *is shown in green.*

4308 The weighted KNN algorithm contained both the optimised working points from the random
4309 forest algorithms and therefore it was selected as the final choice in this analysis. Within this
4310 algorithm, the working point (0.86, 0.64) is suggested for a real-life scenario. This working
4311 point improves the performance of the current clinical standard by doubling the sensitivity
4312 when maintaining the same specificity.

4313 It might be argued that medications might have affected the concentration of the metabolites.
4314 It was experimentally verified that, for this population, the treatment did not influence the
4315 concentration of the metabolites under test. To do this, the PCa group was divided in sub-
4316 groups, according to the ongoing treatment. No statistically relevant correlation was
4317 identified in the subgroups.

4318 The proposed metabolic biomarker panel was based on literature review and discussion with
4319 PCa clinician experts. However, the metabolic panel can be potentially improved by
4320 including additional or different metabolites. Regardless, it is out of the scope of this work
4321 to identify the best metabolic panel for PCa, which remains an open medical question.
4322 Differently, this study aimed to stress that such a platform can assay the metabolites with
4323 accuracy suitable for the determination of pathological conditions. These findings are
4324 particularly promising if both diagnostic approaches based on PSA and metabolomics are
4325 combined.

4326 In summary, the results from the PCa clinical evaluation reported promising development
4327 after comparison with the current clinical standard. However, certain limitations of the study
4328 may not allow generalising the findings at this stage. Considering the finite set of metabolite
4329 biomarkers, the platform demonstrated its potential for the quantification of multiple
4330 metabolites with accuracy suitable for diagnostically relevant information.

4331

4332 **6.5. Ischemic Stroke Clinical Evaluation**

4333 A clinical evaluation to perform lactate assay on-chip for ischemic stroke stratification was
4334 performed on ten plasma samples from patients which had been affected by an ischaemic
4335 stroke event. Target analytes were lactate and creatinine. However, the volume of the clinical
4336 sample obtained was not enough for performing both the assays. Thus, only lactate
4337 determination was performed. Results from the clinical evaluation were compared with the
4338 results obtained from conventional gold standard measurements used in the National Health
4339 Service (NHS) laboratories.

4340 **6.5.1. Materials and Methods**

4341 **Reagents.** Reagents were purchased from Sigma Aldrich. Formulations were optimised
 4342 using a trial-and-error approach. To save sample volume and avoid platform saturation,
 4343 stroke samples were diluted with DI water (ratio 1:4). Calibrators were also used in diluted
 4344 form. Dilution factors were numerically compensated in the data-analysis stage.
 4345 Environmental temperature and humidity were also monitored. Table 6.7 summarises the
 4346 formulations for ischemic stroke clinical evaluation.

4347 **Clinical samples.** Ten samples of human plasma from people diagnosed with ischemic
 4348 stroke were sourced from the Queen Elizabeth University Hospital, Glasgow, UK, under
 4349 ethical approval, thanks to the collaboration with Dr Samadhan B. Patil, lecturer in medical
 4350 engineering at the University of York, and Prof Jessie Dawson, professor of stroke medicine
 4351 and consultant stroke physician at the Queen Elizabeth Hospital, Glasgow. Donors were
 4352 adults recently diagnosed ischemic stroke. The approximate available volume, for each
 4353 sample, was 100 μ L. A numeric sample IDs from 1 to 10 was randomly assigned to each
 4354 sample. Calibration samples (calibrators) were sourced from the Institute of Cardiovascular
 4355 and Medical Sciences, University of Glasgow. Calibrators were used in diluted form. The
 4356 protocol for sample collection is reported in Appendix L.

4357 **Procedure.** The setup used for lactate clinical evaluation was the same as the one used for
 4358 cancer clinical evaluation. Similarly, reagents were mixed with the sample off-chip and
 4359 immediately introduced into the cartridge in a few seconds. Metabolites were tested
 4360 individually, using cartridges with four microchannels. The adopted protocol is the same as
 4361 the one illustrated for PCa and previously shown in Figure 6.1.

4362 *Table 6.7 Assay formulation for ischemic stroke clinical evaluation.*

	Lactate
Cartridge	4 parallel and identical microchannel (h ~ 290 μ m)
Microchannel volume	0.348 μ L
Light source	LED @ 490nm (3 mW, FWHM = 20 nm)
Total Volume	60 μ L
Sample Volume	6 μ L
DI water	24 μ L
Reagent mix volume	30 μ L
Reagent buffer	DI water
1 st reaction stage	10 μ L LaOx 10 U/ml
2 nd reaction stage	10 μ L HRP 300U/ml 5 μ L Phenol 44.5mM 5 μ L 4AAP 10.5mM
Negative control	1 st reaction stage was substituted with 10 μ L of DI water
Positive control	The sample was spiked with a known concentration of analyte of interest

4363 **Data handling.** Each measurement had four independent repeats. Measurements were
4364 performed in biological triplicates, each composed of four technical replicates.

4365 **Cartridge reuse.** Cartridges were cleaned and re-used using the same procedure used during
4366 cancer clinical evaluation. Two cartridges were used for this experiment.

4367 **Substrate quantification.** Lactate is routinely measured in the clinical environment. Thus,
4368 a similar clinical protocol was adopted in this project, which can be divided into two stages:
4369 calibration and testing. In the clinical environment, calibration is performed every day. The
4370 calibration procedures consist of testing two commercial calibration solutions with known
4371 concentrations of lactate, x_1 and x_2 . Let us refer with y_1 and y_2 to the output of the equipment
4372 when testing the calibrators. The points on a Cartesian coordinates system (x_1, y_1) and ($x_2,$
4373 y_2) identify a calibration line, which is usually obtained by a linear fit of the calibrator
4374 outputs. After calibration, samples were tested in triplicates. Substrate concentration was
4375 determined by comparing the output with the calibration curve.

4376

4377 **6.5.2. Calibration**

4378 **Method.** Calibration was performed using two commercial calibrator solutions. The
4379 concentrations of lactate in the calibrators were 440 μM and 2070 μM . Calibrators were also
4380 used in diluted form.

4381 **Results.** Table 6.8 summarises the results of the calibration stage. Figure 6.10(a) shows data
4382 from a microchannel for both the calibration solutions. The average initial reaction rates over
4383 the biological triplicates were used to determine a linear calibration curve. The 2-points
4384 calibration curve is presented in Figure 6.10(b). The concentration reported in the calibration
4385 curve is the lactate level after dilution. Dilution impact was subsequently compensated using
4386 the appropriate dilution factor. The calibration curve showed a sensitivity of 6.302 mVs^{-1}
4387 mM^{-1} and a baseline of 0.1484 mVs^{-1} . Results are summarised in Figure 6.10. The values
4388 obtained for LOD and LOQ during the PCa clinical evaluation can be assumed to be valid
4389 also for lactate evaluation. This is a conservative assumption since experiments in diluted
4390 samples are more likely to provide lower LOD and LOQ. LOD and LOQ were adjusted
4391 according to the dilution factor and therefore refer to the undiluted sample. LOD and LOQ
4392 were 206.0 μM and 229.0 μM , respectively.

4393

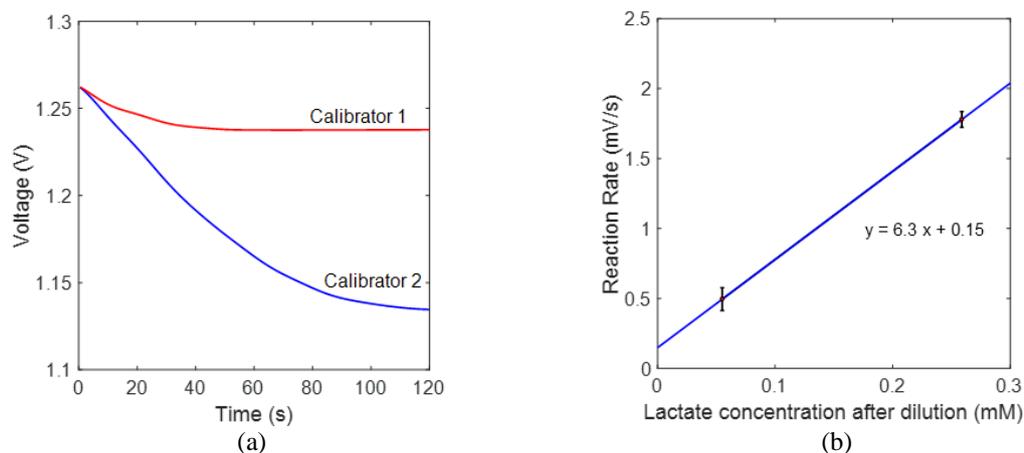
4394

4395 *Table 6.8 Platform Characterisation in human plasma for ischemic stroke metabolites.*
 4396 *Metrics have been defined in Table 2.3.*

	Lactate
Physiological Range	300 - 2000
Relation with stroke	↑
Linear Model	$Y = S \cdot x + C$
Dilution factor	8
Analytical Sensitivity (S) ($\text{mV s}^{-1} \text{mM}^{-1}$)	6.302
C (mV s^{-1})	0.1484
Negative control (mV s^{-1}) ¹	0.005 ± 0.0027
LOD (mV s^{-1})	0.014
LOQ (mV s^{-1})	0.032
LOD (μM) ²	206.0 μM
LOQ (μM) ²	229.0 μM
Resolution (μM) ³	3.44 μM

¹ From the PCA measurements. The composition of the control measurement remains the same.
² Converted using the linear model presented in this table. LOD and LOQ were adjusted according to the dilution factor therefore refer to the undiluted sample.
³ Calculated as the ratio between the standard deviation of the control measurements and the sensitivity in the linear range [58]. The resolution was adjusted according to the dilution factor therefore refers to the undiluted sample.

4397



4398 *Figure 6.10 Calibration data. (a) Output signals from single microchannels for calibrator 1*
 4399 *and calibrator 2. (b) Linear calibration curve resulting from the 2-points calibration*
 4400 *procedure.*

4401

4402

4403

4404

4405 **6.5.3. Clinical evaluation**

4406 **Method.** Lactate plasma level of the ischemic stroke samples was assessed using the
 4407 developed platform. Lactate plasma levels in the samples were known during the
 4408 experiments.

4409 **Results.** Results are shown in Table 6.9. Concentrations were in the range of 0.40 – 2.52
 4410 mM. The average standard deviation of the measurements was 11.15%. Data normalised to
 4411 the average is represented in Figure 6.11.

4412

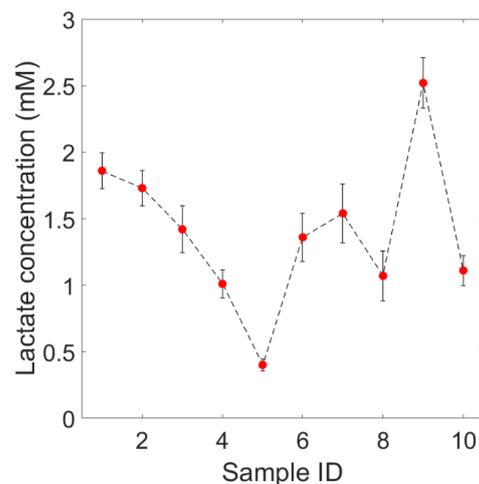
4413

Table 6.9 Clinical evaluation results on ischemic stroke group.

Group	Sample ID	Lactate	
		Avg. mM	Std. %
Stroke	1	1.86	7.23
	2	1.73	7.69
	3	1.42	12.38
	4	1.01	10.37
	5	0.40	11.13
	6	1.36	13.27
	7	1.54	14.40
	8	1.07	17.45
	9	2.52	7.51
	10	1.11	10.07
Ischemic stroke group			
average (mM)		1.40	
median (mM)		1.39	
std. dev. (mM)		0.54	
Range (mM)		0.40 – 2.52	
Avg. environmental. Temp. (°C)		24.7 ± 0.4	
Avg. environmental humidity (%)		34.7 ± 2	

4414

4415



4416

4417

Figure 6.11 Normalised lactate concentrations for ischemic stroke samples

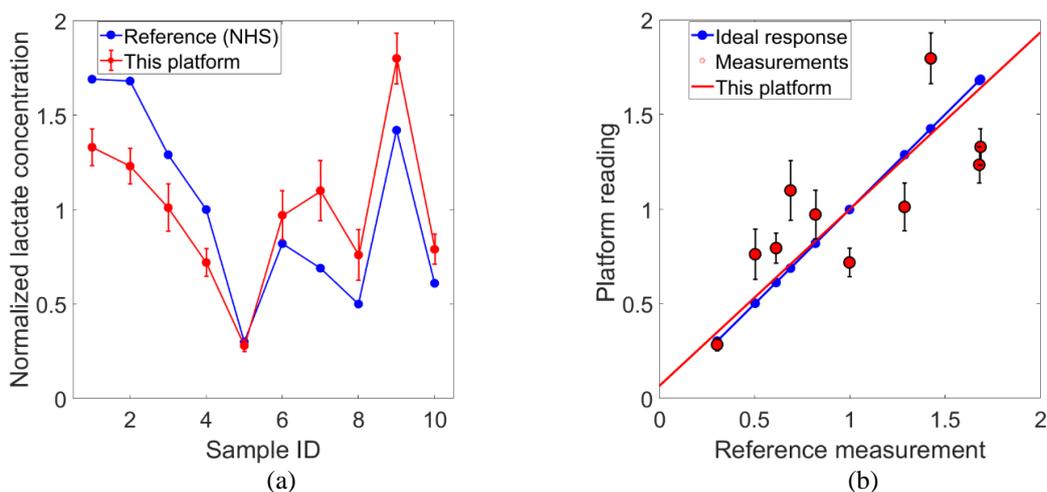
4418 6.5.4. Validation against standard method

4419 **Method.** Samples were independently tested in the Institute of Cardiovascular and Medical
 4420 Sciences, University of Glasgow, routinely used by NHS, by trained personnel. These
 4421 measurements were performed using the Cobas C 311 analyser from Roche Hitachi. The
 4422 analyser was calibrated with a 2-points linear approach, using the same calibrator solutions.
 4423 Both normalised datasets have been overlapped in Figure 6.12(a).

4424 **Results.** The average lactate concentration determined with the gold standard measurement
 4425 was $1.45 \text{ mM} \pm 0.39 \text{ mM}$. When comparing the average of the group obtained with both the
 4426 methods, an average error of $50 \text{ } \mu\text{M}$ was observed. The standard deviation of the
 4427 measurements performed with the developed platform was $150 \text{ } \mu\text{M}$. When comparing the
 4428 two datasets normalised to the respective average, a correlation coefficient $R = 0.77$ was
 4429 observed. For this population, the average relative error of the platform when quantifying
 4430 lactate with respect to the reference method was 27.8%.

4431 A linear fitting was performed using the obtained measurement. The linear fit of the platform
 4432 is compared to the ideal response in Figure 6.12(b). The correlation between the linear fitting
 4433 of the platform measurements and the ideal response was $R^2 > 0.98$.

4434



4435 *Figure 6.12 (a) Normalised gold standard measurement (blue) overlapped to the normalised*
 4436 *measurements performed with the proposed platform (red) for lactate levels. (b) Platform*
 4437 *response (red) compared to ideal response (blue).*

4438

4439

4440 **6.5.5. Discussion**

4441 Clinical evaluation of ischemic stroke samples underlined the ability of the handheld setup
4442 to perform the measurements of a clinical biomarker with performance comparable to
4443 established practice. The handheld platform provided comparable values highlighting its
4444 potential for its use in resource-limited settings. The device used in the gold standard
4445 laboratory-based method (Cobas C 311 analyser from Roche Hitachi) is bulky (width: 1338
4446 mm, depth: 855 mm, height: 1262 mm), heavy (weight: 270 kg), requires to be connected to
4447 the electric grid (230/400 Volts AC 50 Hz) and can only be operated by trained personnel
4448 [320]. Laboratory-centric systems also require patient admission into the hospital, sample
4449 collection, sample testing, result production and communication. These steps inevitably need
4450 additional time which might be not affordable in situations when the timing is crucial.

4451 Differently, the platform has the potential to allow on-the-spot patient stratification in
4452 minutes. Thus, the precision and accuracy of the test might be de-prioritised, in favour of
4453 readiness of the result. Arguably, there are lactate meters already in the market, which could
4454 provide similar results. However, devices on the market only enable the determination of a
4455 single metabolite. This platform can be scaled for the determination of additional markers,
4456 like in the PCa clinical evaluation. Unfortunately, due to the small available volume, it was
4457 not possible to perform additional measurements for other metabolites. However, there is
4458 potential merit in using a panel of markers also for the stroke patients at the risk of other
4459 complications such as multiple organ failure. As previously mentioned, creatinine is another
4460 biomarker routinely used to monitor organ functions in ICU. Availability of data on a larger
4461 marker panel would enable comprehensive analysis of the patients at the higher risk of
4462 mortality. Clinical evaluation of ischemic stroke samples also has some of the limitations
4463 already outlined for PCa, including the lack of detailed information about the samples and
4464 the small size of the population.

4465

4466 **6.6. Multiplexed Assay with Clinical Samples**

4467 Multiplexed assays were performed on two clinical samples from the prostate cancer study.
4468 This study aimed at demonstrating that the platform can perform simultaneous quantification
4469 of the proposed biomarker panel.

4470 **Materials and methods.** Reagents were preloaded into the microchannels. Since sarcosine
4471 has been observed not to be a potential biomarker in the analysed population, it was omitted
4472 from the simultaneous assays. Instead of sarcosine, the remaining channel was used as a
4473 common negative control. The microchannels were functionalised in the following order
4474 from left to right: control, choline, glutamate, LAA. This sequence was selected to reduce
4475 any potential cross-contamination with other measurements. While the control channel was
4476 susceptible to crosstalk, LAA channel was expected to produce the highest absorbance drop.
4477 Thus, they were confined to the sides of the cartridge. Choline was expected to provide a
4478 lower absorbance drop than glutamate, so it was more suitable to be tested adjacently to the
4479 control. Four different solutions were prepared for drying into the microchannels for (i)
4480 negative control, (ii) choline assay, (iii) glutamate assay, (iv) LAA assay. The protocol for
4481 solution preparation is reported in Appendix I. 1 μL of each solution was deposited in the
4482 respective microchannel. The deposition was achieved by manual pipetting, but printing
4483 would have also been suitable. After the deposition of the solution, the cartridge was dried
4484 for 1 hour at room temperature in a vacuum chamber. Dried reagents slightly increased the
4485 light absorbance of the platform in the steady-state. Consequently, the intensity of the light
4486 produced by the LED was increased to keep the platform in its operating point.

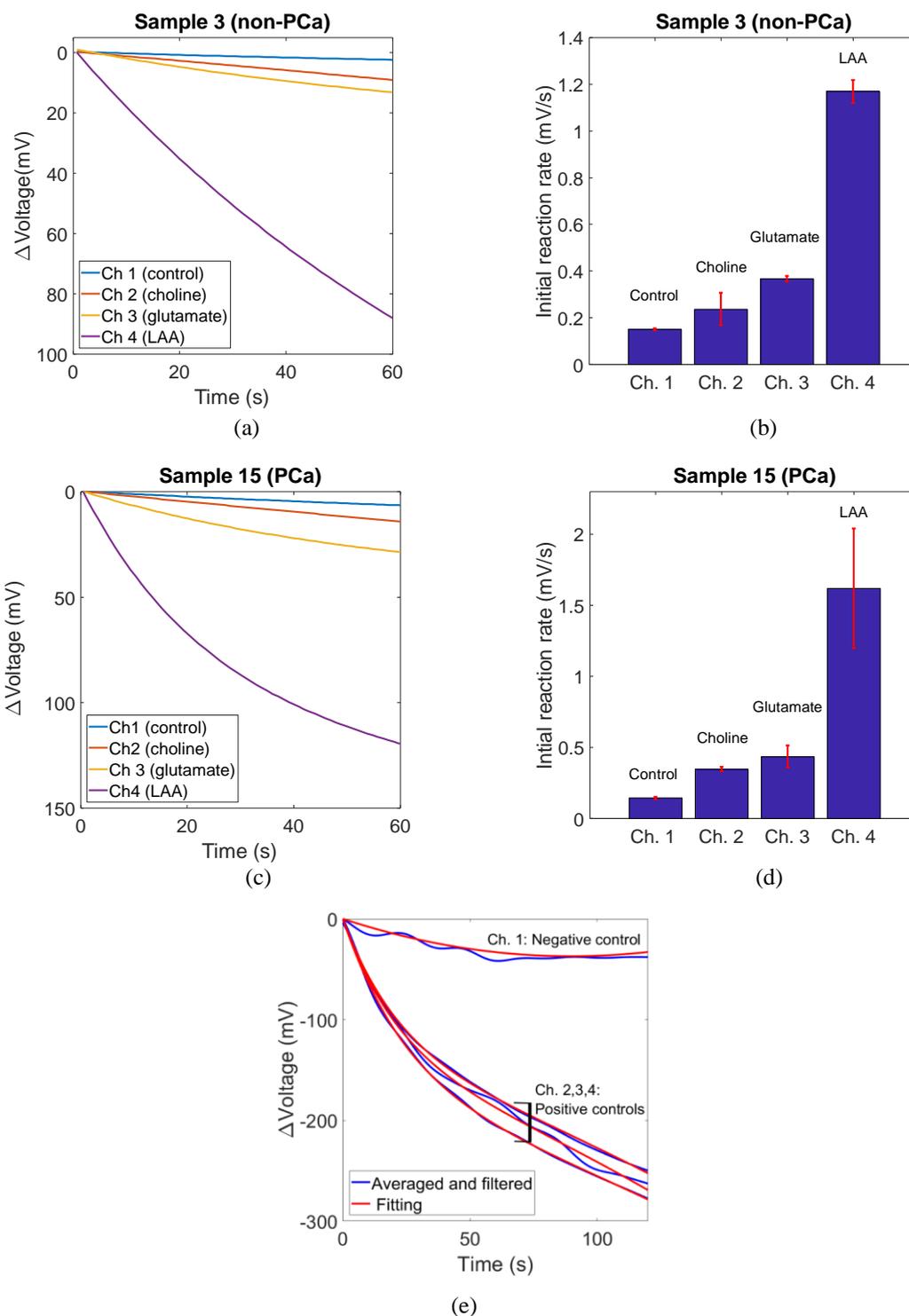
4487 Cartridges were used immediately after the drying step. 15 μL of clinically sourced human
4488 plasma samples were introduced into the cartridge with preloaded reagents without any
4489 further dilution step. Experiments were conducted in duplicates.

4490 **Results.** Figure 6.13 demonstrates that the platform was suitable for measuring multiple
4491 metabolites simultaneously. Figure 6.13(a) and (c) show average data from each channel
4492 after processing. Figure 6.13(b) and (d) reports the average initial reaction rates calculated
4493 in each channel for the two samples under test.

4494 As already discussed in Paragraph 5.5.1, it is not possible to directly compare the rates
4495 obtained with dried reagents with the one obtained with reagents in solution due to different
4496 working conditions. However, dried assays had high correlation with the results obtained in
4497 the clinical testing for all the metabolites and all the replicates ($R^2 > 0.91$). When comparing

4498 rates normalised to the negative control from sample 3 (non-PCa group) with sample 15
4499 (PCa group) for respective metabolites, rates were consistently higher for the PCa sample,
4500 corroborating data obtained during the clinical evaluation.

4501 **Discussion.** The experiments demonstrated that the platform is suitable for multi-metabolite
4502 testing with preloaded reagents. Expectedly, higher variability was observed due to the
4503 reasons discussed in Paragraph 5.5.1. It is worth noticing that the estimation of the potential
4504 metabolic biomarker for PCa clinical evaluation was performed using positive and negative
4505 controls. Here, only a model-based substrate estimation can be achieved. An example of on-
4506 chip positive controls is presented in Figure 6.13(e). Channel 1 was functionalised for the
4507 negative control, as described above with the substitution of HRP 10 μL by DI water. The
4508 remaining channels were functionalised for LAA positive control using a solution obtained
4509 by mixing 6 μL of 25 mM LAA substrate, 4 μL of DI water, 10 μL of 150 U/mL HRP, 5 μL
4510 of 44.5 mM phenol and 5 μL of 10.5 mM 4AAP (total LAA concentration: 5 mM). 15 μL
4511 of human plasma was mixed off-chip with 10 μL of LAA (4 U/mL) and immediately
4512 introduced into the platform. Figure 6.13(e) demonstrates that the platform can perform
4513 positive controls to extrapolate sample-specific calibration. As expected, the lowest rate was
4514 detected for the channel functionalised for negative control. The remaining channels
4515 recorded a considerably high rate due to LAA substrate dried into the microchannels.
4516



4517 *Figure 6.13 Simultaneous testing of PCa-related metabolites in clinical samples. (a) Output*
 4518 *signals from each of the microchannel for sample 3 (non-PCa group). (b) Initial rate*
 4519 *calculations in each of the microchannel for sample 3 (non -PCa group). (c) Output signals*
 4520 *from each of the microchannel for sample 15 (PCa group). (d) Initial rate calculations in*
 4521 *each of the microchannel for sample 15 (PCa group). (e) Simultaneous control*
 4522 *measurements for LAA assay. Ch. 1 is functionalised for negative control. Ch. 3-4 are*
 4523 *functionalised for positive control with known quantity of preloaded substrate.*

4524

4525 6.7. Summary of the Chapter

- 4526 • The platform was evaluated using clinical samples for both PCa and ischemic stroke
4527 aiming to quantify both clinical and analytical performance (see Table 6.10).
- 4528 • For PCa, LAA, glutamate, choline and sarcosine were first quantified in undiluted human
4529 plasma for calibration and validation. Afterwards, the platform was used for the
4530 quantification of the metabolites panel over 10 healthy men and 16 patients affected by
4531 PCa. Measurements, which had comparable value with respect to commercially available
4532 methods, showed increased levels of LAA, glutamate and choline in the PCa group.
4533 Metabolic profiles were then used to train a weighted KNN algorithm with k-fold
4534 validation which scored AUC = 0.862. With the same specificity (around 0.86), the
4535 classifier had higher sensitivity than PSA in this population (0.64 vs 0.32). The
4536 sensitivity of the weighted KNN algorithm could also be increased to 0.95 when
4537 specificity was reduced to 0.68. Based on the PCa clinical evaluation, the platform
4538 demonstrated to potentially be capable of providing metabolic information with
4539 precision suitable to improve the current clinical standard and address the need for new
4540 and complementary diagnostic tools.
- 4541 • For ischemic stroke, lactate was quantified in diluted human plasma from 10 subjects
4542 affected by an ischemic stroke. Results were compared with lactate levels measured by
4543 NHS after admission in the hospital. Measurements with the platform were in the range
4544 0.4 – 2.52 mM and were comparable with the gold reference ($R = 0.77$). Gold reference
4545 measurements were acquired with bulky and expensive equipment. Based on the
4546 ischemic stroke clinical evaluation, the platform demonstrated to be potentially suitable
4547 for rapid and on-the-spot testing in acute medical events.
- 4548 • Multi-metabolite testing was demonstrated using two clinical samples, respectively from
4549 the non-PCa and PCa groups. The four channels of the platform were functionalised with
4550 different reagents allowing to measure, at the same time, negative control, LAA,
4551 glutamate and choline. Output signals were consistent with measurements performed
4552 without lyophilising the reagents ($R^2 > 0.91$).
- 4553
- 4554
- 4555
- 4556

Table 6.10 Performance of the platform in clinically sourced human plasma.

Criterion	This Platform	Reference
Diagnostic performance for prostate Cancer		
Approach	LAA, glutamate, choline 4 microchannels on CMOS Microchannel height ~ 290 μm	PSA is clinically used for PCa diagnosis and typically measured with laboratory equipment.
Sensitivity/Specificity	0.95/0.68 or ¹ 0.64/0.86	0.32/0.86 [18]
Diagnostic performance for Ischemic stroke		
Approach	Lactate 4 microchannels on CMOS Microchannel height ~ 290 μm	Lactate is clinically used for ischemic stroke stratification and typically measured with laboratory equipment (e.g., Cobas C 311 analyser).
Sensitivity/Specificity	The same biomarker was used. Therefore, clinical capabilities depend on the analytical performance of the platform.	
Analytical performance		
Relative error of the measurements	LAA: 18.5% ² Glutamate: 13.81% ² Choline: 21.37% ³ Sarcosine: 44.4% ² Lactate: 27.8% ⁴	Glucose meters: <15% [16] Lactate meter: < 13 % [321]
LOD	LAA: 11.1 μM Glutamate: 1.4 μM Choline: 1.7 μM Sarcosine: 1.4 μM Lactate: 206.0 μM	Physiological ranges: LAA: 1.7 – 4.6 mM Glutamate: 40 – 150 μM Choline: 10 – 40 μM Sarcosine: 0 – 20 μM Lactate: 300 - 2000 μM
Resolution	LAA: 3.25 μM Glutamate: 0.45 μM Choline: 0.27 μM Sarcosine: 0.35 μM Lactate: 3.44 μM	Glucose meters: ~ 50 μM [322] Lactate meter: ~ 100 μM [323]
Sample volume	20 μL	Glucose meters: < 20 μL [16] Lactate meters: < 100 μL [324]
Test duration	2 - 5 min	Glucose meters: < 30s [16] Lactate meters: < 5 min [324]
Portability	Handheld	- Measurements for PCa and ischemic stroke are typically performed in a laboratory. - Other commercial POC devices (i.e. glucose and lactate meters) are handheld [16].
Multi-analyte capabilities	- 6 metabolites in diluted serum and 5 metabolites in human plasma were demonstrated. - 4 simultaneous assays were demonstrated. - The platform was used for 2 different applications. - The platform can support further modalities (e.g. ISFET)	- Most of the POC devices on the market have single metabolite capabilities. - A small number of POC devices on the market have multi-metabolite capabilities (e.g. i-stat) [16].
¹ Different operating selected from the ROC can be used. ² Average value vs. fluorescent plate-based assays. ³ Average value vs. ultra-performance liquid chromatography-tandem mass spectrometry. ⁴ Average value vs. Cobas C 311 analyser (NHS equipment)		

4558 **Chapter 7: Conclusion**

4559 **7.1. Introduction**

4560 Metabolomics POC platforms have vast unexplored potential in modern society. POC testing
4561 aims at a different healthcare model which diverges from the classic laboratory-based
4562 approach and favours portable, rapid, on-the-spot, and low-cost testing.

4563 This thesis illustrated the development of a POC platform used for the diagnosis of PCa and
4564 ischemic stroke using candidate metabolic biomarkers. The main achievements of this PhD
4565 research project are:

- 4566 • The understanding of the CMOS sensor array chip designed and manufactured within
4567 the ‘Multicorder project’. The chip was employed as the sensing unit in this project.
- 4568 • The development of a cartridge, which integrated on the same ceramic package the
4569 CMOS chip, passive microfluidics, and biological reagents. Specifically:
 - 4570 ○ A novel method for integrating microfluidics on the CMOS chip was conceived,
4571 developed, and tested.
 - 4572 ○ A versatile method for bioreagents preloading, based on lyophilisation, was
4573 developed and tested on the chip.
 - 4574 ○ A packaging procedure enabling the use of the cartridge in an aqueous environment
4575 was developed and tested.
- 4576 • The development of a reader and a GUI for interfacing with the cartridge.
- 4577 • The characterisation of all the units composing the POC platform: the sensor array, the
4578 microfluidics, the bioreagents, the reader and the GUI.
- 4579 • The identification of two case-studies, namely PCa and ischemic stroke. Six potential
4580 metabolic biomarkers to identify these conditions were selected: LAA, glutamate,
4581 choline, sarcosine (for PCa), lactate and creatinine (for ischemic stroke).
- 4582 • The development of colorimetric enzymatic assays for the on-chip quantification of the
4583 selected metabolic biomarkers.
- 4584 • The characterisation of the platform for the quantification of all the six metabolites in
4585 diluted human plasma.
- 4586 • The development of a scalable strategy for on-chip preloading of reagents involving the
4587 use of inkjet printing and lyophilisation.

- 4588 • The demonstration of the potential use of the platform for simultaneous multi-metabolite
4589 testing achieved by preloading different reagents in different microfluidic channels on
4590 the same chip.
- 4591 • The demonstration of alternative platform configurations, involving the use of paper
4592 microfluidics and on-chip sample processing.
- 4593 • The clinical evaluation of the platform for PCa diagnosis on a population composed of
4594 10 healthy samples and 16 men diagnosed with PCa.
- 4595 • The clinical evaluation of the platform for ischemic stroke stratification on a population
4596 composed of 10 samples from patients affected by ischemic stroke.
- 4597 • The demonstration of multi-analyte capabilities with clinically sourced human plasma.
- 4598 The rest of this chapter discusses the main limitations of this research and presents some
4599 potential future works.

4600

4601 **7.2. Limitations and Future Works**

4602 The limitations of this research project can be grouped into two categories: (i) limitations of
4603 the platform and (ii) limitations of the clinical studies. Accordingly, the research work has
4604 the potential for improvement in term of the electronic platform used as well as the biological
4605 experiments. Future works are here proposed for mitigating the effects of the limitations
4606 identified.

4607

4608 **7.2.1. Technology limitations and future works**

4609 The limitations of the platform from a technology point of view and future works to mitigate
4610 their effects are discussed here.

4611 **CMOS chip limitations.** The CMOS chip had a limited number of sensors. The geometry
4612 of the sensing platform, especially considering the position of the pads used for wire-bonds,
4613 limited the number of microchannels and the layout of the microfluidics. The CMOS chip
4614 had no embedded temperature sensor. The temperature of the sample is a relevant variable
4615 potentially affecting reagents activity. The design of a new CMOS chip integrating a larger
4616 sensor array and minimising the use of bonding pads (e.g. using serialised solutions) could
4617 be used to improve the accuracy of the measurement and/or increase the number of tests
4618 simultaneously performed on-chip. The integration of an on-chip temperature sensor to
4619 monitor the temperature of the sample within the microstructure has the potential to enable

4620 strategies to compensate for temperature-related effects. The availability of a large area, for
4621 example by wire-bonding the CMOS chip to a PCB or the use of a different package,
4622 alongside with the planarization, can allow the implementation of more sophisticated
4623 microfluidic networks. The optimisation of the GUI, especially by developing software for
4624 all the major operative systems, would enable the sample-to-answer test with no user
4625 interaction. The use of wireless technologies, together with miniaturisation strategies, has
4626 the potential to improve the user-friendliness of the apparatus.

4627 **Assay formulations.** The formulation of the colorimetric assays did not satisfactorily
4628 investigate the use of cofactors, inhibitors, and stabiliser agents. The lyophilisation process
4629 was a disruptive process for the CMOS chip, which became unresponsive after a few
4630 processing cycles. This was a limitation for the reuse of the cartridges since the number of
4631 available chips was limited.

4632 Additional works regarding the optimisation of the formulations and aiming to improve the
4633 shelf life of the reagents as well as the accuracy and precision of the platform are encouraged.
4634 A potential compensation strategy can, for example, employ the Arrhenius' law [325], [326].
4635 This model could be used to estimate the loss of activity of the reagents due to storage time
4636 and condition and numerical compensation of the measured rate. The optimisation of the
4637 formulations used for colorimetric assays can be optimised to enhance stability, reliability,
4638 and sensitivity of the test. The use of cofactors and inhibitors, for instance, can be used to
4639 reduce sample-to-sample variability. The use of stabiliser agents can improve the shelf life
4640 of the reagents preloaded on the chip.

4641 **Sample pre-processing.** The platform was mainly tested with processed samples. Although
4642 a feasibility study was demonstrated, further optimisation of the platform is required to
4643 reliably use unprocessed samples. A more elaborated microfluidics' network, integrating,
4644 for example, capillary pumps or gratings, can be necessary to develop a reliable strategy for
4645 on-chip blood filtration [327]. Finger-powered pumps can also be a viable solution [328].
4646 The use of different H₂O₂ colorimetric dyes, working at a different wavelength, can also be
4647 a successful strategy for quantifying metabolites in unprocessed blood. Amplitie™, for
4648 instance, is a H₂O₂ colorimetric probe working at 650 nm and therefore should minimise the
4649 optical interference of whole blood.

4650 **Target analytes.** The class of analytes which measured with the platform was limited to
4651 substrates which can be converted into H₂O₂ using specific enzymatic reactions.

4652 Future work is also suggested to investigate other capabilities embedded onto the CMOS
4653 chip. Other researchers of the MST group are parallelly working using different integrated
4654 capabilities developed during the Multicorder project, including amperometry [45],
4655 fluorescent sensing [86], SPR [85] and pH sensing [85], [243], [251]. The combination of
4656 the findings has the potential to lead the way to multi-sensing POC platform [85]. The use
4657 of different sensing capability can also widen the class of analytes that can be quantified
4658 with the developed platform.

4659 **Affordability of the platform.** In Table 2.11 maximum costs for reader and cartridge were
4660 set to £5200 and £10 – respectively – after comparison with POC platforms on the market.
4661 The reader can be manufactured at a cost largely lower than the requirement. The use of
4662 affordable off-the-shelf components and a simple custom PCB yield to an estimate price in
4663 the order of hundred pounds. However, the target cost of the cartridge was not met in this
4664 PhD work because cartridges were not produced in high-volume. This raises the question if
4665 the cartridge can meet the requirement when mass-produced.

4666 Fabrication costs for the cartridge can be divided into 4 addends: (1) CMOS chip, (2) fluidics
4667 and packaging, (3) functionalization and (4) human work and instrumentation costs.

- 4668 1. When mass-produced, the cost of CMOS technology can be dramatically reduced. Texas
4669 Instruments estimates that the cost per die for CMOS 0.35 μm technology can be as low
4670 as 2.7 $\text{£}/\text{cm}^2$ [329]. Considering the area of CMOS chip used in this work (12.24 mm^2),
4671 each CMOS chip would cost approximately £0.33 if mass-produced.
- 4672 2. The chip could be packed onto a PCB slot (1x2 cm) rather than on a ceramic package.
4673 Such a PCB slot would cost approximately £0.1 each. For the fabrication of the fluidics,
4674 a SU-8 fabricated onto a 6-inch wafer would cost about £100. However, this would be
4675 allocating around 135 patterns which can be re-used at least 10 times. This results in
4676 £0.08 per pattern. SU-8 mould is used to fabricate a PDMS microstructure. Considering
4677 the cost of PDMS on the market (1.1 kg = £170) we estimate that each PDMS pattern
4678 would cost £0.04 per cartridge. Finally, epoxy (302-3M 1LB by Epoxy Technology Inc.)
4679 was used for the final microstructure and encapsulation. The estimated cost for epoxy is
4680 £0.1 per cartridge. In summary, the total cost for fluidics and packaging is estimated to
4681 be around £0.32 per cartridge.
- 4682 3. Functionalization costs depend on the assay to be performed. The worst-case scenario is
4683 a choline assay, where 1 kU of ChOx costs £703 from Sigma. For 1 test, 1 μl of reaction
4684 solution with 200 U/ml of ChOx was used. This yield to approximately £0.2 per test. If

4685 4 tests are run on the same cartridge, reagents for functionalisation will cost £0.8 per
4686 cartridge.

4687 4. Human costs and equipment should include the amortization of equipment used for chip
4688 bonding, SU-8 mould fabrication and functionalisation. It is reasonable to assume a
4689 +200% cost for this addend.

4690 In summary, the cost per cartridge when mass-produced is estimated to be £4.35. Retail price
4691 is likely to have a +100% surcharge. As such, a retail cost of £8.72 can be estimated. This
4692 figure falls within the cost required for the cartridge.

4693 The cost of the cartridge depends on the application and could be reduced by simplifying the
4694 system. For instance, paper-strip based solutions (such as the one demonstrated in paragraph
4695 5.5.2) can be used to reduce the cost for determined applications. However, based on the
4696 versatility requirement, the research team believed that a reduction of the functionalities of
4697 the platform was not advised at the prototypal stage. Optimisations aimed at cost reduction
4698 will be part of future works.

4699

4700 **7.2.2. Limitations and future work of the clinical studies**

4701 The limitations of the platform concerning the biological experiments and future works to
4702 mitigate their effects are discussed here.

4703 **Population.** For both clinical evaluations, the sample population was small. Relevant
4704 information on clinical samples was also missing ethical reasons.

4705 Future works are encouraged on a larger population. Availability of data on a larger scale is
4706 necessary to potentially verify and generalise the findings. Additional details of the
4707 population, including age, ethnicity, co-morbidities, drug treatment, is necessary to
4708 understand possible interferences in the study. Larger trials with standardised protocol will
4709 be needed to confirm the validity of the platform and achieve medical approval.

4710 **Procedure.** For both clinical evaluations, when metabolites were individually tested,
4711 samples were off-chip mixed with the reagent solution. Some commercial POC platforms
4712 are needing this procedure [296]. However, a pre-processing procedure should be avoided
4713 for a commercial POC platform for in-home use. Due to limited resources, cartridges were
4714 reused in this work, adopting appropriate cleaning procedures. However, the degradation of
4715 performance is possible after multiple tests. The reuse of the cartridges also increased the
4716 risk of cross-contamination. Appropriate metabolic quenching techniques (i.e. freezing) was

4717 necessary. Plasma samples were frozen and contained anticoagulant agents. There is the
4718 possibility that sample storage and additives might have interfered with the measurements.
4719 Methods for future works need to be modified to mitigate several limitations of the clinical
4720 studies at the current state. Clinical studies should also be widened to cartridges with
4721 preloaded reagents, which would better mimic a real-life scenario. Ideally, a definitive
4722 disposable cartridge prototype embedding the technological improvement outlined above
4723 should be employed. The study should also include freshly collected samples, ideally
4724 seconds after the collection from a fingerpick.

4725 **Prostate Cancer.** For PCa, the population of the studies included people with advanced
4726 disease. The advanced stage of the disease might have exacerbated the concentration of the
4727 metabolites. Also, healthy and control samples were collected from different institutions.
4728 Although protocols were in place to ensure the coherence of the study, there is the possibility
4729 that this introduced systematic errors in the groups. Furthermore, the performance of the
4730 classifier was characterised using the measured metabolic profile, which was averaged over
4731 biological triplicates.

4732 Additional work is encouraged for improving the results achieved during clinical testing.
4733 For PCa, a more extensive clinical study also involving third parties laboratory is required
4734 to: (i) validate or modify the metabolic panel; (ii) validate the classification performance of
4735 the platform; (iii) consolidate the evidence that the developed platform can provide
4736 diagnostically relevant information. Accordingly, a more significant number of PCa samples
4737 and controls are required. Specifically, controls and PCa samples should be collected in the
4738 same clinic. Controls donors should be selected to have similar age and lifestyle than PCa
4739 samples. PCa donors should be selected in various stage of the disease. To consolidate the
4740 suitability of the platform for PCa detection, early-stage donors are particularly needed.
4741 Detailed information about PSA levels, eventual drug treatments, co-morbidities, ethnicity,
4742 are required. Validation with high-performance equipment, such as mass spectroscopy, is
4743 needed to characterise the platform performance. The robusticity of the classifier against
4744 single measurements needs to be quantified.

4745 **Ischemic stroke.** For ischemic stroke, the analysed population included people after hospital
4746 admission for ischemic stroke. As for PCa clinical testing, the advanced state of the disease
4747 might have increased the metabolite levels which can potentially be different at an early
4748 stage. Also, due to limited resources, only one metabolite (i.e. lactate) was quantified in the
4749 available samples.

4750 A larger clinical study also involving third parties laboratories is required to: (i) include
4751 additional metabolites in the panel, (ii) develop classification algorithms, (iii) consolidate
4752 the evidence that the platform can provide comparable results with NHS equipment.
4753 Consistently, a larger number of ischemic stroke samples are required. Control samples
4754 should be included too. Ischemic stroke samples should be selected in various stages of the
4755 cardiovascular event. People at high risk of developing ischemic stroke should also be
4756 analysed. Detailed information about the population would also be necessary. Validation
4757 with clinical standards, such as the Cobas C 311 analyser from Roche Hitachi, should be
4758 used to consolidate the performance of the platform. The use of additional metabolites
4759 alongside lactate and creatinine should also be analysed to develop classification procedure
4760 leading to a rapid on-the-spot patient stratification in emergency scenarios.

4761

4762 **7.2.3. Additional potential applications**

4763 A multitude of potential users can take advantage of the developed platform in a variety of
4764 scenarios. Prospective users of the platform include the general population, healthcare
4765 (NHS) staff, insurance groups, pharmacies, drug companies, general practice (GP) surgeries,
4766 paramedics, private healthcare sector, researchers, care homes, social care, athletics bodies,
4767 online doctor, wellbeing monitoring, or online physicians.

4768 The large variety of potential users opens countless opportunities for different
4769 metabolomics-based applications where the potential of metabolomics has been
4770 acknowledged. The use of a similar platform could be employed, for example, for the
4771 diagnosis of other cancer types, other CVDs, sepsis, kidney failure and dementia. Similarly,
4772 the platform can be used for the monitoring of chronic disease where treatment is already in
4773 place, for example, haemophilia or arthritis. Applications other than healthcare are also
4774 equally achievable. For instance, such a platform could be employed for personal wellbeing
4775 or environmental monitoring.

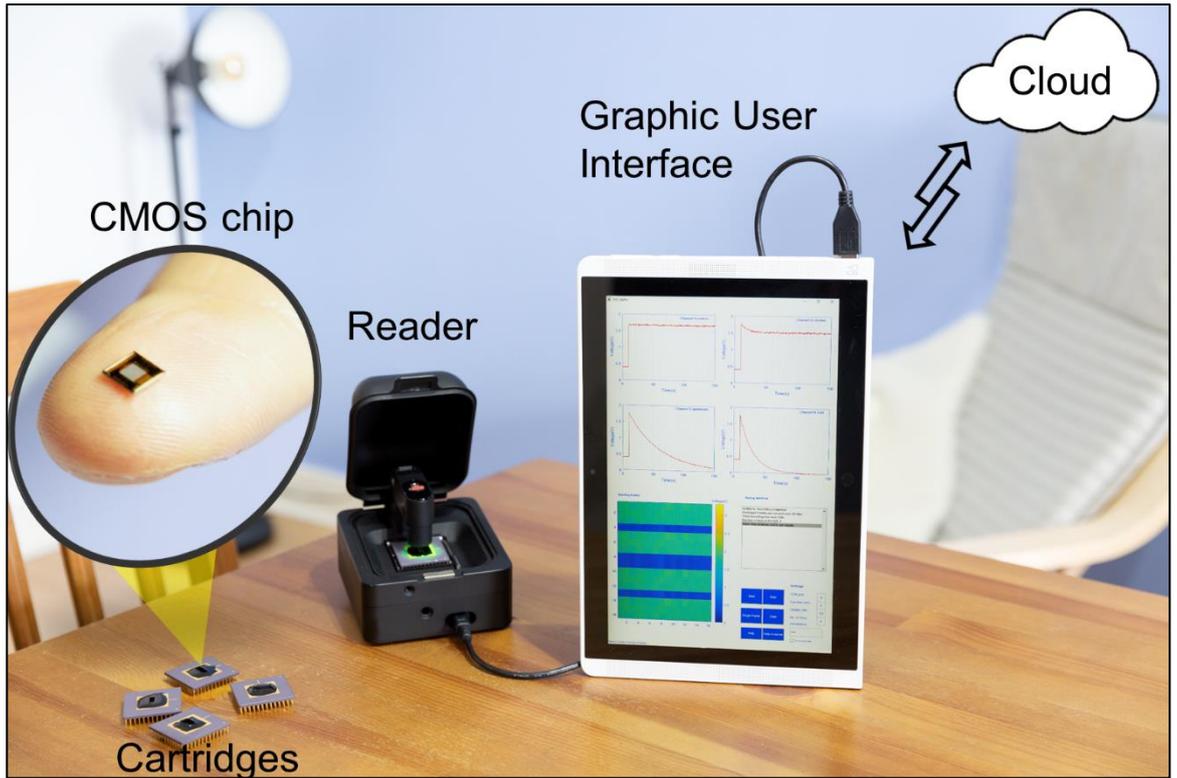
4776 All the mentioned potential applications can be accommodated with minimal modification
4777 of the platform. The use of different reagents within the microfluidics chapter can target
4778 application-specific analytes. Similar chemistry and procedures (such as printing and
4779 lyophilisation) can be employed. Apart from the utilisation of different reagents, the platform
4780 would not require any substantial modification, which makes it ideal for a wide range of
4781 applications.

4782

4783 **7.2.4. Towards a commercial device**

4784 The findings of this research partially contributed to the foundation of ‘Multicorder DX
4785 limited’, a University of Glasgow spin-off company [330]. Multicorder DX aims to bring
4786 technology for rapid and low-cost metabolic biomarkers quantification to the market [330].
4787 The start-up, which to date filed three patents, is now in the process of securing new funding
4788 aiming to develop a commercial product [330]. In this frame, a working prototype of the
4789 platform was developed. The prototype is shown in Figure 7.1. Cartridges are
4790 interchangeable, disposable and can be functionalised in different ways to address various
4791 diseases. For improved storage, cartridges can be vacuum-sealed and labelled. The reader of
4792 the prototype has been reworked to facilitate the use of the device. A black box encloses
4793 both the PCB and the microcontroller board, which remain identical to the ones described in
4794 the dedicated section of Chapter 3. The box of the prototype encapsulates a light-emitting
4795 diode (LED) operating at 490 nm wavelength, and lenses for colorimetric sensing. The
4796 system is aligned so that collimated light is shone onto the active area of the cartridge. The
4797 box also encloses a top lid, which can be closed during the colorimetric assay, to exclude
4798 interference from ambient visible light when the reaction takes place. The black box
4799 enclosing the reader has been outsourced from a specialised company. The GUI works the
4800 same way as described in the dedicated section of this chapter. Only minor modifications of
4801 the layout have been performed to improve the usability onto a tablet device. The platform
4802 shown in the figure was not employed for any of the experiments reported in this thesis but
4803 was used for public and industrial engagements. It has been demonstrated in numerous
4804 events such as ‘BIOCHIP: International Forum on Biochips & Biochip Solutions’, Berlin 7-
4805 8.5.2019. The prototype provides a demonstration that the platform can be optimised for in-
4806 home use by non-trained users and can potentially become a commercial POC device. The
4807 presented POC device has the potential to lead the way for a new generation of diagnostic
4808 tools for low-cost, portable, rapid, and user-friendly disease-related multi-metabolite
4809 quantification.

4810



4811

4812

4813

4814

Figure 7.1 Working prototype of the platform

4815 Appendix

4816 A. Matlab Modelling of Colorimetric Reactions

4817 This appendix illustrates a custom Matlab model for simulating colorimetric reactions. The
 4818 model is based on the Michaelis-Menten model and Beer-Lambert's law. Model parameters
 4819 have been reported in the thesis (Table 3.3). The model has been modified for performing
 4820 other simulations reported in the thesis.

4821

```

4822 clear all
4823 close all
4824
4825 Vm = 0.025;      % Value assumed from the literature in mM/s
4826 km = 3;         % Value assumed from the literature in mM
4827 % Initializations
4828 N = 1000; c = zeros(1,N); v = zeros(1,N); A = zeros(1,N); perT = zeros(1,N); d = zeros(1,N); t = linspace(0,120,N);
4829 % Initial substrate concentrations in mM
4830 concentrations = [0 0.01 0.02 0.03 0.04 0.05 0.075 0.1 0.125 0.15 0.2]
4831 for z = 1:length(concentrations)
4832 c(1) = concentrations(z);      % Initial concentration of the substrate
4833 v(1) = Vm*c(1)/(km+c(1));      % Initial reaction rate
4834 d(1) = 0;                      % Initial concentration of the light absorbing species
4835 T(1) = 100;                    % Initial transmission level
4836 A(1) = 0;                      % Initial absorbance level
4837 ep = 7.5                       % @500nm for oxidised o-dionisidine (brown) - use L/mmol cm according to Sigma
4838 l = 0.5;                       % optical length vector in cm
4839
4840 for j = 2:N
4841 v(j) = Vm*c(j-1)/(km+c(j-1));  % Apply Michaelis-Menten
4842 c(j) = c(1) - v(j)*t(j);       % Rate equation
4843 d(j) = d(1) + v(j)*t(j);       % Rate equation
4844 A(j) = ep*l*d(j);              % Apply Beer-Lambert's law
4845 T(j) = 1./10.^A(j);            % Calculate transmittance
4846 perT(j) = T(j)*100;           % Calculate relative transmittance
4847
4848 if c(j) < 0 || c(j)>c(j-1)      % Break the loop when substrate concentration is zero
4849 c(j:N) = c(j-1).*ones(1,N-j+1);
4850 v(j:N) = v(j-1).*ones(1,N-j+1);
4851 A(j:N) = A(j-1).*ones(1,N-j+1);
4852 perT(j:N) = perT(j-1).*ones(1,N-j+1);
4853 d(j:N) = d(j-1).*ones(1,N-j+1);
4854 break
4855 end
4856
4857 Absorbance(z,:) = A; Transmittance(z,:) = perT; % Save variables and repeat
4858
4859 end
4860
4861 clearvars -except t Vm km N c v A perT d t concentrations Absorbance Transmittance
4862
4863 end
4864
4865 % Graphic Representation
4866 figure(); plot(t,Transmittance'); axis('square'); ylim([50 105]); xlim([0.2 120]); xlabel('time (s)'); ylabel('Transmittance (%)')
4867
4868

```

4869 B. Microcontroller firmware (C++)

4870 This appendix reports the custom C++ code implemented on the mbed board of the reader.

4871

```

4872 #include "mbed.h"
4873 #include "delay.h"
4874
4875 PortOut PDcol(PortB, 0x0f00); // Define 4 bits for columns addressing
4876 PortOut PDrow(PortB, 0x00f0); // Define 4 bits for row addressing
4877 AnalogIn PD(PB_0); // Define pin for analog input
4878 DigitalOut PDrst(PD_2); // Define pin for reset signal
4879 Serial pc(PC_4, PC_5); //Set pin for serial communication (USBTX, USBRX);
4880
4881 int main()
4882 {
4883     int i,j;
4884     int PDv;
4885     pc.baud(921600); // Set baud rate
4886     PDrst = 0;
4887
4888     while(1)
4889     {
4890         PDrst = 1; // Reset
4891         PDcol.write(0);
4892         PDrow.write(0);
4893         wait(0.000500); // Pulse width
4894         PDrst = 0;
4895         PDv = 0; // Deliver starting frame sequence
4896         pc.putc(PDv>>8); // Send 32 zeros, 8 at a time
4897         pc.putc(PDv&0xff);
4898         pc.putc(PDv>>8);
4899         pc.putc(PDv&0xff);
4900
4901         wait(0.020000); // Integration time
4902
4903         for (i=0; i<16; i++) {
4904
4905             PDrow.write(j<<4); // Address row
4906
4907             for(j=0; j<16; j++) {
4908
4909                 PDcol.write(j<<4); // Address column
4910                 wait(0.000005); // wait
4911                 PDv = PD.read_u16(); // Read and convert in 16 bits
4912                 pc.putc(PDv>>8); // send first 8 bits (MSB)
4913                 pc.putc(PDv&0xff); // send last 8 bits (LSB)
4914             }}}
4915
4916
4917

```

4917 C. Extract of the data acquisition code (Matlab)

4918 This appendix reports the custom Matlab code for data acquisition.

4919

```

4920 function pushbutton2_Callback(hObject, eventdata, handles) % RECORDING ROUTINE
4921 % Tidy up
4922 axes(handles.axes1); grid on; hold on; cla; axes(handles.axes2); grid on; hold on; cla;
4923 axes(handles.axes3); grid on; hold on; cla; axes(handles.axes4); grid on; hold on; cla;
4924 axes(handles.axes5); grid on; hold on; cla;
4925 set(handles.text7,'String',''); set(handles.text8,'String',''); set(handles.text10,'String','');
4926 set(handles.text9,'String','');
4927

```

```

4928 % Start communication
4929 instrreset; set(handles.togglebutton2, 'Value',0); COM =str2num(get(handles.edit2,'String'));
4930 uno = 'com'; due = num2str(COM); port = strcat(uno,due);
4931 one_frame = 516; N = 1; buff = one_frame*N; % in Bytes if PD@16bits
4932 MSB = (1:2:buff-2); LSB = (2:2:buff-1); clim = [5000 60000];
4933 frame = str2num(get(handles.edit1,'String'));
4934 display_rate = str2num(get(handles.edit3,'String')); % if 1 display every display_rate
4935
4936 % Test Connection & Select pixel to display
4937 try
4938 clu = 0; trial = 0; s = serial(port); s.InputBufferSize = 2*buff;
4939 set(s,'BaudRate',921600);
4940 fopen(s); % ←-----% Open communication
4941 clear k SS index
4942 tic; trial = trial +1; flushinput(s);
4943 clc;
4944 k = fread(s); % ←----- % Read data
4945 SS = movsum(k,4); index = find(SS==0); n_flags = length(index); % Find frame start
4946 for y = 1:n_flags-1
4947     clu = (index(y+1)-index(y));
4948     if clu == one_frame
4949         frame_start = index(y); frame_stop = index(y+1);
4950         break
4951     end
4952 end
4953 if trial == 100 % Try up to 100 times to get a valid frame
4954     break
4955 end
4956 toc
4957 end
4958 fclose(s) % ←-----% Close communication
4959 % If connection is good go ahead, otherwise 'catch me' is executed.
4960 str1 = 'Connected: Nice to meet you Multicorder Chip!';
4961 str2 = 'Choose 4 pixels to be shown during acquisition';
4962 new_str = strvcats(str1, str2);
4963 set(handles.listbox2,'String', new_str);
4964
4965 catch ME % An error in the communication occurred. Display error accordingly.
4966 fclose (s); % ←-----% Close communication
4967 str1 = 'Ooops something went wrong: I was not able to get data!';
4968 str2 = 'Check your connection/settings and try again.';
4969 new_str = strvcats(str1, str2); set(handles.listbox2,'String', new_str);
4970 pause() % Standby for new command
4971 end
4972
4973 % Test data handling
4974 try
4975 primo = k(frame_start+1:frame_stop-2); binarydata = dec2bin(primo,8);
4976 value = bin2dec([binarydata(MSB,:),binarydata(LSB,:)]);
4977 value = value*-1+2^16; axes(handles.axes1); cla; grid on; drawnow;
4978 mat = vec2mat(value,16); % Plot test frame
4979 xlim([1,16]); ylim([1,16]); imagesc(mat,clim); colorbar;
4980 [column,row] = ginput(4) % Select 4 pixels to be displayed
4981 column = round(column); row = round(row); clc;
4982 catch ME % Error in data handling occurred. Display error accordingly.
4983 close (s) % ←-----% Close communication
4984 str1 = 'Ooops something went wrong: I was not able to plot data!';
4985 str2 = 'Check your connection/settings and try again.';
4986 new_str = strvcats(str1, str2);
4987 set(handles.listbox2,'String', new_str);
4988 pause()
4989 end
4990
4991 % Data recording loop
4992 % tidy up

```

```

4993 axes(handles.axes1); cla; colorbar('off'); set(handles.axes1,'visible','off'); set(handles.axes2,'visible','on');
4994 set(handles.axes3,'visible','on'); set(handles.axes4,'visible','on'); set(handles.axes5,'visible','on');
4995 set(handles.axes1,'visible','on'); axes(handles.axes1); grid on; hold on; cla; axes(handles.axes2); grid on; hold on; cla;
4996 axes(handles.axes3); grid on; hold on; cla; axes(handles.axes4); grid on; hold on; cla;
4997 axes(handles.axes5); grid on; hold on; cla; set(handles.text7,'BackgroundColor','white');
4998 set(handles.text7,'String',''); set(handles.text8,'BackgroundColor','white'); set(handles.text8,'String','');
4999 set(handles.text9,'BackgroundColor','white'); set(handles.text9,'String',''); set(handles.text10,'BackgroundColor','white');
5000 set(handles.text10,'String',''); drawnow
5001 % Initialisations
5002 try
5003 t = datetime('now'); Day_month_year = datestr(t); set(handles.text5,'String',Day_month_year )
5004 axes(handles.axes1); cla; grid on; xlim([1,16]); ylim([1,16]); colorbar; clear k
5005 p = NaN; pp = NaN; ppp = NaN; pppp = NaN;
5006 i_p = 1; i_pp = 1; i_ppp = 1; i_pppp = 1;
5007 time = ones(1,frame)*NaN;
5008 ch1 = 16*(row(1)-1)+column(1); ch2 = 16*(row(2)-1)+column(2); ch3 = 16*(row(3)-1)+column(3); ch4 = 16*(row(4)-
5009 1)+column(4);
5010 ad = get(handles.checkbox3, 'Value');
5011 s.InputBufferSize = buff;
5012 fopen(s); % ←-----% Open communication
5013 flushinput(s);
5014 set(handles.listbox2,'String','Recording...'); drawnow; tic;
5015 for i=1:frame-1
5016     k((i-1)*buff+1:buff*i) = fread(s); % ←-----% Read frame
5017     time(i) = toc; % ←-----% Save time label frame
5018     if ad == 1
5019         P = sprintf('Progress : %2.1f/100',i/frame*100); set(handles.listbox2,'String',P); drawnow;
5020     end
5021     if get(handles.togglebutton2, 'Value') == 1 break; end
5022     if (rem(i, display_rate) == 0)&&(ad==0)
5023         if get(handles.togglebutton3, 'Value') == 1
5024             % Clean the axes
5025             axes(handles.axes2); cla; grid on;hold on; axes(handles.axes3); cla; grid on;hold on;
5026             axes(handles.axes4); cla; grid on;hold on; axes(handles.axes5); cla; grid on;hold on;
5027             axes(handles.axes1); cla; grid on; hold on; set(handles.togglebutton3, 'Value',0);
5028         end
5029         % Manipulate date for plotting
5030         temp = k(end-1027:end);
5031         index = find(movsum(temp,2)==0);
5032         current_frame = temp(index(1)+1:index(1)+512);
5033         value = (current_frame(MSB).*2^8+current_frame(LSB))*-1+2^16;
5034         mat = vec2mat(value,16); i_p = i-display_rate;
5035         % Plot current frame
5036         d = value(ch1); dd = value(ch2); ddd = value(ch3); dddd = value(ch4);
5037         axes(handles.axes2); plot([i_p, i], [p,d], '-b'); set(handles.text7,'String',d);
5038         axes(handles.axes3); plot([i_p, i], [pp,dd], '-r'); set(handles.text8,'String',dd);
5039         axes(handles.axes4); plot([i_p, i], [ppp,ddd], '-k'); set(handles.text9,'String',ddd);
5040         axes(handles.axes5); plot([i_p, i], [pppp,dddd], '-g'); set(handles.text10,'String',dddd);
5041         axes(handles.axes1); imagesc(mat,clims); drawnow;
5042         p = d; pp = dd; ppp = ddd; pppp = dddd; % Save save
5043     end
5044 end
5045 a = toc; % Total recording time
5046 fps = i/a; % Average frame per second
5047 fclose(s); % ←-----% Close communication
5048 catch ME % In case of error save automatically and give error
5049     uisave; % ←-----% Save
5050     fclose(s); % ←-----% Close communication
5051     str1 = 'Oooops something went during the recording!';
5052     str2 = 'You can save anyway your data (not handled).';
5053     new_str = strvcats(str1, str2);
5054     set(handles.listbox2,'String', new_str);
5055 end
5056 % Confirm recording completed
5057 str1 = 'Welldone, Recording completed!!!'; str2 = 'Averaged frames per second was: ';
5058 str3 = num2str(fps); str4 = 'Total recording time was (sec):';

```

```

5059 str5 = num2str(a); new_str = strvcats(str1, str2,str3, str4,str5); set(handles.listbox2,'String', new_str);
5060
5061 % Data handling _____
5062 %Find flags
5063 S = movsum(k,2); index = find(S==0); j = 1;
5064 % Search and exclude invalid frames
5065 for i = 1:length(index)-1
5066     if (index(i+1)-index(i)) == one_frame; good_index(j) = index(i); j = j+1; end
5067 end
5068 clear index; index = good_index;
5069 % Extract frames and convert
5070 for i = 1:length(index)-1
5071     frame_rec = k(index(i)+1:index(i)+512); binarydata = dec2bin(frame_rec,8);
5072     value = bin2dec([binarydata(MSB,:),binarydata(LSB,:)]); value = value*-1+2^16; data(:,i) = value;
5073     clear value frame_rec binarydata
5074 end
5075 % Exclude time-lables of invalid frames
5076 good_time = time(floor(good_index(1:end-1)/514)+1);
5077 % Plot final data
5078 axes(handles.axes2); cla; plot(data((16*(row(1)-1)+column(1)),:)); axes(handles.axes3); cla; plot(data((16*(row(2)-
5079 1)+column(2)),:)); axes(handles.axes4); cla; plot(data((16*(row(3)-1)+column(3)),:));
5080 axes(handles.axes5); cla; plot(data((16*(row(4)-1)+column(4)),:));
5081 % Save
5082 NoC = get(handles.edit4,'String'); Notes = get(handles.edit5,'String');
5083 clearvars -except data fps good_time k Day_month_year time NoC Notes
5084 B = datestr(datetime('now'), 30); yyyy = B(1:4); mm = B(5:6); dd = B(7:8); hh = B (10:11); minu = B (12:13); sec = B
5085 (14:15); div1 = '-'; div2 = '_'; titolo = horzcat([yyyy, div1, mm,div1, dd, div2, hh, div1, minu, div1, sec]);
5086 uisave({'data', 'fps', 'good_time', 'k', 'Day_month_year', 'time','titolo','NoC','Notes'},titolo) % <---% Save
5087
5088

```

5089 D. Extract of the data processing Code (Matlab)

5090 This appendix reports the custom Matlab code for data processing.

```

5091
5092 % Initialisation _____
5093 Clc; clearvars -except dark eps L data Day_month_year fps good_time NoC Notes titolo; close all;
5094 seconds = 10; dark = 0.3989; %Volts eps = 10000; %M-1cm-1 L = 0.027; %cm-1 start_after_x_seconds= 10;
5095 Niir = 8; Fst = 0.05; Fs = fps; % Filter settings SP1 = 0;SP2 = 0;SP3 = 0;SP4 = 0;
5096 % default structure with 4 channels
5097 ch1 = 1:16*3; wall1 = 16*3+1:16*4; ch2 = 16*4+1:16*7; wall2 = 16*7+1:16*9; ch3 = 16*9+1:16*12; wall3 =
5098 16*12+1:16*13; ch4 = 16*13+1:16*16;
5099
5100 % Pixel inspection and exclusion _____
5101 pix = 1:256; data_label = [pix', data];
5102
5103 % Channel 1
5104 figure(99); plot(data_label(ch1,:)); plotedit on; title('channel 1'); xlim = [2,size(data_label,2)]; pause()
5105 figure(99); a = get(gca,'Children'); ydata = get(a, 'YData'); close all; ch1_default = ch1; clear ch1;
5106 for i=1:size(ydata,1)
5107     temp = ydata{i,1}; ch1(i) = temp(1);
5108 end
5109 clear ydata;
5110
5111 % Channel 2
5112 figure(99); plotedit on; plot(data_label(ch2,:)); title('channel 2'); xlim = [2,size(data_label,2)]; pause()
5113 figure(99); a = get(gca,'Children'); ydata = get(a, 'YData'); close all; ch2_default = ch2; clear ch2;
5114 for i=1:size(ydata,1)
5115     temp = ydata{i,1}; ch2(i) = temp(1);
5116 end
5117 clear ydata;
5118
5119 % Channel 3
5120 figure(99); plot(data_label(ch3,:)); plotedit on; title('channel 3'); xlim = [2,size(data_label,2)]; pause()

```

```

5121 figure(99); a = get(gca,'Children'); ydata = get(a, 'YData'); close all; ch3_default = ch3; clear ch3;
5122 for i=1:size(ydata,1)
5123     temp = ydata{i,1}; ch3(i) = temp(1);
5124 end
5125 clear ydata;
5126
5127 % Channel 4
5128 figure(99); plot(data_label(ch4,:)); plottedit on; title('channel 4'); xlim = [2,size(data_label,2)]; pause()
5129 figure(99); a = get(gca,'Children'); ydata = get(a, 'YData'); close all; ch4_default = ch4; clear ch4;
5130 for i=1:size(ydata,1)
5131     temp = ydata{i,1}; ch4(i) = temp(1);
5132 end
5133 clear ydata;
5134
5135 % Pixel map
5136 map=zeros(1,16*16); map(ch1)=1; map(ch2)=2; map(ch3)=3; map(ch4)=4;
5137 figure(); imagesc(vec2mat(map,16)); colormap('Jet'); title('Pixel map');
5138 % convert and normalize
5139 data1 = data(ch1,:)*3.3/2^16-dark; data2 = data(ch2,:)*3.3/2^16-dark;
5140 data3 = data(ch3,:)*3.3/2^16-dark; data4 = data(ch4,:)*3.3/2^16-dark;
5141 % Spatial average
5142 medio1 = mean(data1); medio2 = mean(data2);medio3 = mean(data3); medio4 = mean(data4);
5143 stand1 = std(data1); stand2 = std(data2); stand3 = std(data3); stand4 = std(data4);
5144 figure(); plot(good_time, medio1); hold on; plot(good_time, medio2); plot(good_time, medio3); plot(good_time,
5145 medio4); legend('ch1','ch2','ch3','ch4');
5146
5147 % Select starting point
5148 _____
5149 % Ch1
5149 figure(); plot(medio1);hold on; plot(medio1,'or'); title('Channel 1'); zoom on; waitfor(gcf, 'CurrentCharacter',
5150 char(13));zoom reset; zoom off; [x1,y1] = ginput(1);
5151 % Ch2
5152 figure(); plot(medio2);hold on; plot(medio2,'or'); title('Channel 2'); zoom on; waitfor(gcf, 'CurrentCharacter',
5153 char(13));zoom reset; zoom off; [x2,y2] = ginput(1);
5154 %Ch3
5155 figure(); plot(medio3);hold on; plot(medio3,'or'); title('Channel 3'); zoom on; waitfor(gcf, 'CurrentCharacter',
5156 char(13));zoom reset; zoom off; [x3,y3] = ginput(1);
5157 %Ch4
5158 figure(); plot(medio4);hold on; plot(medio4,'or'); title('Channel 4'); zoom on; waitfor(gcf, 'CurrentCharacter',
5159 char(13));zoom reset; zoom off; [x4,y4] = ginput(1);
5160
5161 % Processing Ch1
5162 _____
5162 % Filtering
5163 x= round(x1); filt_this = data1(:,x:end);
5164 iir = designfilt('lowpassiir','FilterOrder',Niir,'HalfPowerFrequency',Fst,'SampleRate',Fs);
5165 for j = 1:size(filt_this,1)
5166     data_filt(j,:) = filtfilt(iir,filt_this(j,:));
5167 end
5168 % Match the initial value
5169 time = good_time(x:end)-good_time(x); off = mean(data_filt(:,1:250),2); off_mode = mean(off); adj = off - off_mode;
5170 data_filt = data_filt - repmat(adj,1,size(data_filt,2));
5171 SP1 = off_mode;
5172 % Spatial average
5173 step = floor(fps*1); medio = mean(data_filt,1);
5174 %Crop
5175 temp = find(time>330); try five = temp(1); catch five = find(medio == medio(end-step)); end
5176 % Temporal average
5177 k = 1;
5178 for j = 1:step:length(medio(1:five))
5179     mediot(k) = mean(medio(1,j:j+step)); timet(k) = mean(time(j:j+step)); k = k + 1;
5180 end
5181 % Calculate Rates in defined windows; do not start rate calculation from 0; start from si. This would avoid discrepances
5182 between average and fitted data at the end point
5183 si = min(find(timet>start_after_x_seconds));
5184
5185 % Process over 30 seconds
5186 window = 30+2*start_after_x_seconds;

```

```

5187 % Curve fitting
5188 try end_pointt = find(timet>window); end_point = end_pointt(1);
5189 catch end_point = find(mediott == mediott(end)); end
5190 [xData, yData] = prepareCurveData( timet(1:end_point), mediott(1:end_point)); ft = fitype( 'exp2' );
5191 opts = fitoptions( 'Method', 'NonlinearLeastSquares' ); opts.Display = 'Off'; opts.Robust = 'LAR';
5192 [fitresult, gof] = fit( xData, yData, ft, opts ); timef_30s = timet(1:end_point); fitted_30s = feval(fitresult, xData);
5193 % Transmittance, Absorbance
5194 T_30s = fitted_30s./fitted_30s(1); A_30s = -log10(T_30s); i30 = min(find(timet>(30+si)));
5195 if isempty(i30) == 1 i30 = -si; end
5196 % Rates
5197 index = i30 ; P = polyfit(timet(si:index),mediott(si:index),1); R30 = P(1)*1000; clear P; % On average
5198 P = polyfit(timef_30s(si:index),fitted_30s(si:index)',1); F30 = P(1)*1000; clear P; % On fitting
5199 P = polyfit(timet(si:index),T_30s(si:index)',1); T30 = P(1)*1000; clear P; % On Transmittance
5200 P = polyfit(timet(si:index),A_30s(si:index)',1); A30 = P(1)*1000; clear P; % On Absorbance
5201
5202 % Process over 60 seconds
5203 window = 60+2*start_after_x_seconds;
5204 % Curve fitting
5205 try end_pointt = find(timet>window); end_point = end_pointt(1);
5206 catch end_point = find(mediott == mediott(end)); end
5207 [xData, yData] = prepareCurveData( timet(1:end_point), mediott(1:end_point)); ft = fitype( 'exp2' );
5208 opts = fitoptions( 'Method', 'NonlinearLeastSquares' ); opts.Display = 'Off'; opts.Robust = 'LAR';
5209 [fitresult, gof] = fit( xData, yData, ft, opts ); timef_60s = timet(1:end_point); fitted_60s = feval(fitresult, xData);
5210 % Transmittance, Absorbance
5211 T_60s = fitted_60s./fitted_60s(1); A_60s = -log10(T_60s); i60 = min(find(timet>(60+si)));
5212 if isempty(i60) == 1 i60 = -si; end
5213 index = i60; P = polyfit(timet(si:index),mediott(si:index),1); R60 = P(1)*1000; clear P; % On average
5214 P = polyfit(timef_60s(si:index),fitted_60s(si:index)',1); F60 = P(1)*1000; clear P; % On fitting
5215 P = polyfit(timet(si:index),T_60s(si:index)',1); T60 = P(1)*1000; clear P; % On Transmittance
5216 P = polyfit(timet(si:index),A_60s(si:index)',1); A60 = P(1)*1000; clear P; % On Absorbance
5217
5218 % Process over 90 seconds
5219 window = 90+2*start_after_x_seconds;
5220 % Curve fitting
5221 try end_pointt = find(timet>window); end_point = end_pointt(1);
5222 catch end_point = find(mediott == mediott(end)); end
5223 [xData, yData] = prepareCurveData( timet(1:end_point), mediott(1:end_point)); ft = fitype( 'exp2' );
5224 opts = fitoptions( 'Method', 'NonlinearLeastSquares' ); opts.Display = 'Off'; opts.Robust = 'LAR';
5225 [fitresult, gof] = fit( xData, yData, ft, opts ); timef_90s = timet(1:end_point); fitted_90s = feval(fitresult, xData);
5226 % Transmittance, Absorbance
5227 T_90s = fitted_90s./fitted_90s(1); A_90s = -log10(T_90s); i90 = min(find(timet>(90+si)));
5228 if isempty(i90) == 1 i90 = -si; end
5229 index = i90; P = polyfit(timet(si:index),mediott(si:index),1); R90 = P(1)*1000; clear P; % On average
5230 P = polyfit(timef_90s(si:index),fitted_90s(si:index)',1); F90 = P(1)*1000; clear P; % On fitting
5231 P = polyfit(timet(si:index),T_90s(si:index)',1); T90 = P(1)*1000; clear P; % On Transmittance
5232 P = polyfit(timet(si:index),A_90s(si:index)',1); A90 = P(1)*1000; clear P; % On Absorbance
5233
5234 % Process over 120 seconds
5235 window = 120+2*start_after_x_seconds;
5236 % Curve fitting
5237 try end_pointt = find(timet>window); end_point = end_pointt(1);
5238 catch end_point = find(mediott == mediott(end)); end
5239 [xData, yData] = prepareCurveData( timet(1:end_point), mediott(1:end_point)); ft = fitype( 'exp2' );
5240 opts = fitoptions( 'Method', 'NonlinearLeastSquares' ); opts.Display = 'Off'; opts.Robust = 'LAR';
5241 [fitresult, gof] = fit( xData, yData, ft, opts ); timef_120s = timet(1:end_point); fitted_120s = feval(fitresult, xData);
5242 % Transmittance, Absorbance
5243 T_120s = fitted_120s./fitted_120s(1); A_120s = -log10(T_120s); i120 = min(find(timet>(120+si)));
5244 if isempty(i120) == 1 i120 = -si; end
5245 index = i120; P = polyfit(timet(si:index),mediott(si:index),1); R120 = P(1)*1000; clear P; % On average
5246 P = polyfit(timef_120s(si:index),fitted_120s(si:index)',1); F120 = P(1)*1000; clear P; % On fitting
5247 P = polyfit(timet(si:index),T_120s(si:index)',1); T120 = P(1)*1000; clear P; % On Transmittance
5248 P = polyfit(timet(si:index),A_120s(si:index)',1); A120 = P(1)*1000; clear P; % On Absorbance
5249
5250 % Process over 300 seconds
5251 window = 300+2*start_after_x_seconds;
5252 % Curve fitting

```

```

5253 try end_pointt = find(timet>window); end_point = end_pointt(1);
5254 catch end_point = find(mediat == mediot(end)); end
5255 [xData, yData] = prepareCurveData( timet(1:end_point), mediot(1:end_point)); ft = fittype( 'exp2' );
5256 opts = fitoptions( 'Method', 'NonlinearLeastSquares' ); opts.Display = 'Off'; opts.Robust = 'LAR'; [fitresult, gof] = fit(
5257 xData, yData, ft, opts ); timef_300s = timet(1:end_point); fitted_300s = feval(fitresult, xData);
5258 % Transmittance, Absorbance
5259 T_300s = fitted_300s./fitted_300s(1); A_300s = -log10(T_300s); i300 = min(find(timet>(120+si)));
5260 if isempty(i300) == 1 i300 = -si; end
5261 index = i300; P = polyfit(timet(si:index),mediot(si:index),1); R300 = P(1)*1000; clear P; % On average
5262 P = polyfit(timef_300s(si:index),fitted_300s(si:index),1); F300 = P(1)*1000; clear P; % On fitting
5263 P = polyfit(timet(si:index),T_300s(si:index),1); T300 = P(1)*1000; clear P; % On Trasmittance
5264 P = polyfit(timet(si:index),A_300s(si:index),1); A300 = P(1)*1000; clear P; % On Absorbance
5265 Rates = [SP1, R30, R60, R90, R120, R300; SP1, F30, F60, F90, F120, F300; SP1, T30, T60, T90, T120, T300; SP1, A30,
5266 A60, A90, A120, A300];
5267
5268 %Graphical Representations
5269 figure(); plot(time, filt_this,'k'); hold on; plot(timet,mediot,'b'); plot(timef_300s,fitted_300s,'g');
5270 plot(timef_30s,fitted_30s,'r') legend('Raw pixels', 'blue - Filtered & Averaged', 'Red - Fitted 30s', 'Green - Fitted 5min')
5271
5272 % Save variables and clean
5273 start1 = x; %Starting point
5274 time1 = time; %Re-scaled time axis
5275 data_filt1 = data_filt; %Filtered data
5276 medio1 = medio; %Spatial average
5277 mediot1 = mediot; %Spatio-temporal average
5278 timet1 = timet; % Re-scaled axis for spatio-temporal axis
5279 T1 = T_300s; % Transmittance
5280 A1 = A_300s; % Absorbance
5281 Rates1=Rates;
5282 %Line 1 in mV/s; Line 2 in mV/s using fitted data; Line 3 in %/s, Line 4 in absorbance units/s
5283 fitted1 = fitted_300s; % Fitted data
5284 timef1 = timef_300s; % Time diagram for fitted signal
5285 clearvars -except dark eps L data Day_month_year fps good_time NoC Notes titolo ...
5286 x1 x2 x3 x4 data1 data2 data3 data4 SP1 SP2 SP3 SP4...
5287 start1 time1 timet1 data_filt1 medio1 mediot1 T1 A1 Rates1 fitted1 timef1...
5288 Niir Fst Fs start_after_x_seconds
5289
5290 % Processing Ch2
5291 x= round(x2); filt_this = data2(:,x:end);
5292 { ... } Code is here omitted, been very similar to the one reported for channel 1.
5293 % Save variables and clean
5294 start2 = x; %Starting point
5295 time2 = time; %Re-scaled time axis
5296 data_filt2 = data_filt; %Filtered data
5297 medio2 = medio; %Spatial average
5298 mediot2 = mediot; %Spatio-temporal average
5299 timet2 = timet; % Re-scaled axis for spatio-temporal axis
5300 T2 = T_300s; % Transmittance
5301 A2 = A_300s; % Absorbance
5302 Rates2 = Rates; % Rates
5303 fitted2 = fitted_300s; % Fitted data
5304 timef2 = timef_300s; % Time diagram for fitted signal
5305 clearvars -except dark eps L data Day_month_year fps good_time NoC Notes titolo ...
5306 x1 x2 x3 x4 data1 data2 data3 data4 SP1 SP2 SP3 SP4...
5307 start1 time1 timet1 data_filt1 medio1 mediot1 T1 A1 Rates1 fitted1 timef1...
5308 start2 time2 timet2 data_filt2 medio2 mediot2 T2 A2 Rates2 fitted2 timef2...
5309 Niir Fst Fs start_after_x_seconds
5310
5311 % Processing Ch3
5312 x= round(x3); filt_this = data3(:,x:end);
5313 { ... } Code is here omitted, been very similar to the one reported for channel 1.
5314 % Save variables and clean
5315 start3 = x; %Starting point
5316 time3 = time; %Re-scaled time axis
5317 data_filt3 = data_filt; %Filtered data
5318 medio3 = medio; %Spatial average

```



```

5319 mediot3 = mediot;           %Spatio-temporal average
5320 timet3 = timet;           % Re-scaled axis for spatio-temporal axis
5321 T3 = T_300s;              % Transmittance
5322 A3 = A_300s;              % Absorbance
5323 Rates3 = Rates;           % Rates
5324 fitted3 = fitted_300s;    % Fitted data
5325 timef3 = timef_300s;      % Time diagram for fitted signal
5326 clearvars -except dark eps L data Day_month_year fps good_time NoC Notes titolo ...
5327     x1 x2 x3 x4 data1 data2 data3 data4 SP1 SP2 SP3 SP4...
5328     start1 time1 timet1 data_filt1 medio1 mediot1 T1 A1 Rates1 fitted1 timef1...
5329     start2 time2 timet2 data_filt2 medio2 mediot2 T2 A2 Rates2 fitted2 timef2...
5330     start3 time3 timet3 data_filt3 medio3 mediot3 T3 A3 Rates3 fitted3 timef3...
5331     Niir Fst Fs start_after_x_seconds
5332
5333 % Processing Ch4
5334 x= round(x4); filt_this = data4(:,x:end);
5335 { ... } Code is here omitted, been very similar to the one reported for channel 1.
5336 % Save variables and clean
5337 start4 = x;                 %Starting point
5338 time4 = time;               %Re-scaled time axis
5339 data_filt4 = data_filt;     %Filtered data
5340 medio4 = medio;            %Spatial average
5341 mediot4 = mediot;          %Spatio-temporal average
5342 timet4 = timet;            % Re-scaled axis for spatio-temporal axis
5343 T4 = T_300s;               % Transmittance
5344 A4 = A_300s;               % Absorbance
5345 Rates4 = Rates;           % Rates
5346 fitted4 = fitted_300s;    % Fitted data
5347 timef4 = timef_300s;      % Time diagram for fitted signal
5348 clearvars -except dark eps L data Day_month_year fps good_time NoC Notes titolo ...
5349     x1 x2 x3 x4 data1 data2 data3 data4 SP1 SP2 SP3 SP4...
5350     start1 time1 timet1 data_filt1 medio1 mediot1 T1 A1 Rates1 fitted1 timef1...
5351     start2 time2 timet2 data_filt2 medio2 mediot2 T2 A2 Rates2 fitted2 timef2...
5352     start3 time3 timet3 data_filt3 medio3 mediot3 T3 A3 Rates3 fitted3 timef3...
5353     start4 time4 timet4 data_filt4 medio4 mediot4 T4 A4 Rates4 fitted4 timef4...
5354     Niir Fst Fs start_after_x_seconds
5355
5356 % Show and save
5357 Rates = [Rates1, Rates2, Rates3, Rates4];
5358 figure(); title('PD Output (mV)'); plot(timef1,fitted1); hold on; plot(timef2,fitted2); plot(timef3,fitted3);
5359 plot(timef4,fitted4); figure(); title('Transmittance and Absorbance'); yyaxis left; plot(timef1,T1,'b-o'); hold on;
5360 plot(timef2,T2,'b-v'); plot(timef3,T3,'b-s'); plot(timef4,T4,'b-p'); yyaxis right; plot(timef1,A1,'r-o'); hold on;
5361 plot(timef2,A2,'r-v') plot(timef3,A3,'r-s'); plot(timef4,A4,'r-p'); uisave;
5362

```

5363 E. Contact angle measurements

5364 The capillary pressure within a passive microfluidic channel depends on the cosine of the
5365 contact angles of the employed materials. The static contact angle θ is one of the
5366 conventional ways to measure the wettability of a material. It is defined as the angle that
5367 encompasses a liquid between two interfaces with materials in the solid and vapour phase.
5368 Figure E.1 (a)-(c) shows static contact angles for hydrophobic ($\theta > 90^\circ$) and hydrophilic (θ
5369 $< 90^\circ$) surfaces, as well as the case of $\theta = 90^\circ$. Aiming to maximise the capillary pressure,
5370 hydrophobic and hydrophilic materials can both be employed, as long as their contact angle
5371 is as far as possible from 90° .

5372 PDMS is a slightly hydrophobic material with static water contact angle ranging from 100°
 5373 to 110°, but its wettability can be modified [285]. Exposure of PDMS to oxygen plasma
 5374 gives the material super hydrophilic properties ($\theta < 10^\circ$) [285]. Unfortunately, this surface
 5375 modification is only temporary, and the surface recovers its hydrophobic behaviour in a few
 5376 hours [285]. Polyvinyl alcohol (PVA) deposition on PDMS is another method for the surface
 5377 modification of PDMS. Authors in [285] show that PVA-coated PDMS has a permanent
 5378 hydrophilic behaviour with a contact angle in the range 20°- 40° [285]. The recipe reported
 5379 in [285] has been replicated in this PhD research project. Epoxy resin materials have a slight
 5380 hydrophobic/hydrophilic behaviour depending on the recipe [290].

5381 A custom setup was developed to measure the contact angle of the materials employed in
 5382 the fabrication and is schematically shown in Figure E.1 (d). The experimental setup
 5383 consisted of a digital microscope (Dino-Lite AD4113T-I2V) mounted onto the z-axis, used
 5384 to take micrographs of a 10 μ L drop of water deposited onto the surface. A Matlab-based
 5385 script was written to: (i) identify the droplet, (ii) fit the droplet shape with an elliptical model,
 5386 (iii) identify the liquid-solid interface, (iv) calculate the tangent to the ellipse from the
 5387 surface interface, and (v) compute the contact angle. The script used for the determination
 5388 of the contact angle is reported below. The custom setup for contact angle measurements
 5389 was utilised for estimating the wettability of untreated PDMS, PVA-modified PDMS
 5390 according to the recipe in [285], epoxy resin and the CMOS chip. Figure E.1 (e)-(h) show
 5391 pictures of the measurements conducted with the custom setup. It is interesting noticing that
 5392 the CMOS chip has a slight hydrophilic behaviour, probably related to its irregular surface.

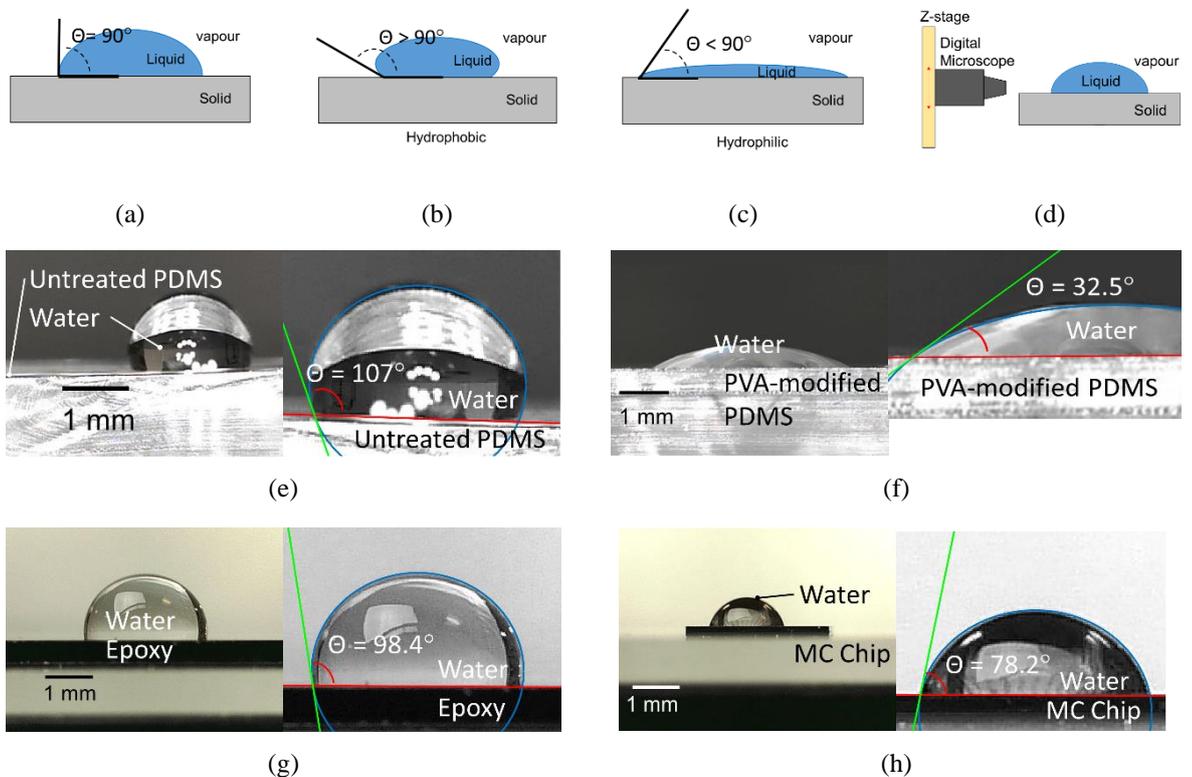
5393

```
5394 RGB = imread('Z:\Digital microscope\2019_01_10\contact angle\epoxy.jpg');
5395 figure(1)
5396 title('select area of interest')
5397 imshow(RGB); drawnow; re = getrect; close.figure(1)
5398 RGB_cut = RGB(re(2):re(2)+re(4),re(1):re(1)+re(3),1);
5399
5400 clear RGB; RGB = RGB_cut;
5401
5402 figure(1); imshow(RGB); title('Select point 1 of the substrate'); drawnow;
5403 zoom on; waitfor(gcf, 'CurrentCharacter', char(13)); [xx1,yy1] = ginput(1); close.figure(1)
5404
5405 figure(1); imshow(RGB); title('Select point 2 of the substrate'); drawnow; zoom on; waitfor(gcf, 'CurrentCharacter',
5406 char(13)); [xx2,yy2] = ginput(1); close.figure(1)
5407
5408 figure(1); imshow(RGB); hold on; coefficients = polyfit([xx1, xx2], [yy1, yy2], 1); a = coefficients (1);
5409 b = coefficients (2); xx = 1:size(RGB,2); yy = a.*xx+b; hold on; plot(xx,yy,'r','LineWidth',6)
5410 title('Drop under test and substrate definition'); close.figure(1)
5411
5412 figure(1); imshow(RGB); drawnow; title('Select multiple points on the edge of the drop')
5413 zoom on; waitfor(gcf, 'CurrentCharacter', char(13)); poly = getline; close.figure(1)
5414
5415 % Ellipse fitting function from Matlab:
```

```

5416 % https://uk.mathworks.com/matlabcentral/fileexchange/22684-ellipse-fit-direct-method
5417 A = EllipseDirectFit(poly);% ax^2 + bxy + cy^2 + dx + ey + f = 0 algebraic solution
5418 % Coordinates conversion function from Matlab:
5419 % https://uk.mathworks.com/matlabcentral/fileexchange/32105-conversion-of-conics-
5420 parameters?focused=5192019&tab=function
5421 [G,w] = AtoG(A);
5422
5423 figure(2); xCenter = G(1); yCenter = G(2); xRadius = G(3); yRadius = G(4); angle = 0;
5424 theta = 0 : 0.01 : 2*pi; x = xRadius * cos(theta) + xCenter; y = yRadius * sin(theta) + yCenter;
5425 imshow(RGB); drawnow; hold on; plot(x, y, 'LineWidth', 3); hold on; plot(xx,yy,'r','LineWidth',3)
5426
5427 figure(3); imshow(RGB); hold on; plot(x, y, 'LineWidth', 3); hold on; title('Select intersection');
5428 plot(xx,yy,'r','LineWidth',3); zoom on; waitfor(gcf, 'CurrentCharacter', char(13));
5429 [px1,py1] = ginput(1);
5430 [slope, intercept] = tangentEllipse(px1, py1, xCenter, yCenter, xRadius, yRadius, angle)
5431 tang1 = slope.*xx+ intercept; hold on; title('Tangent Representation'); plot(xx,tang1,'g','LineWidth',3)
5432
5433 m1 = slope; m2 = a; contact_angle_wet = abs(atan2((m1-m2)/(1-m1*m2)))
5434 contact_angle_not_wet = 180 - atan2((m1-m2)/(1-m1*m2))
5435

```



5436 *Figure E.1 (a) Contact angle definition. (b) Hydrophobic material. (c) Hydrophilic material.*
5437 *(d) Setup for contact angle measurements. (e) Contact angle measurement of untreated*
5438 *PDMS. (f) Contact angle measurement of PVA-modified PDMS. (g) Contact angle*
5439 *measurement of epoxy resin. (h) Contact angle measurement of the CMOS chip.*

5440

5441 F. Matlab Modelling of a Passive Microfluidic Channel with Rectangular Section

5442 This appendix illustrates a custom Matlab model for simulations of capillary laminar flow
 5443 in a straight rectangular microfluidic channel. The model is based on theoretical equations
 5444 for capillary pressure, fluidic resistance, and flow rate.

5445

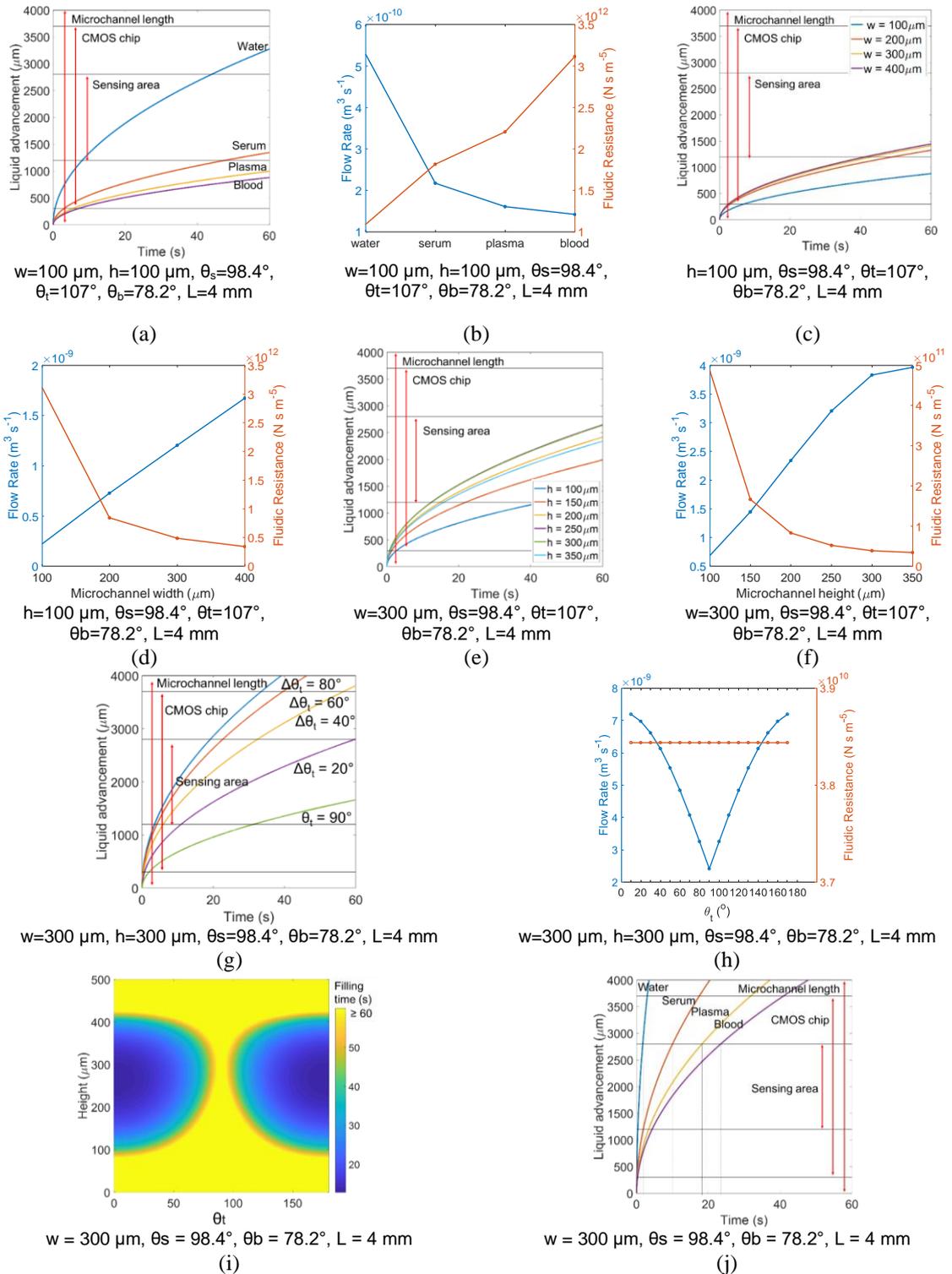
```

5446 clear all
5447 close all
5448
5449 tsim = 60;           % Simulation time
5450 N = 10000;          % Simulation points
5451 t = linspace (0,tsim, N); % Create simulation time vector from 0 to tsim containing N samples
5452 % Variables for graphical representation of the results
5453 Lim1 = t*0+0.3;
5454 Lim2 = t*0+0.3+(3.4-1.6)/2;
5455 Lim3 = t*0+0.3+(3.4-1.6)/2+1.6;
5456 Lim4 = t*0+4-0.3;
5457 Lim5 = t*0+4;
5458
5459 % Sweeping variables
5460 testing = [100*10^-6 150*10^-6 200*10^-6 250*10^-6 300*10^-6 350*10^-6]
5461 testing2 = [0.073 0.050 0.045 0.056]
5462 for g = 1:length(testing)
5463     eta = 0.0024; % Liquid properties (use blood) in [N][s][m]^2
5464     alpha = 0.056; % Liquid properties (use blood) in in [N][m]^1
5465     % Geometry of single channel with rectangular section
5466     h = testing(g); % Height of the microchannel
5467     w = 300*10^-6; % Width of the microchannel
5468     Ltot = 4000*10^-6; % Length of the microchannel
5469
5470     % Materials
5471     tetab= 78.2; % Measured contact angle material back (CMOS)
5472     tetat= 107; % Measured contact angle material top (PDMS or PVA-coated PDMS)
5473     tetas= 98.4; % Measured contact angle material side (Epoxy)
5474
5475     % Calculations
5476     R(g) = 12*eta*Ltot/((1-0.63*h/w)*h^3*w); % Fluidic resistance [N][s][m]^5
5477     deltap = alpha*((abs(cosd(tetab))+abs(cosd(tetat)))/h + 2*abs(cosd(tetas))/w) % Capillary pressure [N][m]-2
5478     chi = 12*eta/((1-0.63*h/w)*h^2); % For convenience [N][m]-2[m]-2[s]
5479     L(g,:) = 2*deltap/chi*sqrt(t); % liquid advancement [m]
5480     Q(g) = abs(deltap)/R(g); % Flow rate [m]^3[s]^-1
5481     end
5482
5483     % Representation of the results
5484     figure()
5485     for g = 1:length(testing)
5486         plot(t,L(g,:)*10^6, 'LineWidth',3); hold on; ylabel('Liquid advancement (\mum)'); xlabel('Time (s)')
5487     end
5488     plot(t,Lim1*10^3,'k-', 'LineWidth',1); hold on; plot(t,Lim2*10^3,'k-', 'LineWidth',1); plot(t,Lim3*10^3, 'k-',
5489     'LineWidth',1); plot(t,Lim4*10^3, 'k-', 'LineWidth',1); plot(t,Lim5*10^3, 'k-', 'LineWidth',1); axis('square')
5490
5491     figure(); yyaxis left; plot(Q,'o-', 'LineWidth',3); ylabel('Flow Rate (m^3 s^-1)'); yyaxis right; plot(R,'o-',
5492     'LineWidth',3); ylabel('Fluidic Resistance (N s m^-5)'); axis('square')
5493

```

5494 In the simulation, the bottom material of the channel was assumed to be the CMOS chip, the
5495 sides consisted of epoxy resin, and the top was PDMS. The model thus considered measured
5496 contact angles of epoxy resin ($\theta_s = 98.4^\circ$), chip surface ($\theta_b = 78.2^\circ$), and untreated PDMS
5497 ($\theta_t = 107^\circ$) in the first instance. The Matlab-based model was first employed to simulate the
5498 behaviour of a single microchannel with several liquids. Simulation results proposed in
5499 Figure F.1(a),(b) model the behaviour of water, serum, plasma and blood flowing into a
5500 rectangular microchannel with $w = 100 \mu\text{m}$, $h = 100 \mu\text{m}$, and $L = 4 \text{ mm}$. Water experiences
5501 an adequate capillary action, covering the entire sensing area in less than 50s. Simulated
5502 water flow rate is considerably higher than that of serum, plasma, and blood. On the other
5503 hand, filling times for serum, plasma and blood are too high for the requirements. Thus,
5504 additional optimisation is required.

5505 A conservative approach was adopted, so the usage of whole blood was assumed for
5506 subsequent simulations. The effect of the variation of the microchannel width was
5507 investigated - see Figure F.1(c),(d). Simulations predict the behaviour of blood flowing into
5508 a rectangular microchannel with w in the range $100 - 400 \mu\text{m}$, $h = 100 \mu\text{m}$, and $L = 4 \text{ mm}$.
5509 Increasing the width of the microchannel increased the flow rate of the channel,
5510 consequently decreasing the filling time of the structure. Despite the lower filling time, this
5511 optimisation step alone is not enough for meeting the requirements of the capillary action.
5512 As previously mentioned, a maximum $w = 300 \mu\text{m}$ can be adopted for manufacturing a 4-
5513 channel passive fluidic network. The effect of the variation of h when flowing blood was
5514 then investigated (see Figure F.1(e),(f)). Simulations studied the behaviour of blood flowing
5515 into a rectangular microchannel with $w = 300 \mu\text{m}$, h in the range $100 - 350 \mu\text{m}$, and
5516 $L = 4 \text{ mm}$. Increasing h led to a decrease in filling time. However, no improvement in the
5517 filling time was recorded with $> 300 \mu\text{m}$. The last parameter than was investigated was the
5518 wettability. PDMS contact angle can be modified by PVA deposition. The effect of the
5519 variation of the contact angle of the top PDMS when flowing blood in a microchannel with
5520 $w = 300 \mu\text{m}$ and $h = 300 \mu\text{m}$ was investigated (see Figure F.1(g),(h).). The worst condition
5521 for capillary action was $\theta_t = 90^\circ$. Filling time then decreases when increasing the difference
5522 $\Delta\theta$ with $\theta_{t0} = 90^\circ$, regardless of the hydrophilic or hydrophobic nature of the material. The
5523 fluidic resistance was not affected by the contact angle of the top PDMS lid.
5524 The simulations highlighted that the contact angle of the top PDMS lid and the height of the
5525 microchannel are probably the most effective and convenient design parameters to be
5526 optimised – see Figure F.1 (i),(j).



5527 *Figure F.1 (a) Liquid advancement vs time (vs specimens). (b) Initial flow rate and fluidic*
 5528 *resistance vs. specimen. (c) Blood advancement vs time (vs w values). (d) Initial flow rate*
 5529 *and fluidic resistance vs. channel width (blood). (e) Blood advancement vs time (vs h values).*
 5530 *(f) Initial flow rate and fluidic resistance vs channel height (blood). (g) Blood advancement*
 5531 *vs time (vs $\Delta\theta_t$). (h) Initial flow rate and fluidic resistance vs. top contact angle (blood). (i)*
 5532 *Time required for the sample to cover the sensing area (i.e. filling time) vs h values vs θ_t*
 5533 *(blood). (j) Simulations of water, serum, plasma, and blood flowing into the optimised*
 5534 *microstructure.*

5535 **G. Wire Bonding and Packaging Protocol**

5536 This appendix illustrates the wire bonding and packaging protocol used for the fabrication
5537 of the cartridge described within this PhD project. Wire bonding was performed in the
5538 cleanroom facility of Glasgow Laboratory for Advanced Detector Development (School of
5539 Physics and Astronomy, University of Glasgow). The Hesse and Knipps Bondjet 710 was
5540 used for the wire bonding of the CMOS onto a ceramic chip package [331]. The CMOS chip
5541 was wire bonded onto a Ceramic Pin Grid Array (CPGA) package with 120 pins purchased
5542 from Europractice [293]. The overall size of the selected CPGA package was 3.3x3.3 cm,
5543 with an 8.3×8.3 mm cavity accommodating the structure to be wire-bonded.

5544 The wire-bonding process consisted of three stages: preparation, programming, and bonding.
5545 **Preparation.** The CMOS chip with the PDMS mould on top of it was glued in the cavity of
5546 the CPGA package using the EPO-TEK H74 epoxy from Epoxy Technology Inc [294]. The
5547 epoxy resin was mixed with the curing agent in a weight ratio 100:3. Approximately 20 µL
5548 of the prepared solution was placed in the centre of the CPGA cavity and spread, before
5549 placing the PDMS mould-topped chip onto the epoxy applying slight pressure. The epoxy
5550 was cured by baking the structure for 5 minutes at 150°C.

5551 **Programming.** The structure was secured in the centre of the stage of the Bondjet 710 with
5552 electrostatic discharge safe tape. The equipment was programmed to automatically perform
5553 the wire bonding, according to the wire-bonding diagram reported in Figure G.1(c). The first
5554 step in the programme was the definition of the source (CMOS chip) and destination
5555 (package) of the bonds. Then reference points, heights and all the parameters summarised in
5556 Table G.1 were set. After that, the bond paths were defined. 58 pads out of the available 64
5557 were wire-bonded (test pads were not used). However, only 18 wire bonds are necessary for
5558 this PhD project. The other connections are needed for other functionalities of the chip not
5559 used in this work. Bond paths were defined via-software using graphical tools supported by
5560 the digital microscope. Configurations were saved and reused in similar wire-bonding jobs.

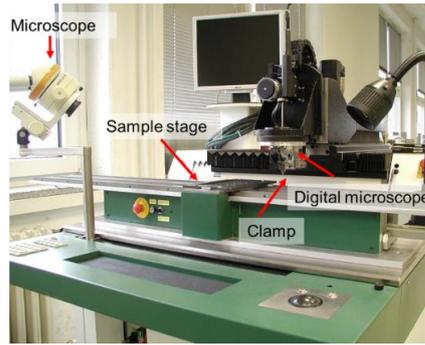
5561 **Bonding.** The Bondjet 710 support different bonding modalities. Usually, the full-automatic
5562 mode has been adopted. However, whenever an error occurred, or a bond failed, it was
5563 necessary to manually re-define the position of the bond and re-bond the pad in manual
5564 mode.

5565

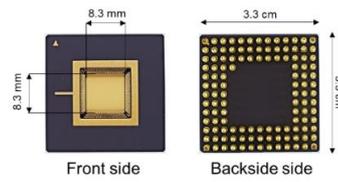
5566

5567

5568

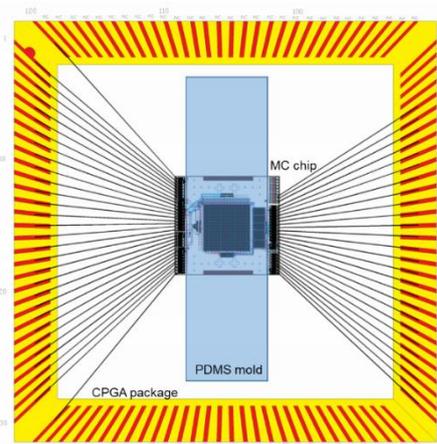


(a)

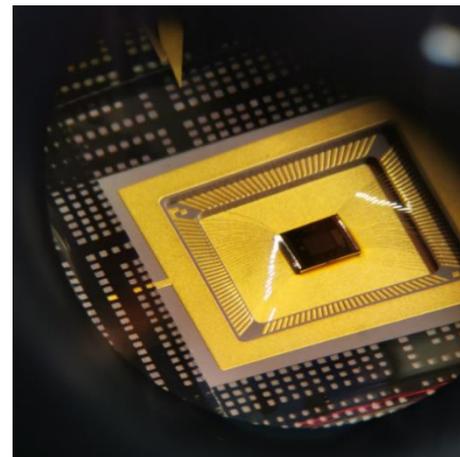


(b)

5569



(c)



(d)

5570 *Figure G.1 (a) The Hesse and Knipps Bondjet 710 ultrasonic automatic wire bonder.*
 5571 *Reproduced and modified from [332]. (b) CPGA with 120 pins. (c) Bonding diagram. (d)*
 5572 *Exemplative micrograph of a bonding process.*

5573

5574

Table G.1. Main parameters used for wire-bonding.

Parameter	Value
Ultrasonic power	30% (source), 20% (destination)
Bond force	24 cN (source), 20 cN (destination)
Start height	1000 μm
Loop height	250 μm
Start angle	45°
Bonding speed	20 %
Position accuracy	5 μm
Touch down area	100 μm
Safety area	80 μm (radius)
Reference Points	Source: (1) top left corner of the top left pad; (2) bottom right corner of the bottom right pad. Destination: (1) top left corner of the top left pad; (2) bottom right corner of the bottom right pad.
Bonding Height	Reset every bonding job

5575

5576 **H. Biochemical Protocol for reagents preparation used for diluted serum experiments**

5577 This appendix illustrates the procedure adopted for the metabolomics experiments in diluted
5578 serum.

5579 **Prostate Cancer Metabolites.** All the chemicals were purchased from Sigma Aldrich.
5580 Dehydrated human serum was also obtained from Sigma Aldrich and reconstituted with DI
5581 water following the recommended protocol. The reconstituted human serum was further
5582 diluted in DI water (volume ratio 1:10). All the reagents were prepared using 0.1 mM Tris
5583 HCl buffer (pH 8). For LAA assay, L-Tryptophan (grade $\geq 98\%$) and L-Arginine were used
5584 to create an LAA solution of 25 mM in buffer. The LAA solution was used to introduce a
5585 known concentration of LAA into the diluted human serum samples. For the first stage of
5586 the reaction, LAAOx (L-Amino Acid Oxidase from *Crotalus adamanteus*) was used to
5587 prepare a 4 U/mL enzymatic solution. LAAOx has different kinetics variable depending on
5588 the substrate under test. The average K_m for LAAOx over all the substrates is 8.5 ± 7.4 mM
5589 [49]. For practical and economic reasons, it was not viable to prepare an LAA testing
5590 solution with all the available LAAs on the market. Thus, tryptophan and arginine have been
5591 selected because they exhibit low (4.2 mM) and high (12.5 mM) K_m , respectively [49].
5592 Accordingly, the expected K_m of LAAOx when reacting with the prepared LAA testing
5593 solution can be assumed to be 8.35 mM [49], when the two amino-acids are equally present
5594 in the solution. Therefore, this was a good approximation for a real-life scenario. For the
5595 glutamate assay, dehydrated glutamate (L-Glutamic acid monosodium salt monohydrate)
5596 was dissolved in the buffer to produce a 5 mM glutamate solution, which was used to
5597 introduce an additional known quantity of metabolite into the diluted serum samples. GLOx
5598 (L-Glutamate Oxidase from *Streptomyces* sp.) was prepared with a concentration of 4 U/mL
5599 to be used for the 1st reaction stage of the glutamate assay. For choline assay, dehydrated
5600 choline (Choline chloride $\geq 99\%$) was dissolved in the buffer for the preparation of a 2.5 mM
5601 solution to be used for increasing the concentration of choline in the diluted serum samples.
5602 For the 1st reaction stage of choline assay, ChOx (Choline Oxidase from *Alcaligenes* sp.)
5603 was dissolved in buffer with a concentration of 150 U/mL. For Sarcosine quantification,
5604 dehydrated sarcosine (sarcosine 98%) was used to prepare two different solutions in buffer
5605 with concentrations of 0.5 mM and 50 mM. Sarcosine solutions were used to introduce an
5606 additional known quantity of the metabolite into the serum samples to be tested. For the 1st
5607 stage of the assay, SaOx (Sarcosine Oxidase from *Bacillus* sp.) was dissolved in buffer to
5608 create a 200 U/mL enzymatic solution. For all the assays, o-dianisidine was selected for the

5609 2nd stage of the assays. Dehydrated o-dianisidine was used to prepare a 41 mM solution in
5610 buffer. The enzyme HRP (Peroxidase from horseradish) was also used to catalyse the o-
5611 dianisidine oxidation. Dehydrated HRP was used to prepare two solutions with different
5612 concentrations of 65.5 U/mL and 300 U/mL. All the chemicals were aliquot and stored in
5613 appropriate refrigerator units in the laboratories of the MST group, Rankine Building,
5614 University of Glasgow.

5615 **Ischemic stroke metabolites.** All the chemicals were purchased from Sigma Aldrich.
5616 Dehydrated human serum was also obtained from Sigma Aldrich and diluted with DI water
5617 (volume ratio of 1:10). Reagents were prepared using a 10 mM PBS (Phosphate-buffered
5618 saline) buffer (pH 7.4).

5619 For lactate assay, lactate (Sodium L-lactate ~98%) was used to create a lactate solution of
5620 10 mM in buffer, which was used to introduce a known concentration of the analyte into the
5621 diluted human serum samples. For the first stage of the reaction, LaOx (Lactate Oxidase
5622 from *Aerococcus viridans*) was used to prepare a 4 U/mL enzymatic solution.

5623 For creatinine assay, creatinine (Creatinine anhydrous, $\geq 98\%$) was used to prepare a testing
5624 solution in buffer with 5 mM concentration. The first reaction stage of the reaction for
5625 creatinine quantification is composed of three enzymatic reactions. For the first reaction,
5626 CNN (Creatininase from *Flavobacterium* sp.) was used to prepare a 200 U/mL solution. For
5627 the second reaction, CTN (Creatinase from *Actinobacillus* sp) was used to develop a solution
5628 with enzyme concentration of 200 U/mL. For the third reaction stage, SaOx (Sarcosine
5629 Oxidase from *Bacillus* sp.) was dissolved in buffer to create a 150 U/mL enzymatic solution.
5630 All the chemicals were aliquot and stored in appropriate refrigerator units in the laboratories
5631 of the MST group, Rankine Building, University of Glasgow.

5632

5633 **I. Biochemical Protocol for reagents preparation used for microchannel** 5634 **functionalisation**

5635 This appendix illustrates the protocol adopted for the preparation of enzymatic solutions for
5636 dry assays. Four different solutions were prepared to be dried/lyophilised into the
5637 microchannels:

5638 1) Solution for negative control: a negative control solution was obtained by mixing 10 μ L
5639 of DI water, 10 μ L of 150 U/mL HRP, 5 μ L of 44.5 mM phenol and 5 μ L of 10.5 mM
5640 4AAP. Instead of an enzyme solution, DI water was used to make it as a control
5641 microchannel.

- 5642 2) Solution for choline assay: a solution containing all the reagents required for choline
5643 testing was obtained by mixing 10 μ L of 150 U/mL ChOx, 10 μ L of 150 U/mL HRP,
5644 5 μ L of 44.5 mM phenol and 5 μ L of 10.5 mM 4AAP.
- 5645 3) Solution for glutamate assay: a solution containing all the reagents required for glutamate
5646 testing was obtained by mixing 10 μ L of 4 U/mL GIOx, 10 μ L of 150 U/mL HRP, 5 μ L
5647 of 44.5 mM phenol and 5 μ L of 10.5 mM 4AAP.
- 5648 4) Solution for LAA assay: a solution containing all the reagents required for LAA testing
5649 was obtained by mixing 10 μ L of 10 U/mL LAAOx, 10 μ L of 150 U/mL HRP, 5 μ L of
5650 44.5 mM phenol and 5 μ L of 10.5 mM 4AAP.

5651 For the immobilisation of these reagents into the microchannel, 1 μ L of each solution was
5652 deposited in the respective microchannel according to the desired configuration. The
5653 deposition was achieved by manual pipetting. After the deposition of the solution, the
5654 cartridge was dried for 1 hour at room temperature in a vacuum chamber.

5655

5656 **J. Enzyme printing protocol**

5657 This appendix illustrates the protocol adopted for the functionalisation of paper-strip with
5658 enzymatic solutions using a printing technique. Two different inks containing reagents for
5659 the lactate assay and glucose assay were printed on the specific paper microfluidic channels
5660 using the Jetlab II printer. Reagents were purchased from Sigma Aldrich. The adopted
5661 patterns were straight line composed of 20 spots with 0.5 mm pitch. The stimulus waveform
5662 was a negative pulse, tuned for each printing job. The total volume of each printed enzymatic
5663 solution was approximately 2.5 μ L. The ink solution for glucose testing was composed as
5664 follows: 190 μ L 100 mM Triethanolamine buffer at pH 8, 30 μ L 600 U/mL peroxidase, 160
5665 μ L 7.89 mM o-dianisidine, and 120 μ L 8 U/mL glucose oxidase. The ink solution for lactate
5666 testing was composed as follows: 210 μ L 100 mM Triethanolamine buffer at pH 8, 60 μ L
5667 600 U/mL peroxidase, 120 μ L 7.89 mM o-dianisidine, and 100 μ L 2 U/mL lactate oxidase.

5668

5669

5670

5671

5672

5673 **K. Ethical approval letters**

5674 This appendix reports ethical approval letters for the clinical evaluation.

5675 **Cancer samples.** Ethical approval number 10/S0704/18 issued by the West of Scotland

5676 Research Ethics Service

Delivering better health
www.nhs.uk



7 July 2010
Professor Jeff Evans
Professor of Translational Cancer Research
University of Glasgow
The Beatson West of Scotland Cancer Centre
1053 Great Western Road
Glasgow
G12 0VN

REC reference number:	10/S0704/18
Protocol number:	Version 1, 20th Mar 2010
Study Title:	An exploratory biomarker analysis in blood and urine of patients with malignant disease

Dear Professor Evans

Thank you for your letter of 29 June 2010, responding to the Committee's request for further information on the above research and submitting revised documentation.

The further information has been considered on behalf of the Committee by the Chair.

Confirmation of Ethical Opinion

On behalf of the Committee, I am pleased to confirm a favourable ethical opinion for the above research on the basis described in the application form, protocol and supporting documentation, as revised, subject to the conditions specified below.

Ethical Review of Research Sites

The favourable opinion applies to all NHS sites taking part in the study, subject to management permission being obtained from the NHS/HSC R&D office prior to the start of the study (see 'Conditions of the favourable opinion' below).

Conditions of the Favourable Opinion

The favourable opinion is subject to the following conditions being met prior to the start of the study.

Management permission or approval must be obtained from each host organisation prior to the start of the study at the site concerned.

5677

For NHS research sites only, management permission for research (R&D approval) should be obtained from the relevant care organisation(s) in accordance with NHS research governance arrangements. Guidance on applying for NHS permission for research is available in the Integrated Research Application System or at <http://www.rdforum.nhs.uk>. Where the only involvement of the NHS organisation is as a Participant Identification Centre, management permission for research is not required but the R&D office should be notified of the study. Guidance should be sought from the R&D office where necessary.

Sponsors are not required to notify the Committee of approvals from host organisations.

It is the responsibility of the sponsor to ensure that all the conditions are complied with before the start of the study or its initiation at a particular site (as applicable).

Approved Documents

The final list of documents reviewed and approved by the Committee is as follows:

Document	Version	Date
Investigator CV	-	17 November 2009
Protocol	1.0	20 March 2010
REC application	-	7 April 2010
Governing Letter	-	9 April 2010
Participant Information Sheet- Final version	2.0	29 June 2010
Response to Request for Further Information	-	29 June 2010
Participant Consent Form	1	20 March 2010

Statement of Compliance

The Committee is constituted in accordance with the Governance Arrangements for Research Ethics Committees (July 2001) and complies fully with the Standard Operating Procedures for Research Ethics Committees in the UK.

After Ethical Review

Now that you have completed the application process please visit the National Research Ethics Service website > After Review

You are invited to give your view of the service that you have received from the National Research Ethics Service and the application procedure. If you wish to make your views known please use the feedback form available on the website.

The attached document 'After ethical review – guidance for researchers' gives detailed guidance on reporting requirements for studies with a favourable opinion, including:

- Notifying substantial amendments
- Adding new sites and investigators
- Progress and safety reports
- Notifying the end of the study

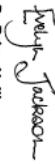
The NRES website also provides guidance on these topics, which is updated in the light of changes in reporting requirements or procedures.

5678

We would also like to inform you that we consult regularly with stakeholders to improve our service. If you would like to join our Reference Group please email referencegroup@nres.npsa.nhs.uk.

10/S0704/18 Please quote this number on all correspondence

Yours sincerely


Dr Brian Neilly
Chair

Enclosures: *After ethical review – guidance for researchers*

Copy to: *Miss Gemma Tall, Beatson West of Scotland Cancer Centre
R&D Office, Tennent Institute, Western Infirmary

5679

5680 **Ischemic stroke samples.** Ethical approval number 17/WS/0252 issued by the West of
5681 Scotland Research Ethics Service.

WOSRES
West of Scotland Research Ethics Service

NHS
Greater Glasgow
and Clyde

Professor Jesse Dawson
Clinical Reader Stroke Medicine/Consultant
Physician
University of Glasgow
Queen Elizabeth University Hospital
Office Block, Ground Floor Some 0.01, Room
M0.05
Glasgow
G51 4TF

West of Scotland REC 1
West of Scotland Research Ethics Service
Clinical Research and Development
West Glasgow Ambulatory Care Hospital
Dalmuir Street
Glasgow G3 83J
research@scot.nhs.uk
Date 08 January 2018 (Re-issued
15 February 2018)
Direct line 0141-232-1806
e-mail WosRec1@ggc.scot.nhs.uk

**Version 2 – Updated at sponsors request to reflect the consent form for the
substudy which was omitted in an error.**

Dear Professor Dawson

Study title: TRIMethS – A novel urinary biomarker for minor stroke
and TIA

REC reference: 17/WS/0252

Protocol number: v1

IRAS project ID: 232258

Thank you for your letter of 18 December 2017, responding to the Committee's request for further information on the above research and submitting revised documentation.

The further information was considered in correspondence by a Sub-Committee of the REC A list of the Sub-Committee members is attached.

We plan to publish your research summary wording for the above study on the HRA website, together with your contact details. Publication will be no earlier than three months from the date of this opinion letter. Should you wish to provide a substitute contact point, require further information, or wish to make a request to postpone publication, please contact ira.studyregistration@nres.nhs.uk outlining the reasons for your request.

Confirmation of ethical opinion

On behalf of the Committee, I am pleased to confirm a favourable ethical opinion for the above research on the basis described in the application form, protocol and supporting documentation as revised, subject to the conditions specified below.

Conditions of the favourable opinion

The REC favourable opinion is subject to the following conditions being met prior to the start of the study:

5682

Management permission must be obtained from each host organisation prior to the start of the study at the site concerned.

Management permission should be sought from all NHS organisations involved in the study in accordance with NHS research governance arrangements. Each NHS organisation must confirm through the signing of agreements and/or other documents that it has given permission for the research to proceed (except where explicitly specified otherwise).

Guidance on applying for NHS permission for research is available in the Integrated Research Application System, www.hra.nhs.uk or at <http://www.tcforum.nhs.uk>.

Where a NHS organisation's role in the study is limited to identifying and referring potential participants to research sites ("Participant Identification centre"), guidance should be sought from the R&D office on the information it requires to give permission for this activity.

For non-NHS sites, site management permission should be obtained in accordance with the procedures of the relevant host organisation.

Sponsors are not required to notify the Committee of management permissions from host organisations

Registration of Clinical Trials

All clinical trials (defined as the first four categories on the IRAS filler page) must be registered on a publicly accessible database within 6 weeks of recruitment of the first participant (for medical device studies, within the timeline determined by the current registration and publication trees).

There is no requirement to separately notify the REC but you should do so at the earliest opportunity e.g. when submitting an amendment. We will audit the registration details as part of the annual progress reporting process.

To ensure transparency in research, we strongly recommend that all research is registered but for non-clinical trials this is not currently mandatory.

If a sponsor wishes to request a deferral for study registration within the required timeframe, they should contact hra.studyregistration@nhs.net. The expectation is that all clinical trials will be registered, however, in exceptional circumstances non registration may be permissible with prior agreement from the HRA. Guidance on where to register is provided on the HRA website.

It is the responsibility of the sponsor to ensure that all the conditions are complied with before the start of the study or its initiation at a particular site (as applicable).

Ethical review of research sites

NHS sites

The favourable opinion applies to all NHS sites taking part in the study, subject to management permission being obtained from the NHS/HSR R&D office prior to the start of the study (see

5683

"Conditions of the favourable opinion" below).

Approved documents

The final list of documents reviewed and approved by the Committee is as follows:

Document	Version	Date
Evidence of Sponsor insurance or indemnity (from NHS Sponsors only)	2.0	27 July 2017
SP/consultant information sheets or letters [(Clean)]	2.0	12 December 2017
RA5 Application Form [RA5_Form_16112017]		16 November 2017
Letter from funder		04 July 2017
Participant consent form [(Track changes)]	2.0	12 December 2017
Participant consent form [(Clean)]	2.0	12 December 2017
Participant consent form [T7 Sub-study]	1	21 September 2017
Participant information sheet (PIS) [T7 Info]	2.0	16 November 2017
Participant information sheet (PIS) [(Track changes)]	2.0	12 December 2017
Participant information sheet (PIS) [(Clean)]	2.0	12 December 2017
Research protocol or project proposal [(Clean)]	1.1	12 December 2017
Research protocol or project proposal [(Track changes)]	1.1	12 December 2017
Response to Request for Further Information		
Summary CV for Chief Investigator (CI)		18 December 2017

Statement of compliance

The Committee is constituted in accordance with the Governance Arrangements for Research Ethics Committees and complies fully with the Standard Operating Procedures for Research Ethics Committees in the UK.

After ethical review

Reporting requirements

The attached document "After ethical review – guidance for researchers" gives detailed guidance on reporting requirements for studies with a favourable opinion, including:

- Notifying substantial amendments
- Adding new sites and investigators
- Notification of serious breaches of the protocol
- Progress and safety reports
- Notifying the end of the study

The HRA website also provides guidance on these topics, which is updated in the light of changes in reporting requirements or procedures.

5684

User Feedback

The Health Research Authority is continually striving to provide a high quality service to all applicants and sponsors. You are invited to give your view of the service you have received and the application procedure. If you wish to make your views known please use the feedback form available on the HRA website: <http://www.hra.nhs.uk/about-the-traingovmance/quality-assurance/>

HRA Training

We are pleased to welcome researchers and R&D staff at our training days – see details at <http://www.hra.nhs.uk/nra-training/>

17/WS/0252 Please quote this number on all correspondence

With the Committee's best wishes for the success of this project.

Yours sincerely



On behalf of
Dr Malcolm Booth
Chair

Enclosures: *List of names and professions of members who were present at the meeting and those who submitted written comments*
"After ethical review – guidance for researchers"

Copy to: *Dr Maureen Travers, NHS Greater Glasgow and Clyde*

West of Scotland REC 1

Attendance at Sub-Committee of the REC meeting on 08 January 2018

Committee Members:

Name	Profession	Present	Notes
Dr Malcolm Booth	Consultant in Anaesthesia and Intensive Care (Chair)	Yes	Chair of Meeting
Dr Audrey Morrison	Research Practitioner	Yes	

Also in attendance:

Name	Position (or reason for attending)
Ms Kirsty Burt	Senior Co-ordinator

5687 **L. Procedure for clinical sample collection**

5688 This appendix illustrates the protocol for clinical sample collection.

5689 **Control group.** Ten samples of human plasma from healthy people were sourced by
5690 Cambridge Bioscience. Plasma samples of healthy people are herein referred to as ‘non-
5691 PCa’ and constituted the control group. Non-PCa donors were selected to be adult male
5692 subjects only. The average age of the non-PCa group was 34 ± 10 years. The ethnicity of the
5693 group was diversified including, European, Asian, and African donors. Samples were
5694 already pre-screened for the most common infections, including HIV, syphilis, Hepatitis B,
5695 Hepatitis C, and all resulted negative. Approximately 10 mL of fresh blood samples were
5696 collected in various research clinical facilities in England, mixed with 10 mg of dipotassium
5697 ethylenediaminetetraacetic acid (K₂EDTA) anticoagulant, centrifuged and the generated 4
5698 mL of plasma samples were frozen at -80° . Frozen plasma samples were shipped under dry-
5699 ice. After collection, plasma samples were aliquoted in 200 μ L vials and stored at -80° . No
5700 additional freeze and thaw cycles were performed. A table listing details on the non-PCa
5701 group is reported below.

5702 **Prostate cancer group.** Sixteen human plasma samples from people diagnosed with PCa
5703 were sourced from the Beatson Cancer Institute, Glasgow, UK, under ethical approval, with
5704 the collaboration with Dr Robert Jones and Prof Jeff Evans. Plasma samples from cancer
5705 patients herein are referred to as ‘PCa’ samples and constituted the cancer or PCa group.
5706 Donors were selected to be adults who had already been diagnosed with PCa. However, due
5707 to ethical reason, detailed information, such as age and ethnicity, about the samples was not
5708 available. General information about the therapeutic course of the treatment for the patients
5709 such as the use of drugs was available. All the patients were under similar standard therapy
5710 involving the administration of triptorelin (or similar), omeprazole/esomeprazole, and
5711 statins. Approximately 10 mL of blood samples were collected at the Beatson Cancer
5712 Institute, mixed with 10 mg of K₂EDTA anticoagulant, centrifuged, and the resulting plasma
5713 samples were frozen at -80° C. Samples were collected from the Beatson Cancer Institute
5714 and transported to Institute of Infection Immunity and Inflammation (III), Glasgow
5715 Biomedical Research Centre, University of Glasgow, where most of the measurements were
5716 carried out in dry ice. Afterwards, plasma samples were aliquoted in 200 μ L vials and stored
5717 at -80° C. No additional freeze and thaw cycles were performed except an initial thaw just
5718 before the testing. Samples were stored and tested in the same facilities as the non-PCa
5719 group.

5720 **Ischemic stroke group.** Ten samples of human plasma from people diagnosed with
 5721 ischemic stroke were sourced from the Queen Elizabeth University Hospital, Glasgow, UK,
 5722 under ethical approval, thanks to the collaboration with Dr Samadhan B. Patil, lecturer in
 5723 Medical Engineering at the University of York, and Prof Jessie Dawson, Professor of Stroke
 5724 Medicine and Consultant Stroke Physician at The Queen Elizabeth Hospital, Glasgow.
 5725 Donors were selected to be adults recently diagnosed with ischemic stroke. Due to ethical
 5726 reasons, detailed information, such as age and ethnicity, related to patients were not
 5727 available. The approximate available volume, for each sample, was 100 μ L. Blood samples
 5728 were collected from the West Glasgow Ambulatory Care Hospital, mixed with
 5729 anticoagulant, centrifuged, and the resulting plasma samples were frozen at -80° . Samples
 5730 were transported from West Glasgow Ambulatory Care Hospital in dry-ice. Afterwards,
 5731 vials were stored into a -80° freezer. No additional freeze and thaw cycle was performed
 5732 except premeasurement thawing. Samples were stored and tested in the same facilities as the
 5733 clinical cancer samples. Calibration samples (calibrators) were sourced from the Institute of
 5734 Cardiovascular and Medical Sciences, University of Glasgow. Calibrators were used in
 5735 diluted form.

5736

5737

5738

Table L.1 General information of the control group.

Sample #	1	2	3	4	5	6	7	8	9	10	Average	Std
Collect. date	18/07/2019 12:12	18/07/2019 13:34	18/07/2019 11:51	18/07/2019 14:30	18/07/2019 11:44	18/07/2019 13:23	18/07/2019 14:09	18/07/2019 08:11	18/07/2019 12:22	18/07/2019 08:34	-	-
Blood Group	O RhD Pos	O RhD neg	A RhD neg	O RhD pos	O RhD pos	A RhD pos	A RhD pos	B RhD neg	O RhD pos	A RhD pos	Various	-
Gender	Male	Male	Male	Male	Male	Male	Male	Male	Male	Male	Male	-
Male	32	22	36	45	20	53	27	29	29	40	33.3	9.8
Ethnicity	Asian	Brithis/Irish	Brithis/Irish	Brithis/Irish	Black	Brithis/Irish	Brithis/Irish	Black	Black	Brithis/Irish	Various	-
HIV 1&2, p24	Negative	Negative	Negative	Negative	Negative	Negative	Negative	Negative	Negative	Negative	Negative	-
HBsAg	Negative	Negative	Negative	Negative	Negative	Negative	Negative	Negative	Negative	Negative	Negative	-
HCV	Negative	Negative	Negative	Negative	Negative	Negative	Negative	Negative	Negative	Negative	Negative	-
Syphilis	Negative	Negative	Negative	Negative	Negative	Negative	Negative	Negative	Negative	Negative	Negative	-
WBC (1/L)	6.76E+09	5.04E+09	5.50E+09	5.20E+09	5.29E+09	5.88E+09	5.55E+09	2.44E+09	5.14E+09	5.13E+09	5.19E+09	1.04E+09
RBC (1/L)	4.82E+12	4.25E+12	5.12E+12	4.81E+12	5.45E+12	4.72E+12	4.92E+12	5.65E+12	4.78E+12	5.67E+12	5.019E+12	4.30E+11
HGB (g/L)	148	140	157	142	150	146	143	133	147	160	146.6	7.5
HCT (L/L)	0.425	0.394	0.453	0.422	0.452	0.422	0.425	0.417	0.425	0.482	0.4317	0.0
MCV (fl)	88.2	92.7	88.5	87.7	82.9	89.4	86.4	73.8	88.9	85	86.35	4.9
MCH (pg)	30.7	32.9	30.7	29.5	27.5	30.9	29.1	23.5	30.8	28.2	29.38	2.4
MCHC (g/L)	348	355	347	336	332	346	336	319	346	332	339.7	10.1
PLT (1/L)	3.32E+11	1.41E+11	2.45E+11	2.24E+11	2.9E+11	2.19E+11	2.24E+11	2.12E+11	2.28E+11	2.85E+11	2.4E+11	4.97E+10
RDW (%)	11.4	11.3	12.2	12.6	13.8	13	13.2	12.1	12.1	14.3	12.6	0.9
Neut (1/L)	3.29E+09	3.01E+09	2.88E+09	3.02E+09	2.33E+09	3.15E+09	3.62E+09	8.90E+08	2.69E+09	2.81E+09	2.77E+09	7.07E+08
Lymph (1/L)	2.73E+09	1.10E+09	1.69E+09	1.60E+09	2.09E+09	1.92E+09	1.31E+09	1.20E+09	1.73E+09	1.75E+09	1.71E+09	4.51E+08
Mono (1/L)	5.30E+08	5.20E+08	6.20E+08	4.00E+08	6.60E+08	5.20E+08	4.90E+08	2.70E+08	4.90E+08	4.10E+08	4.91E+08	1.06E+08
EO (1/L)	1.40E+08	3.80E+08	2.80E+08	1.70E+08	1.50E+08	2.40E+08	7.00E+07	5.00E+07	2.10E+08	1.20E+08	1.81E+08	9.47E+07
Baso (1/L)	7.00E+07	3.00E+07	3.00E+07	1.00E+07	6.00E+07	5.00E+07	6.00E+07	3.00E+07	2.00E+07	4.00E+07	4.00E+07	1.84E+07

5739

5740

5741

5742 **M. PCA scores for classification**

5743 This appendix reports the dataset for prostate cancer clinical evaluation (after Principal
5744 Component Analysis – PCA).

5745 *Table M.1 PCA scores for prostate cancer samples.*

Sample	PC 1 (88.33%)	PC 2 (7.56%)	PC 3 (4.11%)
1	1.696752	0.37309	-0.08331
2	1.737893	-0.39242	-0.02927
3	0.901266	-0.35921	0.295321
4	1.618211	0.021794	0.50435
5	1.640694	0.367556	-0.03393
6	1.58718	0.032493	0.024632
7	0.977501	-0.36137	0.142953
8	0.994047	0.268857	-0.00329
9	1.185934	-0.02453	-0.11917
10	1.129113	-0.19346	0.033888
11	1.448242	-0.68844	-0.29005
12	1.717073	0.973358	0.502618
13	2.350504	-0.09969	0.469352
14	2.381458	-0.55839	0.98048
15	2.307302	0.185646	0.548527
16	3.053422	-1.14177	-0.61908
17	1.904028	0.520958	0.277342
18	1.480935	0.104297	0.291933
19	1.519043	-0.25816	-0.17274
20	2.271879	0.821612	-0.10654
21	3.237712	1.315546	-0.93454
22	1.575352	-0.49917	-0.30436
23	1.661074	-0.22037	-0.03577
24	1.668592	-0.30158	-0.46687
25	1.56468	-0.43482	-0.19961
26	1.407768	-0.41207	0.026069

5746

5747

5748 **Bibliography**

- 5749 [1] A. St John and C. P. Price, "Existing and Emerging Technologies for Point-of-Care Testing.," *Clin. Biochem. Rev.*, vol. 35, no. 3, pp. 155–67, Aug. 2014.
- 5750 [2] V. Gubala, L. F. Harris, A. J. Ricco, M. X. Tan, and D. E. Williams, "Point of care diagnostics: Status and future," *Anal. Chem.*, vol. 84, no. 2, pp. 487–515, 2012, doi: 10.1021/ac2030199.
- 5751 [3] S. L. Weiss *et al.*, "Delayed antimicrobial therapy increases mortality and organ dysfunction duration in pediatric sepsis," *Crit. Care Med.*, vol. 42, no. 11, pp. 2409–2417, 2014.
- 5752 [4] M. Hand, "Access to timely and optimal care of patients with acute coronary syndromes - Community planning considerations: A report by the National Heart Attack Alert Program," *J. Thromb. Thrombolysis*, vol. 6, no. 1, pp. 19–46, 1998, doi: 10.1023/A:1008820104852.
- 5753 [5] G. Giordano *et al.*, *Modelling the COVID-19 epidemic and implementation of population-wide interventions in Italy*. 2020.
- 5754 [6] P. C. Walsh, "Operating characteristics of prostate-specific antigen in men with an initial PSA level of 3.0 Ng/ml or lower: Commentary," *J. Urol.*, vol. 175, no. 2, pp. 562–563, 2006, doi: 10.1016/S0022-5347(05)00385-X.
- 5755 [7] N. Gómez-Cebrián, A. Rojas-Benedicto, A. Albors-Vaquer, J. A. López-Guerrero, A. Pineda-Lucena, and L. Puchades-Carrasco, "Metabolomics contributions to the discovery of prostate cancer biomarkers," *Metabolites*, vol. 9, no. 3, Mar. 2019, doi: 10.3390/metabo9030048.
- 5756 [8] X. Ma *et al.*, "The cost implications of prostate cancer screening in the Medicare population," *Cancer*, vol. 120, no. 1, pp. 96–102, 2014, doi: 10.1002/cncr.28373.
- 5757 [9] A. Fridhammar, U. Axelsson, U. Persson, A. Bjartell, and C. A. K. Borrebaeck, "The Value of a New Diagnostic Test for Prostate Cancer: A Cost-Utility Analysis in Early Stage of Development," *PharmacoEconomics - Open*, 2020, doi: 10.1007/s41669-020-00226-7.
- 5758 [10] R. D. Beger *et al.*, "Metabolomics enables precision medicine: 'A White Paper, Community Perspective,'" *Metabolomics*, vol. 12, no. 10, Oct. 2016, doi: 10.1007/s11306-016-1094-6.
- 5759 [11] U. Roessner and J. Bowne, "What is metabolomics all about?," *Biotechniques*, vol. 46, no. 5 SPEC. ISSUE, pp. 363–365, 2009, doi: 10.2144/000113133.
- 5760 [12] D. K. Trivedi, K. A. Hollywood, and R. Goodacre, "Metabolomics for the masses: The future of metabolomics in a personalized world," *New Horizons in Translational Medicine*, vol. 3, no. 6. Elsevier Ltd, pp. 294–305, Mar. 01, 2017, doi: 10.1016/j.nhtm.2017.06.001.
- 5761 [13] "WHO | World Health Organization." <https://www.who.int/> (accessed Jan. 17, 2020).
- 5762 [14] D. S. Wishart, "Emerging applications of metabolomics in drug discovery and precision medicine," *Nat. Rev. Drug Discov.*, vol. 15, no. 7, pp. 473–484, 2016, doi: 10.1038/nrd.2016.32.
- 5763 [15] F. R. Pinu, S. A. Goldansaz, and J. Jaine, "Translational metabolomics: Current challenges and future opportunities," *Metabolites*, vol. 9, no. 6, Jun. 2019, doi: 10.3390/metabo9060108.
- 5764 [16] S. B. Patil, V. F. Annese, and D. R. S. Cumming, "Commercial Aspects of Biosensors for Diagnostics and Environmental Monitoring," in *Advances in Nanosensors for Biological and Environmental Analysis*, Elsevier, 2019, pp. 133–142.
- 5765 [17] S. Publications, "Statistical Problems in Assessing Methods of Medical Diagnosis , with Special Reference to X-Ray Techniques Author (s): Jacob Yerushalmy Source : Public Health Reports (1896-1970), Vol . 62 , No . 40 , Tuberculosis Control Issue No . 20 Stable URL : h," vol. 62, no. 40, pp. 1432–1449, 2020.
- 5766 [18] I. M. Thompson *et al.*, "Operating Characteristics of Prostate-Specific Antigen in Men With an Initial PSA Level of 3 . 0 ng / mL or Lower," vol. 78229, 2005.
- 5767 [19] J. P. Goddard and J. L. Reymond, "Recent advances in enzyme assays," *Trends in Biotechnology*, vol. 22, no. 7. pp. 363–370, Jul. 2004, doi: 10.1016/j.tibtech.2004.04.005.
- 5768 [20] J. Kimura, Y. Kawana, and T. Kuriyama, "An immobilized enzyme membrane fabrication method using an ink jet nozzle," *Biosensors*, vol. 4, no. 1, pp. 41–52, 1989, doi: 10.1016/0265-928X(89)80033-1.
- 5769 [21] C. D. Chin, V. Linder, and S. K. Sia, "Commercialization of microfluidic point-of-care diagnostic devices," *Lab Chip*, vol. 12, no. 12, pp. 2118–2134, 2012, doi: 10.1039/c2lc21204h.
- 5770 [22] "The Multicorder." <https://gow.epsrc.ukri.org/NGBOViewGrant.aspx?GrantRef=EP/K021966/1> (accessed May 07, 2020).
- 5771 [23] "Glasgow university scientists invent hand-held Star Trek gizmo that scans your skin to find illness at the touch of a button." <https://www.thescottishsun.co.uk/news/3256042/glasgow-university-hand-held-device-scan-skin-illness/> (accessed May 07, 2020).
- 5772 [24] M. F. (Martin F. . Chaplin and C. Bucke, *Enzyme technology*. Cambridge University Press, 1990.

- 5805 [25] M. Mascini, "A Brief Story of Biosensor Technology," in *Biotechnological Applications of*
5806 *Photosynthetic Proteins: Biochips, Biosensors and Biodevices*, Springer US, 2007, pp. 4–10.
- 5807 [26] A. P. F. Turner, "Biosensors: Sense and sensibility," *Chem. Soc. Rev.*, vol. 42, no. 8, pp. 3184–3196,
5808 Mar. 2013, doi: 10.1039/c3cs3528d.
- 5809 [27] L. C. Clark and C. Lyons, "ELECTRODE SYSTEMS FOR CONTINUOUS MONITORING IN
5810 CARDIOVASCULAR SURGERY," *Ann. N. Y. Acad. Sci.*, vol. 102, no. 1, pp. 29–45, 1962, doi:
5811 10.1111/j.1749-6632.1962.tb13623.x.
- 5812 [28] M. Staiano *et al.*, *Enzymes as Sensors*, 1st ed., vol. 589. Elsevier Inc., 2017.
- 5813 [29] R. Monošík, M. Stred'anský, and E. Šturdík, "Biosensors-classifi cation, characterization and new
5814 trends," doi: 10.2478/v10188-012-0017-z.
- 5815 [30] F. Gorjikhah *et al.*, "Improving 'lab-on-a-chip' techniques using biomedical nanotechnology: a
5816 review," *Artificial Cells, Nanomedicine and Biotechnology*, vol. 44, no. 7. Taylor and Francis Ltd., pp.
5817 1609–1614, Oct. 02, 2016, doi: 10.3109/21691401.2015.1129619.
- 5818 [31] J. P. Conde *et al.*, "Lab-on-chip systems for integrated bioanalyses," *Essays Biochem.*, vol. 60, no. 1,
5819 pp. 121–131, Jun. 2016, doi: 10.1042/EBC20150013.
- 5820 [32] S. D'Auria and J. R. Lakowicz, "Enzyme fluorescence as a sensing tool: New perspectives in
5821 biotechnology," *Curr. Opin. Biotechnol.*, vol. 12, no. 1, pp. 99–104, Feb. 2001, doi: 10.1016/S0958-
5822 1669(00)00164-6.
- 5823 [33] A. Mulchandani, K. Rogers, and A. Mulchandani, "Principles of Enzyme Biosensors," in *Enzyme and*
5824 *Microbial Biosensors*, Humana Press, 2003, pp. 3–14.
- 5825 [34] P. D. Boyer *et al.*, *The Enzymes*. Academic Press, 1970.
- 5826 [35] E. Fischer, "Einfluss der Configuration auf die Wirkung der Enzyme. II," *Berichte der Dtsch. Chem.*
5827 *Gesellschaft*, vol. 27, no. 3, pp. 3479–3483, Oct. 1894, doi: 10.1002/cber.189402703169.
- 5828 [36] G. M. Cooper, *The cell : a molecular approach*. ASM Press, 2000.
- 5829 [37] T. O. Tiffany, J. M. Jansen, C. A. Burtis, J. B. Overton, and C. D. Scott, "Enzymatic Kinetic Rate and
5830 End-Point Analyses of Substrate, by Use of a GeMSAEC Fast Analyzer," *Clin. Chem.*, vol. 18, no. 8,
5831 1972.
- 5832 [38] P. Takhistov, "Biosensor technology for food processing, safety, and packaging," in *Handbook of Food*
5833 *Science, Technology, and Engineering - 4 Volume Set*, CRC Press, 2005, pp. 2312–2331.
- 5834 [39] Y. Song, Y. Y. Huang, X. Liu, X. Zhang, M. Ferrari, and L. Qin, "Point-of-care technologies for
5835 molecular diagnostics using a drop of blood," *Trends Biotechnol.*, vol. 32, no. 3, pp. 132–139, 2014,
5836 doi: 10.1016/j.tibtech.2014.01.003.
- 5837 [40] E. H. Yoo and S. Y. Lee, "Glucose biosensors: An overview of use in clinical practice," *Sensors*, vol.
5838 10, no. 5. pp. 4558–4576, May 2010, doi: 10.3390/s100504558.
- 5839 [41] H. W. Yeh and H. W. Ai, "Development and Applications of Bioluminescent and Chemiluminescent
5840 Reporters and Biosensors," *Annu. Rev. Anal. Chem.*, vol. 12, pp. 129–150, 2019, doi: 10.1146/annurev-
5841 anchem-061318-115027.
- 5842 [42] J. W. Lichtman and J. Conchello, "Fluorescence microscopy," vol. 2, no. 12, 2005, doi:
5843 10.1038/NMETH817.
- 5844 [43] O. Pashchenko, T. Shelby, T. Banerjee, and S. Santra, "A Comparison of Optical, Electrochemical,
5845 Magnetic, and Colorimetric Point-of-Care Biosensors for Infectious Disease Diagnosis," *ACS*
5846 *Infectious Diseases*, vol. 4, no. 8. American Chemical Society, pp. 1162–1178, Aug. 10, 2018, doi:
5847 10.1021/acsinfecdis.8b00023.
- 5848 [44] W. Chen, S. Cai, Q. Q. Ren, W. Wen, and Y. Di Zhao, "Recent advances in electrochemical sensing
5849 for hydrogen peroxide: A review," *Analyst*, vol. 137, no. 1. Royal Society of Chemistry, pp. 49–58,
5850 Jan. 07, 2012, doi: 10.1039/c1an15738h.
- 5851 [45] C. Giagkoulovits *et al.*, "A 16 × 16 CMOS amperometric microelectrode array for Simultaneous
5852 Electrochemical Measurements," *IEEE Trans. Circuits Syst. I Regul. Pap.*, vol. 65, no. 9, pp. 2821–
5853 2831, Sep. 2018, doi: 10.1109/TCSI.2018.2794502.
- 5854 [46] J. K. Tung, K. Berglund, C.-A. Gutekunst, U. Hochgeschwender, and R. E. Gross, "Bioluminescence
5855 imaging in live cells and animals," *Neurophotonics*, vol. 3, no. 02, p. 1, 2016, doi:
5856 10.1117/1.nph.3.2.025001.
- 5857 [47] F. Serra and E. M. Terentjev, "Nonlinear dynamics of absorption and photobleaching of dyes," *J.*
5858 *Chem. Phys.*, vol. 128, no. 22, 2008, doi: 10.1063/1.2937455.
- 5859 [48] G. C. Genshaw MA, "Optical bleaching in o-dianisidine glucose tests," *Clin. Chem.*, vol. 19(10):122,
5860 1973.
- 5861 [49] "Enzyme Database - BRENDA." <https://www.brenda-enzymes.org/index.php> (accessed Jan. 22,
5862 2020).
- 5863 [50] D. F. Swinehart, "The Beer-Lambert Law," *J. Chem. Educ.*, vol. 39, no. 7, p. 333, Jul. 1962, doi:

- 5864 10.1021/ed039p333.
- 5865 [51] A. Dwevedi and A. Dwevedi, "Basics of Enzyme Immobilization," in *Enzyme Immobilization*, Springer International Publishing, 2016, pp. 21–44.
- 5866 [52] K. Nakagawa, A. Tamura, and C. Chaiya, "Preparation of proteolytic microreactors by freeze-drying immobilization," *Chem. Eng. Sci.*, vol. 119, pp. 22–29, 2014, doi: 10.1016/j.ces.2014.07.054.
- 5867 [53] A. Aksan, D. Irimia, X. He, and M. Toner, "Desiccation kinetics of biopreservation solutions in microchannels," *J. Appl. Phys.*, vol. 99, no. 6, 2006, doi: 10.1063/1.2181280.
- 5868 [54] John G. Day and Glyn N. Stacey, *Methods in molecular biology. Cryopreservation and freeze-drying protocols.*, 2nd ed., vol. 368. 2007.
- 5871 [55] T. Garcia-Perez, S. G. Hong, J. Kim, and S. Ha, "Entrapping cross-linked glucose oxidase aggregates within a graphitized mesoporous carbon network for enzymatic biofuel cells," *Enzyme Microb. Technol.*, vol. 90, pp. 26–34, Aug. 2016, doi: 10.1016/j.enzmictec.2016.04.010.
- 5872 [56] S. Ghosh and C. H. Ahn, "Lyophilization of chemiluminescent substrate reagents for high-sensitive microchannel-based lateral flow assay (MLFA) in point-of-care (POC) diagnostic system," *Analyst*, vol. 144, no. 6, pp. 2109–2119, Mar. 2019, doi: 10.1039/c8an01899e.
- 5873 [57] N. Bhalla, P. Jolly, N. Formisano, and P. Estrela, "Introduction to biosensors," *Essays Biochem.*, pp. 60–61, 2016, doi: 10.1042/EBC20150001.
- 5874 [58] G. L. Long and J. D. Winefordner, "Limit of Detection: A Closer Look at the IUPAC Definition," *Anal. Chem.*, vol. 55, no. 7, pp. 712A–724A, 1983, doi: 10.1021/ac00258a001.
- 5875 [59] U. S. N. B. of Standards, *NBS Special Publication*, no. v. 1;v. 300. The Bureau, 1969.
- 5876 [60] L. A. Currie and G. Svehla, "INTERNATIONAL UNION OF PURE AND APPLIED CHEMISTRY ANALYTICAL CHEMISTRY DIVISION COMMISSION ON ANALYTICAL NOMENCLATURE* t NOMENCLATURE FOR THE PRESENTATION OF RESULTS OF CHEMICAL ANALYSIS," 1994.
- 5877 [61] K. Y. Mehta *et al.*, "Metabolomic biomarkers of pancreatic cancer: a meta-analysis study," *Oncotarget*, vol. 8, no. 40, pp. 68899–68915, 2017, doi: 10.18632/oncotarget.20324.
- 5878 [62] "Error Sum of Squares." https://hlab.stanford.edu/brian/error_sum_of_squares.html (accessed Dec. 08, 2020).
- 5879 [63] J. Benesty, J. Chen, Y. Huang, and I. Cohen, "Pearson Correlation Coefficient," 2009, pp. 1–4.
- 5880 [64] "Unmounted LEDs." https://www.thorlabs.com/newgrouppage9.cfm?objectgroup_id=2814 (accessed Mar. 16, 2020).
- 5881 [65] A. S. Sedra and K. C. Smith, "Microelectronic Circuits Revised Edition," *Oxford Ser. Electr. Comput. Eng.*, p. 1392, 2007.
- 5882 [66] S. Voinigescu, *High-frequency integrated circuits*. Cambridge University Press, 2013.
- 5883 [67] G. E. Moore, "The role of fairchild in silicon technology in the early days of 'Silicon Valley,'" *Proc. IEEE*, vol. 86, no. 1, pp. 53–62, 1998, doi: 10.1109/5.658759.
- 5884 [68] R. J. (Robert J. Keyes, *Optical and infrared detectors*. Springer-Verlag, 1977.
- 5885 [69] H. Photonics, "Si photodiodes." https://www.hamamatsu-news.de/hamamatsu_optosemiconductor_handbook/14/ (accessed Oct. 28, 2020).
- 5886 [70] O. Optoelectronics, "Photodiode Characteristics and Applications." <http://www.osioptoelectronics.com/application-notes/an-photodiode-parameters-characteristics.pdf> (accessed Oct. 28, 2020).
- 5887 [71] A. H., M. C-K., and V. P., "CMOS Photodetectors," in *Photodiodes - World Activities in 2011*, InTech, 2011.
- 5888 [72] R. A. Yotter and D. M. Wilson, "A review of photodetectors for sensing light-emitting reporters in biological systems," *IEEE Sensors Journal*, vol. 3, no. 3, pp. 288–303, Jun. 2003, doi: 10.1109/JSEN.2003.814651.
- 5889 [73] R. Hui, "Photodetectors," *Introd. to Fiber-Optic Commun.*, pp. 125–154, 2020, doi: 10.1016/b978-0-12-805345-4.00004-4.
- 5890 [74] and P. K. B. Deen, M. Jamal, *Silicon photonics: fundamentals and devices*, Vol. 44. J. .
- 5891 [75] B. Van Zeghbroeck, *Principles of semiconductor devices*, 2004th ed. Colorado University.
- 5892 [76] "Application Notes n4 - Modes of Operation - Photovoltaic vs. Photoconductive." <https://www.farnell.com/datasheets/2302133.pdf>.
- 5893 [77] B. Bahreyni, "Chapter 7 - Noise," in *Fabrication and Design of Resonant Microdevices*, B. Bahreyni, Ed. Norwich, NY: William Andrew Publishing, 2009, pp. 129–141.
- 5894 [78] A. S. Junhao Chu, *Device physics of narrow gap semiconductors*. Springer, 2010.
- 5895 [79] R. F. Pires and V. D. B. Bonifácio, "Journal of Materials NanoScience Photodiodes : Principles and recent advances," vol. 6, no. 2, pp. 38–46, 2019.
- 5896 [80] M. Bigas, E. Cabruja, J. Forest, and J. Salvi, "Review of CMOS image sensors," 2005, doi:

- 10.1016/j.mejo.2005.07.002.
- 5924 [81] S. A. Taylor, "CCD and CMOS Imaging Array Technologies : Technology Review - Technology
5925 Review -," 1998.
- 5926 [82] E. K. Bolton, et al., "Integrated CMOS photodetectors and signal processing for very low-level
5927 chemical sensing with the bioluminescent bioreporter integrated circuit," *Sensors Actuators, B Chem.*,
5928 vol. 85, no. 1–2, pp. 179–185, Jun. 2002, doi: 10.1016/S0925-4005(02)00106-5.
- 5929 [83] D. Sander, M. Dandin, H. Ji, N. Nelson, and P. Abshire, "Low-noise CMOS fluorescence sensor," in
5930 *Proceedings - IEEE International Symposium on Circuits and Systems*, 2007, pp. 2007–2010, doi:
5931 10.1109/iscas.2007.378431.
- 5932 [84] S. B. Patil *et al.*, "An integrated portable system for single chip simultaneous measurement of multiple
5933 disease associated metabolites," *Biosens. Bioelectron.*, vol. 122, no. August, pp. 88–94, 2018, doi:
5934 10.1016/j.bios.2018.09.013.
- 5935 [85] M. A. Al-Rawhani *et al.*, "Multimodal Integrated Sensor Platform for Rapid Biomarker Detection.,"
5936 *IEEE Trans. Biomed. Eng.*, Jun. 2019, doi: 10.1109/TBME.2019.2919192.
- 5937 [86] C. Accarino *et al.*, "A 64×64 spad array for portable colorimetric sensing, fluorescence and x-ray
5938 imaging," *IEEE Sens. J.*, vol. 19, no. 17, pp. 7319–7327, Sep. 2019, doi: 10.1109/JSEN.2019.2916424.
- 5939 [87] W. Jiang, Y. Chalich, and M. J. Deen, "Sensors for positron emission tomography applications,"
5940 *Sensors (Switzerland)*, vol. 19, no. 22, 2019, doi: 10.3390/s19225019.
- 5941 [88] N. Zurich, "CCD versus CMOS--has CCD imaging come to an end?," 2001, Accessed: Jan. 17, 2020.
5942 [Online]. Available: <http://citeseerx.ist.psu.edu/viewdoc/summary?doi=10.1.1.4.6048>.
- 5943 [89] D. Litwiller, "CCD vs. CMOS: Facts and Fiction. Photonics Spectra," 2001.
- 5944 [90] N. Psychogios *et al.*, "The human serum metabolome," *PLoS One*, vol. 6, no. 2, 2011, doi:
5945 10.1371/journal.pone.0016957.
- 5946 [91] M. Vailati-Riboni, V. Palombo, and J. J. Loor, "What Are Omics Sciences?," in *Periparturient*
5947 *Diseases of Dairy Cows*, Cham: Springer International Publishing, 2017, pp. 1–7.
- 5948 [92] A. K. Kosmides, K. Kamisoglu, S. E. Calvano, S. A. Corbett, and I. P. Androulakis, "Metabolomic
5949 fingerprinting: Challenges and opportunities," *Crit. Rev. Biomed. Eng.*, vol. 41, no. 3, pp. 205–221,
5950 2013, doi: 10.1615/CritRevBiomedEng.2013007736.
- 5951 [93] D. J. Beale, A. V. Karpe, and W. Ahmed, "Beyond metabolomics: A review of multi-omics-based
5952 approaches," in *Microbial Metabolomics: Applications in Clinical, Environmental, and Industrial*
5953 *Microbiology*, Springer International Publishing, 2016, pp. 289–312.
- 5954 [94] J. L. Markley *et al.*, "The future of NMR-based metabolomics," *Curr. Opin. Biotechnol.*, vol. 43, pp.
5955 34–40, 2017, doi: 10.1016/j.copbio.2016.08.001.
- 5956 [95] I. P. GEROTHANASSIS, A. TROGANIS, V. EXARCHOU, and K. BARBAROSSOU, "NUCLEAR
5957 MAGNETIC RESONANCE (NMR) SPECTROSCOPY: BASIC PRINCIPLES AND PHENOMENA,
5958 AND THEIR APPLICATIONS TO CHEMISTRY, BIOLOGY AND MEDICINE," *Chem. Educ. Res.*
5959 *Pr.*, vol. 3, no. 2, pp. 229–252, 2002, doi: 10.1039/b2rp90018a.
- 5960 [96] J. J. Pitt, "Principles and applications of liquid chromatography-mass spectrometry in clinical
5961 biochemistry.," *Clin. Biochem. Rev.*, vol. 30, no. 1, pp. 19–34, Feb. 2009, Accessed: Jan. 20, 2020.
5962 [Online]. Available: <http://www.ncbi.nlm.nih.gov/pubmed/19224008>.
- 5963 [97] J.-S. Kang, "Principles and Applications of LC-MS/MS for the Quantitative Bioanalysis of Analytes
5964 in Various Biological Samples," *Tandem Mass Spectrom. - Appl. Princ.*, 2012, doi: 10.5772/32085.
- 5965 [98] E. R. Perez, J. A. Knapp, C. K. Horn, S. L. Stillman, J. E. Evans, and D. P. Arfsten, "Comparison of
5966 LC-MS-MS and GC-MS analysis of benzodiazepine compounds included in the drug demand
5967 reduction urinalysis program," *J. Anal. Toxicol.*, vol. 40, no. 3, pp. 201–207, Apr. 2016, doi:
5968 10.1093/jat/bkv140.
- 5969 [99] Cancer Research UK, "Cancer in the UK: Overview, Prevention, Early diagnosis, Treatment & Data,"
5970 pp. 1–20, 2018, [Online]. Available: stats.team@cancer.org.uk.
- 5971 [100] R. Landy, F. Pesola, A. Castañón, and P. Sasieni, "Impact of cervical screening on cervical cancer
5972 mortality: Estimation using stage-specific results from a nested case-control study," *Br. J. Cancer*, vol.
5973 115, no. 9, pp. 1140–1146, Oct. 2016, doi: 10.1038/bjc.2016.290.
- 5974 [101] S. Koo, L. J. Neilson, C. Von Wagner, and C. J. Rees, "The NHS bowel cancer screening program:
5975 Current perspectives on strategies for improvement," *Risk Management and Healthcare Policy*, vol.
5976 10, Dove Medical Press Ltd, pp. 177–187, Dec. 04, 2017, doi: 10.2147/RMHP.S109116.
- 5977 [102] A. Zhang, H. Sun, G. Yan, P. Wang, Y. Han, and X. Wang, "Metabolomics in diagnosis and biomarker
5978 discovery of colorectal cancer," *Cancer Lett.*, vol. 345, no. 1, pp. 17–20, Apr. 2014, doi:
5979 10.1016/j.canlet.2013.11.011.
- 5980 [103] B. Kalyanaraman, "Teaching the basics of cancer metabolism: Developing antitumor strategies by
5981 exploiting the differences between normal and cancer cell metabolism," *Redox Biology*, vol. 12.

- Elsevier B.V., pp. 833–842, Aug. 01, 2017, doi: 10.1016/j.redox.2017.04.018.
- 5982
5983 [104] J. Shen, L. Yan, S. Liu, C. B. Ambrosone, and H. Zhao, “Plasma metabolomic profiles in breast cancer
5984 patients and healthy controls: By race and tumor receptor subtypes,” *Transl. Oncol.*, vol. 6, no. 6, pp.
5985 757–765, 2013, doi: 10.1593/tlo.13619.
- 5986 [105] T. Zhang *et al.*, “Discrimination between malignant and benign ovarian tumors by plasma metabolomic
5987 profiling using ultra performance liquid chromatography/mass spectrometry,” *Clin. Chim. Acta*, vol.
5988 413, no. 9–10, pp. 861–868, May 2012, doi: 10.1016/j.cca.2012.01.026.
- 5989 [106] G. D. Dakubo, *Cancer Biomarkers in Body Fluids*. Springer International Publishing, 2017.
- 5990 [107] A. B. Leichtle *et al.*, “Pancreatic carcinoma, pancreatitis, and healthy controls: Metabolite models in a
5991 three-class diagnostic dilemma,” *Metabolomics*, vol. 9, no. 3, pp. 677–687, Jun. 2013, doi:
5992 10.1007/s11306-012-0476-7.
- 5993 [108] L. Wang *et al.*, “¹H-NMR based metabonomic profiling of human esophageal cancer tissue,” *Mol.*
5994 *Cancer*, vol. 12, no. 1, p. 25, Apr. 2013, doi: 10.1186/1476-4598-12-25.
- 5995 [109] A. Vazquez, J. J. Kamphorst, E. K. Markert, Z. T. Schug, S. Tardito, and E. Gottlieb, “Cancer
5996 metabolism at a glance,” *J. Cell Sci.*, vol. 129, no. 18, pp. 3367–3373, 2016, doi: 10.1242/jcs.181016.
- 5997 [110] P. Józwiak, E. Forma, M. Bryś, and A. Krześlak, “O-GlcNAcylation and metabolic reprogramming in
5998 cancer,” *Frontiers in Endocrinology*, vol. 5, no. SEP. Frontiers Media S.A., 2014, doi:
5999 10.3389/fendo.2014.00145.
- 6000 [111] L. Vettore, R. L. Westbrook, and D. A. Tennant, “New aspects of amino acid metabolism in cancer,”
6001 *British Journal of Cancer*. Springer Nature, 2019, doi: 10.1038/s41416-019-0620-5.
- 6002 [112] T. B. Salisbury and S. Arthur, “The regulation and function of the L-type amino acid transporter 1
6003 (LAT1) in cancer,” *International Journal of Molecular Sciences*, vol. 19, no. 8. MDPI AG, Aug. 12,
6004 2018, doi: 10.3390/ijms19082373.
- 6005 [113] K. Glunde, M. F. Penet, L. Jiang, M. A. Jacobs, and Z. M. Bhujwalla, “Choline metabolism-based
6006 molecular diagnosis of cancer: An update,” *Expert Review of Molecular Diagnostics*, vol. 15, no. 6.
6007 Expert Reviews Ltd., pp. 735–747, Jun. 01, 2015, doi: 10.1586/14737159.2015.1039515.
- 6008 [114] U. E. Martinez-Outschoorn, M. Peiris-Pagés, R. G. Pestell, F. Sotgia, and M. P. Lisanti, “Cancer
6009 metabolism: A therapeutic perspective,” *Nat. Rev. Clin. Oncol.*, vol. 14, no. 1, pp. 11–31, 2017, doi:
6010 10.1038/nrclinonc.2016.60.
- 6011 [115] S. R. V. Knott *et al.*, “Asparagine bioavailability governs metastasis in a model of breast cancer,”
6012 *Nature*, vol. 554, no. 7692, pp. 378–381, Feb. 2018, doi: 10.1038/nature25465.
- 6013 [116] O. Olivares, J. H. M. Däbritz, A. King, E. Gottlieb, and C. Halsey, “Research into cancer
6014 metabolomics: Towards a clinical metamorphosis,” *Semin. Cell Dev. Biol.*, vol. 43, pp. 52–64, 2015,
6015 doi: 10.1016/j.semcdb.2015.09.008.
- 6016 [117] C. Oakman *et al.*, “Identification of a serum-detectable metabolomic fingerprint potentially correlated
6017 with the presence of micrometastatic disease in early breast cancer patients at varying risks of disease
6018 relapse by traditional prognostic methods,” *Ann. Oncol.*, vol. 22, no. 6, pp. 1295–1301, 2011, doi:
6019 10.1093/annonc/mdq606.
- 6020 [118] Y. Li, X. Song, X. Zhao, L. Zou, and G. Xu, “Serum metabolic profiling study of lung cancer using
6021 ultra high performance liquid chromatography/quadrupole time-of-flight mass spectrometry,” *J.*
6022 *Chromatogr. B Anal. Technol. Biomed. Life Sci.*, vol. 966, pp. 147–153, Sep. 2014, doi:
6023 10.1016/j.jchromb.2014.04.047.
- 6024 [119] W. Lv and T. Yang, “Identification of possible biomarkers for breast cancer from free fatty acid profiles
6025 determined by GC-MS and multivariate statistical analysis,” *Clin. Biochem.*, vol. 45, no. 1–2, pp. 127–
6026 133, Jan. 2012, doi: 10.1016/j.clinbiochem.2011.10.011.
- 6027 [120] L. Tenori *et al.*, “Serum metabolomic profiles evaluated after surgery may identify patients with
6028 oestrogen receptor negative early breast cancer at increased risk of disease recurrence. Results from a
6029 retrospective study,” *Mol. Oncol.*, vol. 9, no. 1, pp. 128–139, Jan. 2015, doi:
6030 10.1016/j.molonc.2014.07.012.
- 6031 [121] J. Budczies *et al.*, “Comparative metabolomics of estrogen receptor positive and estrogen receptor
6032 negative breast cancer: Alterations in glutamine and beta-alanine metabolism,” *J. Proteomics*, vol. 94,
6033 pp. 279–288, Dec. 2013, doi: 10.1016/j.jprot.2013.10.002.
- 6034 [122] N. Lefort *et al.*, “¹H NMR metabolomics analysis of the effect of dichloroacetate and allopurinol on
6035 breast cancers,” *J. Pharm. Biomed. Anal.*, vol. 93, pp. 77–85, 2014, doi: 10.1016/j.jpba.2013.08.017.
- 6036 [123] A. S. Krall, S. Xu, T. G. Graeber, D. Braas, and H. R. Christofk, “Asparagine promotes cancer cell
6037 proliferation through use as an amino acid exchange factor,” *Nat. Commun.*, vol. 7, pp. 1–13, Apr.
6038 2016, doi: 10.1038/ncomms11457.
- 6039 [124] H. Nam, B. C. Chung, Y. Kim, K. Y. Lee, and D. Lee, “Combining tissue transcriptomics and urine
6040 metabolomics for breast cancer biomarker identification,” *Bioinformatics*, vol. 25, no. 23, pp. 3151–

- 6041 3157, Sep. 2009, doi: 10.1093/bioinformatics/btp558.
- 6042 [125] A. B. Leichtle *et al.*, “Serum amino acid profiles and their alterations in colorectal cancer,”
- 6043 *Metabolomics*, vol. 8, no. 4, pp. 643–653, Aug. 2012, doi: 10.1007/s11306-011-0357-5.
- 6044 [126] H. Wang, V. K. Tso, C. M. Slupsky, and R. N. Fedorak, “Metabolomics and detection of colorectal
- 6045 cancer in humans: A systematic review,” *Future Oncology*, vol. 6, no. 9, pp. 1395–1406, Sep. 2010,
- 6046 doi: 10.2217/fon.10.107.
- 6047 [127] Y. Qiu *et al.*, “Serum metabolite profiling of human colorectal cancer using GC-TOFMS and UPLC-
- 6048 QTOFMS,” *J. Proteome Res.*, vol. 8, no. 10, pp. 4844–4850, 2009, doi: 10.1021/pr9004162.
- 6049 [128] A. Huang, D. Fuchs, B. Widner, C. Glover, D. C. Henderson, and T. G. Allen-Mersh, “Tryptophan and
- 6050 quality of life in colorectal cancer,” in *Advances in Experimental Medicine and Biology*, 2003, vol.
- 6051 527, pp. 353–358, doi: 10.1007/978-1-4615-0135-0_39.
- 6052 [129] S. A. Ritchie *et al.*, “Reduced levels of hydroxylated, polyunsaturated ultra long-chain fatty acids in
- 6053 the serum of colorectal cancer patients: Implications for early screening and detection,” *BMC Med.*,
- 6054 vol. 8, Feb. 2010, doi: 10.1186/1741-7015-8-13.
- 6055 [130] B. Jiménez *et al.*, “¹H HR-MAS NMR spectroscopy of tumor-induced local metabolic ‘field-effects’
- 6056 enables colorectal cancer staging and prognostication,” *J. Proteome Res.*, vol. 12, no. 2, pp. 959–968,
- 6057 Feb. 2013, doi: 10.1021/pr3010106.
- 6058 [131] K. Raina, K. Ravichandran, S. Rajamanickam, K. M. Huber, N. J. Serkova, and R. Agarwal, “Inositol
- 6059 hexaphosphate inhibits tumor growth, vascularity, and metabolism in TRAMP mice: A
- 6060 multiparametric magnetic resonance study,” *Cancer Prev. Res.*, vol. 6, no. 1, pp. 40–50, Jan. 2013, doi:
- 6061 10.1158/1940-6207.CAPR-12-0387.
- 6062 [132] G. F. Giskeødegård *et al.*, “Spermine and Citrate as Metabolic Biomarkers for Assessing Prostate
- 6063 Cancer Aggressiveness,” *PLoS One*, vol. 8, no. 4, Apr. 2013, doi: 10.1371/journal.pone.0062375.
- 6064 [133] J. E. McDunn *et al.*, “Metabolomic signatures of aggressive prostate cancer,” *Prostate*, vol. 73, no. 14,
- 6065 pp. 1547–1560, Oct. 2013, doi: 10.1002/pros.22704.
- 6066 [134] O. F. Bathe *et al.*, “Feasibility of identifying pancreatic cancer based on serum metabolomics,” *Cancer*
- 6067 *Epidemiol. Biomarkers Prev.*, vol. 20, no. 1, pp. 140–147, 2011, doi: 10.1158/1055-9965.EPI-10-0712.
- 6068 [135] D. O. Yang, J. Xu, H. Huang, and Z. Chen, “Metabolomic profiling of serum from human pancreatic
- 6069 cancer patients Using ¹H NMR spectroscopy and principal component analysis,” *Appl. Biochem.*
- 6070 *Biotechnol.*, vol. 165, no. 1, pp. 148–154, 2011, doi: 10.1007/s12010-011-9240-0.
- 6071 [136] L. Zhang *et al.*, “Distinguishing pancreatic cancer from chronic pancreatitis and healthy individuals by
- 6072 ¹H nuclear magnetic resonance-based metabolomic profiles,” *Clin. Biochem.*, vol. 45, no. 13–14, pp.
- 6073 1064–1069, Sep. 2012, doi: 10.1016/j.clinbiochem.2012.05.012.
- 6074 [137] S. Chen *et al.*, “Pseudotargeted metabolomics method and its application in serum biomarker discovery
- 6075 for hepatocellular carcinoma based on ultra high-performance liquid chromatography/triple quadrupole
- 6076 mass spectrometry,” *Anal. Chem.*, vol. 85, no. 17, pp. 8326–8333, 2013, doi: 10.1021/ac4016787.
- 6077 [138] S. Urayama, W. Zou, K. Brooks, and V. Tolstikov, “Comprehensive mass spectrometry based
- 6078 metabolic profiling of blood plasma reveals potent discriminatory classifiers of pancreatic cancer,”
- 6079 *Rapid Commun. Mass Spectrom.*, vol. 24, no. 5, pp. 613–620, Mar. 2010, doi: 10.1002/rcm.4420.
- 6080 [139] J. F. Xiao *et al.*, “LC-MS based serum metabolomics for identification of hepatocellular carcinoma
- 6081 biomarkers in Egyptian cohort,” *J. Proteome Res.*, vol. 11, no. 12, pp. 5914–5923, Dec. 2012, doi:
- 6082 10.1021/pr300673x.
- 6083 [140] S. A. Ritchie *et al.*, “Metabolic system alterations in pancreatic cancer patient serum: Potential for early
- 6084 detection,” *BMC Cancer*, vol. 13, Sep. 2013, doi: 10.1186/1471-2407-13-416.
- 6085 [141] P. Tripathi *et al.*, “Delineating metabolic signatures of head and neck squamous cell carcinoma:
- 6086 Phospholipase A2, a potential therapeutic target,” *Int. J. Biochem. Cell Biol.*, vol. 44, no. 11, pp. 1852–
- 6087 1861, Nov. 2012, doi: 10.1016/j.biocel.2012.06.025.
- 6088 [142] J. D. Clarke *et al.*, “Characterization of hepatocellular carcinoma related genes and metabolites in
- 6089 human nonalcoholic fatty liver disease,” *Dig. Dis. Sci.*, vol. 59, no. 2, pp. 365–374, Feb. 2014, doi:
- 6090 10.1007/s10620-013-2873-9.
- 6091 [143] H. Wen *et al.*, “A new NMR-based metabolomics approach for the diagnosis of biliary tract cancer,”
- 6092 *J. Hepatol.*, vol. 52, no. 2, pp. 228–233, Feb. 2010, doi: 10.1016/j.jhep.2009.11.002.
- 6093 [144] X. H. He *et al.*, “Metabonomic studies of pancreatic cancer response to radiotherapy in a mouse
- 6094 xenograft model using magnetic resonance spectroscopy and principal components analysis,” *World*
- 6095 *J. Gastroenterol.*, vol. 19, no. 26, pp. 4200–4208, Jul. 2013, doi: 10.3748/wjg.v19.i26.4200.
- 6096 [145] W. Struck, D. Siluk, A. Yumba-Mpanga, M. Markuszewski, R. Kaliszan, and M. J. Markuszewski,
- 6097 “Liquid chromatography tandem mass spectrometry study of urinary nucleosides as potential cancer
- 6098 markers,” *J. Chromatogr. A*, vol. 1283, pp. 122–131, Mar. 2013, doi: 10.1016/j.chroma.2013.01.111.
- 6099 [146] J. V. Alberice *et al.*, “Searching for urine biomarkers of bladder cancer recurrence using a liquid

- 6100 chromatography-mass spectrometry and capillary electrophoresis-mass spectrometry metabolomics
6101 approach,” *J. Chromatogr. A*, vol. 1318, pp. 163–170, Nov. 2013, doi: 10.1016/j.chroma.2013.10.002.
- 6102 [147] P. Tripathi *et al.*, “HR-MAS NMR tissue metabolomic signatures cross-validated by mass spectrometry
6103 distinguish bladder cancer from benign disease,” *J. Proteome Res.*, vol. 12, no. 7, pp. 3519–3528, Jul.
6104 2013, doi: 10.1021/pr4004135.
- 6105 [148] J. Huang *et al.*, “Serum metabolomic profiling of prostate cancer risk in the prostate, lung, colorectal,
6106 and ovarian cancer screening trial,” *Br. J. Cancer*, vol. 115, no. 9, pp. 1087–1095, Oct. 2016, doi:
6107 10.1038/bjc.2016.305.
- 6108 [149] M. Kdadra, S. Höckner, H. Leung, W. Kremer, and E. Schiffer, “Metabolomics biomarkers of prostate
6109 cancer: A systematic review,” *Diagnostics*, vol. 9, no. 1, pp. 1–44, Feb. 2019, doi:
6110 10.3390/diagnostics9010021.
- 6111 [150] R. S. Kelly, M. G. V. Heiden, E. Giovannucci, and L. A. Mucci, “Metabolomic biomarkers of prostate
6112 cancer: Prediction, diagnosis, progression, prognosis, and recurrence,” *Cancer Epidemiol. Biomarkers
6113 Prev.*, vol. 25, no. 6, pp. 887–906, Jun. 2016, doi: 10.1158/1055-9965.EPI-15-1223.
- 6114 [151] G. F. Giskeødegård *et al.*, “Metabolic markers in blood can separate prostate cancer from benign
6115 prostatic hyperplasia,” *Br. J. Cancer*, vol. 113, no. 12, pp. 1712–1719, Dec. 2015, doi:
6116 10.1038/bjc.2015.411.
- 6117 [152] M. Johansson *et al.*, “One-carbon metabolism and prostate cancer risk: Prospective investigation of
6118 seven circulating B vitamins and metabolites,” *Cancer Epidemiol. Biomarkers Prev.*, vol. 18, no. 5,
6119 pp. 1538–1543, May 2009, doi: 10.1158/1055-9965.EPI-08-1193.
- 6120 [153] C. Myers *et al.*, “Suramin: A novel growth factor antagonist with activity in hormone- refractory
6121 metastatic prostate cancer,” *J. Clin. Oncol.*, vol. 10, no. 6, pp. 881–889, 1992, doi:
6122 10.1200/JCO.1992.10.6.881.
- 6123 [154] S. J. Weinstein, K. Mackrain, R. Z. Stolzenberg-Solomon, J. Selhub, J. Virtamo, and D. Albanes,
6124 “Serum creatinine and prostate cancer risk in a prospective study,” *Cancer Epidemiol. Biomarkers
6125 Prev.*, vol. 18, no. 10, pp. 2643–2649, Oct. 2009, doi: 10.1158/1055-9965.EPI-09-0322.
- 6126 [155] P. M. Quilty *et al.*, “A comparison of the palliative effects of strontium-89 and external beam
6127 radiotherapy in metastatic prostate cancer,” *Radiother. Oncol.*, vol. 31, no. 1, pp. 33–40, 1994, doi:
6128 10.1016/0167-8140(94)90411-1.
- 6129 [156] B. J. Trock, “Application of metabolomics to prostate cancer,” *Urologic Oncology: Seminars and
6130 Original Investigations*, vol. 29, no. 5, pp. 572–581, Sep. 2011, doi: 10.1016/j.urolonc.2011.08.002.
- 6131 [157] A. Sreekumar *et al.*, “Metabolomic profiles delineate potential role for sarcosine in prostate cancer
6132 progression,” *Nature*, vol. 457, no. 7231, pp. 910–914, Feb. 2009, doi: 10.1038/nature07762.
- 6133 [158] E. Thysell *et al.*, “Metabolomic characterization of human prostate cancer bone metastases reveals
6134 increased levels of cholesterol,” *PLoS One*, vol. 5, no. 12, 2010, doi: 10.1371/journal.pone.0014175.
- 6135 [159] J. W. Locasale, “Serine, glycine and one-carbon units: Cancer metabolism in full circle,” *Nature
6136 Reviews Cancer*, vol. 13, no. 8, pp. 572–583, Aug. 2013, doi: 10.1038/nrc3557.
- 6137 [160] A. C. Ogilvie, et al., “Lactic Acidosis in Prostate Cancer: Consider the Warburg Effect Keywords
6138 Mutation · p53 mutations · PIK3CA mutations · PTEN mutations · IDH1 mutations · Prostate cancer
6139 · Lactic acidosis · Warburg effect · Metabolic reprogramming · Case report,” *Case Rep Oncol*, vol. 10,
6140 pp. 1085–1091, 2017, doi: 10.1159/000485242.
- 6141 [161] K. Fabyan, A. Holtzclaw, and J. Sherner, “PROSTATE LACTATE: A CASE OF SEVERE LACTIC
6142 ACIDOSIS WITH AN INTERESTING MECHANISM OF ACTION,” *Chest*, vol. 156, no. 4, p.
6143 A2105, Oct. 2019, doi: 10.1016/j.chest.2019.08.2050.
- 6144 [162] X. Zhang *et al.*, “Metabolic signatures of esophageal cancer: NMR-based metabolomics and UHPLC-
6145 based focused metabolomics of blood serum,” *Biochim. Biophys. Acta - Mol. Basis Dis.*, vol. 1832, no.
6146 8, pp. 1207–1216, Aug. 2013, doi: 10.1016/j.bbadis.2013.03.009.
- 6147 [163] J. Zhang *et al.*, “Esophageal Cancer Metabolite Biomarkers Detected by LC-MS and NMR Methods,”
6148 *PLoS One*, vol. 7, no. 1, p. e30181, Jan. 2012, doi: 10.1371/journal.pone.0030181.
- 6149 [164] T. Wiggins, S. Kumar, S. R. Markar, S. Antonowicz, and G. B. Hanna, “Tyrosine, phenylalanine, and
6150 tryptophan in gastroesophageal malignancy: A systematic review,” *Cancer Epidemiol. Biomarkers
6151 Prev.*, vol. 24, no. 1, pp. 32–38, Jan. 2015, doi: 10.1158/1055-9965.EPI-14-0980.
- 6152 [165] Q. Y. *et al.*, “A distinct metabolic signature of human colorectal cancer with prognostic potential,”
6153 *Clin. Cancer Res.*, vol. 20, no. 8, pp. 2136–2146, 2014, doi: 10.1158/1078-0432.CCR-13-1939 LK.
- 6154 [166] K. Yonezawa *et al.*, “Serum and tissue metabolomics of head and neck cancer,” *Cancer Genomics and
6155 Proteomics*, vol. 10, no. 5, pp. 233–238, 2013.
- 6156 [167] T. Wen *et al.*, “Exploratory investigation of plasma metabolomics in human lung adenocarcinoma,”
6157 *Mol. Biosyst.*, vol. 9, no. 9, pp. 2370–2378, 2013, doi: 10.1039/c3mb70138g.
- 6158 [168] Y. Guo *et al.*, “Probing gender-specific lipid metabolites and diagnostic biomarkers for lung cancer

- 6159 using Fourier transform ion cyclotron resonance mass spectrometry,” *Clin. Chim. Acta*, vol. 414, pp.
6160 135–141, Dec. 2012, doi: 10.1016/j.cca.2012.08.010.
- 6161 [169] L. Gao, Z. Wen, C. Wu, T. Wen, and C. Ong, “Metabolic Profiling of Plasma from Benign and
6162 Malignant Pulmonary Nodules Patients Using Mass Spectrometry-Based Metabolomics,” *Metabolites*,
6163 vol. 3, no. 3, pp. 539–551, Jul. 2013, doi: 10.3390/metabo3030539.
- 6164 [170] M. Serizawa *et al.*, “Identification of metabolic signatures associated with erlotinib resistance of non-
6165 small cell lung cancer cells,” *Anticancer Res.*, vol. 34, no. 6, pp. 2779–87, Jun. 2014.
- 6166 [171] A. P. J. Van Den Heuvel, J. Jing, R. F. Wooster, and K. E. Bachman, “Analysis of glutamine
6167 dependency in non-small cell lung cancer: GLS1 splice variant GAC is essential for cancer cell
6168 growth,” *Cancer Biol. Ther.*, vol. 13, no. 12, pp. 1185–1194, Oct. 2012, doi: 10.4161/cbt.21348.
- 6169 [172] S. Nakamizo *et al.*, “GC/MS-based metabolomic analysis of cerebrospinal fluid (CSF) from glioma
6170 patients,” *J. Neurooncol.*, vol. 113, no. 1, pp. 65–74, May 2013, doi: 10.1007/s11060-013-1090-x.
- 6171 [173] S. G. Musharraf, A. J. Siddiqui, T. Shamsi, M. I. Choudhary, and A. U. Rahman, “Serum
6172 metabonomics of acute leukemia using nuclear magnetic resonance spectroscopy,” *Sci. Rep.*, vol. 6,
6173 Aug. 2016, doi: 10.1038/srep30693.
- 6174 [174] D. A. MacIntyre *et al.*, “Serum metabolome analysis by 1H-NMR reveals differences between chronic
6175 lymphocytic leukaemia molecular subgroups,” *Leukemia*, vol. 24, no. 4, pp. 788–797, 2010, doi:
6176 10.1038/leu.2009.295.
- 6177 [175] B. Tan *et al.*, “Metabonomics identifies serum metabolite markers of colorectal cancer,” *J. Proteome
6178 Res.*, vol. 12, no. 6, pp. 3000–3009, 2013, doi: 10.1021/pr400337b.
- 6179 [176] B. S. Li *et al.*, “The downregulation of asparagine synthetase expression can increase the sensitivity of
6180 cells resistant to L-asparaginase [13],” *Leukemia*, vol. 20, no. 12. Nature Publishing Group, pp. 2199–
6181 2201, 2006, doi: 10.1038/sj.leu.2404423.
- 6182 [177] S. Holst *et al.*, “Investigations on aberrant glycosylation of glycosphingolipids in colorectal cancer
6183 tissues using liquid chromatography and matrix-assisted laser desorption time-of-flight mass
6184 spectrometry (MALDI-TOF-MS),” *Mol. Cell. Proteomics*, vol. 12, no. 11, pp. 3081–3093, Nov. 2013,
6185 doi: 10.1074/mcp.M113.030387.
- 6186 [178] R. Etzioni *et al.*, “The case for early detection,” *Nature Reviews Cancer*, vol. 3, no. 4. pp. 243–252,
6187 Apr. 2003, doi: 10.1038/nrc1041.
- 6188 [179] S. O. Lilienfeld, G. Alliger, and K. Mitchell, “Why Integrity Testing Remains Controversial,” *Am.
6189 Psychol.*, vol. 50, no. 6, pp. 457–458, 1995, doi: 10.1037/0003-066X.50.6.457.
- 6190 [180] E. A. Struys, A. C. Heijboer, J. Van Moorselaar, C. Jakobs, and M. A. Blankenstein, “Serum sarcosine
6191 is not a marker for prostate cancer,” *Annals of Clinical Biochemistry*, vol. 47, no. 3. p. 282, May 2010,
6192 doi: 10.1258/acb.2010.009270.
- 6193 [181] A. R. Meyer and M. A. Gorin, “First point-of-care PSA test for prostate cancer detection,” *Nat. Rev.
6194 Urol.*, vol. 16, no. 6, pp. 332–333, 2019, doi: 10.1038/s41585-019-0179-1.
- 6195 [182] S. Koochekpour *et al.*, “Serum glutamate levels correlate with gleason score and glutamate blockade
6196 decreases proliferation, migration, and invasion and induces apoptosis in prostate cancer cells,” *Clin.
6197 Cancer Res.*, vol. 18, no. 21, pp. 5888–5901, Nov. 2012, doi: 10.1158/1078-0432.CCR-12-1308.
- 6198 [183] L. C. Soliman, Y. Hui, A. K. Hewavitharana, and D. D. Y. Chen, “Monitoring potential prostate cancer
6199 biomarkers in urine by capillary electrophoresis-tandem mass spectrometry,” *J. Chromatogr. A*, vol.
6200 1267, pp. 162–169, Dec. 2012, doi: 10.1016/j.chroma.2012.07.021.
- 6201 [184] W. Johnson, O. Onuma, M. Owolabi, and S. Sachdev, “Stroke: A global response is needed,” *Bulletin
6202 of the World Health Organization*, vol. 94, no. 9. World Health Organization, pp. 634A–635A, Sep.
6203 01, 2016, doi: 10.2471/BLT.16.181636.
- 6204 [185] R. W. McGarrah, S. B. Crown, G. F. Zhang, S. H. Shah, and C. B. Newgard, “Cardiovascular
6205 metabolomics,” *Circulation Research*, vol. 122, no. 9. Lippincott Williams and Wilkins, pp. 1238–
6206 1258, 2018, doi: 10.1161/CIRCRESAHA.117.311002.
- 6207 [186] S. M. Grundy and N. J. Stone, “2018 cholesterol clinical practice guidelines: Synopsis of the 2018
6208 American Heart Association/American college of cardiology/ multisociety cholesterol guideline,”
6209 *Annals of Internal Medicine*, vol. 170, no. 11. American College of Physicians, pp. 779–783, 2019,
6210 doi: 10.7326/M19-0365.
- 6211 [187] C. Lazzeri, S. Valente, M. Chiostrì, and G. F. Gensini, “Clinical significance of Lactate in acute cardiac
6212 patients,” *World J. Cardiol.*, vol. 7, no. 8, p. 483, 2015, doi: 10.4330/wjc.v7.i8.483.
- 6213 [188] V. Pucino, M. Bombardieri, C. Pitzalis, and C. Mauro, “Lactate at the crossroads of metabolism,
6214 inflammation, and autoimmunity,” *Eur. J. Immunol.*, vol. 47, no. 1, pp. 14–21, Jan. 2017, doi:
6215 10.1002/eji.201646477.
- 6216 [189] E. Sidorov, D. K. Sanghera, and J. K. P. Vanamala, “Biomarker for ischemic stroke using metabolome:
6217 A clinician perspective,” *J. Stroke*, vol. 21, no. 1, pp. 31–41, Jan. 2019, doi: 10.5853/jos.2018.03454.

- 6218 [190] J. Bakker, M. W. N. Nijsten, and T. C. Jansen, "Clinical use of lactate monitoring in critically ill
6219 patients," *Ann. Intensive Care*, vol. 3, no. 1, pp. 1–8, 2013, doi: 10.1186/2110-5820-3-12.
- 6220 [191] R. Cánovas, M. Cuartero, and G. A. Crespo, "Modern creatinine (Bio)sensing: Challenges of point-of-
6221 care platforms," *Biosens. Bioelectron.*, vol. 130, no. November 2018, pp. 110–124, 2019, doi:
6222 10.1016/j.bios.2019.01.048.
- 6223 [192] J. L. Griffin, H. Atherton, J. Shockcor, and L. Atzori, "Metabolomics as a tool for cardiac research,"
6224 *Nature Reviews Cardiology*, vol. 8, no. 11, pp. 630–643, Nov. 2011, doi: 10.1038/nrcardio.2011.138.
- 6225 [193] V. Chopra and K. A. Eagle, "PRACTITIONERS SECTION; Cardiac biomarkers in the diagnosis,
6226 prognosis and management of coronary artery disease: A primer for internists," *Indian J. Med. Sci.*,
6227 vol. 64, no. 12, pp. 564–576, Dec. 2010, doi: 10.4103/0019-5359.75934.
- 6228 [194] A. A. Rasmiena, T. W. Ng, and P. J. Meikle, "Metabolomics and ischaemic heart disease," *Clin. Sci.*,
6229 vol. 124, no. 5, pp. 289–306, Mar. 2013, doi: 10.1042/CS20120268.
- 6230 [195] V. Bodi, V. G. Marrachelli, O. Husser, F. J. Chorro, J. R. Viña, and D. Monleon, "Metabolomics in
6231 the diagnosis of acute myocardial ischemia," *J. Cardiovasc. Transl. Res.*, vol. 6, no. 5, pp. 808–815,
6232 Oct. 2013, doi: 10.1007/s12265-013-9505-9.
- 6233 [196] Y. G. Y. Y.-G. Wang, Y. G. Y. Y.-G. Wang, T.-F. F. Ma, M. Li, and S.-L. L. Gu, "Dynamic metabolites
6234 profile of cerebral ischemia/reperfusion revealed by 1H NMR-based metabolomics contributes to
6235 potential biomarkers," *Int. J. Clin. Exp. Pathol.*, vol. 7, no. 7, pp. 4067–4075, 2014.
- 6236 [197] P. P. Liu *et al.*, "Discovery of Metabolite Biomarkers for Acute Ischemic Stroke Progression," *J.*
6237 *Proteome Res.*, vol. 16, no. 2, pp. 773–779, Feb. 2017, doi: 10.1021/acs.jproteome.6b00779.
- 6238 [198] E. Trushina and M. M. Mielke, "Recent advances in the application of metabolomics to Alzheimer's
6239 Disease," *Biochimica et Biophysica Acta - Molecular Basis of Disease*, vol. 1842, no. 8. Elsevier, pp.
6240 1232–1239, 2014, doi: 10.1016/j.bbadis.2013.06.014.
- 6241 [199] "Disposable paper-on-CMOS platform for real-time simultaneous detection of metabolites - Enlighten:
6242 Publications." <https://eprints.gla.ac.uk/206483/> (accessed Jan. 20, 2020).
- 6243 [200] B. Reddy *et al.*, "Point-of-care sensors for the management of sepsis," *Nature Biomedical Engineering*,
6244 vol. 2, no. 9. Nature Publishing Group, pp. 640–648, Sep. 01, 2018, doi: 10.1038/s41551-018-0288-9.
- 6245 [201] M. Eckerle *et al.*, "Metabolomics as a Driver in Advancing Precision Medicine in Sepsis,"
6246 *Pharmacotherapy*, vol. 37, no. 9, pp. 1023–1032, Sep. 2017, doi: 10.1002/phar.1974.
- 6247 [202] B. Mickiewicz *et al.*, "Integration of metabolic and inflammatory mediator profiles as a potential
6248 prognostic approach for septic shock in the intensive care unit," *Crit. Care*, vol. 19, no. 1, pp. 1–12,
6249 Jan. 2015, doi: 10.1186/s13054-014-0729-0.
- 6250 [203] S. M. Khan, A. Gumus, J. M. Nassar, and M. M. Hussain, "CMOS Enabled Microfluidic Systems for
6251 Healthcare Based Applications," *Adv. Mater.*, vol. 30, no. 16, pp. 1–26, 2018, doi:
6252 10.1002/adma.201705759.
- 6253 [204] G. M. Whitesides, "The origins and the future of microfluidics," *Nature*, vol. 442, no. 7101, pp. 368–
6254 373, 2006, doi: 10.1038/nature05058.
- 6255 [205] L. Gervais, N. De Rooij, and E. Delamarque, "Microfluidic chips for point-of-care
6256 immunodiagnosics," *Adv. Mater.*, vol. 23, no. 24, 2011, doi: 10.1002/adma.201100464.
- 6257 [206] P. Tabeling, *Introduction to microfluidics*. Oxford University Press, 2010.
- 6258 [207] C. K. Dixit and A. Kaushik, *Micro uidics for Biologists*. 2016.
- 6259 [208] H. Bruus, *Theoretical microfluidics*. Oxford University Press, 2008.
- 6260 [209] J. Castillo-León, "Microfluidics and Lab-on-a-Chip Devices: History and Challenges," in *Lab-on-a-
6261 Chip Devices and Micro-Total Analysis Systems*, Cham: Springer International Publishing, 2015, pp.
6262 1–15.
- 6263 [210] V. Jokinen and S. Franssila, "Capillarity in microfluidic channels with hydrophilic and hydrophobic
6264 walls," *Microfluid. Nanofluidics*, vol. 5, no. 4, pp. 443–448, 2008, doi: 10.1007/s10404-008-0263-y.
- 6265 [211] P. J. Ponce De Leon and L. F. Velásquez-García, "Optimization of capillary flow through open-
6266 microchannel and open-micropillar arrays," *J. Phys. D: Appl. Phys.*, vol. 49, no. 5, 2016, doi:
6267 10.1088/0022-3727/49/5/055501.
- 6268 [212] E. Berthier, A. M. Dostie, U. N. Lee, J. Berthier, and A. B. Theberge, "Open Microfluidic Capillary
6269 Systems," *Analytical Chemistry*, vol. 91, no. 14. American Chemical Society, pp. 8739–8750, Jul. 01,
6270 2019, doi: 10.1021/acs.analchem.9b01429.
- 6271 [213] A. Olanrewaju, M. Beaugrand, M. Yafia, and D. Juncker, "Capillary microfluidics in microchannels:
6272 From microfluidic networks to capillarie circuits," *Lab Chip*, vol. 18, no. 16, pp. 2323–2347, 2018,
6273 doi: 10.1039/c8lc00458g.
- 6274 [214] A. Kreider *et al.*, "Functionalization of PDMS modified and plasma activated two-component
6275 polyurethane coatings by surface attachment of enzymes," *Appl. Surf. Sci.*, vol. 273, pp. 562–569,
6276 2013, doi: 10.1016/j.apsusc.2013.02.080.

- 6277 [215] E. Fialová, K. Zdeňková, E. Jablonská, K. Demnerová, and J. Ovesná, “Digital polymerase chain
6278 reaction: Principle and applications,” *Chem. List.*, vol. 113, no. 9, pp. 545–552, Sep. 2019, doi:
6279 10.5772/intechopen.86491.
- 6280 [216] B. Nagy, M. A. Al-Rawhani, B. C. Cheah, M. P. Barrett, and D. R. S. Cumming, “Immunoassay
6281 Multiplexing on a Complementary Metal Oxide Semiconductor Photodiode Array,” *ACS Sensors*, vol.
6282 3, no. 5, pp. 953–959, May 2018, doi: 10.1021/acssensors.7b00972.
- 6283 [217] B. Hayes, C. Murphy, A. Crawley, and R. O’Kennedy, “Developments in Point-of-Care Diagnostic
6284 Technology for Cancer Detection,” *Diagnostics*, vol. 8, no. 2, p. 39, Jun. 2018, doi:
6285 10.3390/diagnostics8020039.
- 6286 [218] Y. Uludag *et al.*, “An integrated lab-on-a-chip-based electrochemical biosensor for rapid and sensitive
6287 detection of cancer biomarkers,” *Anal. Bioanal. Chem.*, vol. 408, no. 27, pp. 7775–7783, Nov. 2016,
6288 doi: 10.1007/s00216-016-9879-z.
- 6289 [219] T. Zhang, Y. He, J. Wei, and L. Que, “Nanostructured optical microchips for cancer biomarker
6290 detection,” *Biosens. Bioelectron.*, vol. 38, no. 1, pp. 382–388, Oct. 2012, doi:
6291 10.1016/j.bios.2012.06.029.
- 6292 [220] A. I. Barbosa, P. Gehlot, K. Sidapra, A. D. Edwards, and N. M. Reis, “Portable smartphone quantitation
6293 of prostate specific antigen (PSA) in a fluoropolymer microfluidic device,” *Biosens. Bioelectron.*, vol.
6294 70, pp. 5–14, Aug. 2015, doi: 10.1016/j.bios.2015.03.006.
- 6295 [221] S. Sharma, J. Zapatero-Rodríguez, P. Estrela, and R. O’Kennedy, “Point-of-Care diagnostics in low
6296 resource settings: Present status and future role of microfluidics,” *Biosensors*, vol. 5, no. 3. MDPI AG,
6297 pp. 577–601, 2015, doi: 10.3390/bios5030577.
- 6298 [222] “United Kingdom | Sigma-Aldrich.” <https://www.sigmaaldrich.com/united-kingdom.html> (accessed
6299 Jan. 31, 2020).
- 6300 [223] C. S. Pundir, S. Lata, and V. Narwal, “Biosensors for determination of D and L- amino acids: A
6301 review,” *Biosensors and Bioelectronics*, vol. 117. Elsevier Ltd, pp. 373–384, Oct. 15, 2018, doi:
6302 10.1016/j.bios.2018.06.033.
- 6303 [224] B. Hoeben, F. Gunneweg Bsc, and B. W. Hoeben Bsc, “A critical review on glutamate sensing,” doi:
6304 10.13140/RG.2.1.2450.7360.
- 6305 [225] P. Rahimi and Y. Joseph, “Enzyme-based biosensors for choline analysis: A review,” *TrAC - Trends*
6306 *Anal. Chem.*, vol. 110, pp. 367–374, 2019, doi: 10.1016/j.trac.2018.11.035.
- 6307 [226] V. Yamkamon *et al.*, “Development of sarcosine quantification in urine based on enzyme-coupled
6308 colorimetric method for prostate cancer diagnosis,” *EXCLI J.*, vol. 17, pp. 467–478, May 2018, doi:
6309 10.17179/excli2018-1245.
- 6310 [227] M. M. F. Choi, “Progress in enzyme-based biosensors using optical transducers,” *Microchimica Acta*,
6311 vol. 148, no. 3–4, pp. 107–132, Dec. 2004, doi: 10.1007/s00604-004-0273-8.
- 6312 [228] P. Fossati, L. Prencipe, and G. Berti, “Enzymic creatinine assay: a new colorimetric method based on
6313 hydrogen peroxide measurement,” *Clin. Chem.*, vol. 29, no. 8, pp. 1494–1496, Aug. 1983, doi:
6314 10.1093/clinchem/29.8.1494.
- 6315 [229] Y. H. Kwak *et al.*, “A simple and low-cost biofilm quantification method using LED and CMOS image
6316 sensor,” *J. Microbiol. Methods*, vol. 107, pp. 150–156, 2014, doi: 10.1016/j.mimet.2014.10.004.
- 6317 [230] Y. W. Chang, P. C. Yu, Y. T. Huang, and Y. S. Yang, “A CMOS-compatible optical biosensing system
6318 based on visible absorption spectroscopy,” *IEEE Conf. Electron Devices Solid-State Circuits 2007*,
6319 *EDSSC 2007*, pp. 1099–1102, 2007, doi: 10.1109/EDSSC.2007.4450320.
- 6320 [231] C. Dincer, R. Bruch, A. Kling, P. S. Dittrich, and G. A. Urban, “Multiplexed Point-of-Care Testing –
6321 xPOCT,” *Trends Biotechnol.*, vol. 35, no. 8, pp. 728–742, 2017, doi: 10.1016/j.tibtech.2017.03.013.
- 6322 [232] V. Srinivasan, V. Pamula, M. Pollack, and R. Fair, “A digital microfluidic biosensor for multianalyte
6323 detection,” in *Proceedings of the IEEE Micro Electro Mechanical Systems (MEMS)*, 2003, pp. 327–
6324 330, doi: 10.1109/memsys.2003.1189752.
- 6325 [233] D. Wang, C. Ha, C. B. Park, and Y. Joo, “Spectrophotometer on a focal-plane-array chip for the high-
6326 throughput analysis of enzymatic reaction,” *Conf. Proc. - Lasers Electro-Optics Soc. Annu. Meet.*, vol.
6327 1, pp. 19–20, 2003, doi: 10.1109/leos.2003.1251579.
- 6328 [234] Y. T. Wu, C. E. Yang, C. H. Ko, Y. N. Wang, C. C. Liu, and L. M. Fu, “Microfluidic detection platform
6329 with integrated micro-spectrometer system,” *Chem. Eng. J.*, vol. 393, no. February, p. 124700, 2020,
6330 doi: 10.1016/j.cej.2020.124700.
- 6331 [235] J. Liu, Z. Geng, Z. Fan, J. Liu, and H. Chen, “Point-of-care testing based on smartphone: The current
6332 state-of-the-art (2017–2018),” *Biosens. Bioelectron.*, vol. 132, pp. 17–37, May 2019, doi:
6333 10.1016/j.bios.2019.01.068.
- 6334 [236] C. Fernández-Sánchez, C. J. McNeil, K. Rawson, O. Nilsson, H. Y. Leung, and V. Gnanapragasam,
6335 “One-step immunostrip test for the simultaneous detection of free and total prostate specific antigen in

- 6336 serum," *J. Immunol. Methods*, vol. 307, no. 1–2, pp. 1–12, Dec. 2005, doi: 10.1016/j.jim.2005.08.014.
- 6337 [237] L. Ekhlaspour *et al.*, "Comparative Accuracy of 17 Point-of-Care Glucose Meters," *J. Diabetes Sci. Technol.*, vol. 11, no. 3, pp. 558–566, 2017, doi: 10.1177/1932296816672237.
- 6338 [238] "Abbott | Global Healthcare & Research." <https://www.abbott.co.uk/> (accessed Jan. 20, 2020).
- 6339 [239] "Ion Torrent | Thermo Fisher Scientific - UK." <https://www.thermofisher.com/uk/en/home/brands/ion-torrent.html> (accessed Jan. 30, 2020).
- 6340 [240] "US8691509B2 - Multi-primer amplification method for barcoding of target nucleic acids - Google Patents." <https://patents.google.com/patent/US8691509B2/en?q=~patent%2FUS20100291666A1> (accessed Jan. 17, 2020).
- 6341 [241] V. Haag, "(12) United States Patent," 2017, doi: 10.1109/MEMSYS.
- 6342 [242] C. Accarino *et al.*, "Noise characteristics with CMOS sensor array scaling," *Meas. J. Int. Meas. Confed.*, vol. 152, Feb. 2020, doi: 10.1016/j.measurement.2019.107325.
- 6343 [243] C. Hu, M. A. Al-Rawhani, B. C. Cheah, S. Velugotla, and D. R. S. Cumming, "Hybrid Dual Mode Sensor for Simultaneous Detection of Two Serum Metabolites," *IEEE Sens. J.*, vol. 18, no. 2, pp. 484–493, Jan. 2018, doi: 10.1109/JSEN.2017.2774359.
- 6344 [244] B. M. P. Brigham, W. H. Stein, and S. Moore, "THE CONCENTRATIONS OF CYSTEINE AND CYSTINE IN Phenylalanine ETyposine," pp. 1633–1638, 1960.
- 6345 [245] M. J. Hirsch, J. H. Growdon, and R. J. Wurtman, "Relations between dietary choline or lecithin intake, serum choline levels, and various metabolic indices," *Metabolism*, vol. 27, no. 8, pp. 953–960, 1978, doi: 10.1016/0026-0495(78)90139-7.
- 6346 [246] A. B. R. Garnotel and A. H. C. Arndt, "CASE REPORT A Young Adult with Sarcosinemia . No Benefit from Long Duration Treatment with Memantine," 2012, doi: 10.1007/8904.
- 6347 [247] J. Bakker, "Increased blood lactate levels : a marker of ...?," no. June, pp. 1–10, 2003.
- 6348 [248] K. D. EDWARDS and H. M. WHYTE, "Plasma creatinine level and creatinine clearance as tests of renal function," *Australas. Ann. Med.*, vol. 8, p. 218–224, Aug. 1959, doi: 10.1111/imj.1959.8.3.218.
- 6349 [249] S. Natarajan, D. A. Chang-Yen, and B. K. Gale, "Large-area, high-aspect-ratio SU-8 molds for the fabrication of PDMS microfluidic devices," *J. Micromechanics Microengineering*, vol. 18, no. 4, 2008, doi: 10.1088/0960-1317/18/4/045021.
- 6350 [250] V. F. Annese *et al.*, "The Multicorder: A Handheld Multimodal Metabolomics-on-CMOS Sensing Platform," in *Proceedings - 2019 8th International Workshop on Advances in Sensors and Interfaces, IWASI 2019*, 2019, doi: 10.1109/IWASI.2019.8791347.
- 6351 [251] B. C. Cheah *et al.*, "An Integrated Circuit for Chip-Based Analysis of Enzyme Kinetics and Metabolite Quantification," *IEEE Trans. Biomed. Circuits Syst.*, vol. 10, no. 3, pp. 721–730, Jun. 2016, doi: 10.1109/TBCAS.2015.2487603.
- 6352 [252] B. C. Cheah, "METABOLOMIC SENSING SYSTEM FOR PERSONALISED MEDICINE USING AN INTEGRATED CMOS SENSOR," no. July, 2016.
- 6353 [253] M. Al-Rawhani, D. Cumming, D. Chitnis, and S. Collins, "Photocurrent dependent response of a SPAD biased by a charge pump," *Proc. - IEEE Int. Symp. Circuits Syst.*, pp. 789–792, 2011, doi: 10.1109/ISCAS.2011.5937684.
- 6354 [254] "NUCLEO-F334R8 - STM32 Nucleo-64 development board with STM32F334R8 MCU, supports Arduino and ST morpho connectivity - STMicroelectronics." <https://www.st.com/en/evaluation-tools/nucleo-f334r8.html> (accessed Feb. 05, 2020).
- 6355 [255] ST, "STM32F303CC - Mainstream Mixed signals MCUs ARM Cortex-M4 core with DSP and FPU, 256 Kbytes Flash, 72 MHz CPU, MPU, CCM, 12-bit ADC 5 MSPS, PGA, comparators - STMicroelectronics." <https://www.st.com/en/microcontrollers-microprocessors/stm32f303cc.html> (accessed Nov. 25, 2020).
- 6356 [256] "Mbed Compiler Workspace Management." [https://ide.mbed.com/compiler/#nav:/](https://ide.mbed.com/compiler/#nav:/;); (accessed Feb. 05, 2020).
- 6357 [257] P. Abgrall and A. M. Gué, "Lab-on-chip technologies: Making a microfluidic network and coupling it into a complete microsystem - A review," *J. Micromechanics Microengineering*, vol. 17, no. 5, 2007, doi: 10.1088/0960-1317/17/5/R01.
- 6358 [258] B. C. Cheah and D. R. S. Cumming, "Metabolomics on CMOS for personalised medicine," in *CMOS Circuits for Biological Sensing and Processing*, Springer International Publishing, 2017, pp. 23–46.
- 6359 [259] T. Datta-Chaudhuri, E. Smela, and P. A. Abshire, "System-on-Chip Considerations for Heterogeneous Integration of CMOS and Fluidic Bio-Interfaces," *IEEE Trans. Biomed. Circuits Syst.*, vol. 10, no. 6, pp. 1129–1142, Dec. 2016, doi: 10.1109/TBCAS.2016.2522402.
- 6360 [260] B. K. Gale *et al.*, "A review of current methods in microfluidic device fabrication and future commercialization prospects," *Inventions*, vol. 3, no. 3, 2018, doi: 10.3390/inventions3030060.
- 6361 [261] G. T. Roman and R. T. Kennedy, "Fully integrated microfluidic separations systems for biochemical

- 6395 analysis,” *J. Chromatogr. A*, vol. 1168, no. 1–2, pp. 170–188, 2007, doi:
6396 10.1016/j.chroma.2007.06.010.
- 6397 [262] F. Bragheri, R. Martínez Vázquez, and R. Osellame, “Microfluidics,” in *Three-Dimensional*
6398 *Microfabrication Using Two-Photon Polymerization*, Elsevier, 2020, pp. 493–526.
- 6399 [263] J. M. Bustillo, R. T. Howe, and R. S. Muller, “Surface micromachining for microelectromechanical
6400 systems,” *Proc. IEEE*, vol. 86, no. 8, pp. 1552–1573, 1998, doi: 10.1109/5.704260.
- 6401 [264] Y.-K. Hsieh *et al.*, “Direct Micromachining of Microfluidic Channels on Biodegradable Materials
6402 Using Laser Ablation,” *Polymers (Basel)*, vol. 9, no. 12, p. 242, Jun. 2017, doi:
6403 10.3390/polym9070242.
- 6404 [265] “Fluidic Factory 3D Printing System (Using Coc).” [https://www.dolomite-](https://www.dolomite-microfluidics.com/product/fluidic-factory-3d-printer/)
6405 [microfluidics.com/product/fluidic-factory-3d-printer/](https://www.dolomite-microfluidics.com/product/fluidic-factory-3d-printer/) (accessed Jan. 23, 2020).
- 6406 [266] R. Mukhopadhyay, “When PDMS isn’t the best,” *Anal. Chem.*, vol. 79, no. 9, pp. 3249–3253, 2007,
6407 doi: 10.1021/ac071903e.
- 6408 [267] F. Rusmini, Z. Zhong, and J. Feijen, “Protein immobilization strategies for protein biochips,”
6409 *Biomacromolecules*, vol. 8, no. 6, pp. 1775–1789, 2007, doi: 10.1021/bm061197b.
- 6410 [268] Y. Asanomi, H. Yamaguchi, M. Miyazaki, and H. Maeda, “Enzyme-immobilized microfluidic process
6411 reactors,” *Molecules*, vol. 16, no. 7, pp. 6041–6059, 2011, doi: 10.3390/molecules16076041.
- 6412 [269] K. A. Heyries, C. A. Marquette, and L. J. Blum, “Straightforward protein immobilization on Sylgard
6413 184 PDMS microarray surface,” *Langmuir*, vol. 23, no. 8, pp. 4523–4527, 2007, doi:
6414 10.1021/la070018o.
- 6415 [270] C. A. Marquette and L. J. Blum, “Direct immobilization in poly(dimethylsiloxane) for DNA, protein
6416 and enzyme fluidic biochips,” *Anal. Chim. Acta*, vol. 506, no. 2, pp. 127–132, 2004, doi:
6417 10.1016/j.aca.2003.11.015.
- 6418 [271] L. Betancor *et al.*, “Glutaraldehyde in Protein Immobilization,” pp. 57–64, 2006, doi: 10.1007/978-1-
6419 59745-053-9_5.
- 6420 [272] T. Honda, M. Miyazaki, H. Nakamura, and H. Maeda, “Immobilization of enzymes on a microchannel
6421 surface through cross-linking polymerization,” *Chem. Commun.*, no. 40, pp. 5062–5064, 2005, doi:
6422 10.1039/b510605b.
- 6423 [273] R. A. Williams and H. W. Blanch, “Covalent immobilization of protein monolayers for biosensor
6424 applications,” *Biosens. Bioelectron.*, vol. 9, no. 2, pp. 159–167, 1994, doi: 10.1016/0956-
6425 5663(94)80108-8.
- 6426 [274] E. Ghafar-Zadeh, M. Sawan, and D. Therriault, “Novel direct-write CMOS-based laboratory-on-chip:
6427 Design, assembly and experimental results,” *Sensors Actuators, A Phys.*, vol. 134, no. 1, pp. 27–36,
6428 2007, doi: 10.1016/j.sna.2006.05.022.
- 6429 [275] F. J. Blanco *et al.*, “Microfluidic-optical integrated CMOS compatible devices for label-free
6430 biochemical sensing,” *J. Micromechanics Microengineering*, vol. 16, no. 5, pp. 1006–1016, 2006, doi:
6431 10.1088/0960-1317/16/5/018.
- 6432 [276] B. Zhang, Q. Dong, C. E. Korman, Z. Li, and M. E. Zaghoul, “Flexible packaging of solid-state
6433 integrated circuit chips with elastomeric microfluidics,” *Sci. Rep.*, vol. 3, pp. 1–8, 2013, doi:
6434 10.1038/srep01098.
- 6435 [277] K. F. Brennan and A. S. Brown, *Theory of Modern Electronic Semiconductor Devices*. Hoboken, NJ,
6436 USA: John Wiley & Sons, Inc., 2002.
- 6437 [278] Y. Huang and A. J. Mason, “Lab-on-CMOS integration of microfluidics and electrochemical sensors,”
6438 *Lab Chip*, vol. 13, no. 19, pp. 3929–3934, 2013, doi: 10.1039/c3lc50437a.
- 6439 [279] C. P. Hsu, P. C. Chen, and Y. L. Wang, “A novel packaging technology for disposable FET-based
6440 biosensors with microfluidic channels,” *2017 IEEE 12th Int. Conf. Nano/Micro Eng. Mol. Syst. NEMS*
6441 *2017*, pp. 375–378, 2017, doi: 10.1109/NEMS.2017.8017045.
- 6442 [280] H. Lee, Y. Liu, D. Ham, and R. M. Westervelt, “Integrated cell manipulation system -
6443 CMOS/microfluidic hybrid,” *Lab Chip*, vol. 7, no. 3, pp. 331–337, 2007, doi: 10.1039/b700373k.
- 6444 [281] Y. Hwang and R. N. Candler, “Non-planar PDMS microfluidic channels and actuators: A review,” *Lab*
6445 *Chip*, vol. 17, no. 23, pp. 3948–3959, 2017, doi: 10.1039/c7lc00523g.
- 6446 [282] A. Wu, L. Wang, E. Jensen, R. Mathies, and B. Boser, “Modular integration of electronics and
6447 microfluidic systems using flexible printed circuit boards,” *Lab Chip*, vol. 10, no. 4, pp. 519–521,
6448 2010, doi: 10.1039/b922830f.
- 6449 [283] D. Welch and J. B. Christen, “Seamless integration of CMOS and microfluidics using flip chip
6450 bonding,” *J. Micromechanics Microengineering*, vol. 23, no. 3, 2013, doi: 10.1088/0960-
6451 1317/23/3/035009.
- 6452 [284] M. Muluneh and D. Issadore, “A multi-scale PDMS fabrication strategy to bridge the size mismatch
6453 between integrated circuits and microfluidics,” *Lab Chip*, vol. 14, no. 23, pp. 4552–4558, 2014, doi:

- 6454 10.1039/c4lc00869c.
- 6455 [285] T. Trantidou, Y. Elani, E. Parsons, and O. Ces, "Hydrophilic surface modification of pdms for droplet
6456 microfluidics using a simple, quick, and robust method via pva deposition," *Microsystems Nanoeng.*,
6457 vol. 3, no. April 2016, 2017, doi: 10.1038/micronano.2016.91.
- 6458 [286] "DDBST - DDBST GmbH." <http://www.ddbst.com/> (accessed Feb. 17, 2020).
- 6459 [287] "Viscosity of Blood Plasma and Serum." [https://www.rheosense.com/application/viscosity-of-blood-](https://www.rheosense.com/application/viscosity-of-blood-plasma-and-serum)
6460 [plasma-and-serum](https://www.rheosense.com/application/viscosity-of-blood-plasma-and-serum) (accessed Feb. 17, 2020).
- 6461 [288] S. Lewin, "Blood Serum Surface Tension and its Potential," *Br. J. Haematol.*, vol. 22, no. 5, pp. 561–
6462 566, May 1972, doi: 10.1111/j.1365-2141.1972.tb05702.x.
- 6463 [289] E. Hrnčír and J. Rosina1, "Surface Tension of Blood," 1997.
- 6464 [290] A. Syakur, Hermawan, and H. Sutanto, "Determination of hydrophobic contact angle of epoxy resin
6465 compound silicon rubber and silica," in *International Conference on Electrical Engineering, Computer
6466 Science and Informatics (EECSI)*, 2016, vol. 3, no. 1, p. 012025, doi: 10.1088/1757-
6467 899X/190/1/012025.
- 6468 [291] Microchem, "SU-8 3000 Permanent Epoxy," *Prod. Datasheet*, vol. 20, 2000, doi:
6469 10.1146/annurev.matsci.28.1.153.
- 6470 [292] R. Seghir and S. Arscott, "Sensors and Actuators A : Physical Extended PDMS stiffness range for
6471 flexible systems," *Sensors Actuators A. Phys.*, vol. 230, pp. 33–39, 2015, doi:
6472 10.1016/j.sna.2015.04.011.
- 6473 [293] "EUROPRACTICE | IC Service." <https://europactice-ic.com/> (accessed Feb. 10, 2020).
- 6474 [294] "EPO-TEK ® H74," 2017. Accessed: Feb. 10, 2020. [Online]. Available: www.epotek.com.
- 6475 [295] "EPO-TEK ® 302-3M Technical Data Sheet For Reference Only Optically Transparent Epoxy," 2018.
6476 Accessed: Feb. 10, 2020. [Online]. Available: www.epotek.com.
- 6477 [296] Abbott, "Alere Afinion AS100 Analyzer," 2018, [Online]. Available:
6478 <https://www.alere.com/en/home/product-details/afinion-as100-analyzer.html>.
- 6479 [297] "Optical Interface - an overview | ScienceDirect Topics."
6480 <https://www.sciencedirect.com/topics/engineering/optical-interface> (accessed Mar. 25, 2020).
- 6481 [298] "Refractive index of (C₂H₆OSi)_n (Polydimethylsiloxane, PDMS) - Query-NIR."
6482 <https://refractiveindex.info/?shelf=organic&book=polydimethylsiloxane&page=Query-NIR>
6483 (accessed Mar. 25, 2020).
- 6484 [299] G. M. Hale and M. R. Querry, "Optical Constants of Water in the 200-nm to 200- μ m Wavelength
6485 Region," *Appl. Opt.*, vol. 12, no. 3, p. 555, Mar. 1973, doi: 10.1364/ao.12.000555.
- 6486 [300] *IUPAC Compendium of Chemical Terminology*. IUPAC, 2009.
- 6487 [301] C. Rensch, "Creation of Small Microdrops," *MicroFab Technol. Inc.*, pp. 1–51, 2006.
- 6488 [302] D. Ioannou, W. Huda, and A. F. Laine, "Circle recognition through a 2D Hough Transform and radius
6489 histogramming," *Image Vis. Comput.*, vol. 17, no. 1, pp. 15–26, Jan. 1999, doi: 10.1016/S0262-
6490 8856(98)00090-0.
- 6491 [303] H. Liu, S. Lin, and Y. Qian, "Detecting Persons using Hough Circle Transform in Surveillance Video.
6492 DETECTING PERSONS USING HOUGH CIRCLE TRANSFORM IN SURVEILLANCE VIDEO,"
6493 2010.
- 6494 [304] I. Roy and M. N. Gupta, "Freeze-drying of proteins: some emerging concerns," *Biotechnol. Appl.
6495 Biochem.*, vol. 39, no. 2, p. 165, 2004, doi: 10.1042/ba20030133.
- 6496 [305] Astm, "Standard Guide for Accelerated Aging of Sterile Medical Device Packages 1," *Astm F1980-
6497 02*, vol. 11, pp. 1–6, 2002, doi: 10.1520/D7102-10.Copyright.
- 6498 [306] C. Hu *et al.*, "Disposable Paper-on-CMOS Platform for Real-time Simultaneous Detection of
6499 Metabolites," *IEEE Trans. Biomed. Eng.*, pp. 1–1, 2020, doi: 10.1109/tbme.2019.2962239.
- 6500 [307] X. Yang, O. Forouzan, T. P. Brown, and S. S. Shevkoplyas, "Integrated separation of blood plasma
6501 from whole blood for microfluidic paper-based analytical devices," *Lab Chip*, vol. 12, no. 2, pp. 274–
6502 280, 2012, doi: 10.1039/c1lc20803a.
- 6503 [308] T. Songjaroen, W. Dungchai, O. Chailapakul, C. S. Henry, and W. Laiwattanapaisal, "Blood separation
6504 on microfluidic paper-based analytical devices," *Lab Chip*, vol. 12, no. 18, pp. 3392–3398, 2012, doi:
6505 10.1039/c2lc21299d.
- 6506 [309] J. A. Hanley and B. J. McNeil, "The Meaning and Use of the Area under a Receiver Operating
6507 Characteristic (ROC) Curve1."
- 6508 [310] I. T. Jolliffe and J. Cadima, "Principal component analysis: A review and recent developments,"
6509 *Philosophical Transactions of the Royal Society A: Mathematical, Physical and Engineering Sciences*,
6510 vol. 374, no. 2065. Royal Society of London, Apr. 13, 2016, doi: 10.1098/rsta.2015.0202.
- 6511 [311] S. B. Kotsiantis, "Decision trees: A recent overview," *Artificial Intelligence Review*, vol. 39, no. 4.
6512 Springer, pp. 261–283, Apr. 29, 2013, doi: 10.1007/s10462-011-9272-4.

- 6513 [312] Q. Mai, "A review of discriminant analysis in high dimensions," *Wiley Interdisciplinary Reviews: Computational Statistics*, vol. 5, no. 3. John Wiley & Sons, Ltd, pp. 190–197, May 01, 2013, doi: 10.1002/wics.1257.
- 6514 [313] D. De Venuto and G. Mezzina, "FPGA-embedded serial SVM classifier for neuromuscular disorders assessment," in *Proceedings - 2018 International Conference on Computational Science and Computational Intelligence, CSCI 2018*, Dec. 2018, pp. 1392–1397, doi: 10.1109/CSCI46756.2018.00269.
- 6515 [314] A. Kataria, and M. D. Singh, "International Journal of Emerging Technology and Advanced Engineering A Review of Data Classification Using K-Nearest Neighbour Algorithm," 2008.
- 6516 [315] A. Yadav and J. M. Johnson, "Fault detection and classification technique for HVDC transmission lines using KNN," 2016. Accessed: Mar. 10, 2020. [Online]. Available: <https://www.researchgate.net/publication/304526301>.
- 6517 [316] T. Chen *et al.*, "Random forest in clinical metabolomics for phenotypic discrimination and biomarker selection," *Evidence-based Complement. Altern. Med.*, vol. 2013, 2013, doi: 10.1155/2013/298183.
- 6518 [317] A. L. and M. Wiener, "Classification and Regression by randomForest. R News 2," vol. 3, no. December 2002, pp. 18–22, 2003.
- 6519 [318] M. Kuhn, "Building predictive models in R using the caret package," *J. Stat. Softw.*, vol. 28, no. 5, pp. 1–26, 2008, doi: 10.18637/jss.v028.i05.
- 6520 [319] E. D. Crawford and P. A. Abrahamsson, "PSA-based Screening for Prostate Cancer: How Does It Compare with Other Cancer Screening Tests?," *European Urology*, vol. 54, no. 2. pp. 262–273, Aug. 2008, doi: 10.1016/j.eururo.2008.05.032.
- 6521 [320] Roche, "Cobas C 311 Analyzer," pp. 1–12, 2009, [Online]. Available: http://www.roche.hu/content/dam/roche_hungary/hu_HU/docs/cobas_c_311_en.pdf.
- 6522 [321] B. Hall, D. D. Wong, W. D. Rawlinson, M. B. Tracy, and S. K. Tracy, "A validation study: Assessing the reliability of the hand held StatStripXpress lactate meter to test lactate in amniotic fluid," *BMC Res. Notes*, vol. 7, no. 1, p. 935, Dec. 2014, doi: 10.1186/1756-0500-7-935.
- 6523 [322] J. X. J. Zhang and K. Hoshino, "Electrical Transducers," in *Molecular Sensors and Nanodevices*, Elsevier, 2014, pp. 169–232.
- 6524 [323] C. Shivinder Singh, M. Abhishek Bhardawaj, L. Col Ratnesh Shukla, M. Trimbak Jhadav, S. Lt Cdr Anoop Sharma, and D. Basannar, "The handheld blood lactate analyser versus the blood gas based analyser for measurement of serum lactate and its prognostic significance in severe sepsis," *Med. J. Armed Forces India*, vol. 72, pp. 325–331, 2016, doi: 10.1016/j.mjafi.2016.05.007.
- 6525 [324] J. M. Bonaventura, K. Sharpe, E. Knight, K. L. Fuller, R. K. Tanner, and C. J. Gore, "Reliability and accuracy of six hand-held blood lactate analysers," *J. Sport. Sci. Med.*, vol. 14, no. 1, pp. 203–214, 2014.
- 6526 [325] V. F. Annese and D. De Venuto, "On-line shelf-life prediction in perishable goods chain through the integration of WSN technology with a 1st order kinetic model," in *2015 IEEE 15th International Conference on Environment and Electrical Engineering, EEEIC 2015 - Conference Proceedings*, 2015, doi: 10.1109/EEEIC.2015.7165232.
- 6527 [326] V. F. Annese, G. E. Biccario, S. Cipriani, and D. De Venuto, "Organoleptic properties remote sensing and life-time prediction along the perishables goods supply-chain," in *Proceedings of the International Conference on Sensing Technology, ICST*, 2014, vol. 2014-Janua.
- 6528 [327] G. Maltezos, J. Lee, A. Rajagopal, K. Scholten, E. Kartalov, and A. Scherer, "Microfluidic blood filtration device," *Biomed. Microdevices*, vol. 13, no. 1, pp. 143–146, 2011, doi: 10.1007/s10544-010-9479-1.
- 6529 [328] K. Iwai, R. D. Sochol, and L. Lin, "Finger-powered, pressure-driven microfluidic pump," *Proc. IEEE Int. Conf. Micro Electro Mech. Syst.*, pp. 1131–1134, 2011, doi: 10.1109/MEMSYS.2011.5734629.
- 6530 [329] Hans Stork (Texas Instrument), "Economies of CMOS Scaling," 2005. [Online]. Available: https://www.nist.gov/system/files/documents/pml/div683/conference/Stork_2005.pdf.
- 6531 [330] "Multicorder DX – Multi-task Diagnostics." <https://www.multicorderdx.co.uk/> (accessed Jan. 20, 2020).
- 6532 [331] "University of Glasgow - Schools - School of Physics & Astronomy - Research - Research Groups - Particle Physics Experiment - Research Overview - GLADD - Infrastructure." <https://www.gla.ac.uk/schools/physics/research/groups/particlephysicsexperiment/research/gladd/infr astructure/> (accessed Feb. 10, 2020).
- 6533 [332] "Hesse & Knipps Bondjet 710 Wedge Bonder - TaraSemi.com." <https://www.tarasemi.com/product/hesse-knipps-bondjet-710-wedge-bonder/> (accessed Feb. 10, 2020).
- 6534
6535
6536
6537
6538
6539
6540
6541
6542
6543
6544
6545
6546
6547
6548
6549
6550
6551
6552
6553
6554
6555
6556
6557
6558
6559
6560
6561
6562
6563
6564
6565
6566
6567
6568
6569
6570
6571